Hydrogen (H2) generation from hydrogen atom-rich molecules catalyzed by transition-metal nanoalloys and the boosting role of visible light using gold plasmon

Naixin Kang

université de BORDEAUX

THÈSE PRÉSENTÉE
POUR OBTENIR LE GRADE DE

DOCTEUR DE

L'UNIVERSITÉ DE BORDEAUX

ÉCOLE DOCTORALE
SPÉCIALITÉ: CHIMIE ORGANIQUE

Par Naixin Kang

Génération de H_2 à partir de molécules riches en atomes d'hydrogène catalysée par des nano-alliages et accélération de ces réactions par la lumière visible grâce au plasmon de l'or

Sous la direction de :Jean-Luc POZZO
(co-directeur : Didier ASTRUC)

Soutenue le 21 Octobre 2022…

Membres du jury:

M. Jean-Marie BASSET	Professeur à KAUST, Thuwal,Arabie Saoudite	Rapporteur
M. Jean-Yves SAILLARD	Professeur Émérite, Université de Rennes 1	Rapporteur
Mme. Mona TREGUER-DELAPIERRE	Professeure à l'Université de Bordeaux	Examinateure
M. Jean-René HAMON,	Directeur de recherche au CNRS	Examinateur
M. Jean-Luc POZZO	Professeur à l'Université de Bordeaux	Directeur de thèse
M. Didier ASTRUC	Professeur à l'Université de Bordeaux	Co-directeur de thèse

Acknowledgment

This thesis was completed in the Institute des Sciences Moléculaires (ISM), UMR CNRS N° 5255, University of Bordeaux.

I would like to thank to my supervisors Prof. Didier Astruc and Prof. Jean-Luc Pozzo for their support over the last four years. Prof. Didier Astruc is very helpful to as my thesis co-director for his inspiring, patient instruction, insightful criticism and expert guidance on my thesis. His profound knowledge of chemistry, consistent and illuminating instructions, and his contributions of time and ideas, making my Ph.D. experience productive and stimulating. I also would like to be grateful to Prof. Jean-Luc Pozzo, a prestigious scientist, for his precious administrative and scientific help that has greatly facilitated this thesis.

I am also greatly indebted to the reviewers and jury members of the thesis, Prof. Jean-Marie Basset, Prof. Jean-Yves Saillard, Prof., Mona Treguer-Delapierre and Dr. Jean-René Hamon and for having accepted to evaluate my work.

I am greatly grateful to all permanent members of the CSH group in ISM, and in particular Dr. Murielle Berlande for her help in the lab. High tribute shall be paid to Sergio Moya, Lionel Salmon, Marta Martinez Moro, Eduardo Guisasola Cal, Emerson Coy and Bruno Espuche for their excellent collaborations and analyses on samples.

My sincere gratitude also goes to my former and current colleagues, including Fangyu Fu, Qi Wang, Changlong Wang, Wenjuan Wang, Yue Liu, Jianyu Wei of the CSH-group, and Shui Liu of the ORGA group. They gave me valuable advices and helped me solve numerous problems in my daily lab life.

I would like to warmly thank to my friends in Bordeaux: Fenghuan Zhao, Junjin Che, Chenhui Xia, Hongmei Zhu, Lei Hou and Tong Wu for the wonderful time spent with them.

I gratefully acknowledge the funding support from the China Scholarship Council for my 4 years of PhD. The Universities of Bordeaux and the CNRS are greatly acknowledged for research facilities and funding.

Last but not the least, my gratitude also extends to my parents who have been assisting, supporting and caring for me all of my life. Special thanks should also go to all my friends who give me continuous support and encouragement during my thesis.

Table of Content

Resume de la these en Francais

'utilisation des sources d'énergie d'origine fossile produit des gaz à effet de serre dangereux en raison du réchauffement climatique qu'ils provoquent et une pollution considérable dommageable pour la santé humaine. C'est pourquoi il existe une énorme demande de sources d'énergies alternatives telles que H_2 dont la combustion ne produit que de l'eau. Cependant, les risques d'explosion doivent être pris en compte. C'est pourquoi le stockage de H_2 dans des petites molécules stables telles que NaBH4 ou l'ammonia-borane (AB) libérant H_2 par hydrolyse pourrait constituer une solution. Cependant, la lenteur de ces réactions nécessite le développement de catalyseurs efficaces.

Cette thèse adresse ce défi en cinq chapitres de recherche démontrant la mise au point de nouveaux nano-catalyseurs très efficaces avec des systèmes solubles dans l'eau de type “dendrizymes” ou des catalyseurs hétérogènes.

Dans le 1er chapitre, sont reporté des nano-catalyseurs efficaces pour l'hydrolyse de NaBH4 supportés par des dendrimères “click”, c'est-à-dire synthétisés par catalyse au Cu(I) de la cycloaddition d'azotures en terminaison de branches dendritiques avec des dendrons comportant un alcyne au point focal. Les connecteurs triazole ainsi formés servent de ligands doux stabilisant les nanocatalyseurs de l'hydrolyse de NaBH4. Les meilleurs catalyseurs sont des nano-alliages Pt-Co (1/1).

Dans le 2ème chapitre, H_2 est généré par hydrolyse de NaBH4 ou AB catalysée par des nano-alliages Au-métal de transition stabilisés comme au premier chapitre, mais la présence d'or permet d'accélérer les réactions par transfert d'électron chaud de l'or vers le métal actif grâce au plasmon de l'or excité en lumière visible. Cet enrichissement du métal actif permet l'addition oxydante de la liaison O-H de l'eau en surface. Les meilleurs métaux sont Rh, Ru et Pt et, parmi les métaux abondants, Co.

Dans le 3ème chapitre, les MOF de type réseaux zéolite imidazolate (ZIF) sont utilisés comme catalyseurs hétérogènes en impliquant à nouveau l'effet accélérateur de la lumière visible grâce à l'excitation du plasmon de l'or dans les nano-alliages Au-Ni pour lesquels une synergie très positive en catalyse est aussi démontrée. La fréquence de nombres de tours catalytiques est ainsi 3,4 plus grande qu'avec Ni@ZIF-8 seul dans le noir. Les calculs DFT et les mesures cinétiques confirment que l'un des atomes de H_2 provient du borane et l'autre de l'eau dont la coupure est l'étape déterminante de la réaction.

Dans le 4ème chapitre, le support hétérogène ZIF-8 est de nouveau utilisé pour la production de H_2 par méthanolyse de AB catalysée par les nano-alliages Au-Pd en tandem avec la semi-hydrogénation des alcynes (sélective et d'importance industrielle). L'irradiation en lumière visible qui excite le plasmon de l'or permet d'accélérer à la fois les deux réactions en jeu par enrichissement du site Pd, lequel provoque ainsi plus facilement l'addition oxydante de la coupure de la liaison O-H du méthanol dont l'étude cinétique montre qu'elle constitue l'étape déterminante pour la vitesse de la méthanolyse.

Dans le 5ème chapitre, des complexes sandwich du fer sont comparés comme réservoirs recyclables de H_2. Les complexes neutres riches en hydrure réagissent avec le méthanol ou l'éthanol en présence de catalyseur commercial Pd/C en générant H_2 et les complexes du fer pauvres en hydrure (l'un des atomes H de H_2 provient de l'alcool). A l'inverse, ces derniers régénèrent les complexes riches en hydrure en présence de H_2 et de Pd/C dans le THF.

En conclusion, de nouveaux nanocatalyseurs et photocatalyseurs très efficaces ont été mis au point et optimisés, générant H_2 par hydrolyse ou méthanolyse de molécules riches en atomes H dans des conditions ambiantes, et des complexes du fer ont été testés comme réservoirs de H_2.

Chapter 1. General Introduction

1.1. Hydrogen source

Although fossil fuels remain the main energy supplier for our society, concerns about unsustainable development are growing. As a result, there is a strong demand for the development of efficient, low-cost, clean and diverse energy storage systems. Among the solutions proposed, hydrogen is considered the most promising energy carrier with "clean, efficient potential in stationary, portable and transport applications "[1,2] due to its high energy density (142 MJ/kg), abundant earth resources and sustainability. The concept of a "hydrogen economy", first proposed in the mid-1970s, as a viable solution to energy and environmental problems remedy, has gained considerable momentum, if hydrogen can be stored and delivered safely and efficiently[3-6] .

Storage of hydrogen can be physical or chemical,[7] depending on whether it is stored as a hydrogen molecule or in a chemical bond of a material. Liquid-phase hydrogen storage materials (LHSMs), which store hydrogen energy in chemical bonds, are currently considered promising candidates for safe and efficient hydrogen production via catalytic dehydrogenation.[8] Both homogeneous[9-11] and heterogeneous catalysts are essentially designed to enhance hydrogen production from LHSMs as well as to suppress side reactions.[12,13] In this context, metal nanoparticles (MNPs) with tunable properties catalysts exhibit high catalytic performance for catalytic dehydrogenation due to their high activity, ease of separation, recovery and ease of handling. Some excellent reviews have been summarised in the corresponding sub-areas of research, such as the hydrolysis of sodium borohydride[14] and aminoborane,[15-18] as well as the dehydrogenation of metal borohydrides and formic acid.

1.1.1. Hydrogen from sodium borohydride

$NaBH_4$ is by far the best known hydrogen carrier because of its high hydrogen storage capacity (10.8 wt %) and its ease of dissolution in alkaline aqueous solutions, allowing for safe, stable and long-term storage (except for its slow reaction with water). In the case of hydrogen production by thermal decomposition, high temperatures (>500˚C) are required due to the high thermal stability of $NaBH_4$ and the thermal decomposition process is very complex, mainly due to the formation of several intermediate products and gases.[17] $NaBH_4$ reacts slowly with water under ambient conditions, so it is not an ideal source of H_2, but the hydrolysis of $NaBH_4$ has still long been considered to be by catalysis. The seminal study by Schlesinger et al. in 1953 had already shown that 4 equivalents of hydrogen could be released during the acidic homogeneous catalytic hydrolysis of $NaBH_4$ in water.

(**Equation 1.1**).[18]

$$NaBH_4 + 2H_2O \rightarrow NaBO_2 + 4H_2 \uparrow \qquad (\mathbf{1.1})$$

This route is very attractive, because it produces only hydrogen gas that can be directly used in a proton exchange membrane fuel cell. Excess of water is needed, however, due to the moderate $NaBH_4$ solubility

and the hydrolysis of $NaBH_4$ usually forming mixtures of hydrated sodium metaborates (**Equation 1.2**).

$$NaBH_4 + (2 + x)\ H_2O \rightarrow NaBO_2 \cdot xH_2O + 4H_2 \uparrow$$

1.1.2 Hydrogen from ammonia borane

Ammonia borane (NH_3BH_3, AB) is a stable solid at room temperature with a density of 0.780 g cm-3 and a melting point of 112-114 °C.[19-22] Due to its high hydrogen content (19.6 wt%), low molecular weight (30.9 g mol^{-1}) and non-toxicity and environmental friendliness, NH_3BH3 has been considered as a promising material for hydrogen storage. In general, hydrogen release from NH_3BH_3 is by solid-phase thermal decomposition or catalytic leaching under mild conditions (hydrolysis and methanolysis).

$$NH_3BH_3 + 2H_2O \rightarrow NH_4BO_2 + 3H_2 \uparrow \quad (\mathbf{1.3})$$

$$NH_3BH_3 + 4MeOH \rightarrow NH_4B(OMe)_4 + 3H_2 \uparrow \quad (\mathbf{1.4})$$

Considerable investigation has been undertaken in the catalytic dehydrogenation of NH_3BH_3 for use in HER. Xu's group pioneered the use of highly efficient noble metal catalysts (Pt, Rh, Pd, Ru) for the hydrolysis of AB.[23] Subsequently, a series of excellent works have been reported demonstrating the advantages of ammonia borane as a potential hydrogen storage material compared to many other hydrogen storage materials. In our group, a series of transition metal nanocatalysts have been applied to hydrogen production by AB hydrolysis,[21, 24-28] and their mechanisms have been investigated, revealing that the oxidative addition of aqueous O-H bonds is the decisive step in catalyzing the dehydrogenation of AB

1.1.3 Hydrogen from other source

Besides the popular boron-based materials, metal hydrides, liquid organic hydrides are also promising candidate for hydrogen evolution.[3] Metal hydrides, with great advantage for high gravimetric capacity ($Mg(BH_4)_2$:14.9 wt % and $LiBH_4$:18.5 wt %)[29] for hydrogen storage in a quite safe, efficient, compact and repeatedly reversible way, has gained intensive attention for HER.[30] In general, metal hydrides are always nanostructured, which can be grouped into three large classes: (1) binary hydrides MH_x (M = main-group or transition metal, such as in LiH, MgH_2, $PdH_{0.6}$, TiH_2); (2) intermetallic hydrides, AB_xH_y (A is typically the hydriding metal and B is the nonhydriding metal, such as $TiFeH_x$, $TiMn_2H_x$, and $LaNi_5H_x$); and (3) complex metal hydrides, MEH_x (E = boron (borohydrides, e.g., $LiBH_4$, $Mg(BH_4)_2$); nitrogen (amides, e.g., $LiNH_2$, $Mg(NH_2)_2$), aluminum (alanates, e.g., $NaAlH_4$, $Mg(AlH_4)_2$)).[30]

1.2 Catalysts for hydrogen production

In addition to hydrogen carriers, nanocatalysts for catalytic hydrogen evolution are an important area that promote stable hydrogen release with great safety, thus making them available for end-use applications. Nanocatalysts, particularly metal transition nanoparticles, have experienced explosive growth in the last

decades as they combine the advantages of high turnover in homogeneous catalysis and recyclability in heterogeneous catalysis.

Semiconductors have been developed extensively in this area since Fujishima and Honda first reported their work on photocatalytic cracking of water with TiO_2 in 1972, and these materials have dominated research in photocatalysis.

However, nanometallic co-catalysts play an integral role in radically improving the performance of semiconductor photocatalysts. Depending on their ability to activate specific reactions, various nanometals are used as catalysts. Nanometallic co-catalysts are usually derived from Group VIII elements, but are not limited to them. These metals, particularly the noble metals, show a wide range of catalytic functions for a considerable number of reactions. group IB, group IIB and group p metals can also be used as catalysts. These metals may be more effective than group VIII metals in reactions such as carbon dioxide reduction. Currently, limited light absorption and low apparent quantum efficiency (AQE) remain the two main bottlenecks for large-scale applications of semiconductor photocatalysis. The former is determined by the inherent energy band structure of semiconductors, while the latter is mainly caused by the recombination of photogenerated charge carriers. As with semiconductor photocatalysis, light-assisted catalysis mediated by localised surface plasmon resonance (LSPR) of nanometals has become a frontier research area for solar to chemical energy conversion in the last few years. A distinguishing feature that sets plasmonic nanomaterials apart from semiconductor materials is that plasmonic nanomaterials can effectively combine light harvesting, hot electron generation, heating effects and unique catalytic functions in one material. For plasmonic photocatalysis, the reader is referred to a number of excellent reviews to better understand the mechanism of SPR-driven/enhanced photocatalytic reactions. Here, we will selectively discuss the latest research results of nanometallic materials in the fields of semiconductor photocatalysis, plasmonic photocatalysis and plasmonic photothermal catalysis (Section 4), respectively, from a multidisciplinary perspective, in the hope of contributing to future practical research activities.

Before all the discussion, it is necessary to distinguish between the concepts of the various types of catalytic reactions discussed in this paper. The first type of catalytic reaction is semiconductor photocatalysis, in which nanometals act as co-catalysts. It is well known that semiconductor photocatalysis is based on the Honda-Fujishima effect. Since both hot electron and photothermal effects will be generated by plasmonic nanometals during SPR decay and provide the driving force for the catalytic reaction; Here, SPR-mediated catalysis on plasmonic nanometals is divided into plasmonic photocatalysis, where the former is driven by hot electron transfer, and plasmonic photothermal catalysis, where the latter is driven by optical thermal effect (temperature) control. Proton photothermal catalysis as presented here is a concept independent of proton photocatalysis and refers to a light-assisted catalytic process that is entirely dominated by the photothermal effect of proton nanoparticles, with no additional

photoactivation mechanism due to hot electron transfer and injection. In other words, apart from the heating method, plasmonic photothermal catalysis is no different from conventional catalytic reactions. Plasmonic nanomaterials can effectively convert the flux of ultraviolet (UV), visible, and even near-infrared (NIR) photons into heat to directly drive the catalytic reaction. Through the flexible use of nanometallic materials, plasmonic photothermal catalysis can be an important complement to semiconductor photocatalysis and plasmonic photocatalysis to improve the efficiency of solar energy utilisation, especially for low energy photons.

Currently, surface plasmon resonance (SPR) effect was found in applications of nanometals in light-assisted heterogeneous catalysis. Generally, the SPR effect is defined as the resonance of photon-induced valence electrons under the restoring force of the positive nucleus when the frequency of the photon matches the natural frequency of the surface electrons, resulting in oscillations. In fact, SPR is a common feature of many nanometals, while it is widely studied in metals of group IB due to nanometals in this group show the SPR effect among all the metals under visible light irradiation. The alkaline earth metal Mg and the group IIIA metals Al, Ga and In also have strong SPR effects at relatively high energies or in the shorter wavelength region. There are a growing number of examples where the UV plasmonic behaviour of Al, Ga and Rh can be exploited for various applications. According the previous theory, light mediated catalytic reaction based on metal SPR effect from three part. Firstly,

Among a series of plasmonic metals, Au, Ag and Cu have attracted much attention and been studied widely because of their compelling electromagnetic properties and visible light response. Pristine metallic catalyst is difficult to realize the transfer of hot electrons. Bimetallic or multimetallic catalyst is necessary to boost catalytic performance, which has been used in energetic and environmental field.

Visible light mediated hydrogen production either by splitting of water, decomposition of the hydrogen source (ammonia borane, sodium borohydride, formic acid, etc.) was researched. Considering Au, Ag and Cu plasmonic effect, bimetallic catalyst such as Au-based, Ag-based and Cu-based bimetallic catalyst was employed for hydrogen evolution from water splitting, hydrolysis of ammonia borane, or sodium borohydride, decomposition of formic acid under visible light irradiation. Plasmonic effect, synergistic effect is found in the process of hydrogen production.

1.3. References

1. He, T.; Pachfule, P.; Wu, H.; Xu, Q.; Chen, P. Hydrogen carriers. *Nat. Rev. Mater.* **2016,** *1*, 16059.

3. Wang, C.; Astruc, D. Recent developments of nanocatalyzed liquid-phase hydrogen generation. *Chem. Soc. Rev.* **2021,** *50*, 3437-3484.

4. Abe, J. O.; Popoola, A. P. I.; Ajenifuja, E.; Popoola, O. M. Hydrogen energy, economy and storage: Review and recommendation. *Int. J. Hydrog. Energy* **2019,** *44*, 15072-15086.

5. Zhu, B.; Zou, R.; Xu, Q. Metal–Organic Framework Based Catalysts for Hydrogen Evolution. *Advanced Energy Materials* **2018,** *8*, 1801193.

6. Haryanto, A.; Fernando, S.; Murali, N.; Adhikari, S. Current Status of Hydrogen Production Techniques by Steam Reforming of Ethanol: A Review. *Energy & Fuels* **2005,** *19*, 2098-2106.

7. Yu, X.; Tang, Z.; Sun, D.; Ouyang, L.; Zhu, M. Recent advances and remaining challenges of nanostructured materials for hydrogen storage applications. *Prog. Mater Sci.* **2017,** *88*, 1-48.

8. Xiao, P.; Chen, W.; Wang, X. A Review of Phosphide-Based Materials for Electrocatalytic Hydrogen Evolution. *Advanced Energy Materials* **2015,** *5*, 1500985.

9. Zhu, J.; Hu, L.; Zhao, P.; Lee, L. Y. S.; Wong, K. Y. Recent Advances in Electrocatalytic Hydrogen Evolution Using Nanoparticles. *Chem. Rev.* **2020,** *120*, 851-918.

10. Valenti, G.; Boni, A.; Melchionna, M.; Cargnello, M.; Nasi, L.; Bertoni, G.; Gorte, R. J.; Marcaccio, M.; Rapino, S.; Bonchio, M.; Fornasiero, P.; Prato, M.; Paolucci, F. Co-axial heterostructures integrating palladium/titanium dioxide with carbon nanotubes for efficient electrocatalytic hydrogen evolution. *Nat. Commun.* **2016,** *7*, 13549.

11. Zada, A.; Muhammad, P.; Ahmad, W.; Hussain, Z.; Ali, S.; Khan, M.; Khan, Q.; Maqbool, M. Surface Plasmonic-Assisted Photocatalysis and Optoelectronic Devices with Noble Metal Nanocrystals: Design, Synthesis, and Applications. *Adv. Funct. Mater.* **2019,** *30*, 1906744.

12. Gelle, A.; Jin, T.; de la Garza, L.; Price, G. D.; Besteiro, L. V.; Moores, A. Applications of Plasmon-Enhanced Nanocatalysis to Organic Transformations. *Chem. Rev.* **2020,** *120*, 986-1041.

13. Zhang, S.; Li, M.; Zhao, J.; Wang, H.; Zhu, X.; Han, J.; Liu, X. Plasmonic AuPd-based Mott-Schottky Photocatalyst for Synergistically Enhanced Hydrogen Evolution from Formic Acid and Aldehyde. *Appl. Catal. B-Environ.* **2019,** *252*, 24-32.

14. Kojima, Y. Hydrogen storage materials for hydrogen and energy carriers. *Int. J. Hydrog. Energy* **2019,** *44*, 18179-18192.

15. Metin, Ö.; Özkar, S. Hydrogen Generation from the Hydrolysis of Ammonia-borane and Sodium Borohydride Using Water-soluble Polymer-stabilized Cobalt(0) Nanoclusters Catalyst. *Energy & Fuels* **2009,** *23*, 3517-3526.

16. Muir, S. S.; Yao, X. Progress in sodium borohydride as a hydrogen storage material: Development of hydrolysis catalysts and reaction systems. *Int. J. Hydrog. Energy* **2011,** *36*, 5983-5997.

17. Makepeace, J. W.; He, T.; Weidenthaler, C.; Jensen, T. R.; Chang, F.; Vegge, T.; Ngene, P.; Kojima, Y.; de Jongh, P. E.; Chen, P.; David, W. I. F. Reversible ammonia-based and liquid organic hydrogen carriers for high-density hydrogen storage: Recent progress. *Int. J. Hydrog. Energy* **2019,** *44*, 7746-7767.

18. Schlesinger, H. I.; Brown, H. C.; Finholt, A. E.; Gilbreath, J. R.; Hoekstra, H. R.; Hyde, E. K. Sodium Borohydride, Its Hydrolysis and its Use as a Reducing Agent and in the Generation of Hydrogen1. *J. Am. Chem. Soc.* **1953,** *75*, 215-219.

19. Brack, P.; Dann, S. E.; Wijayantha, K. G. U. Heterogeneous and homogenous catalysts for hydrogen generation by hydrolysis of aqueous sodium borohydride ($NaBH_4$) solutions. *Energy Science & Engineering* **2015,** *3*, 174-188.

20. Wu, C.; Zhang, J.; Guo, J.; Sun, L.; Ming, J.; Dong, H.; Zhao, Y.; Tian, J.; Yang, X. Ceria-Induced Strategy To Tailor Pt Atomic Clusters on Cobalt–Nickel Oxide and the Synergetic Effect for Superior Hydrogen Generation. *ACS Sustain. Chem. Eng.* **2018,** *6*, 7451-7457.

21. Kang, N.; Djeda, R.; Wang, Q.; Fu, F.; Ruiz, J.; Pozzo, J. L.; Astruc, D. Efficient "Click"-Dendrimer-Supported Synergistic Bimetallic Nanocatalysis for Hydrogen Evolution by Sodium Borohydride Hydrolysis. *ChemCatChem* **2019,** *11*, 2341-2349.

22. Staubitz, A.; Robertson, A. P. M.; Manners, I. Ammonia-Borane and Related Compounds as Dihydrogen Sources. *Chem. Rev.* **2010,** *110*, 4079-4124.

23. Chandra, M.; Xu, Q. A high-performance hydrogen generation system: Transition metal-catalyzed dissociation and hydrolysis of ammonia–borane. *J. Power Sources* **2006,** *156*, 190-194.

24. Chen, Y.-Z.; Liang, L.; Yang, Q.; Hong, M.; Xu, Q.; Yu, S.-H.; Jiang, H.-L. A seed-mediated approach to the general and mild synthesis of non-noble metal nanoparticles stabilized by a metal–organic framework for highly efficient catalysis. *Materials Horizons* **2015,** *2*, 606-612.

25. Yao, Q.; Ding, Y.; Lu, Z.-H. Noble-metal-free nanocatalysts for hydrogen generation from boron- and nitrogen-based hydrides. *Inorganic Chemistry Frontiers* **2020,** *7*, 3837-3874.

26. Blaquiere, N.; Diallo-Garcia, S.; Gorelsky, S. I.; Black, D. A.; Fagnou, K. Ruthenium-Catalyzed Dehydrogenation of Ammonia Boranes. *J. Am. Chem. Soc.* **2008,** *130*, 14034-14035.

27. Zhan, W.-W.; Zhu, Q.-L.; Xu, Q. Dehydrogenation of Ammonia Borane by Metal Nanoparticle Catalysts. *ACS Catal.* **2016,** *6*, 6892-6905.

28. Ramachandran, P. V.; Gagare, P. D. Preparation of Ammonia Borane in High Yield and Purity, Methanolysis, and Regeneration. *Inorg. Chem.* **2007,** *46*, 7810-7817.

29. Orimo, S.-i.; Nakamori, Y.; Eliseo, J. R.; Züttel, A.; Jensen, C. M. Complex Hydrides for Hydrogen Storage. *Chem. Rev.* **2007,** *107*, 4111-4132.

30. Schneemann, A.; White, J. L.; Kang, S.; Jeong, S.; Wan, L. F.; Cho, E. S.; Heo, T. W.; Prendergast, D.; Urban, J. J.; Wood, B. C.; Allendorf, M. D.; Stavila, V. Nanostructured Metal Hydrides for Hydrogen Storage. *Chem. Rev.* **2018,** *118*, 10775-10839.

Chapter 2. Efficient “Click”-Dendrimer-Supported Synergistic Bimetallic Nanocatalysis for Hydrogen Evolution from Sodium Borohydride Hydrolysis

2.1. Introduction

Hydrogen is considered as one of the most emerging alternative fuels for future energy applications to satisfy the two challenges of fuel exhaustion and global greenhouse emission.[1] Among various approaches including coal gasification,[2] biological hydrogen production,[3] photoelectrochemical water splitting,[4,5] and hydrolysis of hydrogen storage materials,[7] hydrogen generation from hydrogen storage materials has been proposed as a promising solution involved in industrial energy production.[8,9] Sodium borohydride ($NaBH_4$) is one of the simplest and most hydrogen-rich molecules that generate hydrogen.[10-13] As a hydrogen storage material it presents the advantages of small volume, high hydrogen storage capacity and cleanness, which has attracted much attention. Because of its excellent ability of hydrogen production, many efforts have been devoted to accelerating the process of $NaBH_4$ hydrolysis through the development of catalysts.[14-22] The stoichiometry of hydrogen generation from $NaBH_4$ follows equation (2.1):

$$NaBH_4 + 2H_2O \rightarrow NaBO_2 + 4H_2 \quad \uparrow \qquad (2.1)$$

Since Haruta's discovery of the extraordinary efficiency of small (< 5 nm) nanoparticles (NPs) in the catalysis of aerobic CO oxidation under sub-ambient conditions in the 1980's[23-24] the use of this family of catalysts has led to considerable development at the interface between homogeneous and heterogeneous catalysis for a large number of reactions.[25-38] Very small NPs bring about a good catalytic efficiency and selectivity due to the high NP surface/volume ratio and quantum confinement. Such properties have been shown to be crucial in the catalytic hydrolysis of $NaBH_4$. The use of MNPs as catalyst requires their stabilization against self-aggregation and leaching, however. This is particularly critical for catalysis applications in which a robust linkage between the MNPs and the support would improve performances in terms of recovery and re-use of the catalyst as well as inhibition of product contamination.[39,40] This has been demonstrated in particular using functionalized carbon structures,[40,41] polymers[42,43], and mesoporous organosilica.[44,45] Dendrimers have been extensively used as supports in catalysis[46-57] because they often exert the function of nanoreactor[58-66] contributing to protect MNPs and inhibit their agglomeration. It is noteworthy, however, that the reports on the uses of dendrimers as supports in hydrogen generation are rare, [42,67,68] and there has been no report on the use of a dendrimer in the catalysis of $NaBH_4$ hydrolysis.

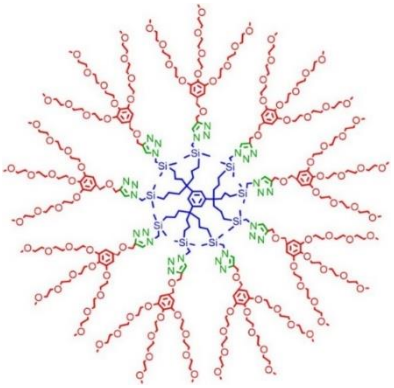

Fig.2.1. Dendrimer **1**

The dendrimer used here is the known "click" dendrimer **1** (Fig. 1),[48,69] i.e. containing intradendritic 1,2,3-triazoles resulting from Cu-catalyzed azide alkyne Huisgen-type cycloaddition. Hence, in this article we report the efficient micro-heterogeneous catalysis of $NaBH_4$ hydrolysis by known late-transition-metal NPs that are stabilized by the "click" dendrimer **1**.[48,69] These NPs, synthesized according to Scheme 1, are noted MNP@dendrimer, and their catalytic efficiencies are compared.

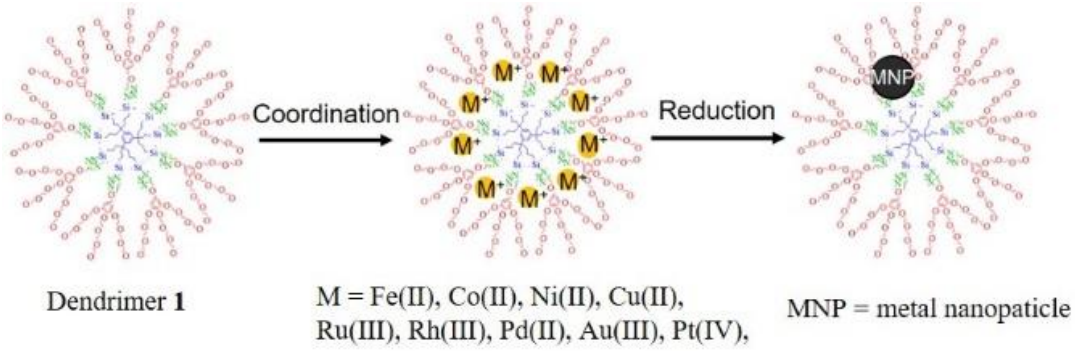

Scheme 2.1 Synthesis of nanocatalysts MNPs@dendrimer

A series of related bimetallic NP catalysts of the late transition metals are also compared with each other and with the monometallic NPs. The kinetics and mechanism of $NaBH_4$ hydrolysis catalyzed by the best "click" dendrimer-supported bimetallic catalyst MM'NP@dendrimer have been investigated, and a mechanism is proposed in particular given the kinetic KIE observed with D_2O for this reaction.

2.2. Results and Discussion

2.2.1. Synthesis and characterization of the nanocatalysts

The various known mono-[42] and bimetallic[68] nanocatalysts are synthesized by reaction of the transition metal salt precusors with the "click" dendrimer 1 (Scheme 1) in order to coordinate the intradendritic 1,2,3-triazole ligands of the dendrimer onto the transition metal cations Fe(II), Co(III), Ni(II), Cu(II), Ru(II), Rh (III), Pd(II), Pt(II) and Au(III) followed by reduction by $NaBH_4$ of the metal cation to neutral atoms that further agglomerate as small NPs. These various NPs of Fe, Co, Ni, Cu, Ru, Rh, Pd, Pt, Au,

Pt/Co, Pd/Co, Pd/Ni, Rh/Co, Pt/Ni, Ru/Co, Ru/Ni, and Rh/Ni have already been reported and characterized by TEM, HRTEM, XPS, and for bimetallic NPs by EDX and HAADF-STEM elemental mapping spectra analysis, and they have been used for the catalysis of ammonia borane (AB) hydrolysis.[42,68] The TEMs of these MNPs showed sizes between 1.8 nm and 4.7 nm. XPS of the analyzed bimetallic NPs confirmed zero oxidation state and EDX and HAADF-STEM elemental mapping spectra showed the alloy structures.[42,68]

2.2.2 Comparison of different monometallic NPs for sodium borohydride hydrolysis

All the nanomaterials used as catalysts for $NaBH_4$ hydrolysis are the same as those already reported for ammonia borane hydrolysis.[42,68] The catalytic performances of various monometallic NPs evaluated for the catalytic hydrolysis of $NaBH_4$ are shown in Fig. 2.2, and the dendrimer-supported PtNPs appear to present the best performances. With these PtNPs the stoichiometric amount of H_2 (4 mol H_2 per mol $NaBH_4$) is obtained after 3 min of reaction with a TOF value of 133.3 $mol_{H2}\cdot mol\ catal^{-1}\cdot min^{-1}$, followed by RuNPs (TOF = 80.0 $mol_{H2}\cdot mol\ catal^{-1}\cdot min^{-1}$), and PdNPs (TOF = 2.2 $mol\cdot H_2\ molcatal^{-1}\cdot min^{-1}$), RhNPs (TOF = 53.3 $mol_{H2}\cdot molcatal^{-1}\cdot min^{-1}$), AuNPs (TOF = 3.3 $mol_{H2}\cdot molcatal^{-1}\cdot min^{-1}$).

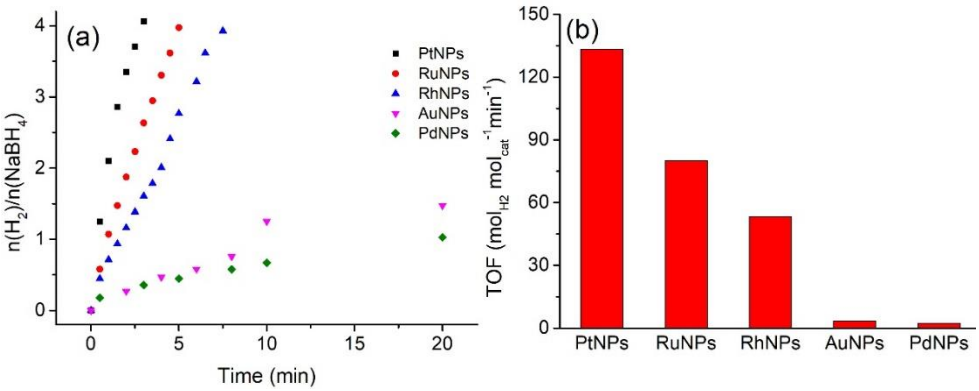

Fig. 2.2. (a) Catalytic efficiencies of various noble MNP catalysts and (b) corresponding TOF values.

Among the first-raw late transition metals, dendrimer-supported CoNPs have the best catalytic activity with a TOF value of 8 $mol_{H2}\cdot mol\ catal^{-1}\cdot min^{-1}$ for $NaBH_4$ hydrolysis. The order of catalytic activity of first-raw transition-metal monometallic NPs is: CoNPs > NiNPs > FeNPs > CuNPs (Fig. 2.3).

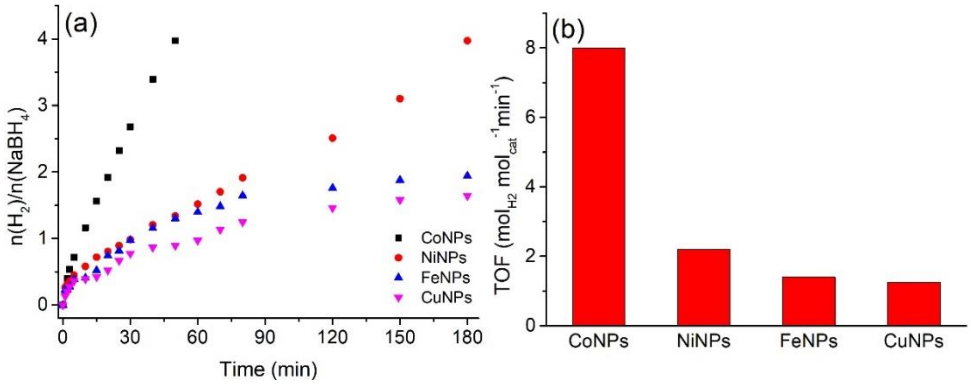

Fig. 2.3 (a) Catalytic efficiencies of late first-raw transition MNP catalysts and (b) corresponding TOF **values.**

2.2.3 Influence of NaOH

In the catalytic hydrolysis of $NaBH_4$, NaOH plays an interesting role. The exploration of the influence of various amounts of NaOH (0.1 M~0.4 M) shows (Table S2.1) that a small amount of NaOH has a positive influence on the $NaBH_4$ hydrolysis catalyzed by all MNPs except PtNPs. The reaction rates are boosted, and higher TOF values are obtained for MNPs in the presence of 0.1~0.2 mM NaOH than in its absence. The best TOF value, 186 $mol_{H2}\cdot mol_{catal}^{-1}\cdot min^{-1}$, is reached for RuNPs in the presence of 0.2 M NaOH (Fig. 2.4), and the TOF value decreases when the NaOH concentration is higher than 0.2 mM. The influence of a base has also been investigated and discussed for AB hydrolysis.[42,68,70]

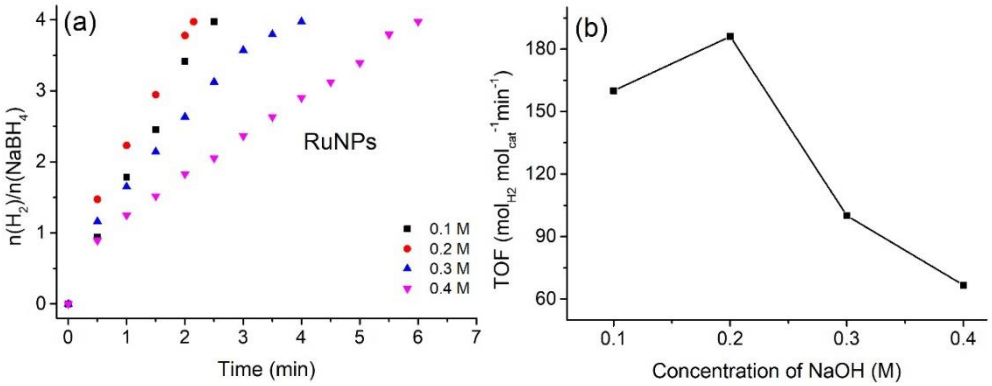

Fig. 2.4 (a) Catalytic efficiencies of RuNPs in the presence of different concentrations of NaOH from 0.1 M to 0.4 M; (b) corresponding TOF values (in $mol_{H2}\cdot mol_{catal}^{-1}\cdot min^{-1}$).

2.2.4 Comparison of various bimetallic NPs for sodium borohydride hydrolysis

According to the results of the catalytic activity in $NaBH_4$ hydrolysis of the monometallic NPs, the best two nanocatalysts in the first-raw group of the transition metals are NiNPs and CoNPs. Therefore, a series of bimetallic NPs were fabricated upon mixing, before reduction by $NaBH_4$ to dendrimer-stabilized NPs,

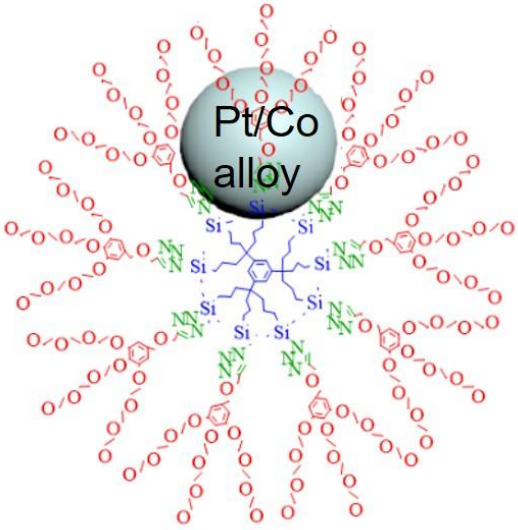

one of the two metal salt precursors (Ni or Co) with one of the noble-metal salts (Pt, Ru, Rh, or Pd). Fig. 2.6 indicates that Pt/Co@dendrimer presents the best catalytic performance compared to the other bimetallic NPs. Interestingly, the performance of Pt/Co@dendrimer is superior to those of both PtNPs and CoNPs (Fig. 2.5 and S2).

Fig. 2.5. Pt/Co@dendrimer

It is in particular remarkable that the addition of the Earth-abundant metal Co improves the performance of the best pure noble metal, Pt. This means that there is a clear positive synergistic effect between Pt and Co in the nanocatalyst Pt/Co@dendrimer. Note that not all bimetallic NP combinations present such a positive synergistic effect. From Figure S3, among the various Co-based and Ni-based bimetallic NPs, Pt/CoNPs, Pd/CoNPs, Pd/NiNPs, and Rh/CoNPs show synergy with better performance in hydrolysis of $NaBH_4$ than the corresponding individual monometallic NPs (Fig. 6). The bimetallic alloys that do not show any synergy in the catalytic reaction, however, are Pt/Ni NPs, Ru/Co NPs, Ru/Ni NPs, and Rh/Ni.

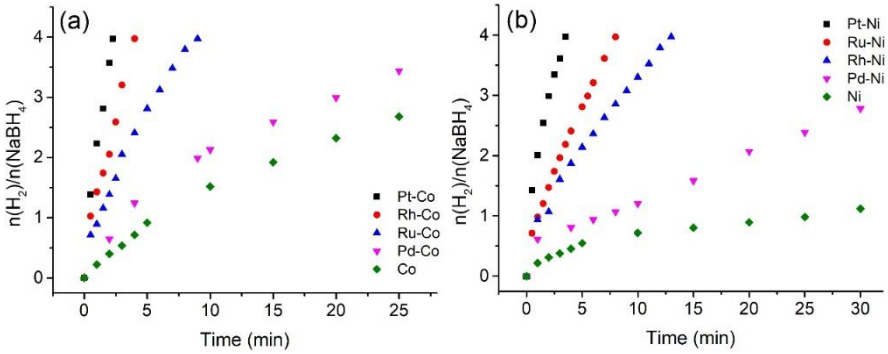

Fig. 2.6 (a) Catalytic efficiencies of various Co based catalysts; (b) catalytic efficiencies of various Ni-based catalysts

2.2.5 Selection of the best performing Pt/Co ratio in Pt/Co@dendrimer

Different combinations of elements reveal a diversity of performances. For example, the variation of the Pt/Co ratio significantly influences the activty of the NPs in the catalyzed $NaBH_4$ hydrolysis. Therefore, investigations of the performances of a selection of ratios of these two metals is required. As shown in Fig. 2.7, when the proportion of Pt increases from 25% to 50%, there is a significant increase in the reduction efficiency compared to each MNP taken individually. The best performance among the different alloys is obtained for the 1:1 alloy. For comparison, the performance of the mixture of the catalysts PtNP@dendrimer and CoNP@dendrimer (i.e. mixed after reduction of the metal cations) does not provide any synergy, as the performance for catalytic H_2 delivery is slightly lower than that of PtNP@dendrimer (Figure S2). Furthermore, when adding NaOH to the bimetallic reaction system, it always exerts a negative effect on the hydrolysis of $NaBH_4$ whatever the amount of each metal in the alloy (Table S2.2).

Fig. 2.7 (a) Catalytic efficiencies with various proportions of Pt and Co in the Pt/Co alloys; (b) corresponding TOF values.

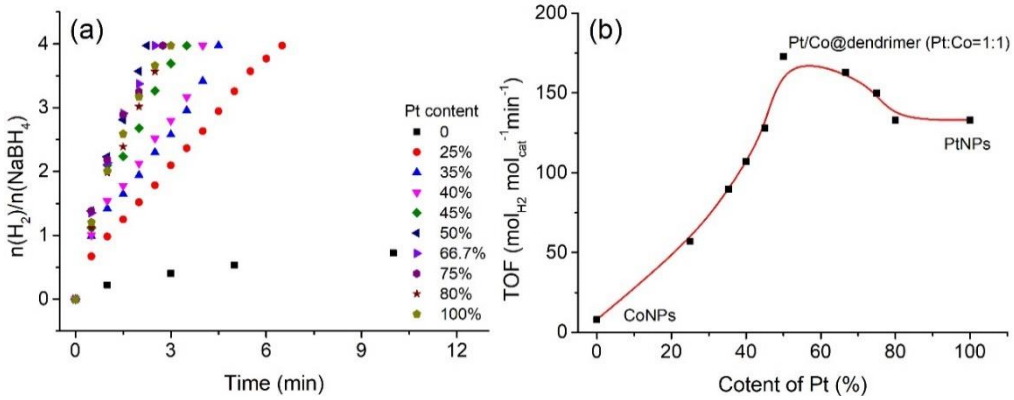

2.2.6 Kinetic study of $NaBH_4$ hydrolysis catalyzed by MNPs@dendrimer

In order to investigate the mechanism of $NaBH_4$ hydrolysis catalyzed by MNP@dendrimer, the best bimetallic NPs are studied under various $NaBH_4$ concentations, catalyst concentrations, and temperatures. Fig. 2.8 shows that hydrogen generation accelerates with the increase of the load of MNPs. The logarithmic of the plot of H_2 generation vs. concentration of Pt/Co@dendrimer is 0.63, which means that the reaction is the first order in catalyst concentration.

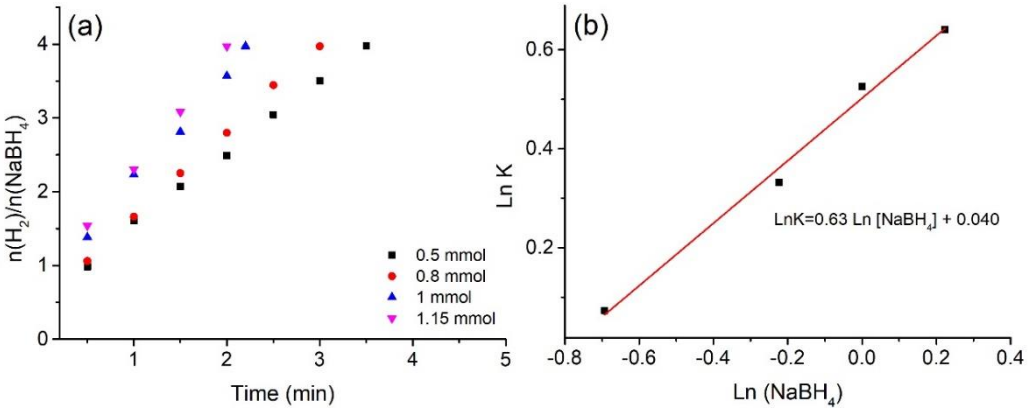

Fig. 2.8 (a) Time plots of the catalytic dehydrogenation of $NaBH_4$ catalyzed by Pt/Co@dendrimer with various concentrations of $NaBH_4$; (b) plot of hydrogen generation rate vs. concentration of $NaBH_4$ (R^2 = 0.98).

As shown in Fig. 2.9a, increasing the concentration of $NaBH_4$ is beneficial for accelerating $NaBH_4$ hydrolysis. Moreover, the slope of logarithmic plot of H_2 generation vs. concentration of $NaBH_4$ is 0.85 (Fig. 2.9b), which means that the reaction is first order in substrate concentration, also demonstrating that activation of $NaBH_4$ is involved in the rate-determining step.

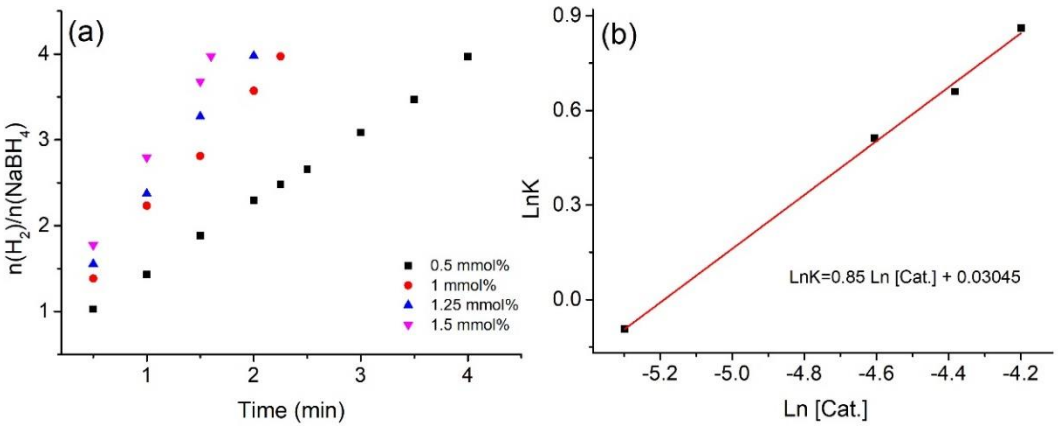

Fig. 2.9 (a) Plots of volume of H_2 generated vs. time for $NaBH_4$ hydrolysis catalyzed by various concentrations of Pt/Co@dendrimer, (b) plot of hydrogen generation rate vs. the concentration of catalyst (R^2 = 0.99).

Fig. 2.10 (a) shows that the temperature exerts a significant influence on the hydrogen production derived by Pt/Co@ dendrimer. The efficiency of $NaBH_4$ hydrolysis increases when the reaction temperature rises from 293 K to 308 K. From Fig. 2.10 (b), the activation energy (Ea) is 24.95 KJ/mol as calculated according to the Arrhenius equation (Eq. 2), in which k is the reaction rate, A is the pre-exponential factor, R is the gas constant (8.314 $J \cdot mol^{-1}K^{-1}$) and T(K) is the reaction temperature.

$$LnK = LnA - \frac{Ea}{RT} \qquad (2)$$

Fig. 2.10 (a) Plots of the volume of H_2 vs. time for the catalytic hydrolysis of $NaBH_4$ at various

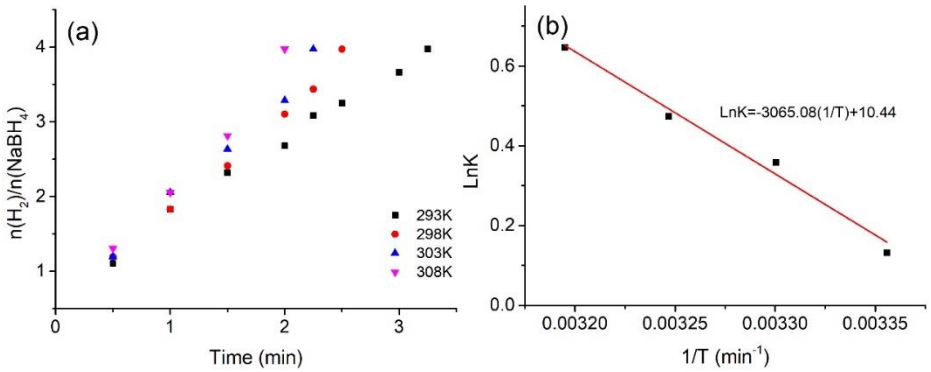

temperatures catalyzed by 1 mol% of Pt/Co@dendrimer; (b) Arrhenius plots obtained from the kinetic data (R^2 = 0.97).

In order to explore the role of H_2O in the catalytic hydrolysis of $NaBH_4$, D_2O is used instead of H_2O to determine the kinetic isotope effect (KIE). The result is presented in Fig. 2.11, showing the comparison between H_2O and D_2O for the catalyzed $NaBH_4$ hydrolysis efficiency. The $NaBH_4$ hydrolysis reaction is significantly faster in H_2O than that in D_2O, and the primary KIE, k_H/k_D, is 3.41. This means that reaction of H_2O, i.e. cleavage of a water O-H bond, is involved in the rate-determining step, confirming that one hydrogen atom of H_2 comes from H_2O. Neither $NaBH_4$ nor H_2O alone can produce H_2 under the reaction conditions, and the first order found in $NaBH_4$ shows that it is also involved in the production of one of the two H atoms of H_2.

Fig. 2.11 Hydrogen evolution from $NaBH_4$ hydrolysis with H_2O compared to that with D_2O, catalyzed by 1 mol% of the nanocatalyst Pt/Co@dendrimer (KIE = 3.41).

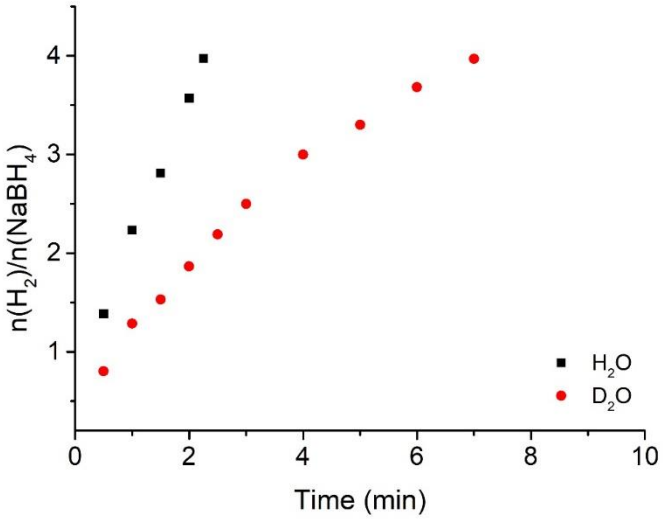

2.2.7 Role of the "click" dendrimer

In order to confirm that the dendrimer plays an efficient protective role as support of the MNPs and to check its practical function together with the catalyst, the best catalyst Pt/Co@dendrimer was chosen to conduct recycling experiments. Specifically, after completing a $NaBH_4$ hydrolysis reaction, another equivalent of $NaBH_4$ (1 mmol) was added into the flask, then the second round was started. The $NaBH_4$ hydrolysis reactions were repeated several times in this way. As shown in Fig. 2.12, after five cycles, despite some decrease, Pt/Co@dendrimer still retains a good catalytic activity for $NaBH_4$ hydrolysis, which means that the "click"-dendrimer-stabilized catalyst has a good stability upon recycling. Agreggation of the NPs was observed, however, after 5-time recycling (Fig. S2.4). The dendrimer **1** is very stable and fully recyclable.

Fig. 2.12 Plots of volume of H_2 vs. time for the hydrolysis of $NaBH_4$ catalyzed by 1 mol% Pt/Co@dendrimer during the reusability test.

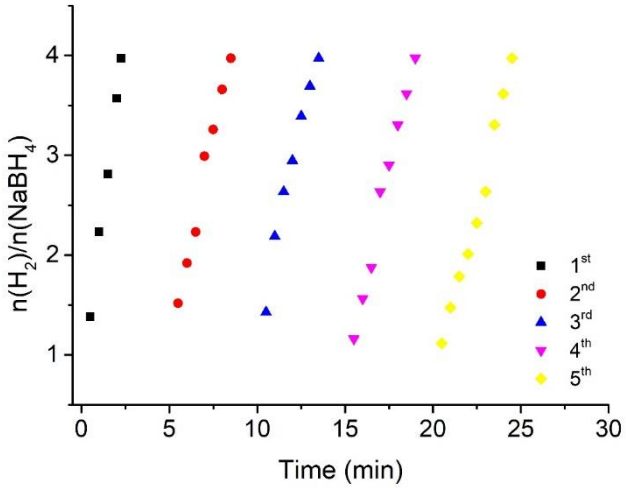

We know that the intradendritic triazole rings resulting from the "click" synthesis of the dendrimer readily coordinates to transition-metal cations in various solvents including water as shown earlier by spectroscopy and electrochemical experiments.[71,72] More recently it was also found that the NPs formed upon reduction with $NaBH_4$ are located near the periphery of the click dendrimer **1**, while the dendritic triazole ligands still loosely coordinate and activate the NP surface atoms in catalytic reactions such as the "click" reaction in the case of the CuNPs.[73] Thus the role of these intradendritic triazole ligands is crucial for NP catalysis, because of their stereoelectronic effects including the electronic donicity of the ligands and the drastic steric constraints of the intradendritic environment. As a result a number of highly performing NP-catalyzed reactions were recorded for a variety of NPs stabilized by the dendrimer **1** including various catalytic C-C and C-N bond forming reactions with ppm or even sometimes sub-ppm

amount of NP metal.[74-77] In the present case the dendritic confinement and this stereoelectronic triazole influence certainly also plays a key role in the excellent catalytic performances of this PdCoNP@dendrimer nanocatalyst. A "click" dendrimer of higher generation with 81 tetraethylene glycol termini was used in previous studies of "click" dendrimer-supported NP catalysis but gave only similar or slightly lower performances (no significant dendritic effect); [42,77] thus a detailed study of that dendrimer was not conducted here.

2.2.8. Reaction mechanism

Valuable mechanistic proposals have been published for the NP-catalyzed hydrogen evolution from borohydride salts under various conditions, emphasizing the crucial role of the NP and NP-H bonds formation and evolution.[12,78-81] Some proposals suggested oxidative addition [82] of a B-H bond to transfer a hydrogen atom onto the MNP and leave the negative charge onto the boron atom followed by electron transfer that may be subsequently used in further steps. Borohydrides present a strong driving force for hydride transfer to the MNP surface atoms to form MNP-H bonds[83] with the negative charge delocalized onto the NP.[25,84] We believe that charge delocalization over the NP is preferred to localization onto the boron atom in the first step, leaving BH_3 coordinated to the electron-rich NP surface atoms.

The primary KIE found with D_2O suggests that water is involved in the rate-determining step, thus with cleavage of an O-H bond. This difficult oxidative addition step is probably much facilitated by hydrogen bonding between a hydridic hydrogen atom of borohydride and an acidic hydrogen atom of water in the ground state, i.e. $[BH_3H^-]$…H-OH, that results in lowering the electron density in the water O-H bond. In the absence of the NP catalyst, this hydrogen bonding very slowly continues at room temperature to form first H_2, "BH_3", and OH^-. In order to facilitate O-H bond oxidative addition cleavage, coordination of $[BH_3H^-]$…H-OH onto the catalyst surface occurs and is likely to provoke both B-H and O-H bond cleavage almost simultaneously, or at least in a concerted way. After reductive elimination[82] of $[BH_3OH]^-$, the same step would occur again with the later leading to the final formation of 4 mol H_2 and $[B(OH)_4]^-$ (Scheme 2).

Scheme 2. Proposed mechanism for the hydrolysis of $NaBH_4$ catalyzed by Pt/Co@ dendrimer

The role of the dendrimer is to serve as a nanoreactor protecting the MNP near the dendrimer periphery and to activate the MNP by triazole coordination. The role of base has already been discussed in the case of hydrogen evolution from AB. [42,68,70] The presence of a small amount of NaOH should lead to coordination of OH^- onto the MNP surface, which would increase its electron density and therefore facilitate oxidative addition of the O-H bond. On the other hand excess NaOH would occupy too many surface MNP sites, thus inhibiting substrate coordination and activation of the substrates on the MNP surface.

In the bimetallic Pt_1Co_1 alloy, one may speculate that hydride transfer from $NaBH_4$ would proceed onto the more electron-poor Co atom in the alloy, while O-H oxidative addition would occur onto the more electron-rich Pd atom; this combination is electronically more favorable than on monometallic NPs.

2.2.9. Comparison between sodium borohydride and ammonia borane

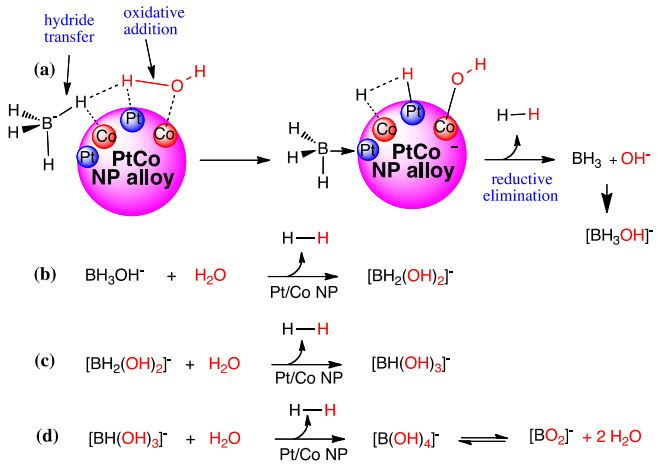

There are resemblances between the catalytic activation of ammonia borane [42,68,70,85-88] and that of sodium borohydride in terms of metal NP catalyst preference and NaOH influence. This analogy implies mechanistic similarities. One may consider AB with the zwitterionic writing H_3N^+-B^-H_3 in which one H atom of NH_4^+ is replaced by BH_3. In both cases a KIE effect is observed upon using D_2O instead of H_2O signifying a common implication of the water O-H bond cleavage in the rate-limiting step favored by hydrogen bonding between the substrate and water. In both cases also, a strong synergy is disclosed between an Earth-abundant metal, Co, that boosts the rate of catalytic H_2 generation by a noble metal NP, Pt. Note that this similar synergy is found only with the "click" dendrimer as a support, whereas with the ZIF-8 support synergy is found only in AB activation, not for $NaBH_4$, probably for stereoelectronic reasons. A major difference appears in the substrate charge of the two boron hydride substrates, however,

that may result in a mechanistic difference in H-atom transfer from neutral AB (oxidative addition of the B-H bond) vs. hydride transfer from negatively charged BH_4^- to the MNP. In terms of performances, the TOF value of AB hydrolysis catalyzed by PtCo@dendrimer was previously found to be 163.6 $mol_{H2} \cdot mol_{catal.}^{-1} \cdot min^{-1}$,[23] which is inferior, under the same reaction conditions, to that found in the present work with $NaBH_4$,177.8 $mol_{H2} \cdot mol_{catal.}^{-1} \cdot min^{-1}$.

2.3 Conclusions

NPs of the late transition metals stabilized by the "click" dendrimer **1** have been compared as catalysts for H_2 generation upon $NaBH_4$ hydrolysis. Among the monometallic first-raw transition metals, CoNPs, and among the noble metal, PtNPs, were found to be the most efficient catalysts for this reaction. Bimetallic NPs also showed synergistic activation in a few cases, and the best performing example of this synergy was that of Pt/CoNP@dendrimer for which the best alloy was that containing equal amounts of Pt and Co. The performances indicated above are excellent as can be noted by comparison with formerly reported data with PtNPs and CoNPs (Table S2.3, p. S8).

Study of the reaction kinetics with this catalyst shows that the reaction is first order in $NaBH_4$ and NP catalyst, with a low activation energy (Ea) of 24.95 KJ/mol. Importantly the significant primary KIE disclosed with D_2O, $k_H/k_D = 3.41$, indicates a participation of the O-H oxidative addition cleavage in the rate-limiting step. Hydrogen bonding between a hydridic hydrogen atom of $NaBH_4$ and an "acidic" hydrogen atom of water much favors this otherwise difficult step by weakening the electron density of the O-H bond and is suggested to provoke concerted activation of both B-H and O-H bonds by the NP surface. In heterobimetallic alloyed nanocatalysts, the role of each of these two bond activations is facilitated compared to monometallic NPs probably by hydride transfer to Co and O-H oxidative addition to Pd.

The nanoreactor role of the "click" dendrimer is not only to stabilize the NPs, but also to activate the NP near the dendrimer periphery by coordination of intradendritic triazole ligands increasing the electron density on the NPs. Positive activation of the performance by small amount of NaOH is taken into account by coordination onto the NP surface that increases the surface electron density, and negative effect of excess NaOH is possibly explained by saturation of the NP surface sites inhibiting substrate coordination and activation. The negative influence of NaOH in all proportions on the bimetallic Pd_1Co_1 alloy seems to increase the role of the latter inhibiting effect.

In addition, the comparison between heterogeneous catalysis with the metal organic framework ZIF-8 support and the microheterogeneous catalysis with "click" dendrimer support shows that activity of the

catalyst in the present work is still retained after five cycles, whereas during the 5th cycle in the heterogeneous catalyst the process is presumably marred by adsorption of the sodium borate product on the support. At last, $NaBH_4$ can produce more hydrogen per mass amount than AB, and also $NaBH_4$ is cheaper than AB. It is also hoped that progress will rapidly involve regeneration of $NaBH_4$ from sodium borate are shown by very recent reports. [89,90]

2.4 Experimental Section

Chemicals and regents

All chemicals and solvents were purchased from Sigma-Aldrich. Prior to the synthesis, all the flasks were washed with aqua regia solution (HCl/HNO3=3:1 v/v) to remove the metal residue. Milli-Qwater (18.2 MW) was used for all preparations. All of the nanocatalysts transferring, loading, and hydrolysis reactions were conducted under nitrogen condition to avoid any oxidation and contamination.

Preparation of the dendrimer 1:

Dendrimer **1** was synthesized according to previous work. Specifically, 9-N3 (0.012 mmol) and the TEG dendron (0.13 mmol, 1.2 equiv per branch) are dissolved in THF. $CuSO_4 \cdot 5H_2O$ is added (0.032 g, 0.13 mmol, 1.2 equiv per branch, 1m in aqueous solution), followed by dropwise with addition of a freshly prepared solution of sodium ascorbate (0.051 g, 0.26 mmol, 2.4 equiv per branch, 1m in water solution) in order to set a 1:1 THF/water ratio. The reaction mixture is stirred for 3 days at ambient temperature under N_2. After removing THF *in vacuo*, CH_2Cl_2 (100 mL) and an aqueous ammonia solution (2.0 M, 50 mL) are added. The mixture is allowed to stir for 10 minutes in order to remove all the Cu(II) trapped inside the dendrimer as $[Cu(NH_3)_2(H_2O)_2][SO_4]$. The organic phase is washed twice with water, then this operation is repeated three more times to ensure complete removal of copper ions. The organic phase is dried with sodium sulfate, and the solvent is removed *in vacuo*. The product is washed with 50 mL pentane several times in order to remove the excess of the dendron. Dendrimer **1** is obtained in 72.8% yield.

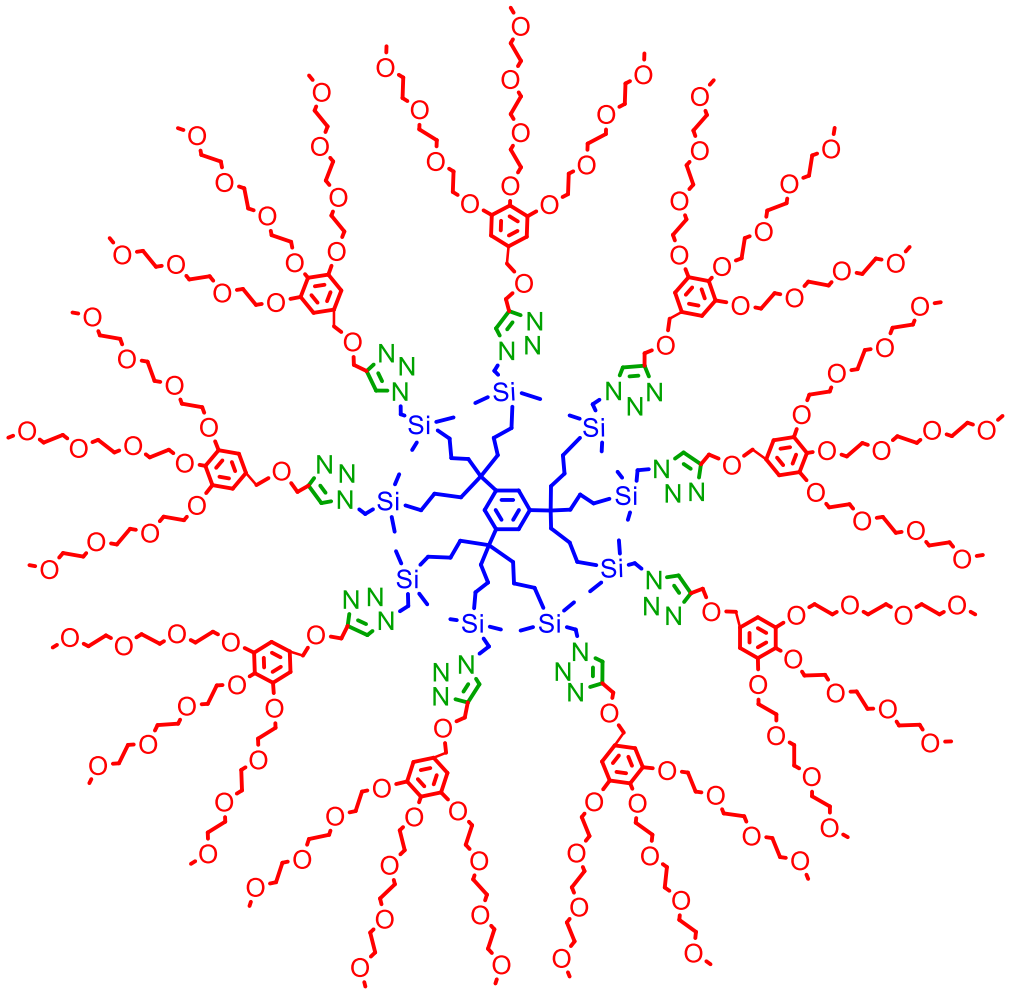

Dendrimer 1

^{1}H NMR ($CDCl_3$, 300 MHz) δ: ppm: 7.51 (CH-triazole), 6.99 (CH-arom. intern), 6.60 (CH-arom. extern), 4.63 (triazole-CH_2-O), 4.48 (O-CH_2-arom. extern), 3.85-4.15 (CH_2CH_2O-arom. extern), 3.80 (Si-CH_2-triazole), 3.53-3.77 (OCH_2CH_2O), 3.37-3.40 (CH_3O), 1.70 ($CH_2CH_2CH_2Si$), 1.13 ($CH_2CH_2CH_2Si$), 0.66 ($CH_2CH_2CH_2Si$), 0.07 ($Si(CH_3)_2$).

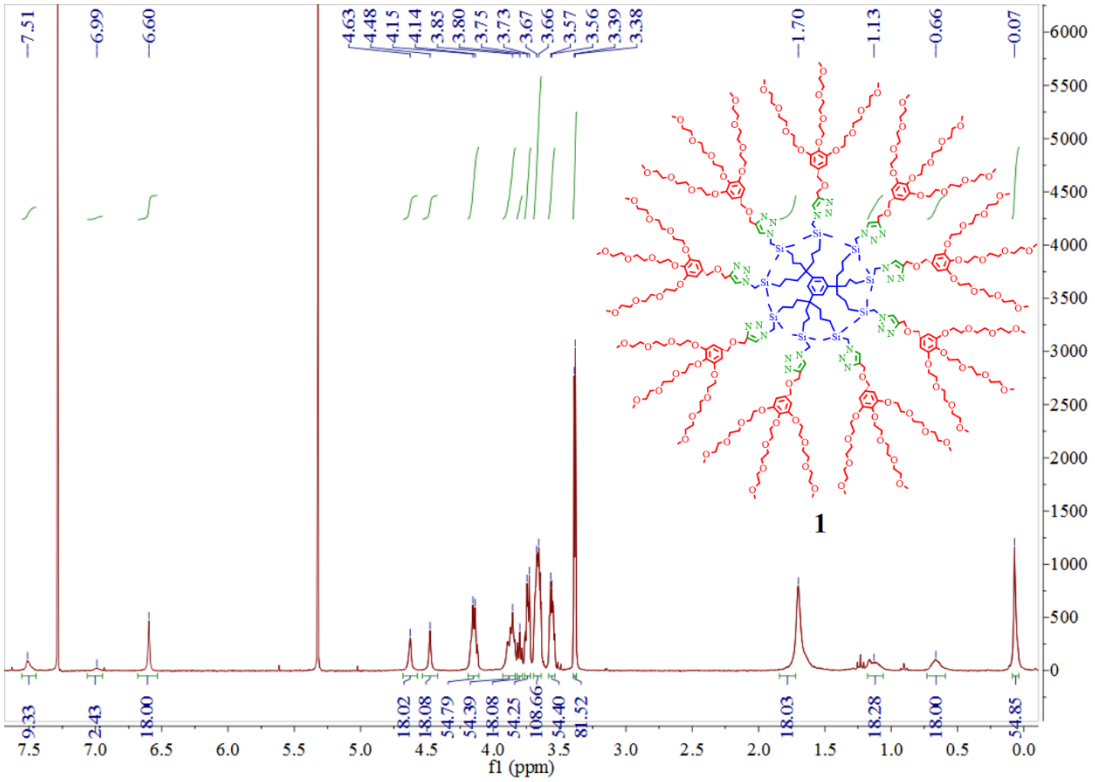

Figure S2.1. ^{1}H NMR spectrum of dendrimer **1** in $CDCl_3$.

Preparation of the dendrimer-supported NPs. The "click" dendrimer **1** and the "click" dendrimer-supported mono- and bimetallic NPs have already been reported.[21,68] They were prepared by mixing the "click" dendrimer **1** and a metal salt in water followed by stirring 30 min under N_2, then addition of a freshly prepared aqueous solution of $NaBH_4$ and further stirring for 30 min. For example, the fabrication of PtNPs@dendrimer was prepared by mixing 0.01 mM $H_2PtCl_6{\cdot}6H_2O$ and 0.015 mM dendrimer **1** (M = 7212.34 g·mol^{-1}) with 3 mL Mili-Q water, then stirring for 30 min, followed by adding 0.1 mM $NaBH_4$ (in 1 mL water) for reduction of Pt (IV); after 30 min stirring, PtNPs@dendrimer was obtained. The synthesis of the bimetallic NPs proceeded similarly by mixing the dendrimer **1** with two different metal salts in water followed by the same treatment as for the monometallic NPs (Scheme 2.1). For instance, the synthesis of Pt_1/Co_1@dendrimer (the Pt/Co ratio is 1) proceded by mixing 0.005 mmol $H_2PtCl_6{\cdot}6H_2O$, 0.005 mmol $CoCl_2$, and 0.01 mmol dendrimer 1, and further steps were as for monometallic NPs.

Hydrolysis of sodium borohydride catalyzed by MNPs. The hydrolysis of $NaBH_4$ was conducted in a 50-mL flask at 25 °C. After preparation of the dendrimer-supported MNPs, 1mL of aqueous solution of $NaBH_4$ was added into the solution with 4 mL of solution of catalyst. In the standard treatment, the content of NMPs was 1%, and the concentration of $NaBH_4$ was 1 mmol. The experiments were conducted with various $NaBH_4$ amounts (0.5, 0.8, 1.0, and 1.25 mM). The concentrations of Pt_1Co_1@dendrimer were 0.5 mmol%, 1 mmol%, 1.25 mmol% and 1.5 mmol% respectively. The reaction temperatures were 293K, 298K, 303K and 308K, respectively.

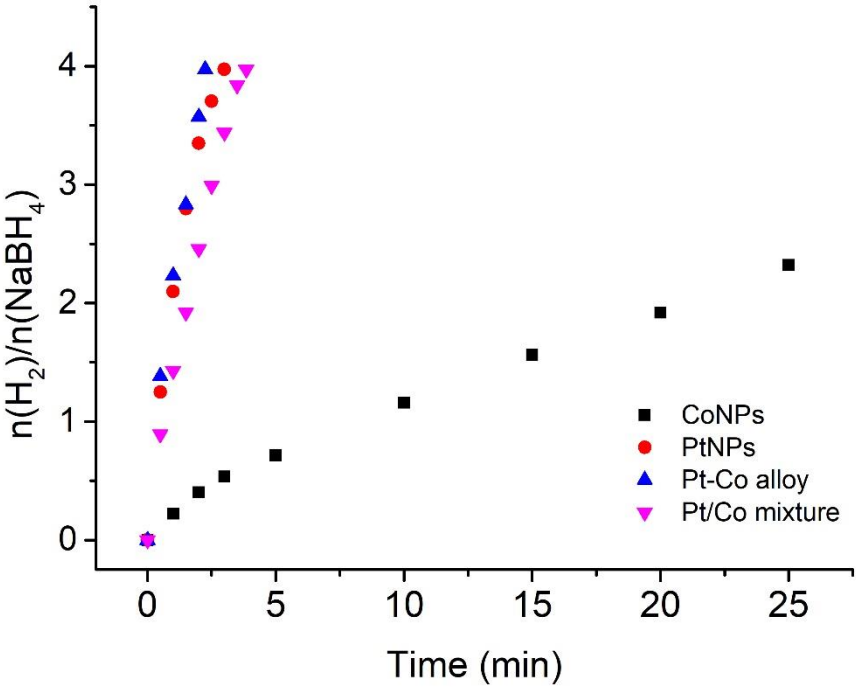

Figure S2.2 the efficiency of $NaBH_4$ hydrolysis derived by CoNPs, PtNPs, Pt-Co alloy and Pt/Co mixture.

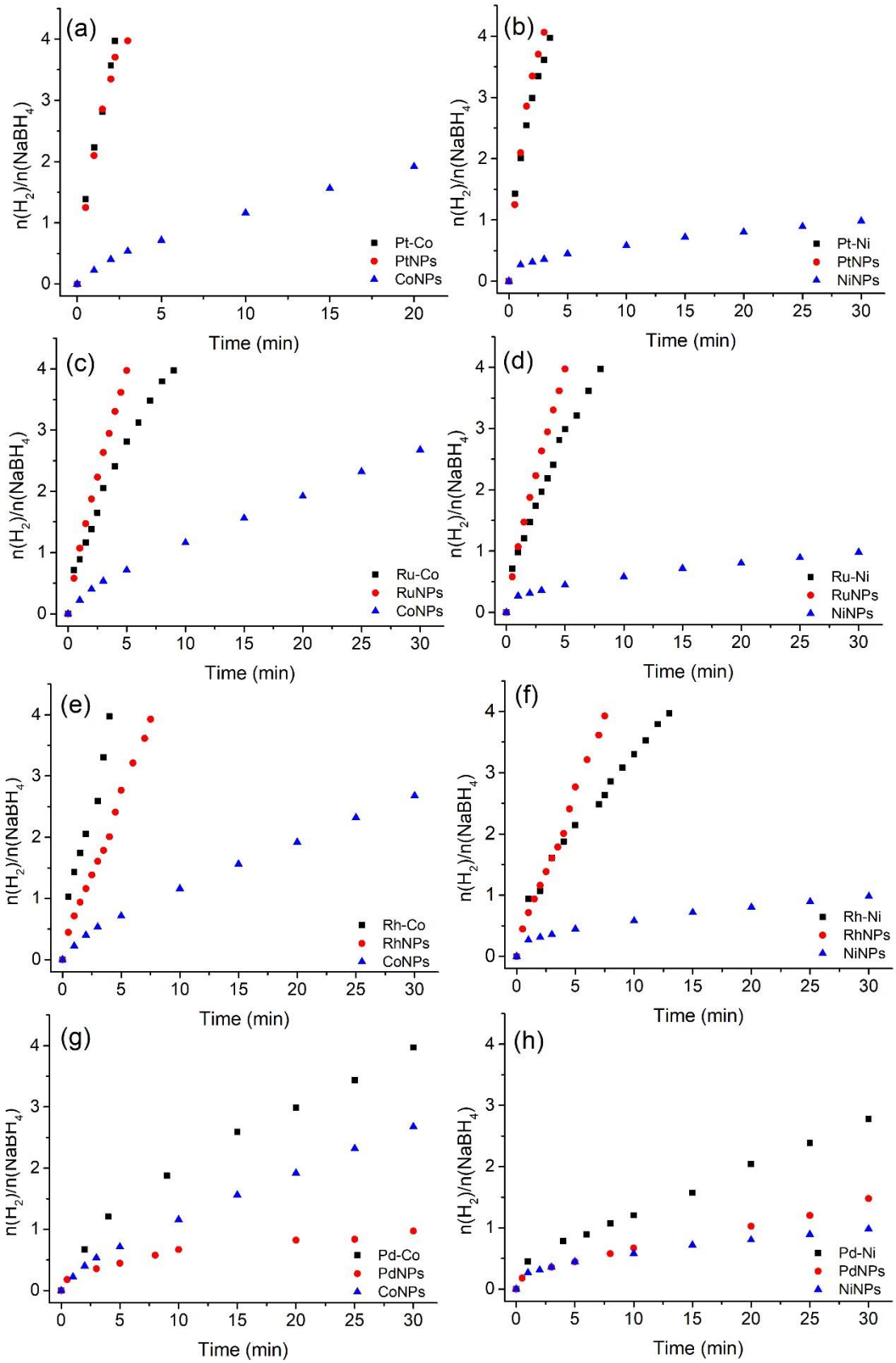

Figure S2.3 Comparation between various bimetallic NPs and their corresponding monometallic NPs.

Table S2.1 catalytic efficiencies of various MNPs in the presence and absence of 0.2 M NaOH at 25°C.

Catalyst	TOF ($mol_{H2} \cdot mol_{cat}^{-1} \cdot min^{-1}$)	TOF with NaOH
PtNPs	133.3	66.0
RuNPs	80.0	133.3
RhNPs	53.3	100.0
AuNPs	3.3	7.5
PdNPs	2.2	5.6
CoNPs	8.0	13.3
FeNPs	1.4	2.7
CuNPs	1.3	2.4

Table S2.2 catalytic efficiencies of various bimetallic NPs in the presence and absence of 0.2 M NaOH at 25°C.

Catalyst	TOF ($mol_{H2} \cdot mol_{cat}^{-1} \cdot min^{-1}$)	TOF with NaOH
Pt-Co	177.8	80.0
Rh-Co	88.0	66.7
Ru-Co	61.5	44.4
Pd-Co	6.7	2.4

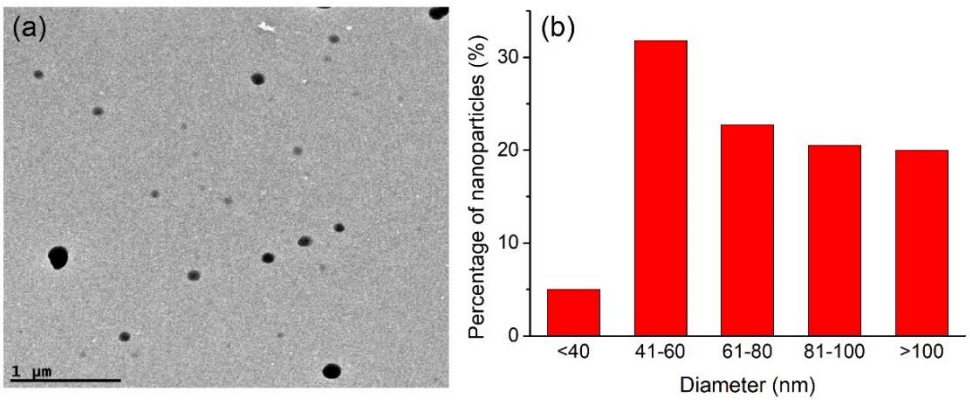

Figure S2.4 (a) TEM image and (b) size distribution of Pt1Co1/1 after 5th recycling.

Table S2.3 Comparison of recent literature results on Pt-based and Co-based catalysts for the hydrolysis of $NaBH_4$.

Catalysts	TOF ($mL_{H2} \cdot min^{-1} \cdot g_{Cat}^{-1}$)	Ea ($kJ \cdot mol^{-1}$)	T(°C)	Ref.
CoPt-PEDOT	6900	47.3	25	[91]

Pt/Si_3N_4	24200	-	80	[92]
Co–Pd–B	2920	36.36	25	[93]
Pt/LiCoO2	2700	-	25	[94]
Pt/CeO2-Co7Ni2Ox	783l	47.4	25	[95]
Pt-Co-G	21446	16.443	30	[96]
NiCoP	3986	38.3	45	[97]
FeCoB	2210	27	30	[98]
CoNiP	3636	38	30	[99]
CoNi alloy	655	-	30	[100]
Ru-Co-C	9310	-	25	[101]
Pt@dendrimer	15213	-		This work
Pt/Co@dendrimer	35636	24.95	25	This work

2.5. References

[1] R.E. Rodríguez-Lugo, M. Trincado, M. Vogt, F. Tewes, G. Santiso-Quinones, H. Grützmacher, *Nat. Chem*. **2013,** *5*, 342–347.

[2] T. da Silva Veras, T.S. Mozer, D. da Costa Rubim Messeder dos Santos, A. da Silva César, *Int. J. Hydrogen Energy* **2017**, *42*, 2018–2033.

[3] I. Sreedhar, K.M. Kamani, B.M. Kamani, B.M. Reddy, A. Venugopal, *Renew. Sustain. Energy Rev*. **2018,** *91,* 838–860.

[4] S.E. Hosseini, M.A. Wahid, *Renew. Sustain. Energy Rev.* **2016,** *57,* 850–866.

[5] M. Luo, Y. Yi, S. Wang, Z. Wang, M. Du, J. Pan, Q. Wang, *Renew. Sustain. Energy Rev*. **2018,** *81,* 3186–3214.

[6] A.M. Pornea, M.W. Abebe, H. Kim, *Chem. Phys.* **2019**, *516,* 152–159.

[7] L. Cui, Y. Xu, L. Niu, W. Yang, J. Liu, *Nano Res*. ,**2017**, *10,* 595–604.

[8] L. Lu, H. Zhang, S. Zhang, F. Li, *Angew. Chemie Int. Ed*. **2015,** *549,* 328–9332.

[9] B.C. Filiz, A.K. Figen, S. Pişkin, *Appl. Catal. B Environ*. **2018,** *238,* 365–380.

[10] A. Staubitz, A. P. M. Robertson, I. Manners, *Chem. Rev*. **2010,** *110,* 4079−4124.

[12] A. Rossin, M. Peruzzini, *Chem. Rev.* **2016**, *116,* 8848−8872.

[13] Q. Xu, M. Chandra, *J. Power Sources* **2006,** *163*, 364−370.

[14] D. M. F. Santos, C. A. C. Sequeira, *Renew. Sust. Energ. Rev.* **2011**, *15*, 3980- 4001.

[15] R. Retnamma, A.Q. Novais, C.M. Rangel, *Int. J. Hydrogen Energy* **2011**, 36, 9772–9790;

[16] N. Patel, A. Miotello, *Int. J. Hydrogen Energy* **2015**, *40*, 1429-1464.

[17] P. Brack, S. E. Dann, K. G. Upul Wijayantha, *Energy Sci. Eng*. **2015**, *3*, 174-188.

[18] H. Sun, J. Meng, L. Jiao, F. Cheng, J. Chen, *Inorg. Chem. Frontiers* **2018,** *5*, 760-772.

[19] P. Brack, S. E. Dann, K. U. Wijayantha, *Energy Sci. Eng*. **2015**, *3*, 174- 188.

[20] Y. Liu, G. Han, X. Zhang, C. Xing, C. Du, H. Cao, B. Li, *Nano Research* **2017**, *10*, 3035-3048.

[21] P. Y. Olu, A. Bonnefont, G. Braesch, V. Martin, E. R. Savinova, M. Chatenet, *J. Power Sources* **2018**, *375*, 300-309.

[22] D. D. Tuan, K. -Y. A. Lin, *Chem. Eng. J.* **2018**, *351*, 48-55.

[23] M. Haruta, T. Kobayashi, H. Sano, N. Yamada, *Catal. Letters* **1987**, 405-408.

[24] M. Haruta, *Catal. Today* **1997**, *36*, 153-166.

[25] M. C. Daniel, D. Astruc, *Chem. Rev*. **2004**, *104*, 293-346.

[26] D. Astruc, F. Lu, J. Ruiz, *Angew. Chem., Int. Ed*. **2005**, *44*, 7852-7872.

[27] N. T. S. Phan, M. Van Der Sluys, C. W. Jones, *Adv. Syn. Catal*. **2006**, 348, 609-679.

[28] V. Polshettiwar, R. S. Varma, *Green Chemistry.* **2010**, *12*, 7433-754.

[29] A. Balanta, C. Godard, C. Claver, *Chem. Soc. Rev*. **2011**, *40*, 4973-4985.

[30] E. Gross, J. H.-C. Liu, F. D. Toste, G. A. Somorjai, *Nat. Chem*. **2012**, *4*, 947-952.

[31] M. Haruta, *Angew. Chem., Int. Ed*. **2014**, *53*, 52−56.

[32] M. Sankar, N. Dimitratos, P. J. Miefziak, G. J. Hutchings, *Chem. Soc. Rev*. **2012**, *41*, 8099-8139.

[33] C. Amiens, D. Ciuculescu-Pradines, K. Philippot, *Coord. Chem. Rev*. **2016**, *308*, 409–432.

[34] M. B. Gawande, A. Goswami, F.-X. Felpin, T. Asefa, X. X. Huang, R. Silva, X. X. Zou, R. Zboril, R. S. Varma, *Chem. Rev*. **2016**, *116*, 3722.

[35] Y. Xia, K. D. Gilroy, H.-C. Peng, X. Xia, *Angew. Chem., Int. Ed*. **2017**, *56*, 60–95.

[36] Z. Shiffrina, L. M. Bronstein, *Frontiers Chem.* **2018**, *6*, 298

[37] M. K. Samantaray, E. Pump, A. Bendjeriou-Sedjerari, V. D' Elia, J. D. A. Pelletier, M. Guidotti, R. Psaro, J.-M. Basset, *Chem. Soc. Rev*. **2018**, *47*, 8403-8437.

[38] L. Liu, A. Corma, *Chem. Rev*. **2018**, *118*, 4981-5079.

[39] D. Wang, D. Astruc, *Chem. Soc. Rev*. **2017**, *46* (3), 816–854.

[40] H. Shu, L. Lu, S. Zhu, M. Liu, Y. Zhu, J. Ni, Z. Ruan, Y. Liu, *Catal. Commun.* **2019**, *118* 30–34.

[41] A. Yapicioglu, I. Dincer, *Renew. Sustain. Energy Rev*. **2019,** *103*, 96–108.

[42] Q. Wang, F. Fu, A. Escobar, S. Moya, J. Ruiz, D. Astruc, *ChemCatChem* **2018**, *10*, 2673–2680.

[43] Y. Wang, D. Astruc, A.S. Abd-El-Aziz, *Chem. Soc. Rev.* **2019.**

[44] F. Fu, C. Wang, Q. Wang, A.M. Martinez-Villacorta, A. Escobar, H. Chong, X. Wang, S. Moya, L. Salmon, E. Fouquet, J. Ruiz, D. Astruc, *J. Am. Chem. Soc*. **2018**, *140*, 10034–10042.

[45] C. Wang, J. Tuninetti, Z. Wang, C. Zhang, R. Ciganda, L. Salmon, S. Moya, J. Ruiz, D. Astruc, *J. Am. Chem. Soc.* **2017**, *139*, 11610–11615.

[46] D. Astruc, F. Chardac, *Chem. Rev*. **2001**, *10*1, 29913023.

[47] R. W. J. Scott, O. M. Wilson, R. M. Crooks, *J. Phys. Chem. B* **2005**, *109*, 692-704.

[48] D. Astruc, E. Boisselier, C. Ornelas, *Chem. Rev*. **2010**, *110*, 1857-1959.

[49] A.-M. Caminade, C.-O. Turin, R. Laurent, A. Ouali, B. Delavaux-Nicot. *Dendrimers. Towards Catalytic, Material and Biomedical Uses*, Wiley, Chichester, U. K., **2011**.

[50] N. Ma , C. Ma, Y. Deng, J. Nanosci. *Nanotechnol.* **2013**, *13*, 33-39.

[51] D. Wang, D. Astruc, *Coord. Chem. Rev*. **2013**, *257*, 2317-2334.

[52] M.-Y. He, Y. Feng, Q.-H. Fan, *Acc. Chem. Res*. **2014**, *47*, 2894-2906.

[53] A.-M. Caminade, A. Ouali, R. Laurent, C. O. Turin, J.-P. Majoral, *Chem. Soc. Rev*. **2015**, *44*, 3890-3899

[54] W. Wang, L.-J. Chen, X.-Q. Wang, *Proc. Nat. Acad. Sci. U. S.* **2015**, *112*, 5597-5601.

[55] D. Wang, C. Deraedt, J. Ruiz, D Astruc, *Acc. Chem. Res.* **2015**, *48*, 1871-1880.

[56] A.-M. Caminade, A. Ouali, R. Laurent, C. -O. Turin, J.-P. Majoral, *Coord. Chem. Rev*. **2016**, *308*, 478-497.

[57] R. Ye, A. V. Zhukhovitskiy, C. Deraedt, G. A. Somorjai, *Acc. Chem. Res*. **2017**, *50*, 1894-1901.

[58] P. Walde, S. Ichikawa, *Biomol. Eng.* **2001**, *18*, 143-177.

[59] L. K. Yeung, R. M. Crooks, *Nano Lett.* **2001**, *1*, 1417.

[60] Z. Chen, Z. M. Cui, F. Niu, L. Jiang, W. G. Song, *Chem. Commun*. **2010**, *46*, 6524-6526.

[61] Y. Lu, M. Ballauff, *Prog. Polym. Sci*. **2011**, *36*, 767-792.

[62] X. L. Fang, Z.-H. Liu, M.-F. Hsieh, M. Chen, P. X. Liu, C. Chen, N. F. Zheng, *ACS Nano* **2012**, *6*, 4434-4444.

[63] C. Deraedt, N. Pinaud, *J. Am. Chem. Soc*. **2014**, *136*, 12092-12098;

[64] C. Deraedt, D. Astruc, *Coord. Chem. Rev*. **2016**, *324*, 106-122.

[65] M. M. Sun, Q. Fu, L. J. Gao, Y. P. Zheng, Y. Y. Li, M. S. Chen, H. H. Bao, *Nano Research* **2017**, *10*, 1403-1412.

[66] H. R. Chen K. Shen, Q. Mao, J. Y. Chen, Y. W. Li, *ACS Catal* **2018**, *8*, 1417-1426.

[67] K. Aranishi, Q.-L. Zhu, Q. Xu, *ChemCatChem* **2014**, *6*, 1375−1379.

[68] Q. Wang, F. Fu, S.Yang, M. Martinez Moro, M. de los A. Ramirez, S. Moya, L. Salmon, J. Ruiz, D. Astruc, *ACS Catal.* **2019**, *9* (2), 1110–1119.

[69] A. K. Diallo, E. Boisselier, L. Liang, J. Ruiz, D. Astruc, *Chem. Eur. J.* **2010**, *16*, 11832−11835.

[70] Q.Yao, K. Yang, X. Hong, X. Chen, Z.-H. Lu. *Catal. Sci. Technol*. **2018**, *8*, 870-877.

[71] C. Ornelas, J. Ruiz, E. Cloutet, S. Alves, D. Astruc, *Angew. Chem. Int. Ed.* **2007,** 46, 872-877.

[72] S. Badèche, J.-C. Daran, J. Ruiz, D. Astruc, *Inorg. Chem*., **2008***, 47,* 4903-4908.

[73] X. Liu, D. Gregurec, J. Irigoyen, A. Martinez, S. Moya, R. Ciganda, P. Hermange, J. Ruiz, D. Astruc, *Nat. Commun*. **2016**, *7*, 13152.

[74] C. Deraedt, D. Astruc, *Acc. Chem. Res*. **2014**, 47, 494-503

[75] Y. Wang, L. Salmon, J. Ruiz, D. Astruc, *Nat. Commun.* **2014**, *5*, 3489.

[76] D. Huang, P. Zhao, D. Astruc *Coord. Chem. Rev*. **2014**, *272*, 145-165.

[77] C. Wang, R. Ciganda, L. Salmon, D. Gregurec, J. Irigoyen, S. Moya, J. Ruiz, D. Astruc, *Angew. Chem., Int. Ed*. **2016**, *55*, 3091-3095.

[78] A. Sermiagin, D. Meyerstein, R. Bar-Ziv, T. Zidki, *Angew. Chem., Int. Ed.* **2018,** *57*, 16525-16528

[79] E. Klindtworth, I. Delidovich, R. Palkovits, *Int. J. Hydrogen Energy,* **2018,** *43*, 20772-20782.

[80] A. E. Genc, A. Akca, B. Kutlu, *Int. J. Hydrogen Energy* **2018**, *43*, 14347-14359

[81] H. M. Sun, J. Weng, L. F. Meng, L. F. Jiao, F. Y. Chen, J. Chen, *Inorg. Chem. Frontiers* **2018**, *5*, 760-772.

[82] D. Astruc. *Organometallic Chemistry and Catalysis*. Springer, Heidelberg, **2007**, Chap. 3.

[83] A. Schneemann, J. L. White, S. Y. Kang, S. Jeong, L. F. Wan, E. S. Cho, T. W. Heo, D. Prendergast, J. J. Urban, B. C. Wood, M. D. Allendorf, V. Stavila, *Chem. Rev.* **2018**, *118*, 10775-10839.

[84] Quinn, B. M.; Liljeroth, P.; Ruiz, V.; Laaksonen, T.; Kontturi, K. *J. Am. Chem. Soc.* **2003,** *125,* 6644-6645.

[85] W.-W. Zhan, Q.-L. Zhu, Q. Xu. *ACS Catal*. **2016**, *6*, 6892-6905.

[86] Z.-H. Lu, J. Li, A. Zhu, Q. Yao, W. Huang, R. Zhou, R. Zhou, X. Chen. *Int. J. Hydrogen Energy* **2013**, *38*, 5330-5337.

[87] Q. Yao, Z-H. Lu, Y. Wang, X. Chen, G. Feng. *J. Phys. Chem. C* **2015**, *119*, 14167-14174.

[88] Q. Yao, Z.-H. Lu, W. Huang, X. Chen, J. Zhu. *J. Mater. Chem. A* **2016**, *4*, 8579-8583.

[89] L. Ouyang, W. Chen, J. W. Liu, M. Felderhoff, H. Wang, M. Zhu, *Adv. En. Mater.* **2017**, *7,* 1700299.

[90] L. Ouyang, H. Zong, H. W. Li, M. Zhu, *Inorganics* **2018,** *6*, 10

[91] X. Wang, Y. Zhao, X. Peng, J. Wang, C. Jing, J. Tian, *Mater. Sci. Eng. B* **2015** *200*, 99–106.

[92] A. Lale, A. Wasan, R. Kumar, P. Miele, U.B. Demirci, S. Bernard, *Int. J. Hydrogen Energy* **2016,** *41*, 15477–15488.

[93] Y. Zhao, Z. Ning, J. Tian, H. Wang, X. Liang, S. Nie, Y. Yu, X. Li, *J. Power Sources* **2012,** *207,* 120–126.

[94] Z. Liu, B. Guo, S.H. Chan, E.H. Tang, L. Hong, *J. Power Sources* **2008,** *176,* 306–311.

[95] C. Wu, J. Zhang, J. Guo, L. Sun, J. Ming, H. Dong, Y. Zhao, J. Tian, X. Yang, *ACS Sustain. Chem. Eng.* **2018,** *6,* 7451–7457.

[96] S. Saha, V. Basak, A. Dasgupta, S. Ganguly, D. Banerjee, K. Kargupta, *Int. J. Hydrogen Energy* **2014,** *39,* 11566–11577.

[97] A.M. Pornea, M.W. Abebe, H. Kim, *Chem. Phys.* **2019,** *516,* 152–159.

[98] Y. Liang, P. Wang, H.-B. Dai, *J. Alloys Compd.* **2010,** *491*, 359–365.

[99] Y. Guo, Q. Feng, J. Ma, *Appl. Surf. Sci.* **2013,** *273,* 253–256.

[100] A. Didehban, M. Zabihi, J.R. Shahrouzi, *Int. J. Hydrogen Energy* **2018,** *43,* 20645–20660.

[101] G.M. Arzac, M. Paladini, V. Godinho, A.M. Beltrán, M.C.J. De Haro, A. Fernández, *Scientific Reports* **2018**, *8*, 9755.

Chapter 3. Visible-light Acceleration of H_2 Evolution from Aqueous Solutions of Inorganic Hydrides Catalyzed by Gold-transition-metal Nanoalloys

3.1 Introduction

Production of hydrogen (H_2) from non-fossil sources has become a priority in the 21st century's research. [1, 2] Since the seminal work of Fujushima and Honda in 1972,[3] solar-light irradiation for water splitting using electron/hole pair formation of semiconductor catalysts has long been considered as an attractive solution, although it finds some practical limits concerning the nanoengineering of the materials involved.[4-8] Recently, hot electrons generated in the 1-100 fs range by visible light irradiation of gold plasmon are also promising for transfer of such electrons to an adjacent semiconductor conduction band.[9] In practice, however, the mismatch between the short lifetimes of hot electrons and the slow kinetics of reactions at the semiconductor surface has been a major limitation to the efficiencies of these plasmonic photocatalyzed reactions.[10-11] Semiconductors may most of the time also be toxic and of modest efficiency, and alternative solutions are continuously searched. Visible-light acceleration of a number of various catalytic reactions of synthetic and environmental interest has been reported for plasmonic gold as part of heterobimetallic catalysts.[12] In particular, interest has recently focused on plasmon induced light acceleration of hydrolysis of ammonia-borane (AB), NH_3BH_3, by coinage metal NPs using heterobimetallic nanocatalysts either coupled to[13-18] or without a semi-conductor.[19-23] Inorganic hydrides such as AB and sodium borohydride, $NaBH_4$, are promising hydrogen storage compounds,[24-26] because they are stable solids with high colloidal solubility in water, contain a high proportion of hydrogen and are easily transported contrary to explosive hydrogen gas.[27, 28] Also, AB is inert toward hydrolysis, and $NaBH_4$ is hydrolyzed only very slowly in the absence of catalyst.[29] Therefore, research efforts have recently been devoted to the optimization of catalysts for H_2 generation from water and such inorganic hydrides.[30-36] Heterobimetallic NP catalysts have attracted much attention because of the possible synergies between the two metals forming the NP.[37-47] Concerning photocatalytic AB dehydrogenation, Li's group reported theoretical calculations showing the presence of a special plasmonic resonance mode at the interphase of bimetallic core-shell NPs, adding to the surface mode.[48] The Yamashita group reported enhanced catalytic activity of small SBA-15 stabilized AgNPs upon visible-light irradiation for H_2 generation from AB hydrolysis without any other metal catalyst.[49] The same group reported an

enhancement factor of 2.8 upon visible-light irradiation of SBA-15-supported Pt-Ag NPs.[13] Huang's group reported the facet-dependent light-assisted hydrogen generation from AB using large (32 nm) Au-Pd core-shell nanocatalysts.[20] Previous studies from our group on hydrogen evolution from AB in the dark have dealt with group 9 and 10 metal nanocatalysts,[30, 32, 50] and positive synergistic effects have been disclosed with Co-Pt [50] and Ni-Pt NPs.[32] AuNPs benefit from an enhanced kinetic stability under aerobic conditions and have attracted an enormous amount of interest in various fields including biomedicine, optics and catalysis.[51]

We report here the acceleration effects of visible-light irradiation on the catalytic activity of a series of bimetallic Au-late transition metal NPs (LTMNPs) for H_2 production upon reaction of water with the boron hydrides AB and $NaBH_4$. During these same reactions, a second light effect observed is the progressive restructuration in several cases of the alloy nanocatalysts to core-shell Au@M. Comparison is made with monometallic LTMNP nanocatalysts that, as nanogold, are not subjected to any light effect under the same conditions. Indeed, remarkable boosting effects of visible light are disclosed here with bimetallic nanogold-containing alloyed nanocatalysts supported by "click" dendrimers or a "click" polymer.

3.2 Results and discussion

3.2.1 Macromolecule-stabilized nanocatalysts

The known water-soluble "click" dendrimers **1** (with an approximate diameter size of 10 nm) and **2** (with an approximate diameter size of 15 nm)[52] (Scheme 3.1) are catalyst templates acting as unimolecular micelles.[19] They stabilize molecular, cationic and LTMNP catalysts with small size leading to excellent catalytic results due to confinement of the catalyst and substrates in the dendritic interior including tris-triazole-containing tripods. The known "click" polymer **3**[53] (Scheme3.1 and S3.2) and poly(vinylpyrrolidone) (PVP) were also used as supports for comparison. Upon mixing the metal salt precursor and the dendrimer **1** or **2** or polymer **3** in water, a H_2O ligand of the metal cation is exchanged by the triazole ligand; thus, the metal cation keeps the same positive charge. In the case of the Pd and Pt tetrachlorometallates, an anionic chloride ligand of the square-planar complex MCl_4^{2-} is replaced by a neutral triazole ligand. Formally, the charge of the metal complex then changes from -2 to -1, whereas the metal oxidation state (II) remains unchanged (Scheme S3.3). Upon reduction of all these macromolecule-coordinated metal derivatives by $NaBH_4$, the oxidation state of all the metals is decreased to zero, and the atoms collapse into a LTMNP catalyst loosely stabilized by both the heteroatoms and bulk of the macromolecule. When 1 mmol AB (or $NaBH_4$) is completely hydrolyzed upon catalysis by the "click"-dendrimer-stabilized LTMNP, 3 (or 4) mmol of H_2 (67 or 89 mL) are produced, indicating reaction completion, in equations (1) or (2), respectively. In both reactions, a metaborate salt is formed in a di-hydrated form MBO_2, $2H_2O$, i.e. $MB(OH)_4$, M = Na or NH_4, and reaction intermediates were not detected.

$$NH_3BH_3 + 4H_2O \rightarrow NH_4^+B(OH)_4^- + 3H_2 \qquad (1)$$

$$NaBH_4 + 4H_2O \rightarrow NaB(OH)_4 + 4H_2 \qquad (2)$$

Most studies have been conducted using the click dendrimer **1** and, unless noted otherwise, results are reported in text with dendrimer **1**. In order to compare the above catalyzed reactions under dark and visible-light conditions, first, click-dendrimer-stabilized monometallic LTMNPs have been synthesized (Scheme 3.1), as previously reported,[50] by reduction of the click-dendrimer-coordinated M(II) or M(III)

species to M(0) using $NaBH_4$. The other LTMNPs were found to be better catalysts than AuNPs (a poor catalyst in this reaction) and, in all these cases, no catalytic enhancement was found upon visible-light irradiation, even with the monometallic AuNPs (Table 3.1). Then, click-dendrimer stabilized bimetallic Au-M NPs (M = Ni, Co, Ru, Rh, Pd, Pt or Ag) were synthesized by pre-coordination of both Au(III) and M(II) species to intra-dendritic triazole ligands followed by reduction of both M(II) and Au(III) to M(0) using $NaBH_4$.

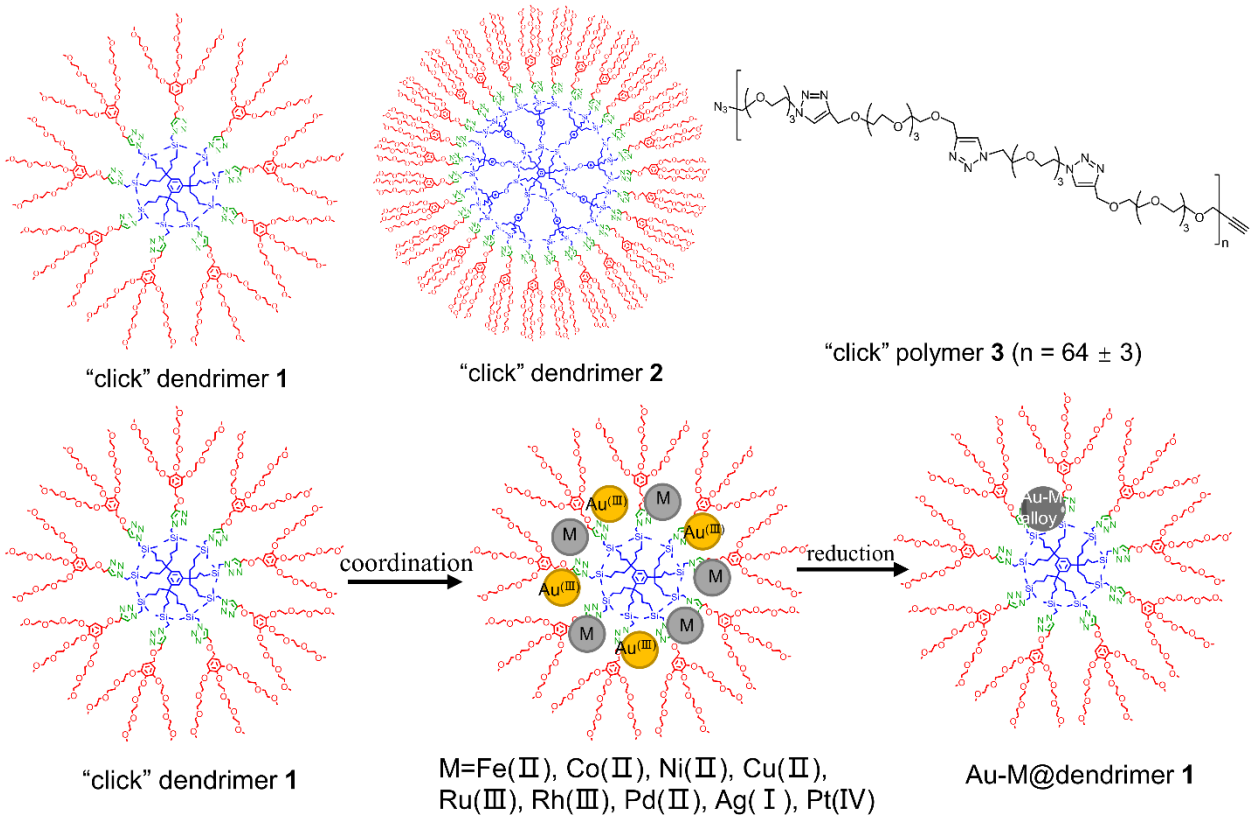

Scheme 3.1. Syntheses of the macromolecule-stabilized nanocatalysts Au-LTMNP.

3.2.2 Characterization of the nanocatalysts

These alloyed Au-M NPs were characterized by their small sizes measured by Transmission Electron Microscopy (TEM, Figure 3.1 and S3.6-S3.12) and low polydispersity, and the zero-oxidation state of both metals, determined by X-ray Photoelectron Spectroscopy (XPS).

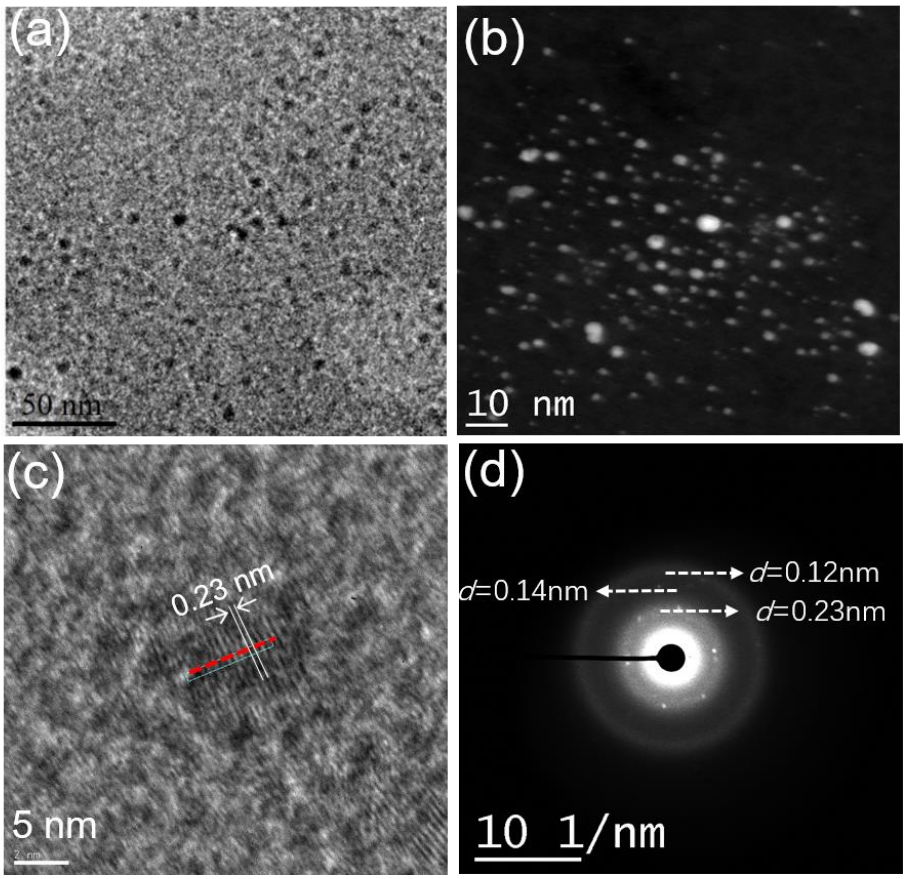

Figure 3.1. Characterization of Au_1Ru_1@dendrimer **1**, (a) TEM image, (b) HRTEM image, (c) interplanar instance, (d) SEAD image.

For instance, the Au_1Ru_1, Au_1Pt_1 and Au_1Co_1 NPs have a diameter size of 1.48, 1.22 and 2.1 nm respectively, with some polydispersities (Table S3.1), this small NP size being directed by the selective coordination to the stabilizing tris-triazole tripods with relatively long tethers of the dendrimer **1**. The Au-RhNPs were larger, 3.78 nm in diameter size, and thus stabilized by several dendrimers at their peripheries, which will have consequences on the recycling process (*vide infra*). A good crystallinity of Au_1Ru_1 NPs was confirmed as shown by the clear lattice fringes with 0.23 nm spacing in HRTEM (Figure 3.1c and 3.1d), if it is assumed that the crystallographic plane of the Au_1Ru_1 nanoalloy is {111}.[54, 55] Energy dispersive X-ray spectroscopy (EDS) of single Au_1Ru_1 NP showed that the Au and Ru elements were present in the 002 and 003 area (Figure S3.13). These techniques confirm that and the Au_1Co_1 and Au_1Ni_1NPs also possess alloyed structures (Figure S3.14-S3.17). XPS showed that all the nanocatalysts

retained the zero-valence state during catalysis. Since the intradendritic triazole ligands are neutral, surface atoms are indeed expected to be zero-valent (Figure S3.18-S3.24).[56]

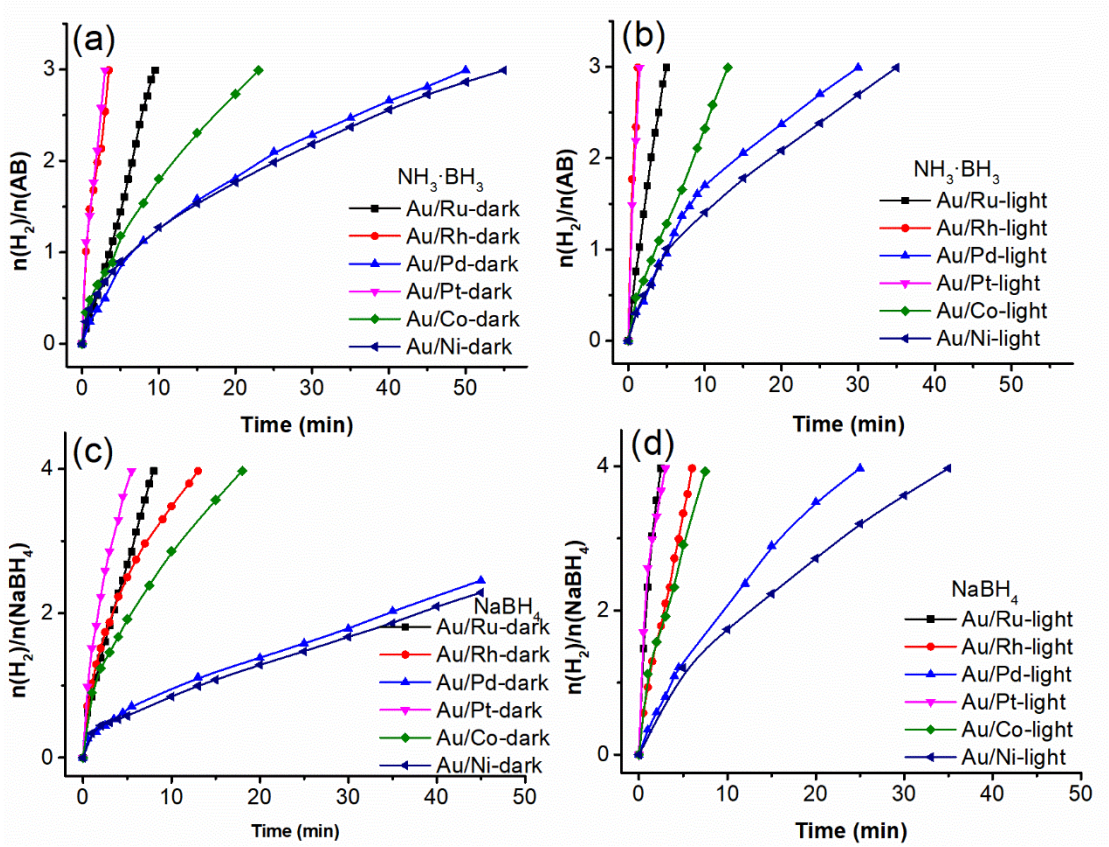

Figure. 3.2 Plot for molar amount of H_2 generated from AB or $NaBH_4$ hydrolysis vs. time for dendrimer **1**-stabilized Au-LTMNP alloys, (a) AB under dark reaction, (b) AB under visible light, (c) $NaBH_4$ under dark reaction, (d) $NaBH_4$ under visible light. In all the experiments, the reaction conditions are: 1 mmol of AB or $NaBH_4$; 1% mmol MNP; the ratio between Au and M is 1:1; temperature: 25 ± 0.2°C

3.2.3 Hydrolytic dehydrogenation of AB and $NaBH_4$ catalyzed by Au-based bimetallic catalysts.

Under dark conditions, the rates of hydrogen production showed the following order upon AB hydrolysis (Figure 3.2a): Au_1Pt_1 > Au_1Rh_1 > Au_1Ru_1 > Au_1Co_1 > Au_1Pd_1 > Au_1Ni_1 > Au, and for $NaBH_4$ hydrolysis (Figure 3.2c): Au_1Pt_1 > Au_1Ru_1 > Au_1Rh_1 > Au_1Co_1 > Au_1Pd_1 > Au_1Ni_1 > Au. In the dark reactions, alloying with gold had various (positive or, most often, negative) synergistic effects on the catalytic activity vs. the monometallic NP catalysts. Positive synergistic effects were observed essentially for Au-Co and Au-Pd alloyed nanocatalysts in both AB and $NaBH_4$ hydrolysis reactions in the dark (Table

3.1). The synergistic effect is due to electronic interaction between the two alloyed metals.[57, 58] The XPS data confirm electronic transfer from Au to Co, and this interaction is beneficial to improve catalytic substrate activation with positive catalytic synergy between these two metals in their nanoalloy. As shown in Figure S3.23, the binding energy of Au 4f (81.9 eV and 85.5 eV) in the AuCo alloy is shifted to lower value compared to that of AuNPs (83.6 eV and 87.1 eV),[59] while its Co 2p band (779.5 eV and 784.2 eV) is shifted to higher value compared to CoNPs (778.9 eV and 780.6 eV). Conversely, when the shifts of the XPS bands are observed in the same direction towards higher energies for the two metal upon alloying them, electronic transfer is not significant, and there is no catalytic synergy, or a negative synergy due to the dilution of the more active metal in the alloy. This is the case here for AuPt and AuRu. For instance, the Au 4f bands (84.8 and 88.3 eV) of AuPt are shifted to higher values compared to monometallic AuNPs (83.6 eV and 87.1 eV), [59] and the Pt 4f band is also shifted to higher energy from 71.6 and 74.8 eV for PtNPs to 72.6 and 76.0 eV for AuPt (Table S3.2).

Remarkably, visible-light irradiation boosted the catalysis by all these Au-containing alloys compared to dark reactions, while no light effect was observed with the monometallic NPs (Figure 3.2b, d, Tables 3.1 and Figure S3.25-S3.29) or bimetallic NPs that did not include Au. Some bimetallic catalysts such as Au-Fe, Au-Cu, and Au-Ag were not effective in quantitatively completing the stoichiometric reactions of equations (1) and (2) (Figure S3.30). The most spectacular acceleration of Au-LTMNP-catalyzed hydrolysis was observed upon visible-light irradiation of RhNPs and RuNPs that were both alloyed with Au for AB and $NaBH_4$ hydrolysis. As shown in Table S3.3, for Au_1Ru_1NPs, compared to hydrolytic dehydrogenation of $NaBH_4$ conducted under dark, the TOF value increased from 63.5 to 240.5 mol_{H2} mol_{cat}^{-1} min^{-1} upon visible light irradiation. The TOF value for AB hydrolysis derived by Au-Rh NPs increased from 288.1 to 813.6 mol_{H2} mol_{cat}^{-1} min^{-1} under visible light (Table S3.3). Increasing the dendrimer generation G_n of the "click" dendrimer stabilizer from G_0 with 27 tethers to G_1 with 81 tethers has a negative influence on the reaction rates (negative dendrimer generation $_1$pletion of the reaction (Figure S3.31, positive dendrimer effect). The Au/Ru and Au/Co and ratios 1/1, 1/2 and 2/1 were tested

in the alloys, and the most efficient catalysts were the alloy Au_1Ru_1 and Au_1Co_1 NPs, respectively (Figure S3.32 and Table S3.4). Although the low-intensity LED light did not appear to increase the temperature of the reaction system, contribution from the photothermal effect still needed to be considered. The thermometer was located inside the reaction vessel, in order to measure the exact solution temperature. The temperature increase of the aqueous solution containing Au_1Ru_1 catalyst in the presence of visible light irradiation has been measured. A temperature increase of only 1 °C was observed over 10 min of irradiation (Figure S3.33a), but the efficient catalysts allowed delivery of hydrogen with reactions that were completed after only 1.3 to 4 min depending on the system. There was no significant increase in the hydrogen production rate at 26 °C compared to that at 25 °C (Figure S3.33b), thus it is concluded that the photothermal effect has no significant contribution to the visible-light induced enhancement of the dehydrogenation reaction.These alloys were also compared with equimolar mixtures of AuNPs and MNPs (M = Ru or Co), and the rate increase upon visible-light irradiation was larger in the alloy than in the mixture of these monometallic NPs (Figure S3.34 and Table S3.4). The Au-LTMNPs absorb light in the visible region as shown from their broad plasmon bands observed in the 450-550 nm region in their UV-vis. spectra. Thus, the lack of light-induced acceleration in both AuNP and other monometallic LTMNPs show that the light-induced acceleration of the catalysis is due to the presence of Au in alloys. Upon light absorption by the Au surface atom, a “hot electron” is formed from the Au plasmon and immediately transferred to the substrate-activating Ru or other atom (Au→Ru or Au→M), whatever the electronic delocalization at the NP surface enhancing its catalytic activation efficiency, particularly at corners and edges. Different wavelength irradiations have also been evaluated in the broad range of the plasmon band from 450 to 550 nm. In Figure S3.35, the catalytic hydrolysis efficiencies of AB and $NaBH_4$ are shown upon 470 nm, 520 nm and 620 nm irradiation. As a result, the 470 nm and 520 nm light irradiations are more efficient to accelerate the hydrolytic dehydrogenation of AB and $NaBH_4$ catalyzed by Au_1Ru_1@denrimer **1**, respectively.

Table 3. 1. Compared TOFs for reactions under dark and visible-light during $NaBH_4$ and AB hydrolysis at 25 ± 0.2°C catalyzed by monometallic and alloyed bimetallic NPs stabilized by the dendrimer **1**.

Catalysts	$NaBH_4$				AB			
	TOF_t[a] (dark)	TOF_t[a] (light)	Synergistic effect [b]	Vis. light effect [c]	TOF^t[a] (dark)	TOF_t[a] (light)	Synergistic effect[b]	Vis. light effect[c]
Au	1.7	1.7	NA[d]	No	1.2	1.2	NA[d]	No
Ru	80	80	NA	No	60	60	NA	No
Au_1/Ru_1	47	178	0.6	3.8	30	67.7	0.5	2.3
Rh	57	57	NA	No	100	100	NA	No
Au_1/Rh_1	33	66	0.6	2	85	240	0.9	2.8
Pd	2.3	2.3	NA	No	1.5	1.5	NA	No
Au_1/Pd_1	6	15	2.6	2.5	6.7	16	4.5	2.4
Pt	133	133	NA	No	133	133	NA	No
Au_1/Pt_1	72	133	0.5	1.85	75	200	0.6	2.7
Co	8	8	NA	No	6	6	NA	No
Au_1/Co_1	22	50	2.75	2.3	17	27	2.8	1.6
Ni	5.2	5.2	NA	No	4	4	NA	No
Au_1/Ni_1	6.1	12.5	1.2	2	5.4	10	1.1	1.9

[a] TOF_t: $mol_{H2\ released}$ / (total $mol_{catalyst}$ × reaction time $_{(min)}$) for all atoms, the unit of TOF_t is $mol_{H2}\ mol_{cat}^{-1}\ min^{-1}$. [b] For reactions in the dark: comparison of the catalytic efficiency between bimetallic NPs and the corresponding monometallic NPs (the better ones). Ratio: TOF_t of the better monometallic NPs/ TOF_t of the alloyed bimetallic NPs. When this ratio is > 1, it shows a positive synergistic effect; conversely, if the ratio is < 1, it shows a negative synergistic effect. [c] Comparison of the efficiencies between the reactions in the dark and with vis. light catalyzed by alloyed bimetallic NPs, expressed as the ratio between TOF_t (alloyed bimetallic NPs under light) and TOF_t (bimetallic NPs under dark). When this effect is >1, it shows a positive vis. light effect. [d] NA: not applicable.

3.2.4. Recycling of Au_1Ru_1 and Au_1Co_1 catalysts for hydrolysis of AB and $NaBH_4$

Interestingly, after boosting AB or $NaBH_4$ hydrolysis upon visible-light irradiation and complete stoichiometric hydrogen generation, the plasmon band then disappeared, and there was no longer visible-light absorption; then the UV-vis. spectra became flat (Figure 3.3a and Figure 3.3d). Upon recycling these catalysts that no longer absorbed visible light, no more light effect was observed upon comparing reactions in the dark and in the presence of light. Surprisingly, however, with most of the alloys the dark

reactions upon recycling were faster than the dark reactions of the original alloyed catalysts for both AB and $NaBH_4$ hydrolysis reactions, although not as fast as upon visible-light irradiating the original alloy nanocatalyst (Figure 3.3b and 3.3c). Only Au-Pd, Au-Rh and Au-Pt tended to agglomerate after AB hydrolysis, which prevented recycling, contrary to $NaBH_4$ hydrolysis (Table S3.5). Up to four reaction recycling were carried out with Au_1Ru_1 and Au_1Co_1 with some (but not dramatic) decrease of the rate compared to the initial reaction under visible-light irradiation (Figure 3.3b). These phenomena were observed for the bimetallic Au_1Ru_1 NPs and Au_1Co_1 NPs tested with both AB hydrolysis and $NaBH_4$ hydrolysis (Figure 3.3e, 3.3f and S3.37). TEM showed that the sizes of the Au-M NPs increased during the light-induced acceleration of the inorganic hydride hydrolysis. For instance, for the Au_1Ru_1 NPs (resp. Au_1Co_1NPs), the NP size increased from 1.5 nm (resp. 2.1 nm) before reaction to 2.5 nm (resp. 5 nm) after visible light reaction (Figure S3.38-3.40). During recycling reactions, the NP size no longer increased significantly, however. XPS showed the presence of both Au and Ru at the NP surface before reaction. After reaction in the presence of light, a dramatic decrease in the intensity of Au peaks compared to those of Ru (Figure S3.41) was observed, in accord with the disappearance of the plasmon band in the UV-vis. spectrum. This reduction in the Au signal hints to an accumulation of the other LTM on the surface of the NP. The disappearance of the plasmon band and the strong decrease of Au at the NP surface both signify removal of Au from the surface and its accumulation on the NP core, reflecting a deep restructuration from an alloy to a core-shell nanostructure in the course of the light-induced reactions catalyzed by the fresh bimetallic Au-M alloys (Figure 3.3a). In addition, shifts of the Au 4f and Ru 3d bands are observed upon comparing the XPS spectra before and after reaction (Figure S3.41). The bands of Au 4f at 84.7 and 88.1 eV before reaction are shifted to lower value (84.0 and 87.6 eV) after reaction, while the Ru 3d bands (284.5 and 286.2 eV) before reaction shifted to higher values (285.1 and 286.7 eV) after reaction. These Au bands are also shifted to lower values compared to those of monometallic AuNP, while the Ru bands are also shifted to higher values compared to those monometallic RuNPs (*vide supra*). This means that electronic transfer from Au to Ru has occurred during the irradiation reaction process,

and Ru is also electronic enriched at the expense of Au compared to monometallic Au and Ru NPs. These data all confirm the Au@Ru@dendrimer structure of the restructured bimetallic catalysts following visible-light irradiation. The superior catalytic activity of these restructured Au@Ru NPs compared to the initial Au_1Ru_1 alloy and to the monometallic Ru@dendrimer NPs results from electronic transfer from the Au core to the Ru surface, and the consecutive improved catalytic activity of the core-shell nanocomposite compared to the related alloys has precedents.[60]

The HRTEM/EDS data also show the strong decrease of the Au content at the LTMNP surface (Figure S3.42a and Table S3.6). These data indicate that the alloyed NPs progressively transform under the effect of visible light into a core-shell structure leaving almost exclusively only Ru or other non-Au metals at the NP periphery (Figure S3.42). This transformation that occurred along with a significant increase in size in the presence of the boron hydride and macromolecular triazole was irreversible during further processes for which the structure and size remained essentially constant. It appears that the energy provided by the plasmonic excitation upon visible-light alloy irradiation under these specific reaction conditions allows reaching a more stable thermodynamic state in the core shell Au@M topology than the original nanoalloy state. Since AuNPs are a poor catalyst of these reactions and most other noble LTMNPs are good catalysts,[41] a decrease of the Au content on the alloy surface and an increase of the content of the more active catalyst along the light-induced reactions explain the much better activity upon recycling in the dark after the restructuration of the catalyst than in the initial alloy (Figure S3.43-S3.46). In summary, in the first run of hydrolytic dehydrogenation of AB and sodium borohydride catalyzed by Au-LTMNPs, visible

light played two roles: 1) visible-light enhanced catalytic activity upon plasmonic effect of Au surface resulting in the formation and transfer of hot electrons from Au atoms to nearby or other atoms M on the NP surface boosting H_2 release; 2) visible-light induced restructuration of the alloy nanocatalyst to core-shell Au@M topology due to plasmonic hot electron energy provoking formation of the more

thermodynamically stable nanomaterial state, in which the Ru or other metal-rich NP surface is much more catalytically active than in the initial Au-containing alloy surface.

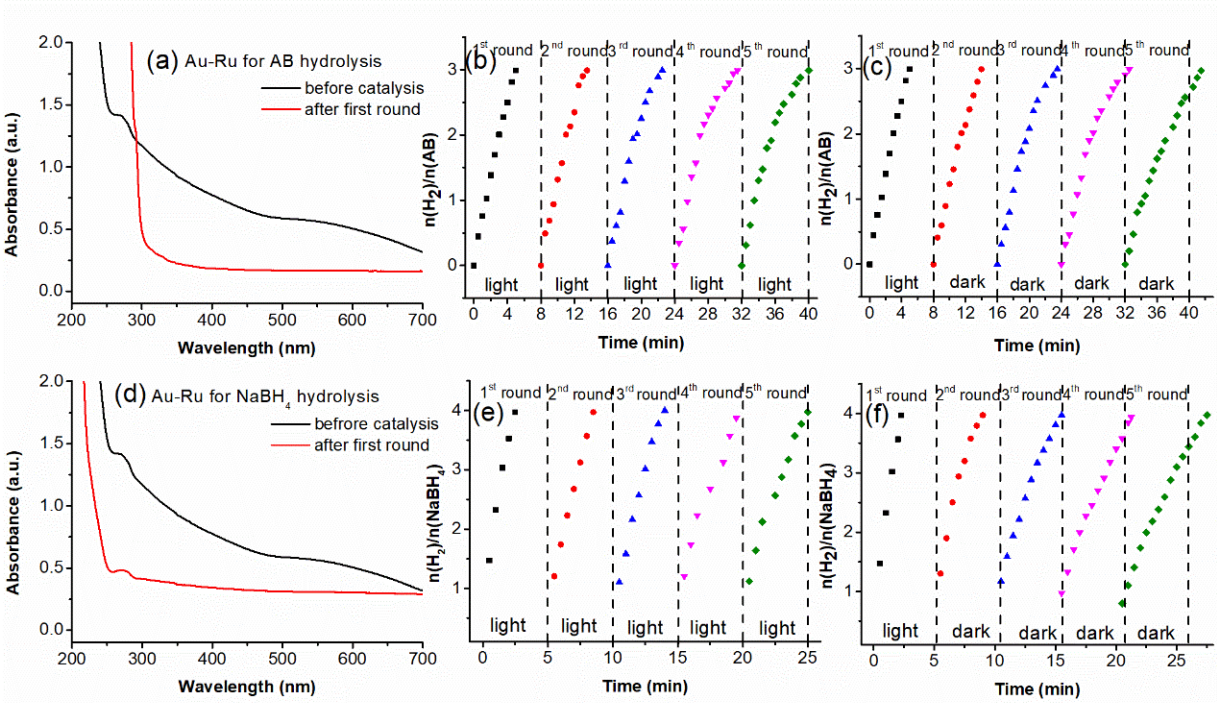

Figure 3.3. (a) UV-vis. spectra of Au_1Ru_1 for AB hydrolysis before catalysis and after the first catalytic cycle. After further catalysis recycling, the UV-vis. spectra remain the same as after the first cycling. (b) Plot of molar amount of H_2 generated from AB hydrolysis vs. time taken by Au_1Ru_1 during visible light irradiation in the reuse test. (c) Plot of molar amount of H_2 generated from AB hydrolysis vs. time taken by Au_1Ru_1 during the reuse test without visible light in the second cycle. (d) UV-vis. spectra of Au_1Ru_1 for $NaBH_4$ hydrolysis before catalysis and after the first catalytic cycle. After further catalysis recycling, the UV-vis. spectra remained the same as after the first cycle (e) Plot of molar amount of H_2 generated from $NaBH_4$ hydrolysis vs. time taken by Au_1Ru_1 with visible-light irradiation during the reuse test. (f) Plot of molar amount of H_2 generated from $NaBH_4$ hydrolysis vs. time taken by Au_1Ru_1 in the reuse test without visible light in the second cycle. Reaction conditions: amount of AB ($NaBH_4$) used: 1 mmol, temperature: 25 ± 0.2°C

3.2.5 Comparison of hydrolysis efficiency of AB and $NaBH_4$ by various nanocatalysts supported by a series of stabilizers

The case of the Au-RhNPs is specific in that, contrary to other Au-LTMNPs these NPs agglomerated after visible-light irradiation, which rendered recycling impossible. This is probably due *inter alia* to the large size of these Au-RhNPs that were stabilized inter-dendritically rather than intra-dendritically, provoking easy agglomeration due to weaker dendritic protection. Except for the Au-RhNPs, dendrimer **1** proved to be an excellent LTMNP support in the catalysis process. Dendrimer **2** could not prevent Au-RhNP agglomeration after catalysis either, due to its small cavities. For all the other Au-LTMNPs, dendrimer **1** was the best support in terms of stabilization, catalysis and recycling, compared to other stabilizers (dendrimer **2**, click polymer **3** and PVP).[53, 61] As shown in table S3.7, dendrimer **1**, dendrimer **2**, and click polymer **3** made a significant difference between visible-light irradiation and dark reaction. Specifically, the TOF values for hydrolysis of AB and $NaBH_4$ increased at least by a factor of 2 upon shifting reactions from dark to visible light with dendrimer **1**, dendrimer **2** and click polymer **3** as supports, respectively (Table S3.8). However, there was no change of efficiency between light and dark when PVP was the support, and the catalysts PVP-LTMNP then quickly agglomerated even before the end of reactions. Therefore, the structure of the stabilizer exerts a considerable influence on the photocatalysis. The main structural difference among dendrimer **1**, dendrimer **2**, click polymer **3** and PVP is the presence of the triazole ligands in the first three stabilizers that play a key role in the photocatalysis. The size of the Au-LTMNP alloy on the triazole-containing stabilizer increased less upon visible-light irradiation, compared to LTMNPs supported on PVP, and consequently Au-LTMNPs stabilized by triazole-containing macromolecular structures can be reused (Figure S3.47-3.49, Table 3.2, S3.7, S3.8) contrary to PVP-supported LTMNPs. The dendrimer **1** is the best triazole-containing support, because of the confinement induced by the dendritic tripodal ligands (positive dendritic structure effect) with less steric inhibition than in dendrimer **2**. In summary, the triazole ligand in the stabilizer allows LTMNP stabilization at a small NP size before and during photocatalysis. Therefore, the triazole-containing support facilitates capture of the visible light by coordination to the Au atoms. This tripodal coordination

increases electronic density on the NP, thereby accelerating plasmonic generation of hot electrons,[53, 56] and the optimized stereo-electronic functions of the triazole-containing stabilizer are best insured by the NP-encapsulating dendrimer **1**.

Table 3.2. Comparison of the different stabilizers for dark and visible-light irradiation derived by Au_1Ru_1 catalyst upon $NaBH_4$ hydrolysis reactions at 25 ± 0.2°C

Supports	TOF_t[a] ($NaBH_4$ under dark)	TOF_t [a] ($NaBH_4$ under light)	TOF_t [a] (AB under dark)	TOF_t[a] (AB under dark)	recycling
Dendrimer **1**	63.5	240.5	40.5	101.4	YES
Dendrimer **2**	51.6	96.7	34.0	68.1	YES
"Click" polymer **3**	27.5	55.3	16.8	31.1	YES
PVP	123.4	123.4	84.0	84.0	NO

[a] $TOF_t = mol_{H2\ released} / (surface\ mol_{catalyst} \times reaction\ time_{(min)})$

3.2.6 Proposed mechanism

The light-induced reaction mechanism must take into account both effects of light on these nanocatalyzed hydrogen evolution reactions: (i) light-induced acceleration of hydrogen release, and (ii) light-induced nanoalloy restructurarion to core@shell NP. Both light effects are causing reaction acceleration at the very beginning of the reaction, whereas by the end on the reaction only the restructuration alloy → Au core@Ru is the cause of hydrogen release acceleration compared to catalysis by the nanoalloy in the dark. Thus, the plasmon-induced acceleration progressively decreases along the reaction with the progressively growing effect of decrease of Au proportion and increase of Ru proportion on the NP surface. In order to distinguish between these two effects of light, the effect of the time of light irradiation on the time necessary to obtain complete hydrogen evolution was investigated. For instance with $NaBH_4$ (Figure S3.50a), complete hydrogen evolution was obtained after 2.5 min of light irradiation, whereas 9 min was necessary in the dark. It was found that one or two min of visible-light irradiation was not sufficient, but only with 2.5 min of visible-light irradiation was complete evolution obtained in 3 min. Consequently, during the last 0.5 min necessary to obtain complete hydrogen evolution from AB, the light had no more effect on the reaction, and the regime was the same as during the recycling, i.e. reaction acceleration compared to reaction of the alloy-nanocatalyzed reaction is

exclusively due to Ru being in higher proportion than Au on surface of the core Au@Ru shell NP than on the surface of the initial alloy.

Concerning the reaction mechanism of AB hydrolytic hydrogen release in the dark, let us recall that one of the hydrogen atoms from H_2 comes from AB and the other one from water. [62-64] The kinetic isotope effect (KIE: k_H/k_D) is an effective way to identify the rate-determining step (RDS) of a reaction.[65, 66] The proposed mechanism earlier with AB for dark reactions was suggested to involve cleavage of a water O-H bond in the rate-limiting step (RLS) based on high values of the KIE values between 2.46 [50] and 2.49 [30] using D_2O combined with low values of KIE using NH_3BD_3 such as 1.33.[30] With Au_1Ru_1@dendrimer **1** in the dark, the KIE found with D_2O was 2.25 (Figure S3.51), which is consistent with earlier studies confirming a primary KIE leading to an analogous suggestion of water O-H bond cleavage in the RLS. In the presence of light, this KIE value raised to 3.00, which even more clearly reflects water bond breaking in the RLS. Interestingly, in the recycling experiment, the KIE value found raised to 3.38 pointing an additional KIE increase compared to the initial experiment under visible light (Figure S3.51), which is due both to the increased activity of the Ru atoms on the alloy surface and to the light-induced NP restructuration bringing a higher proportion of Ru atoms on the NP surface. In the presence of light, this electron density on Ru atoms is strongly enriched by the additional hot electron transmitted from the Au plasmon. Visible light accelerates the reaction, and the KIE with D_2O should be enhanced compared to the KIE of the dark reaction; this was indeed found. Overall, the cleavage of the water O-H bond in the species NP-H...H-OH in the RLS in the presence of visible light for AB hydrolysis appears more clearly, partly due to the privileged role of Ru atoms in this oxidative addition compared to those of other elements such as Au and Ni. Oxidative addition of the water O-H bond can be achieved by a single Ru atom or by two adjacent Ru atoms of the NP surface.[67, 68] This RLS follows the fast B-H bond activation of AB on the NP surface that appears independent from the RLS step due to the insignificant hydrogen bonding between neutral AB and water (Scheme 3.2, top).

After reductive elimination of both H_2 and $[NH_3BH_2OH]$, the same step would occur again with the later, finally leading to the formation from AB of 3 mol H_2 and $[NH_3B(OH)_3]$, then $[NH_3B(OH)_3]$ further hydrolyzed to stable $[NH_4B(OH)_4]$ (Scheme 3.2).

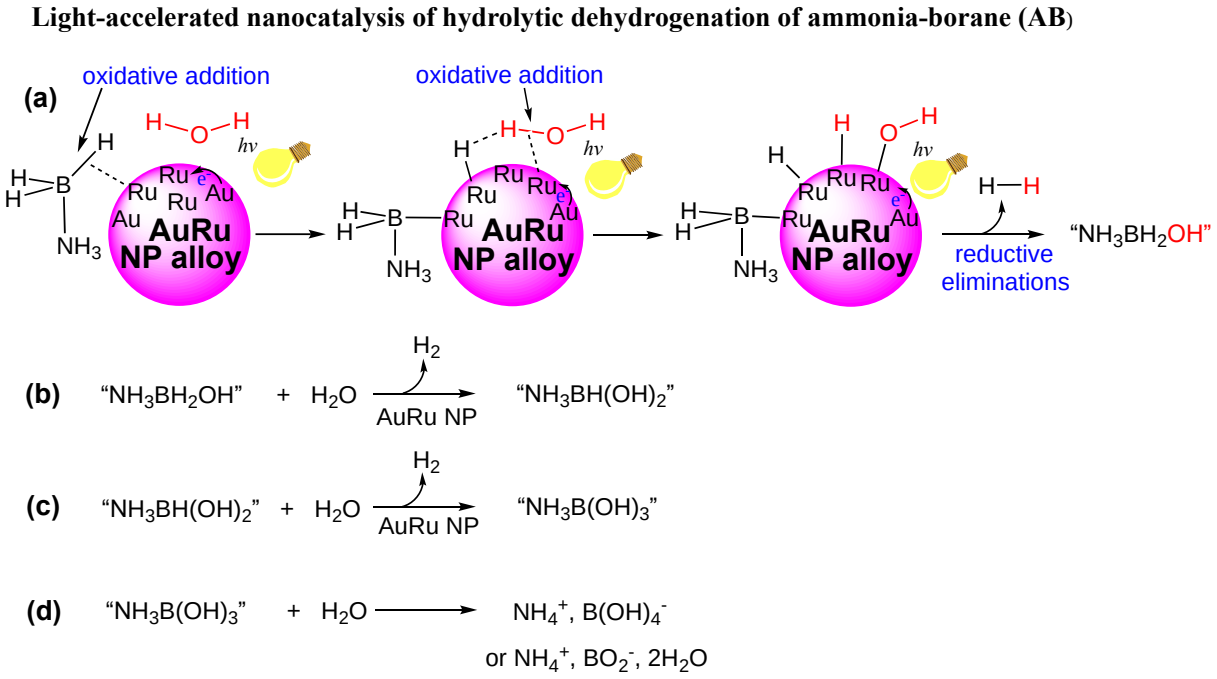

Scheme 3.2. Suggested mechanism for the visible-light-accelerated hydrolytic dehydrogenation of AB nanocatalyzed by Au_1Ru_1@dendrimer **1**.

This mechanism seems relatively similar for $NaBH_4$ and AB. Indeed, with $NaBH_4$ the KIE obtained using D_2O was 2.25 in the dark, 3.40 under visible light and 3.8 in the recycling (Figure S3.52a), which follows the same trends as with AB. Experiments with $NaBD_4$ led to KIE of 1 in the dark, and 1.13 in recycling (Figure. S3.52b), indicating that $NaBH_4$ is not involved in the RLS and that no restructuration occurs along the experiment in the absence of light.

On the other hand, experiments in the presence of visible light led to a KIE of 2.2, whereas 2.6 was obtained in the recycling (Figure S3.52b). This shows that, in the presence of visible-light irradiation, both visible-light and light-induced alloy → Au core @Ru shell restructuration boost the activity of the Ru atoms that synergistically activate both the B-H and O-H bonds in the RLS in a concerted way, although the O-H bond is stronger (493 kJ mol^{-1}) [61] than the B-H bond (430 kJ mol^{-1}).[69] This synergy can

be taken into account by the strong H-bonding between a hydridic hydrogen and H_2O that brings the $NaBH_4$...H_2O ensemble onto the NP surface together with the fact that the Ru atoms, that are strong X-H bond activators, activate both bonds in the same step, also because of O-H bond weakening by hydrogen bonding, contrary to weaker bond activators among the transition metals that are more selective (Scheme 3.3).[65, 66, 68]

Light-accelerated nanocatalysis of hydrolytic dehydrogenation of sodium borohydride

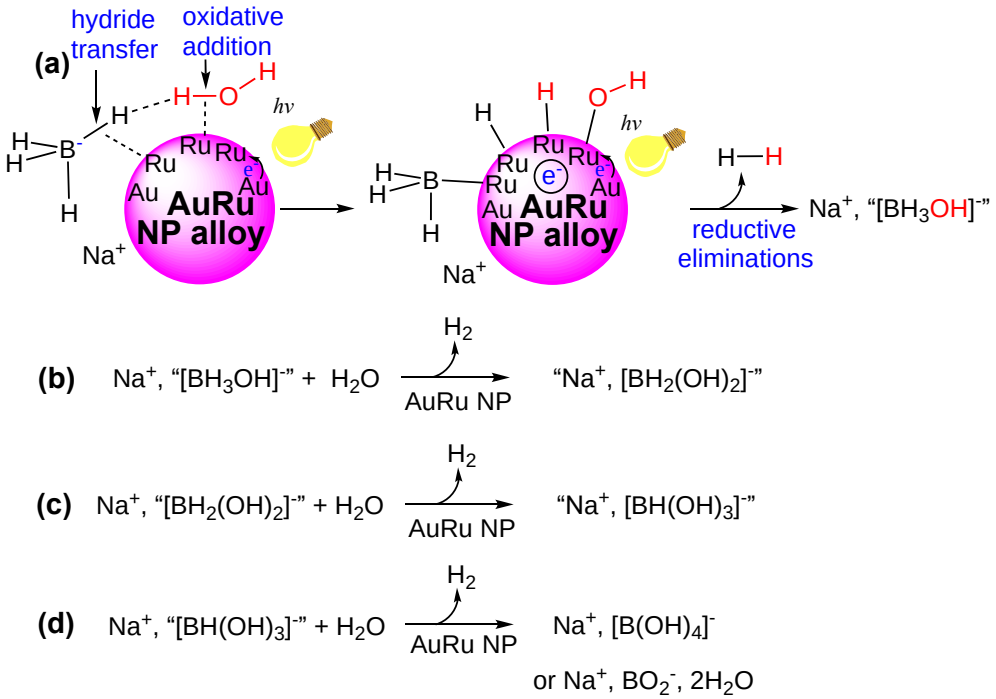

Scheme 3.3 Suggested mechanism for the visible-light-accelerated hydrolytic dehydrogenation of $NaBH_4$ nanocatalyzed by Au_1Ru_1@dendrimer **1**.

$NaBH_4$ is hydrolyzed, to 4 mol H_2, much more easily than AB when Au_1Ru_1 and Au_1Co_1 are the nanocatalysts (Figure S3.52). This is verified in terms of performances. The TOF values of AB hydrolysis catalyzed by Au_1Ru_1 and Au_1Co_1were previously found to be 101.4 and 60.0 mol_{H2}·molcatal.$^{-1}$·min^{-1}, respectively, which is inferior, under the same conditions, to those found with $NaBH_4$ for Au_1Ru_1 and Au_1Co_1 of 240.5 and 111.1 mol_{H2}·molcatal.$^{-1}$·min^{-1}, respectively.

3.3 Conclusion

It has been shown here that visible light boosts the Au-based alloyed nanocatalysts Au-LTMNPs (LTM = Ru, Co, Rh, Ni, and Pt) with a series of triazole-containing macromolecular stabilizers as supports for H_2 production from dehydrogenation reaction of aqueous solutions of the hydrogen-rich boron derivatives AB and $NaBH_4$. Dendrimer **1**-stabilized Au_1Ru_1, $Au_1Pt_1$and Au_1Rh_1NPs showed remarkably high visible-light effects and efficiencies for these hydrolysis reactions, and Au_1Ru_1 was recycled four times in dark reactions. Thus, Ru combines the advantages of being by far the cheapest noble metal and showing excellent light-acceleration effects, efficiencies and recyclabilities in both AB and $NaBH_4$ hydrolysis reactions. In fact, there are two light effects that both favor H_2 evolution from these hydrogen-rich boron derivatives. The first one is photocatalytic, i. e. the light absorption by the Au plasmon produces hot electrons that are transferred to one or several adjacent Ru atoms boosting substrate activation efficiency to produce H_2. The second visible-light effect simultaneously causes progressive alloy → Au core@Ru (or other metal) shell restructuration resulting in higher activity of the surface Ru atoms (or other atoms) than at the alloy surface of the original NP. For instance, with the Au_1Ru_1 alloy, this restructuration is accomplished in 2.5 min, whereas the total time needed for H_2 evolution is 2.5 min. Consistently, the recycling experiment in the dark, following the initial light-accelerated reaction, takes some more time than the latter, but less time than with the original nanocatalyst in the dark. This is explained by the visible-light-induced restructuration from alloy to Au@Ru or Au@M core-shell NPs. Au-Co, although less active than the alloyed Au-noble-metal photocatalysts, showed excellent light effect and was the best alloyed Au-earth-abundant metal photocatalyst for both reactions and, as Au-Ni, was recyclable. The presence of the triazole ligand in the macromolecular structure is a key factor in light enhancement of H_2 evolution and catalyst recycling, the optimized structure being the dendrimer **1**, more efficient than dendrimer **2** and polymer **3** because of its ideal stereo-electronic effects on the NP stabilization and photocatalytic activity of the Au-LTMNPs. Finally, the enhanced KIE values obtained using D_2O under visible-light irradiation and recycling in the dark compared to those obtained in dark reactions of the alloys confirm the strong implication of the water oxidative addition in the RLS for both AB and $NaBH_4$

hydrolytic reactions. Nevertheless, with $NaBH_4$ (only), high KIE values obtained using $NaBD_4$ show that the initial hydride transfer for this substrate to the NP surface also intervenes in a concerted way with the water O-H cleavage in the RLS due to initial strong hydrogen bonding with water. These photocatalysts show superior activity compared to previously reported AB hydrolysis plasmonic metal-based photocatalysts with or without semiconductor (Table S3.9). It is believed that these concepts and findings will find extension to new improved H_2 generation systems and other redox-photocatalyzed transformations of small molecules.

3.4 Experimental section

Chemicals and devices

Chloroauric acid, potassium chloroplatinate, sodium chloropalladate, rhodium chloride, ruthenium chloride, ferrous chloride, copper chloride, nickel chloride, cobalt chloride, sodium borohydride and PVP were purchased from SIGMA-ALDRICH. All flasks were washed by aqua regia (HCl: HNO_3 = 3:1). All solutions and reagents were prepared using ultrapure water from Barnstead NANO water purification system (THERMO FISHER SCIENTIFIC INC., USA).

-**NMR spectra** were recorded at 25 °C with a Bruker AC 300 MHz. All the chemical shifts are reported in parts per million (δ, ppm) with reference to Me_4Si for the ^1H NMR spectra.

-**Transmission Electron Microscopy (TEM)** and high-resolution TEM (HRTEM) were recorded using TEM JEOL JEM 1400 (120 kV)- 2100F.

-**Energy-dispersive X-ray Spectroscopy (EDS)** images were recorded using TEM-JEM-ARM200F Cold FEG equiped with a EDX spectrometer.

-**X-ray photoelectron spectra (XPS) System:** SPECS SAGE HR, X-Ray source: Mg Kα non-monochromatic, operated at 12.5 kV and 250 W. Take-off angle 90°, at ~10^{-8} Torr. Pass energy for survey spectra 30 eV, 15 eV for narrow scans. Analysis: spectra are calibrated to CC carbon 285 eV. Analysis consisted of Shirley background subtraction. Peaks are fitted with symmetrical Gaussian-Lorentzian (GL) line shapes. Samples were dispersed on a silica substrate, and its solvent was evaporated prior to measurement.

Stabilizer syntheses

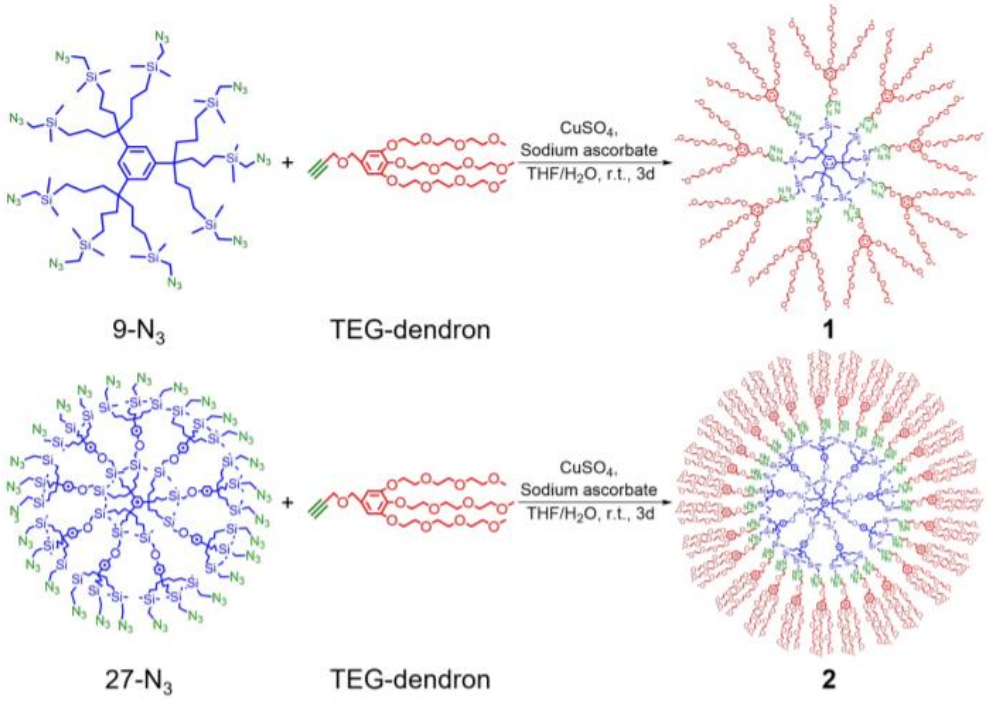

Scheme S3.1. Synthesis of dendrimer **1** and dendrimer **2**

Procedure for the preparations of the dendrimers 1 and 2. Dendrimer **1** has been synthesized following previous reports [S1, S2.] 1,2 9-N_3 (see Scheme S3.1, 0.012 mmol,) and the TEG dendron (see Scheme S3.1, 0.13 mmol, 1.2 equiv. per branch) are dissolved in THF. $CuSO_4.5H_2O$ is added (0.032 g, 0.13 mmol, 1.2 equiv. per branch, 1M in aqueous solution), followed by dropwise addition of a freshly prepared solution of sodium ascorbate (0.051 g, 0.26 mmol, 2.4 equiv. per branch, 1M in water solution) in order to set a 1:1 THF/water ratio. The reaction mixture is stirred for 3 days at 25°C under N_2. After removing THF in vacuo, CH_2Cl_2 (100 mL) and an aqueous ammonia solution (2.0 M, 50 mL) are successively added. The mixture is allowed to stir for 10 minutes in order to remove all the Cu(II) trapped inside the dendrimer as $[Cu(NH_3)_2(H_2O)_2][SO_4]$. The organic phase is washed twice with water, and this operation is repeated three more times to ensure complete removal of copper ions. The organic phase is dried with sodium sulfate, and the solvent is removed *in vacuo*. The product is washed with 50 mL pentane several times in order to remove the excess of the dendron. Dendrimer **1** is obtained in 72.8 % yield. The procedure for the synthesis of dendrimer **2** is similar to that used for **1**, and **2** is obtained in 70 % yield. [S1, S2]

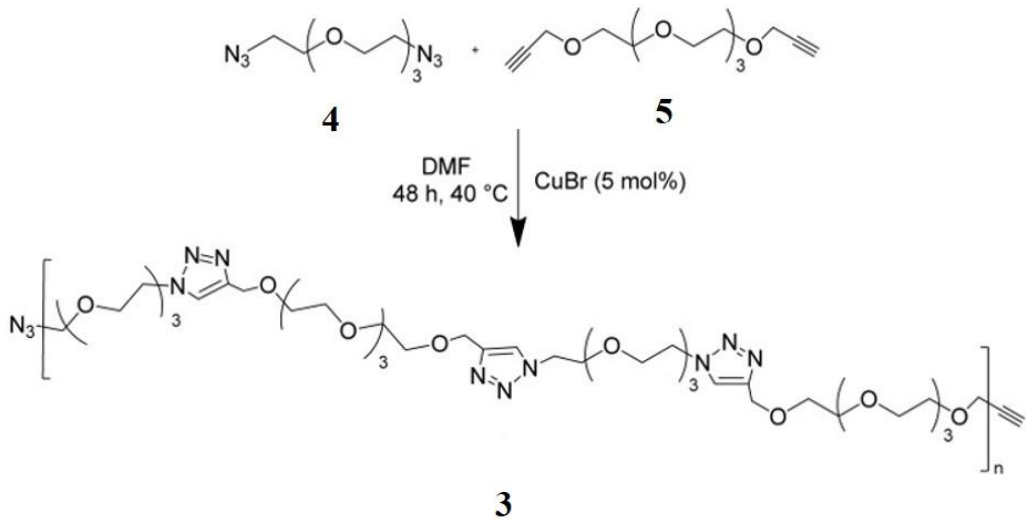

Scheme S3.2. Synthesis of the "click" polymer **3**

Procedure for the synthesis of the "click" polymer 3. 4 (0.244 g, 1 mmol) and **5** (0.270 g, 1 mmol, 1 equiv.) are dissolved in 1 mL DMF in a Schlenk tube. [S3, S4] CuBr is added in the vessel (0.0102 g, 0.05 equiv.). The reaction mixture is stirred for 2 days at 40°C under N_2. The solution is then added to a solution of 200 ml of Et_2O in order to precipitate the polymer formed. The precipitate is filtrated and CH_2Cl_2 (100 mL) and an aqueous ammonia solution (2.0 M, 50 mL) are successively added. The mixture is allowed to stir for 10 minutes in order to remove all the Cu(II) trapped inside the trimer as $[Cu(NH_3)_2(H_2O)_2]$ $[SO_4]$. The mixture is allowed to stir for 10 minutes in order to remove all the Cu(II) trapped inside the polymer as $[Cu(NH_3)_2(H_2O)_2]$ $[SO_4]$. The organic phase is washed twice with water, then this operation is repeated once more to ensure the complete removal of the copper ions. The organic phase is dried with sodium sulfate, and the solvent is removed *in vacuo*. 0.410 g of **3** is obtained (80 % yield) (Scheme S3.2). The product has been characterized by ^{1}H NMR, 13C NMR, IR, MALDI TOF, DLS, and SEC.

Catalyst synthesis. Generally, the metal precursors (0.01mmol in total) dissolved in 2 mL water was injected into a 50-mL Schlenk flask under N2. The compositions of the bimetallic NPs were adjusted by varying the molar ratios of the precursors. Then, the dendrimer 1 (Scheme 3.1 and S1-2, 10 mg, 1.5 equiv. TEG branch per metal) dissolved in 1 mL water was injected, and the mixture allowed to stir for 30 min, then degassed for 10 min. After degassing this solution, 1 mL aqueous solution of freshly prepared $NaBH_4$ (10 equiv. per metal) was quickly added. The mixture was then allowed to stir for 1 h, and the resulting nanocatalyst was directly used *in situ* without further treatment. For the synthesis of the Au-based bimetallic catalysts, the ratio of the two metals was 1：1 without special treatment, and the overall

metal amount was 0.01 mmol. Other steps were the same as mentioned above. For the synthesis of LTMNPs stabilized by another support, the steps are similar to those used for LTMNP@dendrimer 1. These other stabilizers are dendrimer 2 (Scheme 3.1 and Figure S3.3-3.4, 30 mg), "click" polymer 3 (Scheme 3.1 and Figure S3.5, 45 mg), and PVP (15 mg).

Catalysis of the hydrolytic dehydrogenation of the hydrogen-rich boron hydrides by LTMNPs under dark reaction conditions. Under dark reaction conditions, the hydrolysis of AB (or $NaBH_4$) was conducted in a 50-mL Schlenk flask at 25 ± 0.2 °C. Specifically, after preparation of the dendrimer-supported LTMNPs, 1mL of aqueous solution of AB (or $NaBH_4$) was added into the solution with 4 mL of solution of catalyst. In the standard treatment, the content of MNPs was 1% mmol, and the concentration of AB (or $NaBH_4$) was 1 mmol. The reaction time and determination of the volume of H_2 produced began when importing the AB (or $NaBH_4$) by a needle.

Catalysis of the hydrolytic dehydrogenation of the hydrogen-rich boron hydrides by LTMNPs under visible-light irradiation. The photocatalytic reactions were performed by using the 7 W visible LED strips (Sunshine Lighting Limited, France) at a light intensity of 1540 lx (each) with a white light. The LED lamps were turned on for 15 min prior to irradiation to guarantee a stable light intensity. All the reactions under visible light were conducted in a condensate circulation system in order to keep the temperature at 25 ± 0.2 ℃. The dosage of catalyst and AB (or $NaBH_4$) concentration were the same as in dark reactions, and the other steps were also kept the same. The Au/Ru@dendrimer **1** and Au/Co@ dendrimer **1** were recycled five times, including for the recyclability of the other nanocatalyst in this series).

H_2 detection. The reaction flask was connected via the gas outlet to a water-filled gas burette. When the gas generated, the volume of gas evolved was determined periodically by measuring the displacement of water in the burette. In our two cases, 1 mmol AB (or $NaBH_4$) produced 3 mmol (or 4 mmol) H_2, corresponding to 67 and 89 ml H_2 at atmospheric pressure. Prior to the reactions, the volumes were measured at atmospheric pressure and corrected for water vapor pressure at room temperature. Every reaction has been conducted for three times, and the results are averaged.

NH_3 gas detection. The gas generated from the hydrolysis was passed through a 25 mL standard HCl solution (0.01 M) at room temperature, by which the ammonia gas was captured. After gas generation ceased, the resulting solution was titrated with standard NaOH solution (0.01 M) using the acid-base indicator phenolphthalein. The quantity of the liberated ammonia gas was calculated from the difference between two HCl solutions before and after the reaction.

Reusability testing of the nanocatalysts. The reusability of the nanocatalysts Au/Ru@dendrimer **1** and Au/Co@ dendrimer **1** were evaluated by repeating tests with the aged nanocatalysts. Specifically, after the end of the first reaction, another AB (or $NaBH_4$) equivalent (1 mmol) was injected into the reaction

flask, then the second round started. The AB and $NaBH_4$ hydrolysis reactions were repeated in this way several times.

Calculation of the NP surface atoms number (Ns) and TOFs related to the Ns.

$V_{NP} = NV_{atom}$ (eq. 1)

$4/3\pi(R_{NP})^3 = N\ 4/3\pi(R_{atom})^3$ (eq. 2)

Where V is the atom volume of the NP, R is the atomic radius of the NP, and N is the total number of atoms within the NP. Rearranging, we obtain:

$N = (R_NP/R_{atom})^3$ (eq. 3)

Knowing the NP radius, we can also calculate the surface area (S) of a NP with the following equation:

$S_{NP} = 4\pi(R_{NP})^2$ (eq. 4)

So, we may also calculate the number of surface atoms (Ns) directly by dividing the surface area of the NP by the cross section of an individual NP atom and then simplifying using the relationship in (eq. 3):

$N_s = (4\pi(R_{NP})2) / (\pi\ (R_{atom})2) = 4\ N\ (R_{atom}/R_{NP})$ (eq. 5)

The ratio of the $N_s/N = 4\ (R_{atom}/R_{NP})$

So $TOF = TOF_t/(N_s/N)$

Where $TOF_t = mol_{H2\ released}/(total\ mol_{catal.} \times reaction\ time\ (min))$

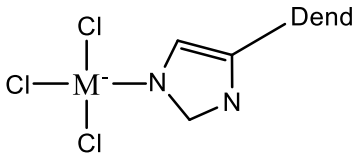

Scheme S3.3. Triazole coordinated M^{n+} ($M = Pt^{4+}, Pd^{2+}$)

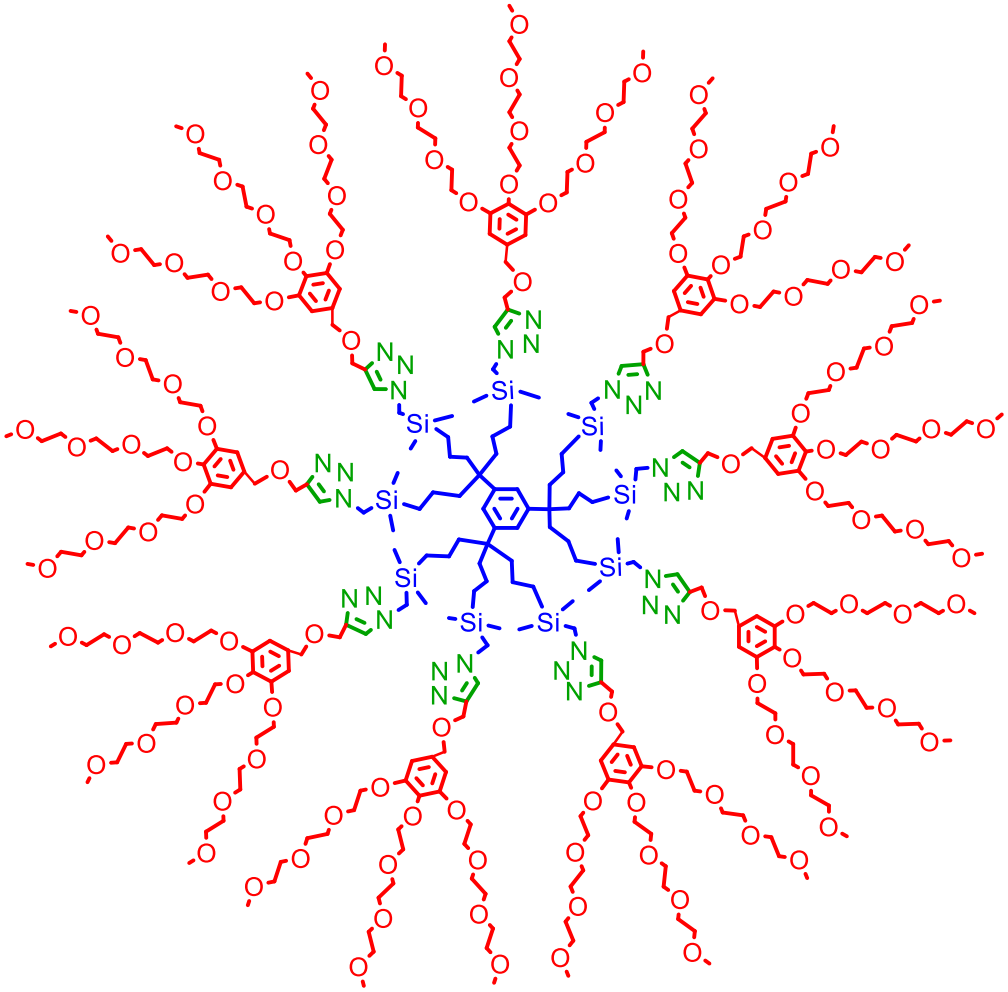

Figure S3.1. 27-TEG "click" dendrimer **2**

^{1}H NMR ($CDCl_3$, 300 MHz) δ: ppm: 7.51 (CH-triazole), 6.99 (CH-arom. intern), 6.60 (CH-arom. extern), 4.63 (triazole-CH_2-O), 4.48 (O-CH_2-arom. extern), 3.85-4.15 (CH_2CH_2O-arom. extern), 3.80 (Si-CH_2-triazole), 3.53-3.77 (OCH_2CH_2O), 3.37-3.40 (CH_3O), 1.70 ($CH_2CH_2CH_2Si$), 1.13 ($CH_2CH_2CH_2Si$), 0.66 ($CH_2CH_2CH_2Si$), 0.07 ($Si(CH_3)_2$).

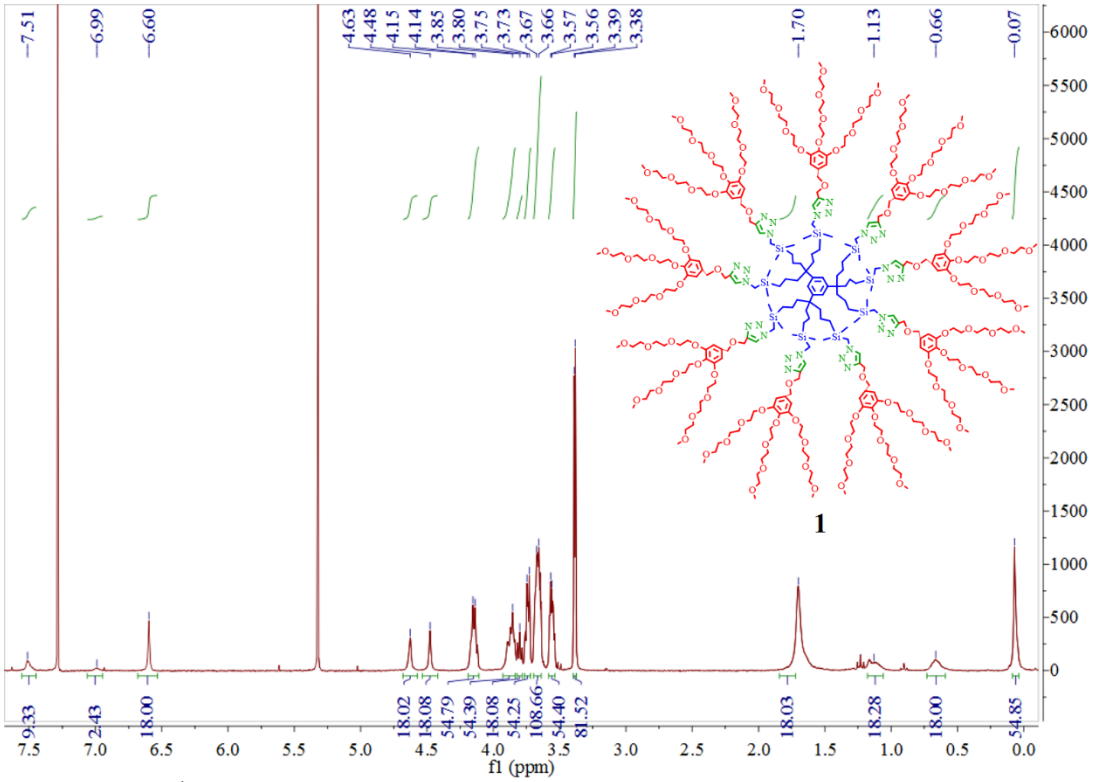

Figure S3.2. ^{1}H NMR spectrum of dendrimer **1** in $CDCl_3$.

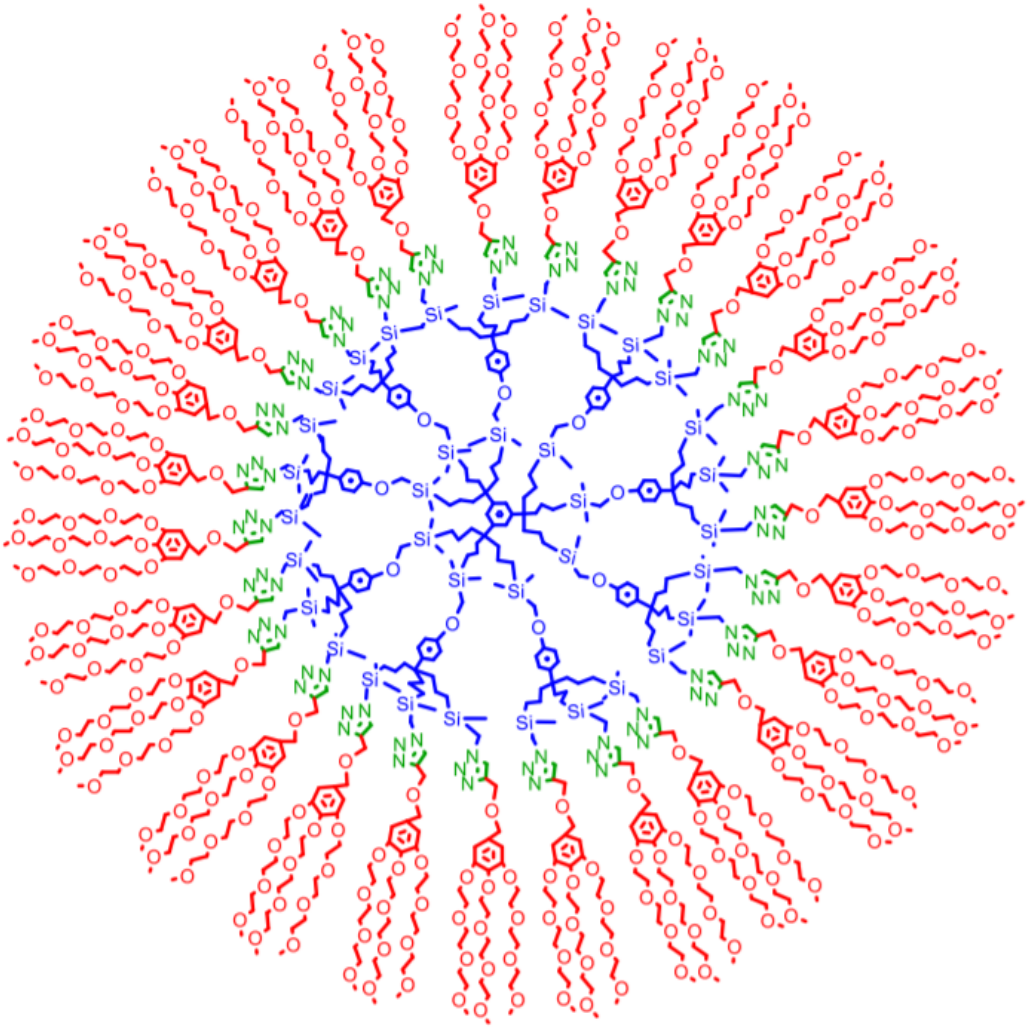

Figure S3.3. Dendrimer **2**

[1]

^{1}H NMR ($CDCl_3$, 300 MHz) δ: ppm: 7.51 (CH-triazole), 6.89-7.15 (CH-arom. intern), 6.60 (CH-arom. extern), 4.64 (triazole-CH_2-O), 4.48 (O-CH_2-arom. extern), 3.85-4.15 (CH_2CH_2O-arom. extern), 3.80 (Si-CH_2-triazole), 3.56-3.74 (OCH_2CH_2O), 3.55 (CH_2O-arom. intern) 3.36-3.40 (CH_3O), 1.63 ($CH_2CH_2CH_2Si$), 1.12 ($CH_2CH_2CH_2Si$), 0.63 ($CH_2CH_2CH_2Si$), 0.06 ($Si(CH_3)_2$).

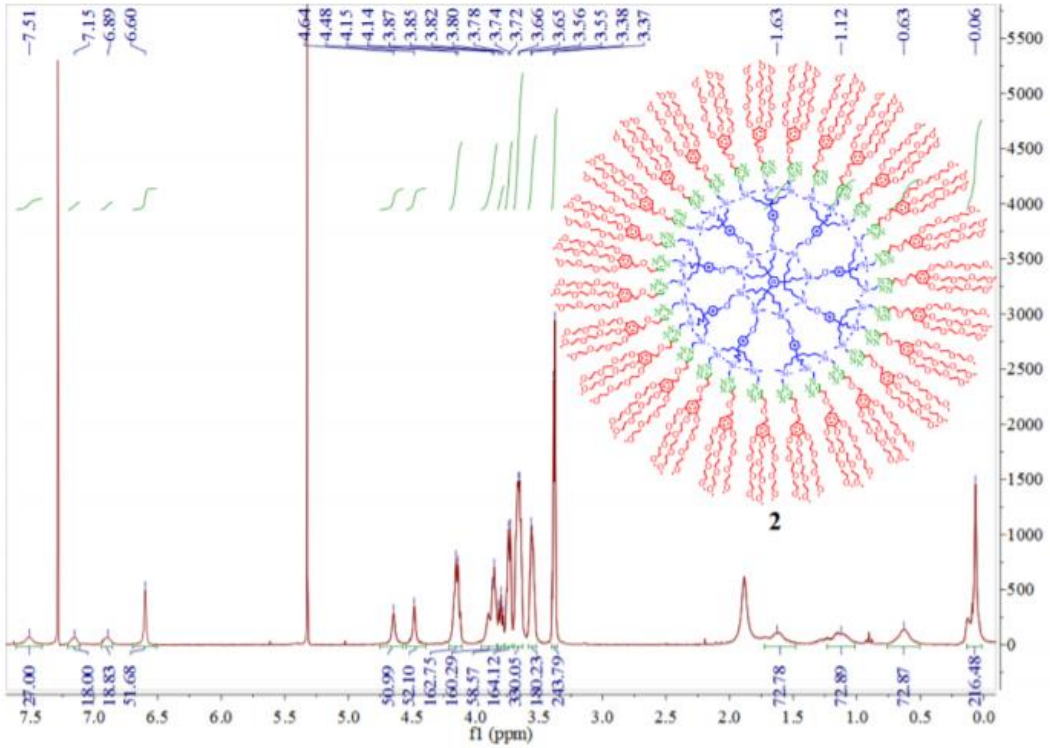

Figure S3.4 NMR ^{1}H NMR spectrum of dendrimer 2 in $CDCl_3$.

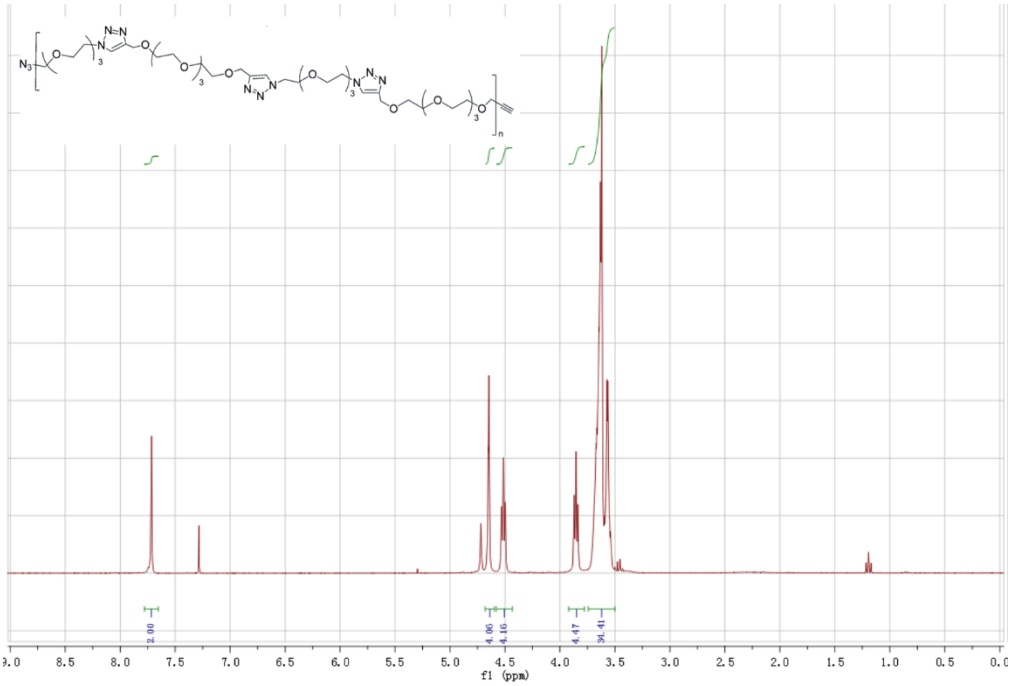

Figure S3.5. ^{1}H RMN ($CDCl_3$, 300 MHz) ppm: 3.53-3.75 (m, 36H, O-CH_2-CH_2-O), 3,84 (t, 4H, N-CH_2-CH_2-O), 4.5 (t, 4H, N-CH_2-CH_2-O), 4,6 (s, 4H, O-CH_2-triazole), 7,74 (s, 2H, CH-triazole). ^{13}C RMN ($CDCl_3$, 300 MHz) ppm: 50 (N-CH_2-CH_2-O), 65 (O-CH_2-triazole), 70 (PEG, N-CH_2-CH_2-O), 124 (CH-triazole), 145 (Cq-triazole)

Characterization

2.1. TEM images and size distribution

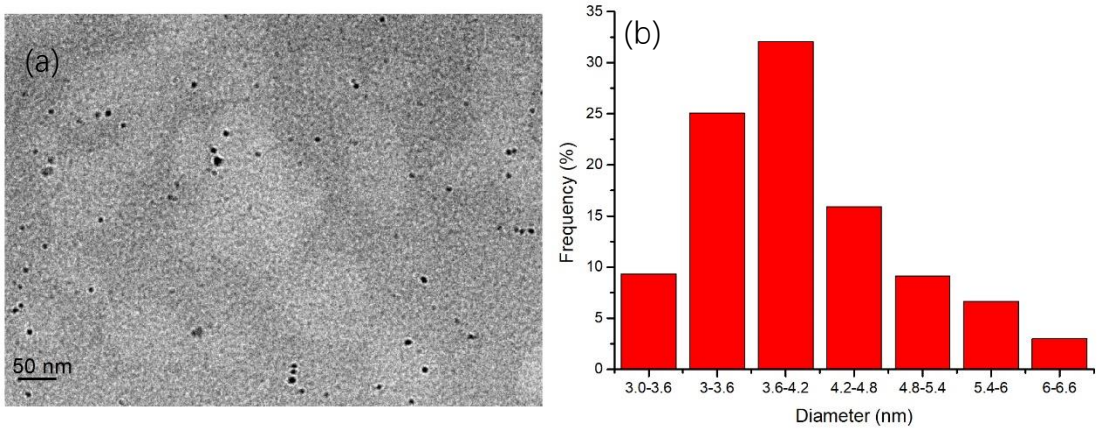

Figure S3.6. (a) TEM image and (b) size distribution of the Au-Rh@dendrimer **1**.

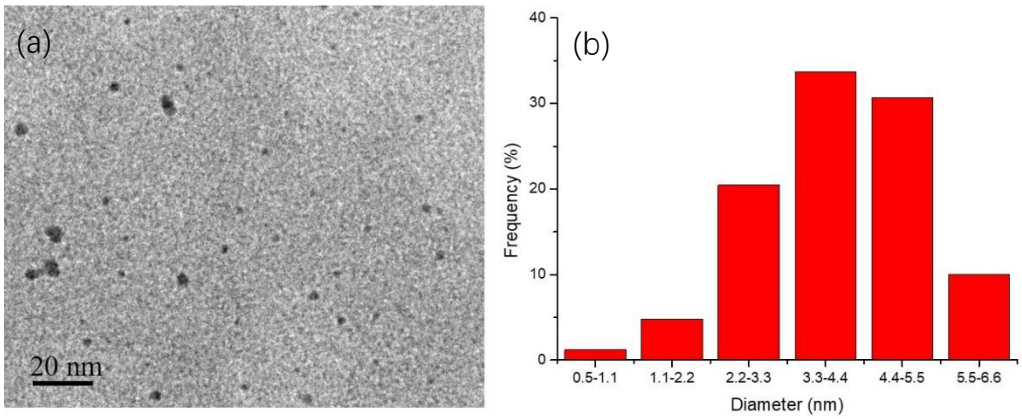

Figure S3.7. (a) TEM image, and (b) size distribution of the Au-Pd@dendrimer **1**

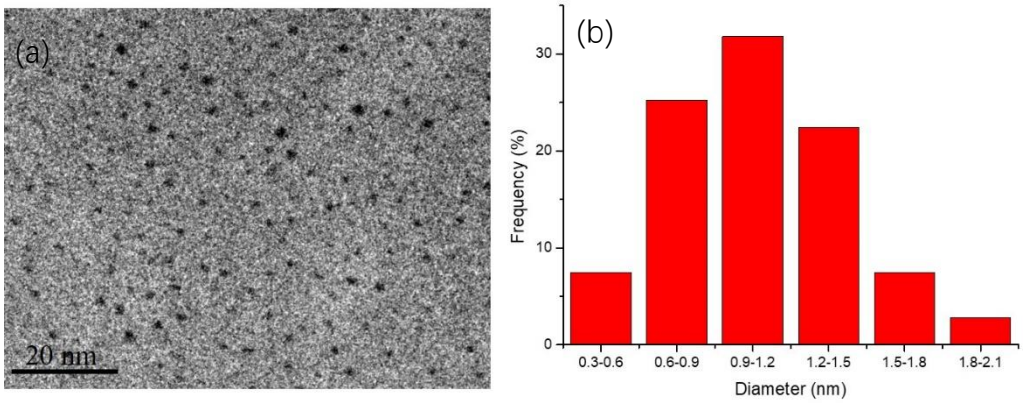

Figure S3.8. (a) TEM image, and (b) size distribution of the Au-Ag@dendrimer **1**.

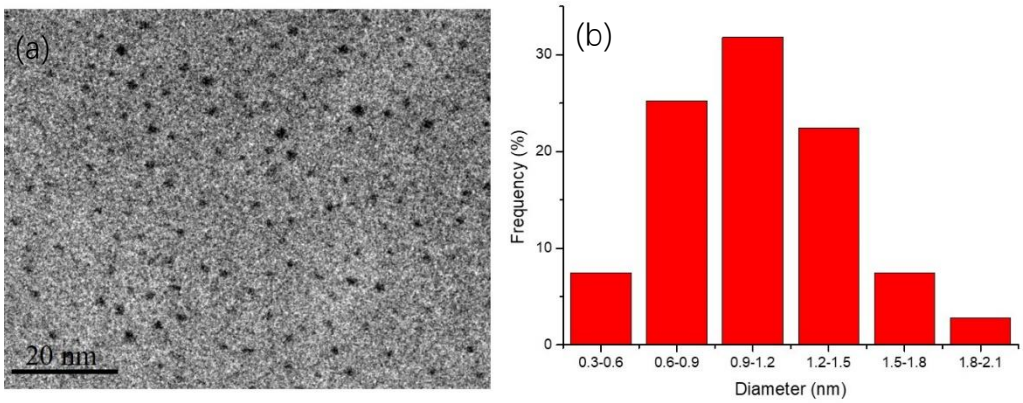

Figure S3.9. (a) TEM image, and (b) size distribution of the Au-Pt@dendrimer **1**.

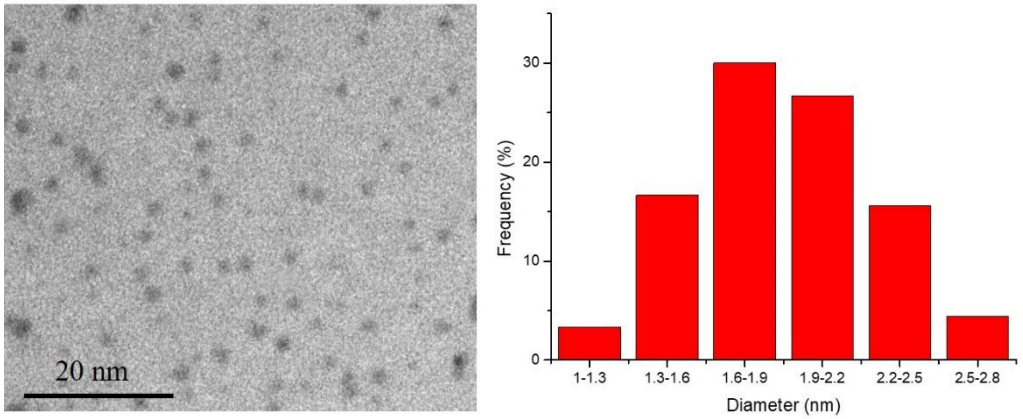

Figure S3.10. (a) TEM image, and (b) size distribution of the Au-Co@dendrimer **1**.

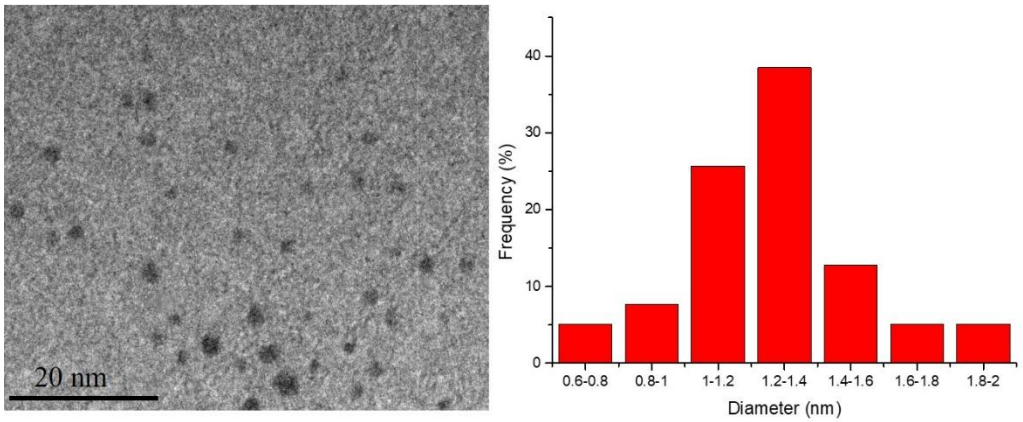

Figure S3.11. (a) TEM image, and (b) size distribution of the Au-Ni@dendrimer **1**.

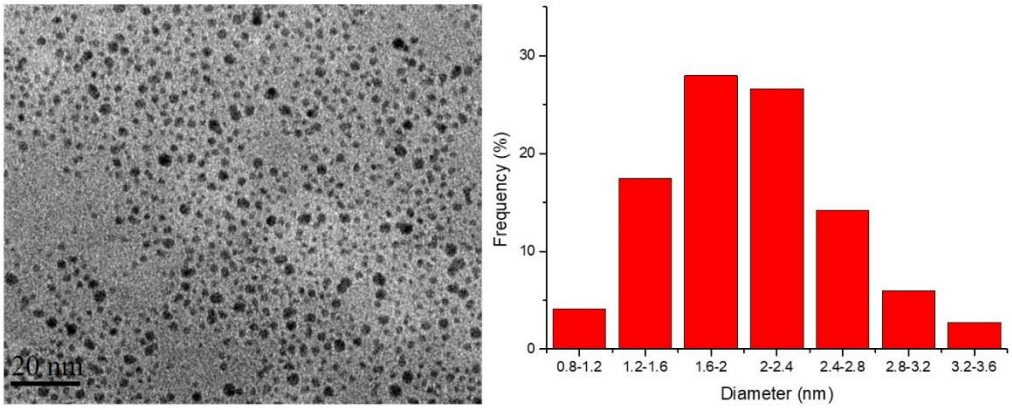

Figure S3.12. (a) TEM image, and (b) size distribution of the Au-Cu@dendrimer **1**.

Table S3.1. Average size of a series of Au-based bimetallic catalysts

Samples	Au-Ru	Au-Rh	Au-Pd	Au-Ag	Au-Pt	Au-Co	Au-Ni	Au-Cu
Average size (nm)	1.48	3.78	3.72	1.82	1.22	2.15	1.47	2.31

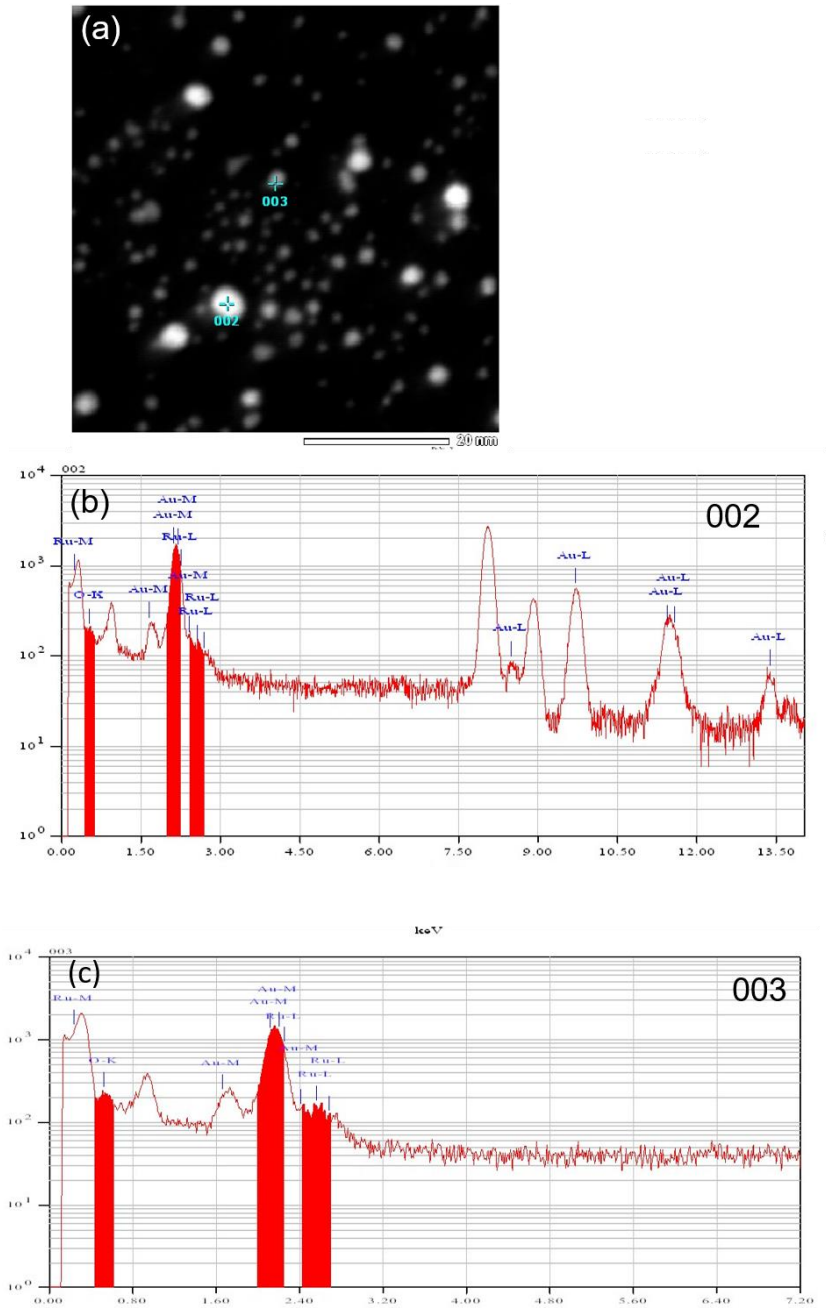

Figure S3.13. (a) HRTEM-EDX image of Au/Ru@dendrimer **1** and (b) element distribution of 002 (c) element distribution of 003

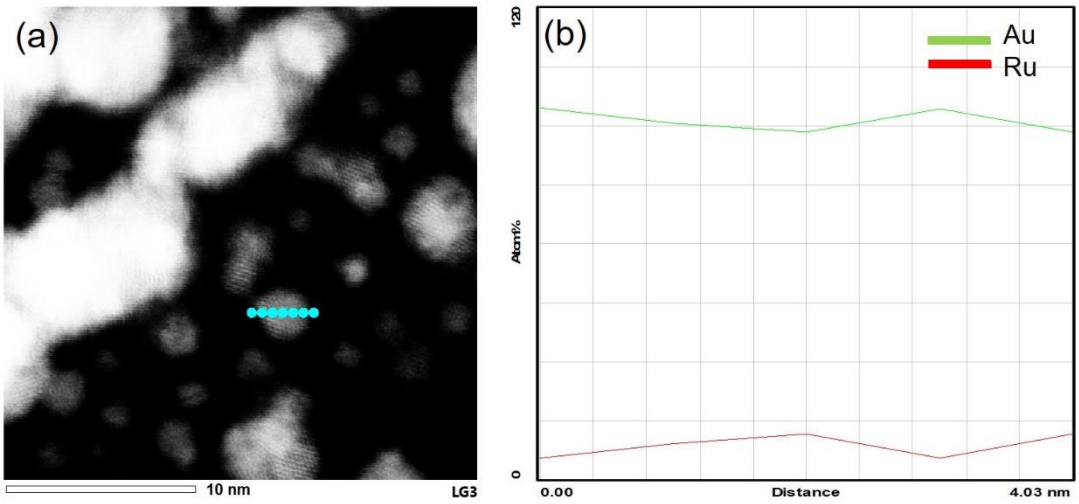

Figure S3.14. (a) HAADF-STEM image of Au/Ru@dendrimer **1** and (b) distributions of Au and Ru along cross-section lines.

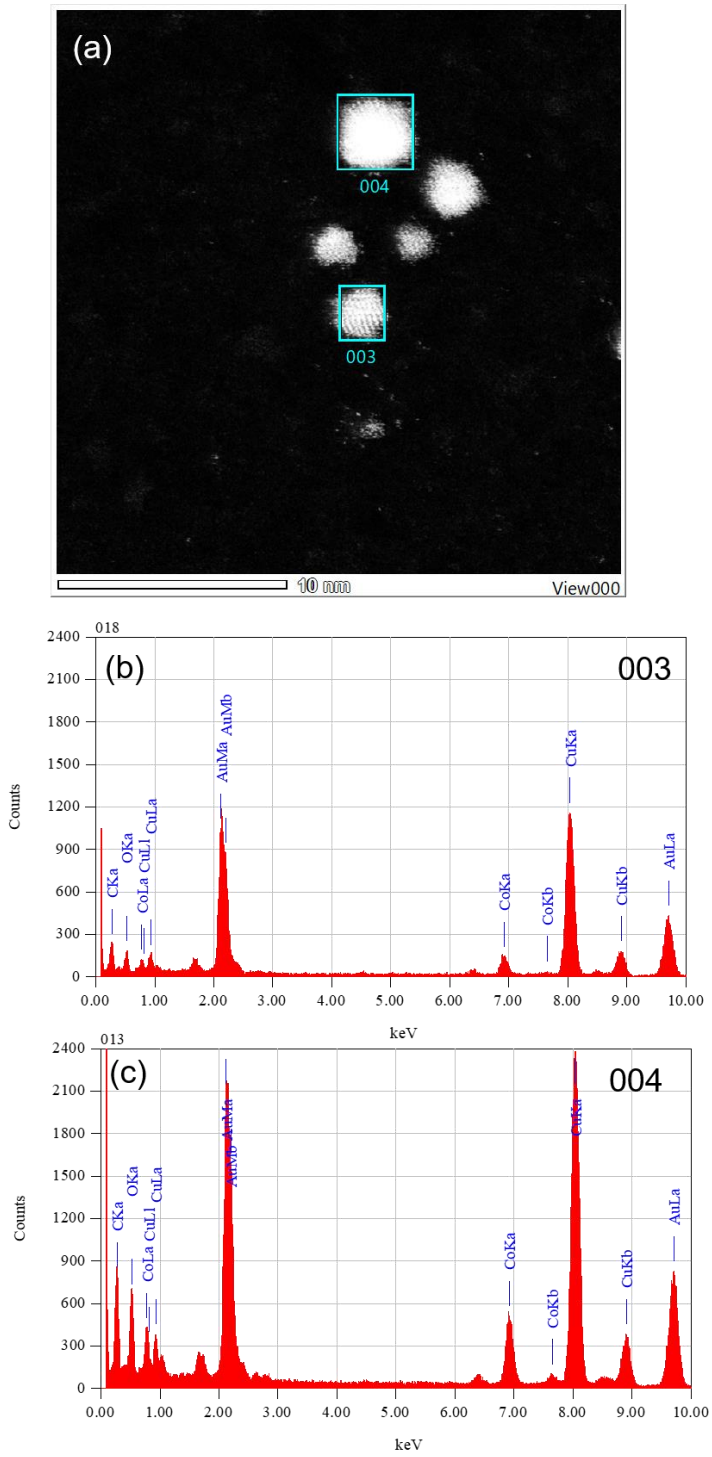

Figure S3.15. (a) HRTEM-EDX image of Au/Co@dendrimer **1** and (b) element distribution of 003 (c) element distribution of 004

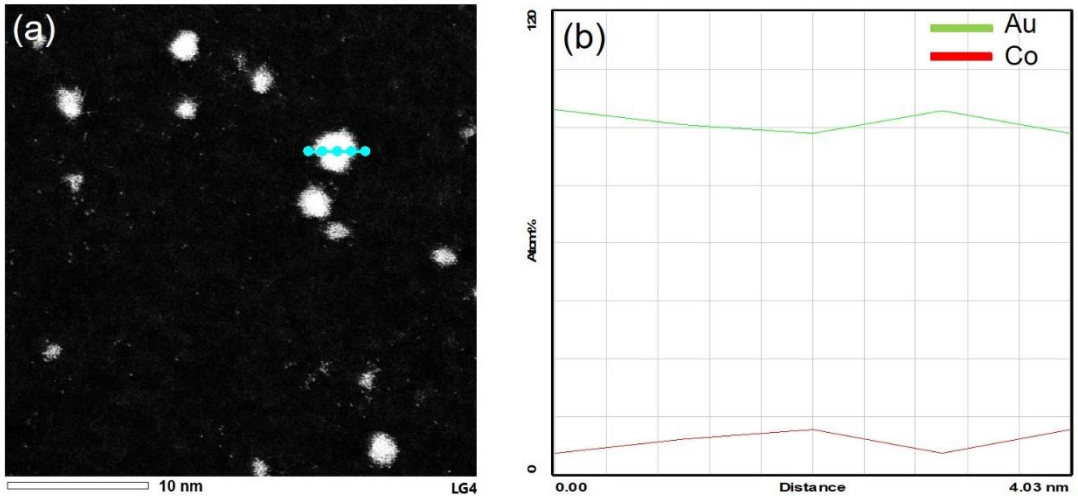

Figure S3.16 (a) HAADF-STEM image of Au/Co@dendrimer **1** and (b) distributions of Au and Co along cross-section lines

2.2 . XPS spectrum of Au-M bimetallic NPs

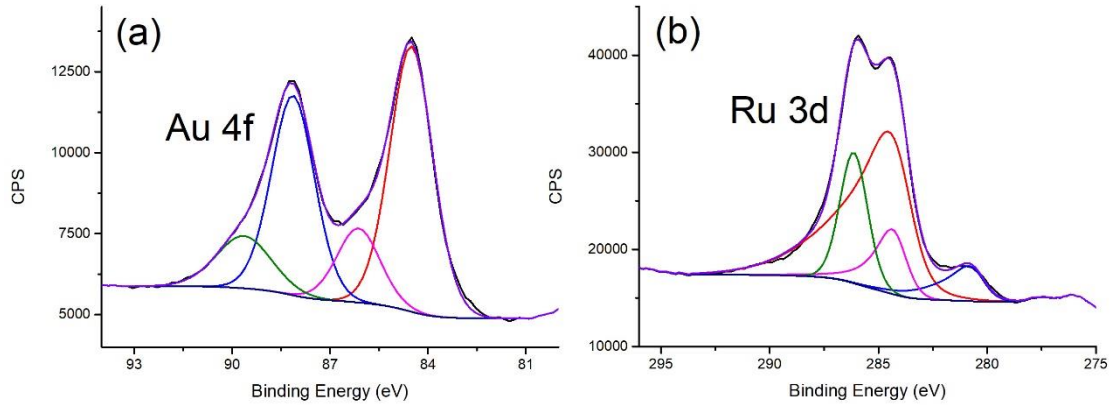

Figure S3.17. XPS analysis of Au-Ru@dendrimer **1**(a) Au 4f region; (b) Ru 3d region

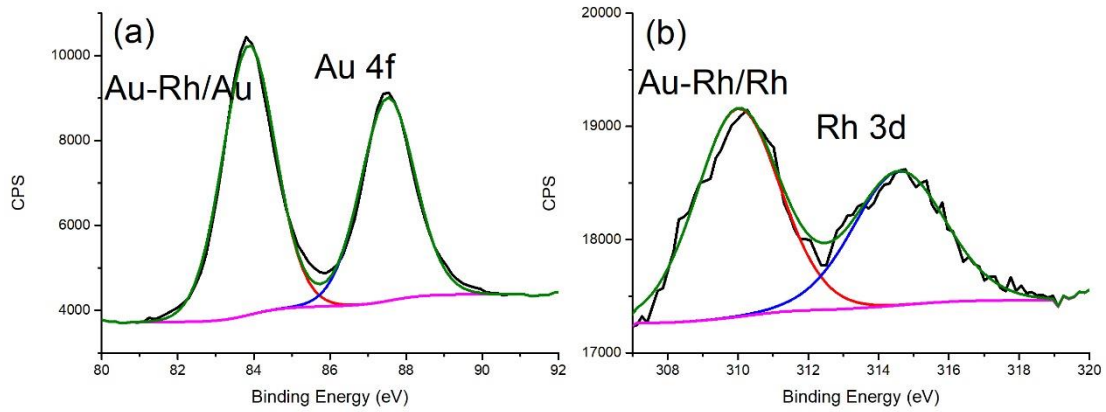

Figure S3.18. XPS spectrum of Au-Rh@dendrimer **1** (a) Au region, and (b) Rh region

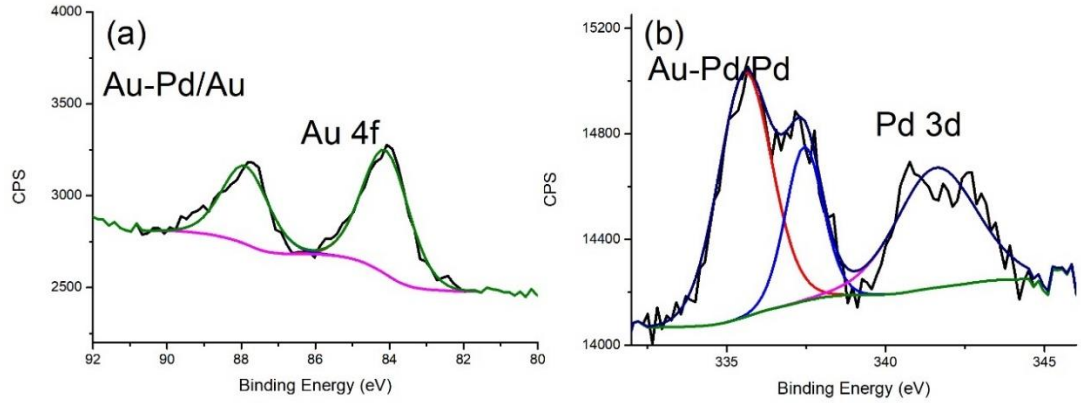

Figure S3.19. XPS spectrum of Au-Pd@dendrimer **1** (a) Au 4f region and (b) Pd 3d region

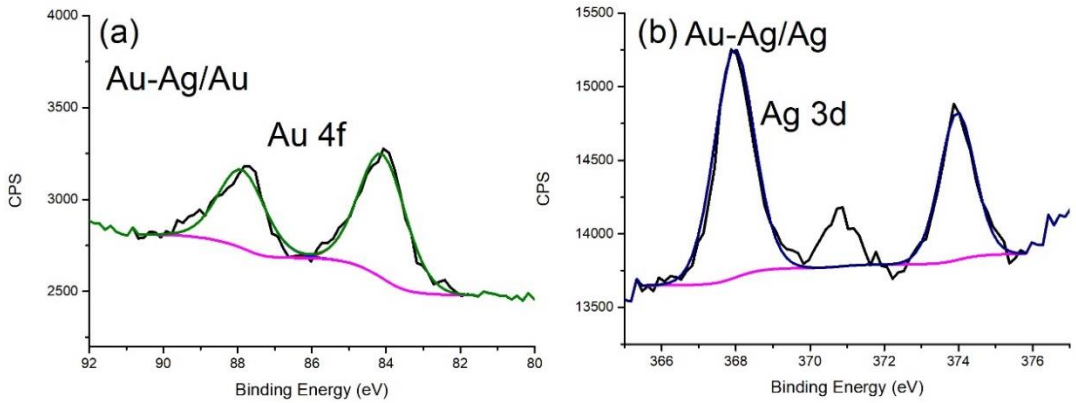

Figure S3.20. XPS spectrum of Au-Ag@dendrimer **1** (a) Au 4f region, and (b) Ag 3d region

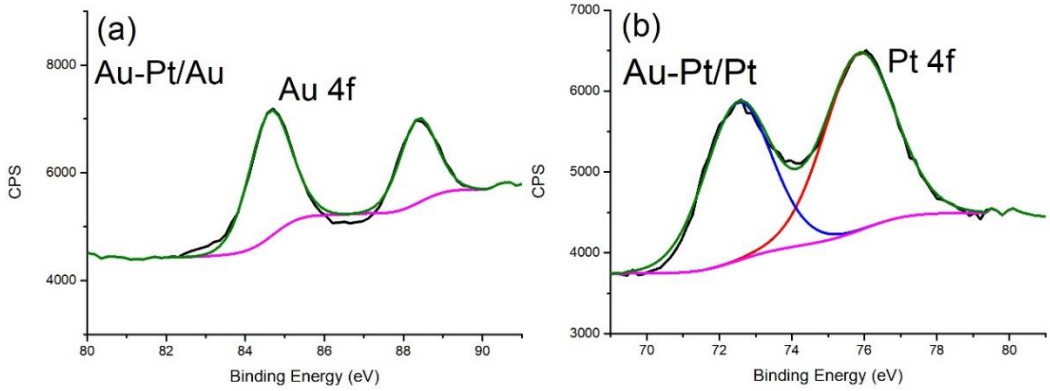

Figure S3.21. XPS spectrum of Au-Pd@dendrimer **1** (a) Au 4f region, and (b) Pt 4f region

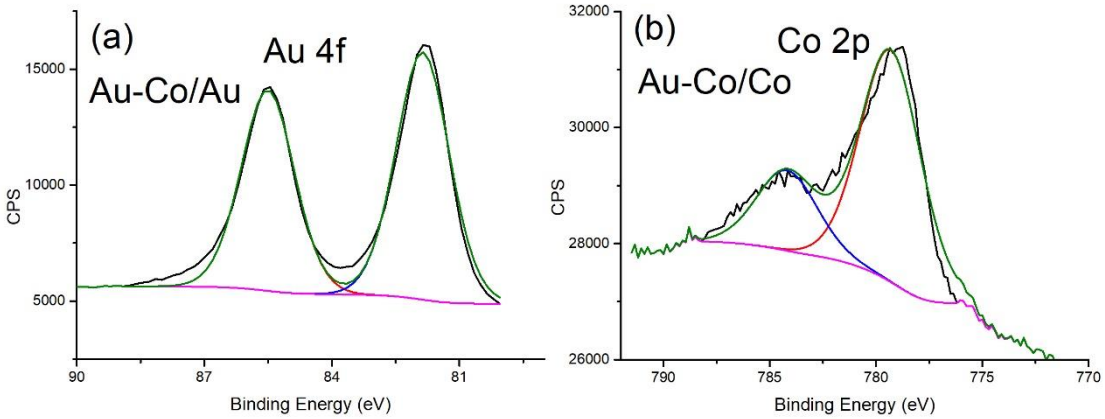

Figure S3.22. XPS spectrum of Au-Co@dendrimer **1** (a) Au 4f region, and (b) Co 2p region

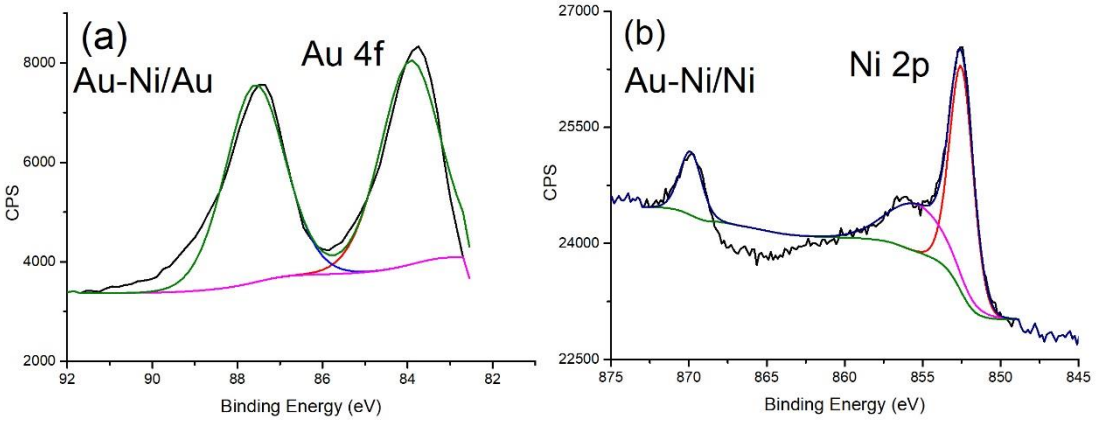

Figure S3.23. XPS spectrum of Au-Ni@dendrimer **1** (a) Au 4f region, and (b)Ni 2p region

Hydrolysis of inorganic hydrides

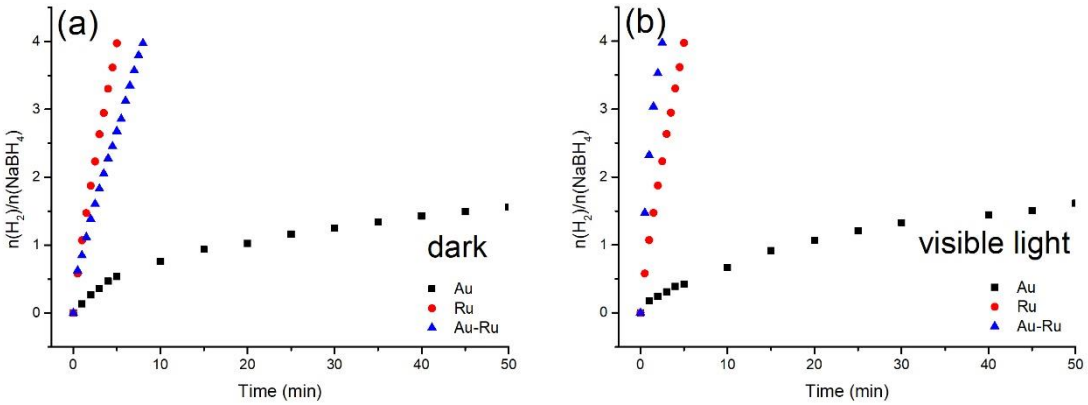

Figure S3.24. Comparison of efficiencies of AuNP@dendrimer **1**, RuNP@dendrimer **1** and Au-Ru@dendrimer **1** for $NaBH_4$ hydrolysis, (a) under dark reaction and (b) with visible light. In all the experiments, the reaction conditions are: 1 mmol of AB or $NaBH_4$; 1% mmol MNP; temperature: 25 ± 0.2°C

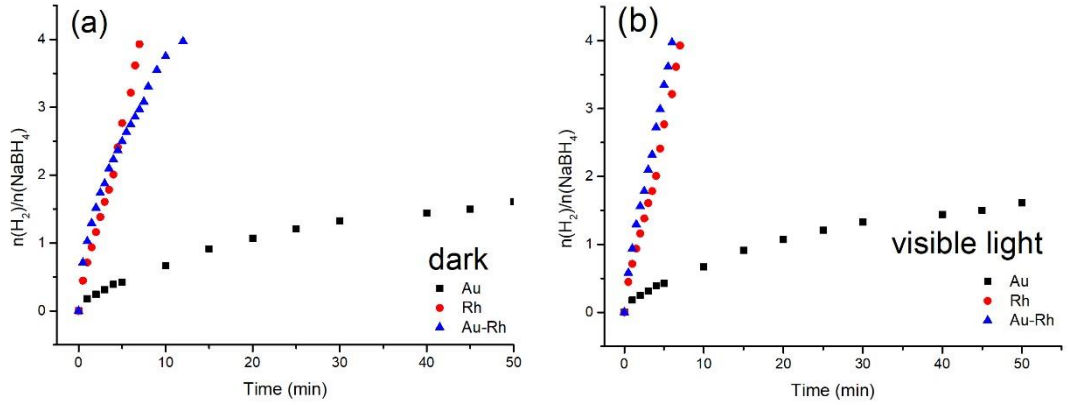

Figure S3.25. Comparison of reaction efficiencies of AuNP@ dendrimer **1**, RhNP dendrimer **1** and Au-Rh@dendrimer**1** for $NaBH_4$ hydrolysis, (a) under dark reaction and (b) with visible light. In all the experiments, the reaction conditions are: 1 mmol of AB or $NaBH_4$; 1% mmol MNP; temperature: 25 ± 0.2°C

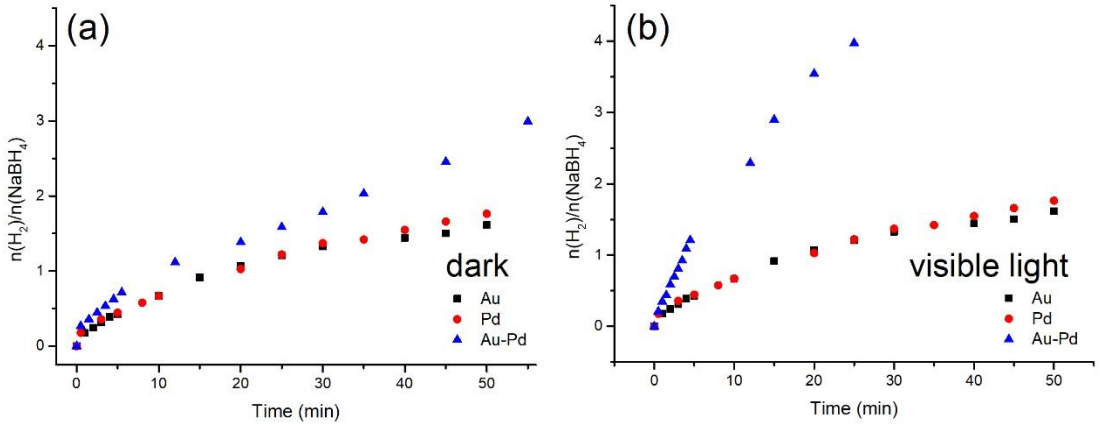

Figure S3.26. Comparison of reaction efficiencies of the nanocatalysts AuNP@dendrimer **1**, PdNP@ dendrimer **1** and Au-Pd@dendrimer **1** for $NaBH_4$ hydrolysis, (a) under dark reaction and (b) with visible

light. In all the experiments, the reaction conditions are: 1 mmol of AB or $NaBH_4$; 1% mmol MNP; temperature: 25 ± 0.2°C

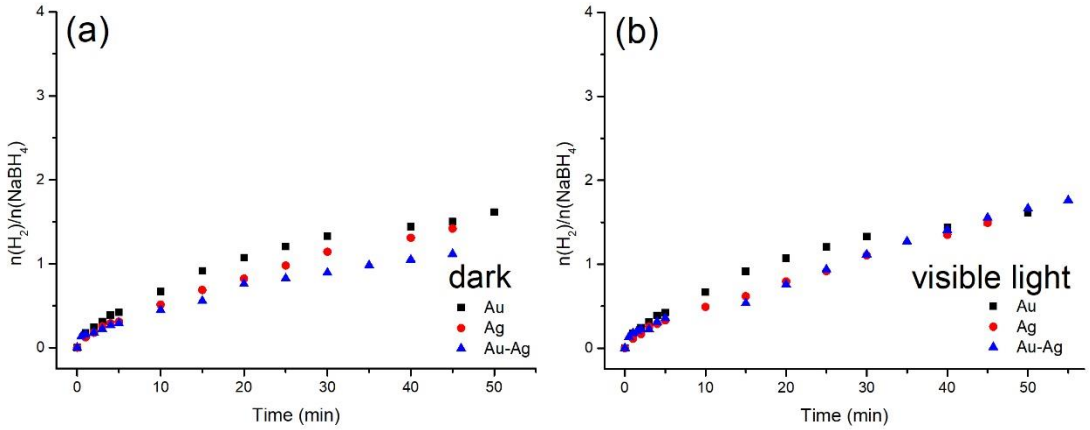

Figure S3.27. Comparision of reaction efficiencies of the nanocatalysts AuNP@dendrimer **1**, AgNP@dendrimer **1** and Au-Ag@dendrimer **1** for $NaBH_4$ hydrolysis, (a) under dark reaction and (b) with visible light. In all the experiments, the reaction conditions are: 1 mmol of AB or $NaBH_4$; 1% mmol MNP; temperature: 25 ± 0.2°C

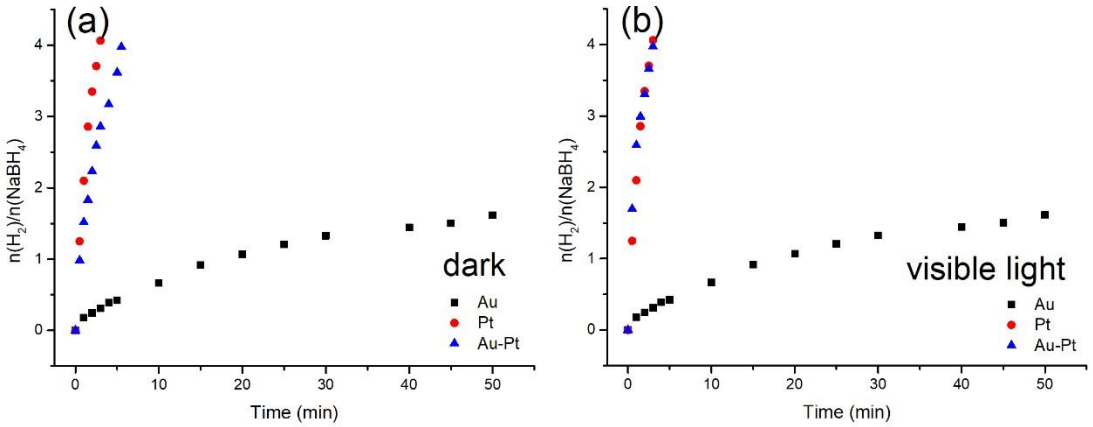

Figure S3.28. Comparision of reaction efficiencies of AuNP@dendrimer **1**, PtNP@dendrimer **1** and Au-Pt@dendrimer **1** for $NaBH_4$ hydrolysis, (a) under dark condition, and (b) with visible light. In all the experiments, the reaction conditions are: 1 mmol of AB or $NaBH_4$; 1% mmol MNP; temperature: 25 ± 0.2°C

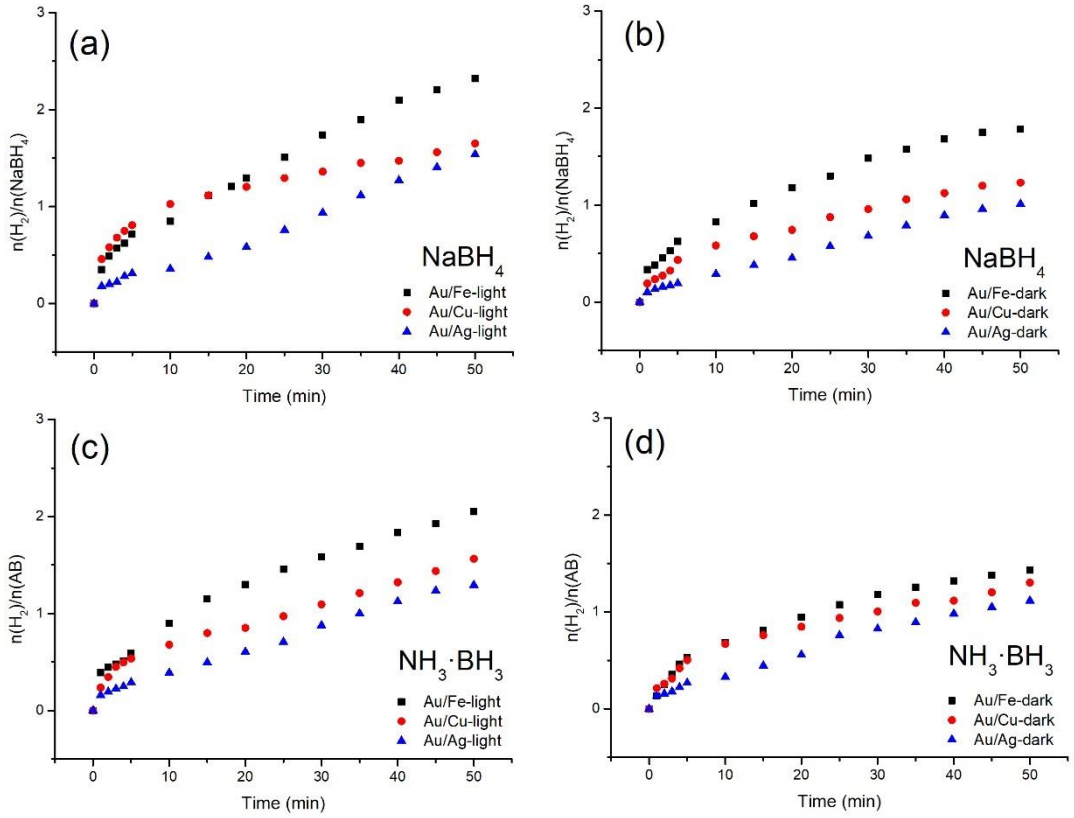

Figure S3.29. Plot for molar amount of H_2 generated from sodium borohydride and AB hydrolysis vs. time taken by different dendrimer **1**-stabilized Au-LMT alloys with and without light irradiation, (a) for sodium borohydride hydrolysis under dark reaction, (b) for sodium borohydride hydrolysis under visible light, (c) for AB hydrolysis under dark reaction, (d) for AB hydrolysis under visible light. In all experiments, the reaction conditions are: 1 mmol of AB or sodium borohydride, temperature: 25 ± 0.2°C

Table S3.2. Physical properties and catalytic efficiencies of the nanocatalysts.

Physical properties				NaHB4			AB				
Catalysts	R_{atom} (nm)	R_{NP} (nm)	Ns/N[a] (nm)	TOF_t[b] (dark)	TOF_t (light)	TOF[c] (dark)	TOF (light)	TOF (dark)	TOF_t (light)	TOF (dark)	TOF (light)
Au_1/Ru_1	0.137	0.74	0.74	47	178	63.5	240.5	30	75	40.5	101.4
Au_1/Rh_1	0.140	2.57	0.22	33	66	11.9	223.7	85	240	288.1	813.6
Au_1/Pd_1	0.140	1.86	0.30	6	15	20.0	50.0	6.7	16	22.3	53.3
Au_1/Pt_1	0.140	0.61	0.92	72	133	78.3	144.6	75	200	81.5	217.4
Au_1/Co_1	0.140	1.07	0.45	22	50	48.9	111.1	17	27	37.8	60.0
Au_1/Ni_1	0.140	0.73	0.76	6.1	12.5	8.0	16.4	5.4	10	7.1	13.2

[a] Ns/N = Number of surface atoms / Number of total atoms; [b] TOFt = mol*H2* released / (total mol*catalyst* × reaction time*(min)*); [c] TOF = TOFt / (N_s/N).

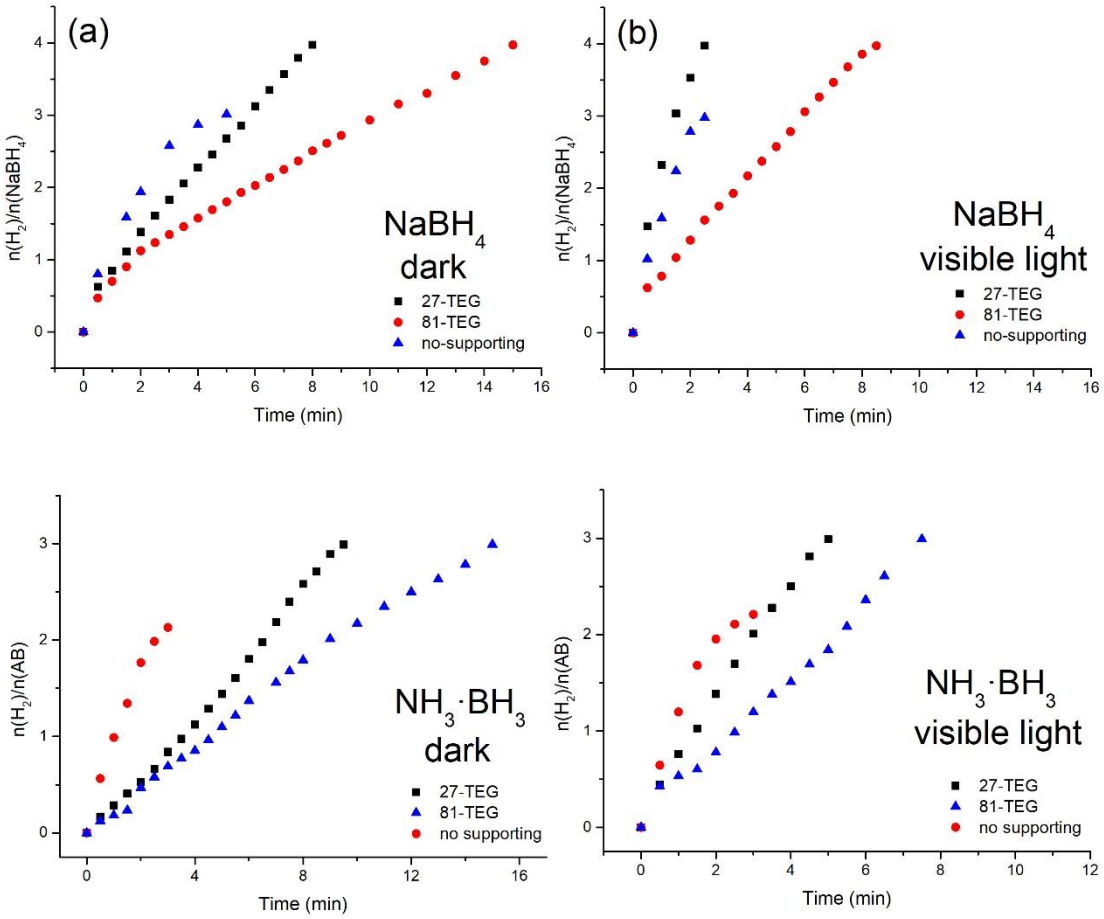

Figure S3.30. Efficiency of the nanocatalysts for $NaBH_4$ and AB hydrolysis (a) for $NaBH_4$ with different supports under dark reaction, (b) for $NaBH_4$ with different supports under visible reaction, (c) for AB with different supports under dark reaction, (d) for AB with different support under visible reaction. Reaction conditions are: 1 mmol of AB or sodium borohydride; temperature: 25 ± 0.2°C

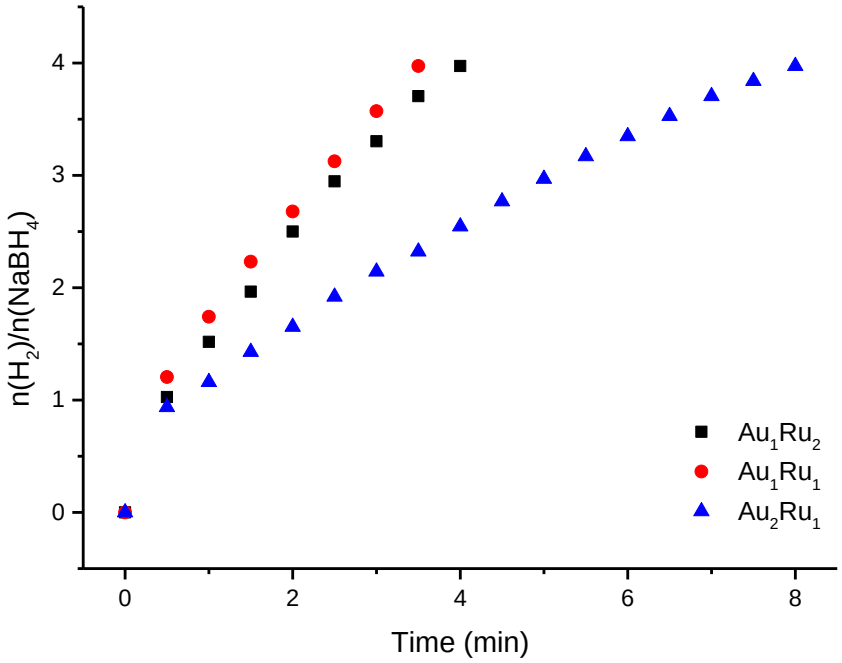

Figure S3.31. Plot for molar amount of H_2 generated from sodium borohydride hydrolysis vs. time taken by different ratios of Au-Ru alloys in the presence of visible light irradiation. Reaction conditions: amount of sodium borohydride used: 1 mmol, temperature: 25 ± 0.2°C

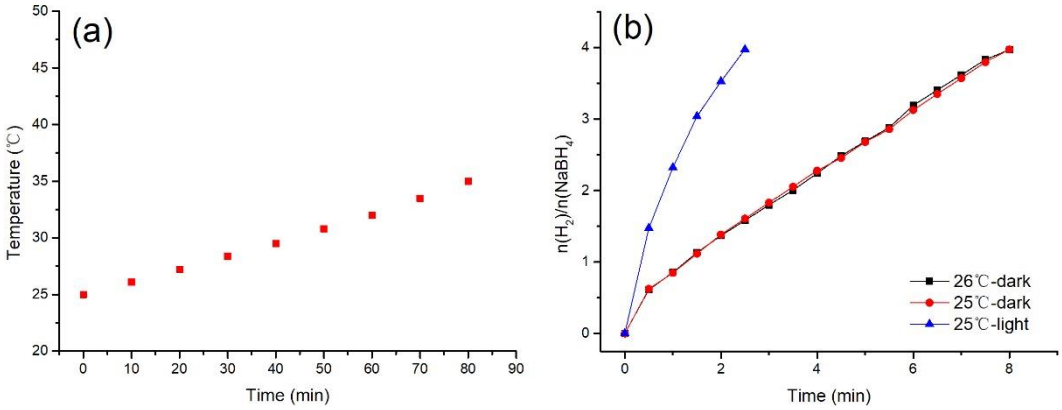

Figure S3.32. (a) Temperature change of reaction medium with time, (b) comparison of efficiency for $NaBH_4$ hydrolysis on different reaction temperatures.

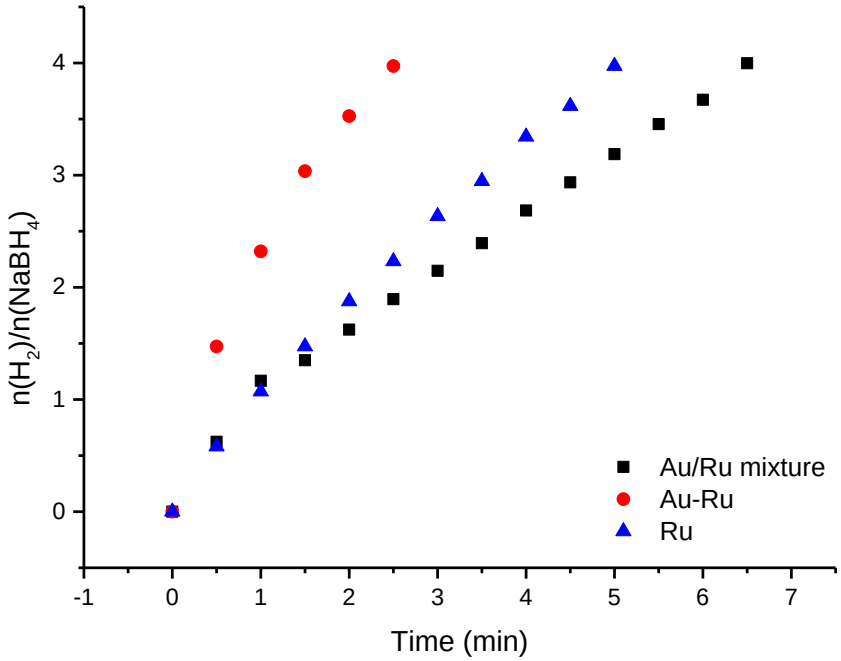

Figure S3.33. Efficiency of $NaBH_4$ hydrolysis derived by Au-Ru@dendrimer **1**, RuNPs and Au/Ru mixture under visible light. Reaction conditions: amount of sodium borohydride used: 1 mmol, temperature: 25 ± 0.2 °C

Table S3.3. TOF_t value of hydrolysis of sodium borohydride and AB under visible light derived by a series of Au-Co catalysts.

Catalysts	TOF_t[a] ($NaBH_4$ under vis. light)	TOF_t[a] (AB under vis. light)
Au_1Co_1@dendrimer **1**	50.0	27.3
Au_1Co_2@dendrimer **1**	30.7	20.0
Au_2Co_1@dendrimer **1**	26.7	17.6
Au/Co mixture	11.4	10.7

[a] $TOF_t = mol_{H2\ released} / (total\ mol_{catalyst} \times reaction\ time_{(min)})$

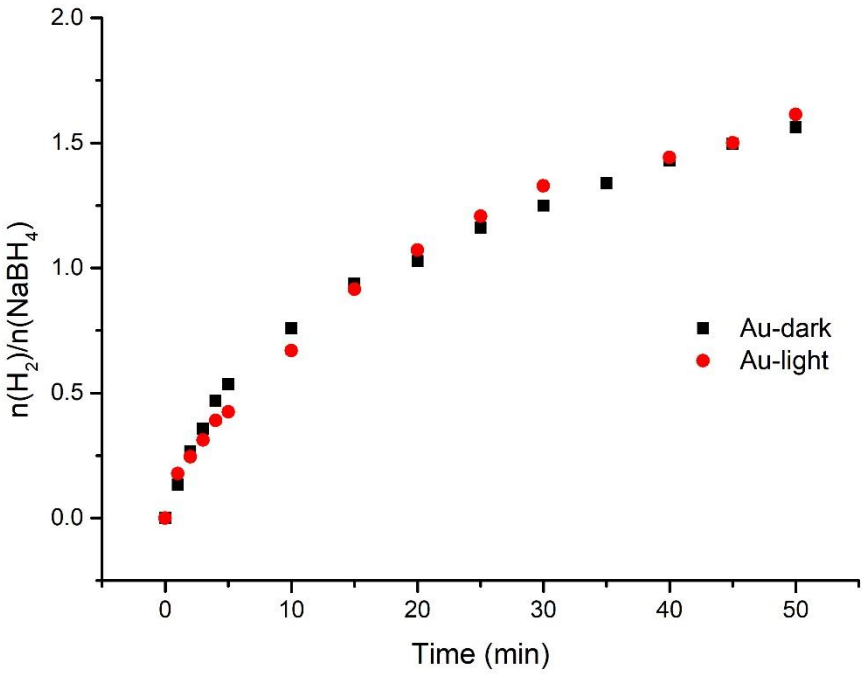

Figure S3.34. Plot for molar amount of H_2 generated from sodium borohydride hydrolysis vs. time taken by dendrimer **1**-stabilized AuNPs with visible light and without visible light irradiation. Reaction conditions: amount of sodium borohydride used: 1 mmol, temperature: 25 ± 0.2 °C

Table S3.4. The reusability of dendrimer **1**-stabilized Au-based bimetallic catalysts for hydrolysis of AB and $NaBH_4$

Catalysts	Recycling (AB)	Recycling ($NaBH_4$)
Au_1/Ru_1	YES	YES
Au_1/Rh_1	NO	YES
Au_1/Pd_1	NO	NO
Au_1/Pt_1	NO	YES
Au_1/Co_1	YES	YES
Au_1/Ni_1	YES	YES

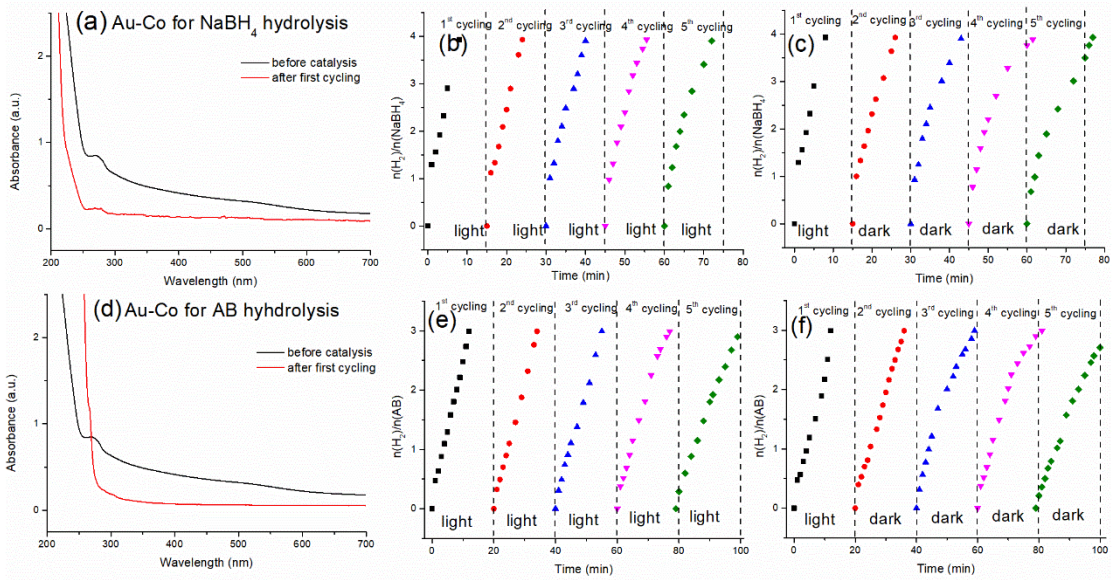

Figure S3.35. UV-vis. spectra of Au-Co for sodium borohydride hydrolysis before catalysis and after the first catalytic cycle. After further catalysis recycling, the UV-vis. spectra remain the same as after the first catalytic cycle; (b) plot of molar amount of H_2 generated from sodium borohydride hydrolysis vs. time taken by Au-Co during visible light irradiation in the reuse test; (c) plot of molar amount of H_2 generated from sodium borohydride hydrolysis vs. time taken by Au-Co during the reuse test without visible light in the second cycle; (d) UV-vis. spectra of Au-Co for AB hydrolysis before catalysis and after the first catalytic cycle. After further catalysis recycling, the UV-vis. spectra remain the same as after the first cycling; (e) plot of molar amount of H_2 generated from AB hydrolysis vs. time taken by Au-Co with visible-light irradiation during the reuse test; (f) plot of molar amount of H_2 generated from AB hydrolysis vs. time taken by Au-Co in the reuse test without visible light in the second cycle. Reaction conditions: amount of sodium borohydride used: 1 mmol, temperature: 25±0.2°C

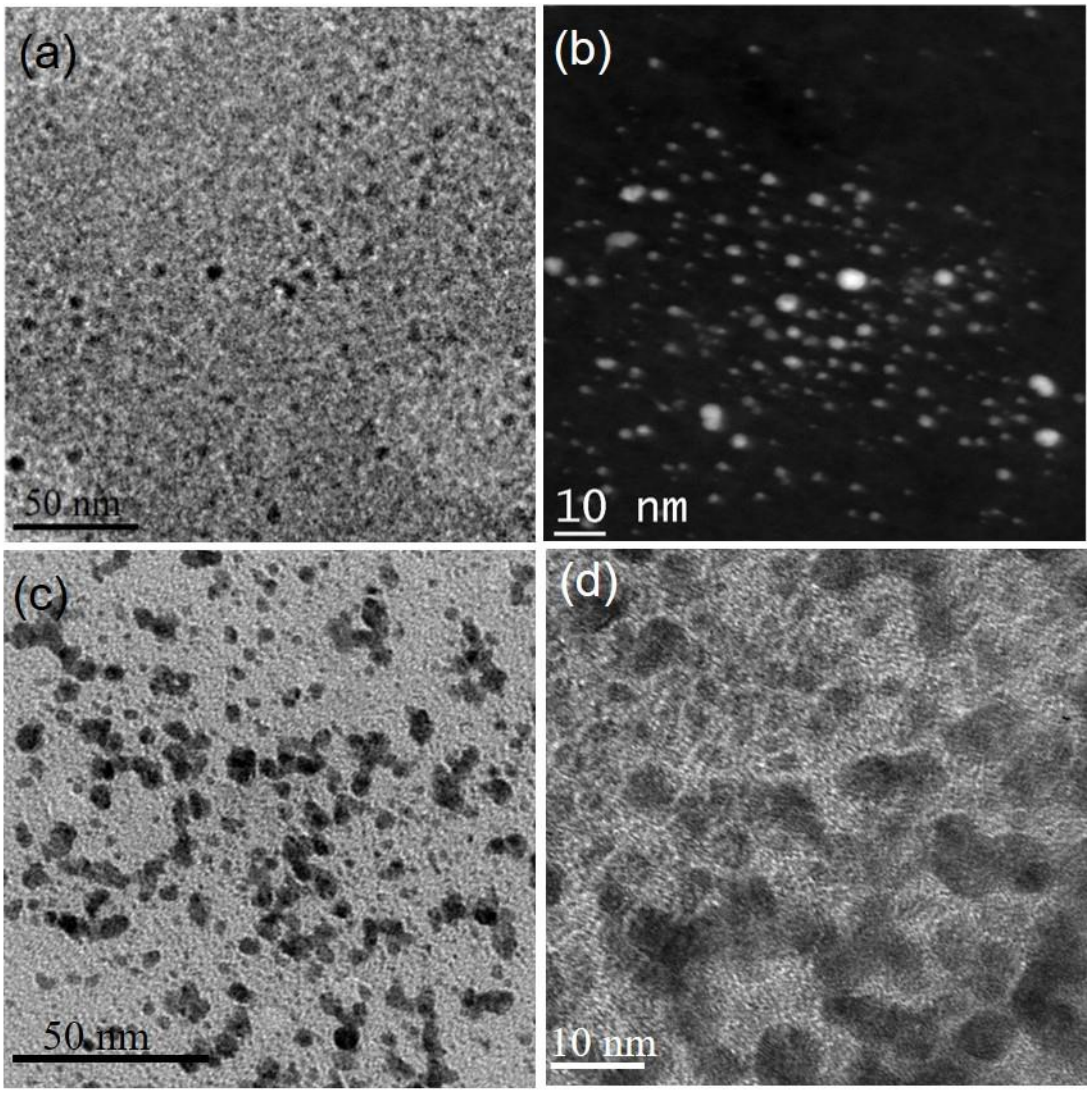

Figure S3.36. (a) TEM image of Au-Ru@dendrimer **1** before reaction, (b) HRTEM image of Au-Ru@dendrimer **1** before reaction, (c) TEM image of Au-Ru@dendrimer **1** after reaction, (d) HRTEM image of Au-Ru@dendrimer **1** after reaction.

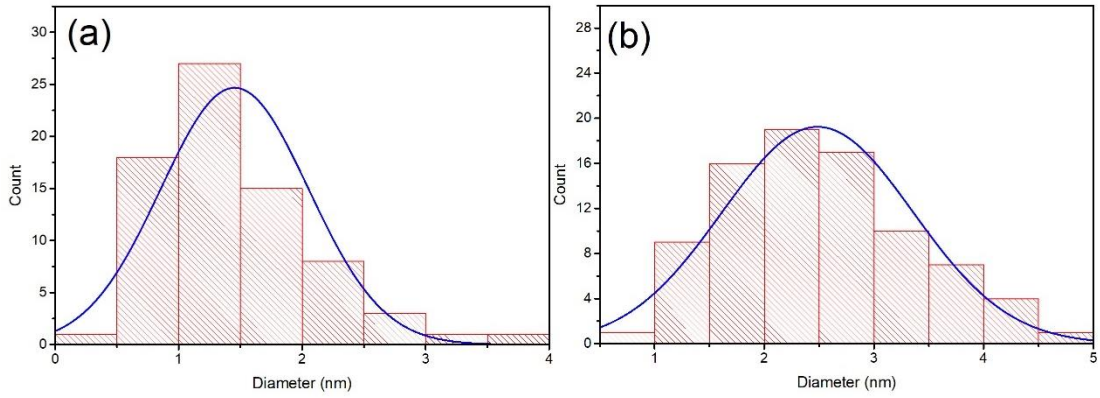

Figure S3.37. Size distribution of the Au-Ru@dendrimer **1**, (a) before reaction, and (b) after reaction.

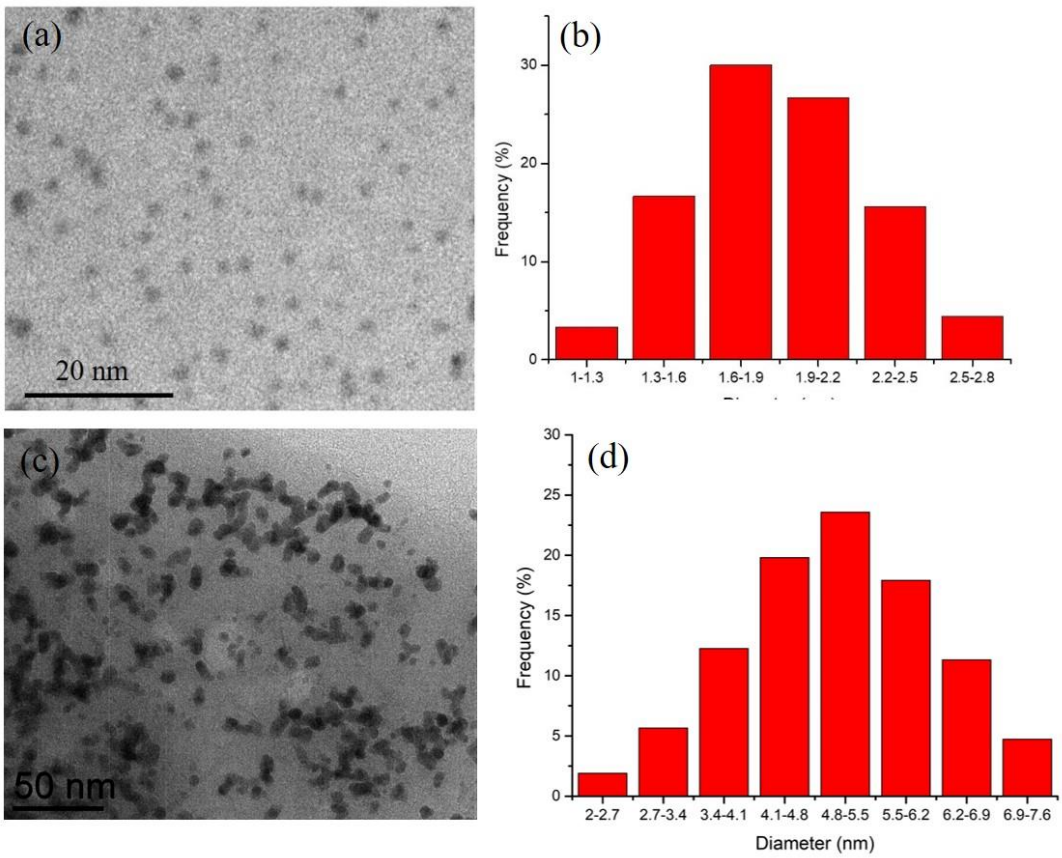

Figure S3.38. (a) TEM image of Au-Co@dendrimer **1** before reaction; (b) size distribution before reaction; (c) TEM image of Au-Co@dendrimer **1** after reaction; (d) size distribution after reaction.

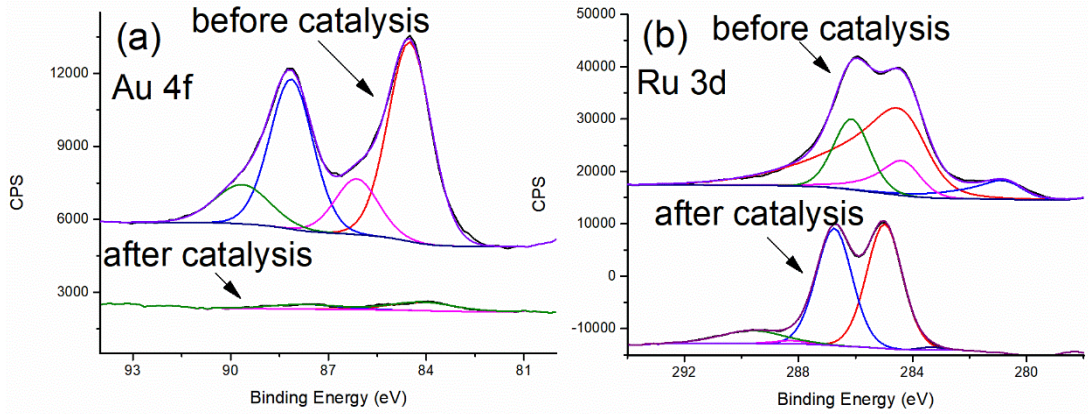

Figure S3.39. XPS analysis (a) Au 4f region before reaction and after reaction of Au-Ru@dendrimer **1**, (b) Ru 3d region before reaction and after reaction of Au-Ru@dendrimer **1**.

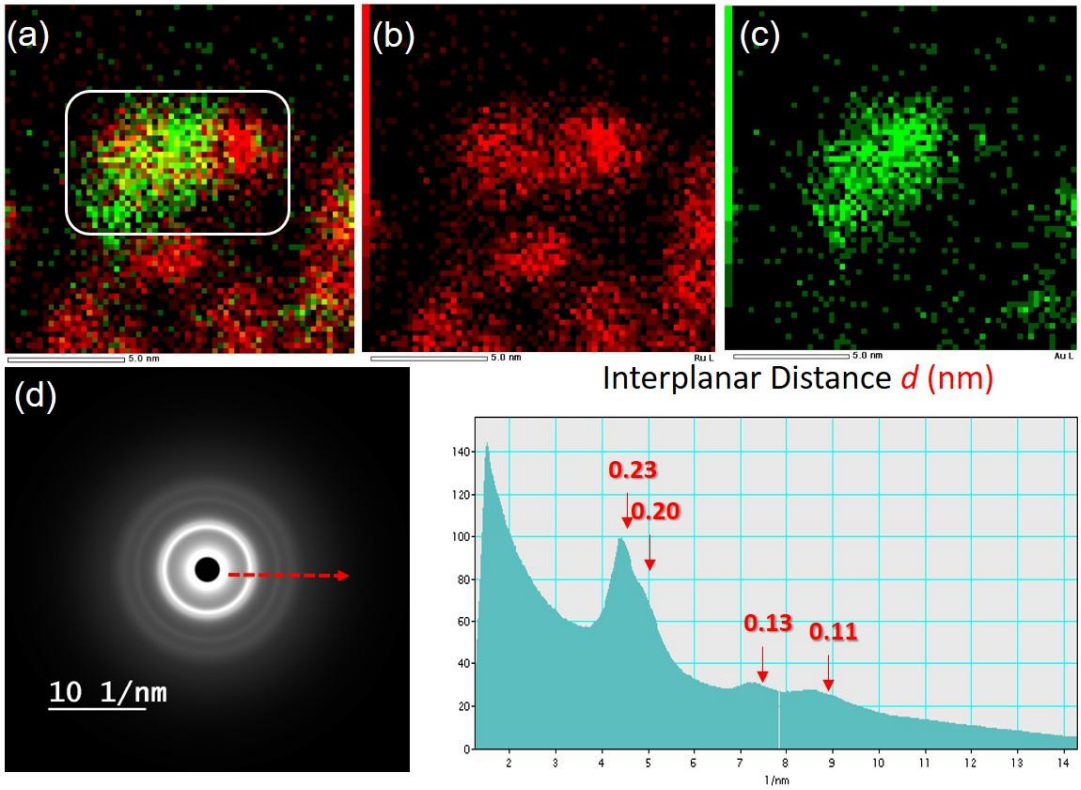

Figure S3.40. (a) EDS-mapping of Au-Ru@dendrimer **1** after reaction, (b) Ru region, (c) Au region, (d) SEAD image and corresponding interplanar distance reconstructed using Difftools. [S5]

Table S3.5. Element proportions in the part marked in **Figure** S41a.

Element	Mass %	Error %	Atom %
Au	7.16	0.41	0.86
Ru	47.69	0.03	11.2
O	42.59	0.01	84.15
C	2.55	0.11	3.78

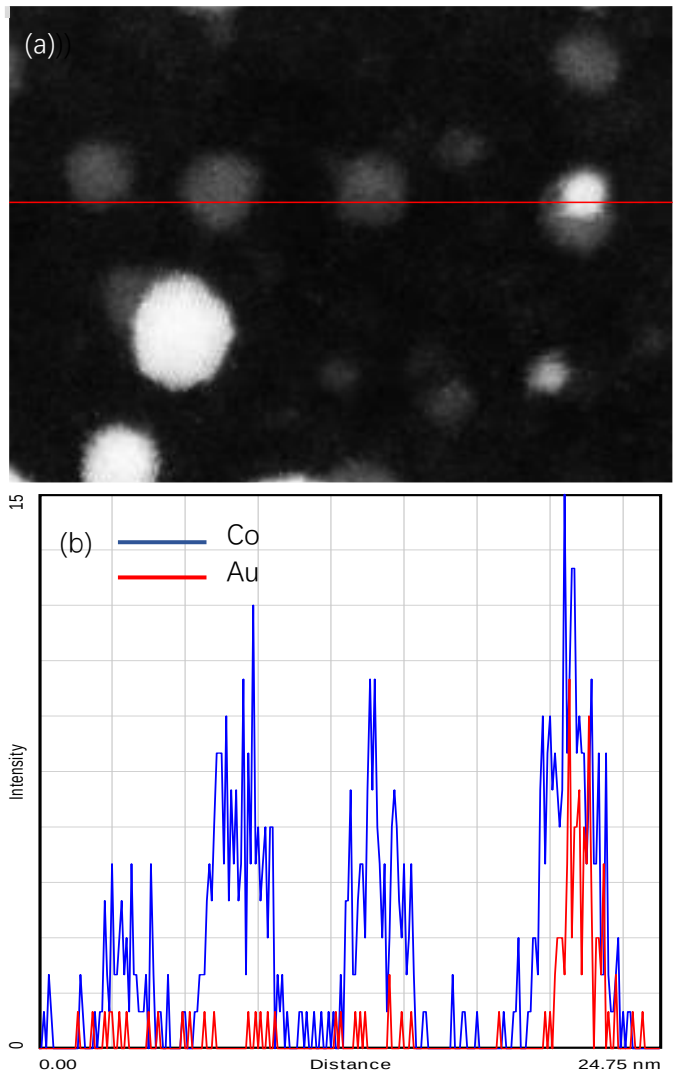

Figure S3.41. (a) HAADF-STEM image of Au/Co @ dendrimer 1 and (b) distributions of Au and Co along cross-section lines.

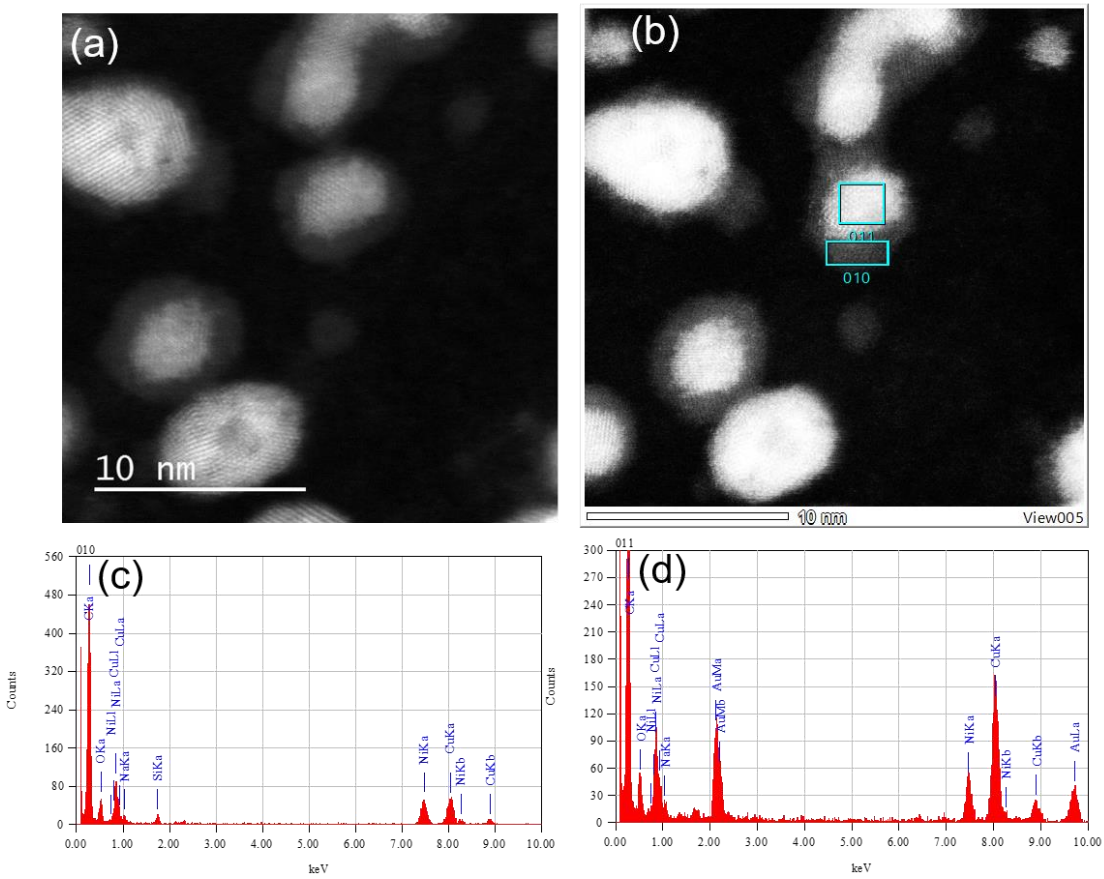

Figure S3.42. (a) HRTEM image of Au-Ni @dendrimer **1** after reaction, (b) HRTEM-EDX image of Au-Ni @dendrimer **1** after reaction, (c) metal content of 010 region marked in **Figure** S3.43 (b), (d) metal content of 011 region marked in **Figure** S3.43 (b).

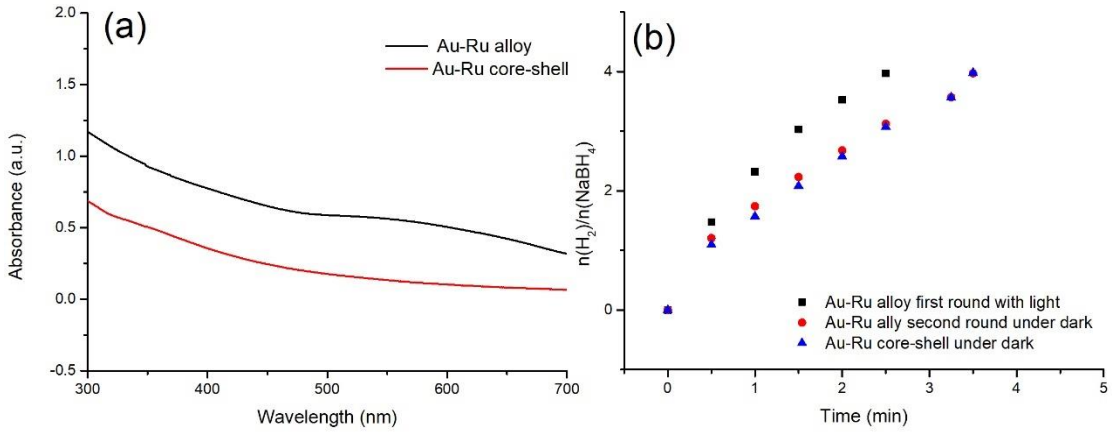

Figure S43. (a) UV-vis. spectra of Au-Ru alloy and Au-Ru core-shell, (b) comparison of hydrolysis efficiency for sodium borohydride among Au-Ru alloy under visible light, second round of Au-Ru alloy after removal of visible light and Au-Ru core-shell under dark.

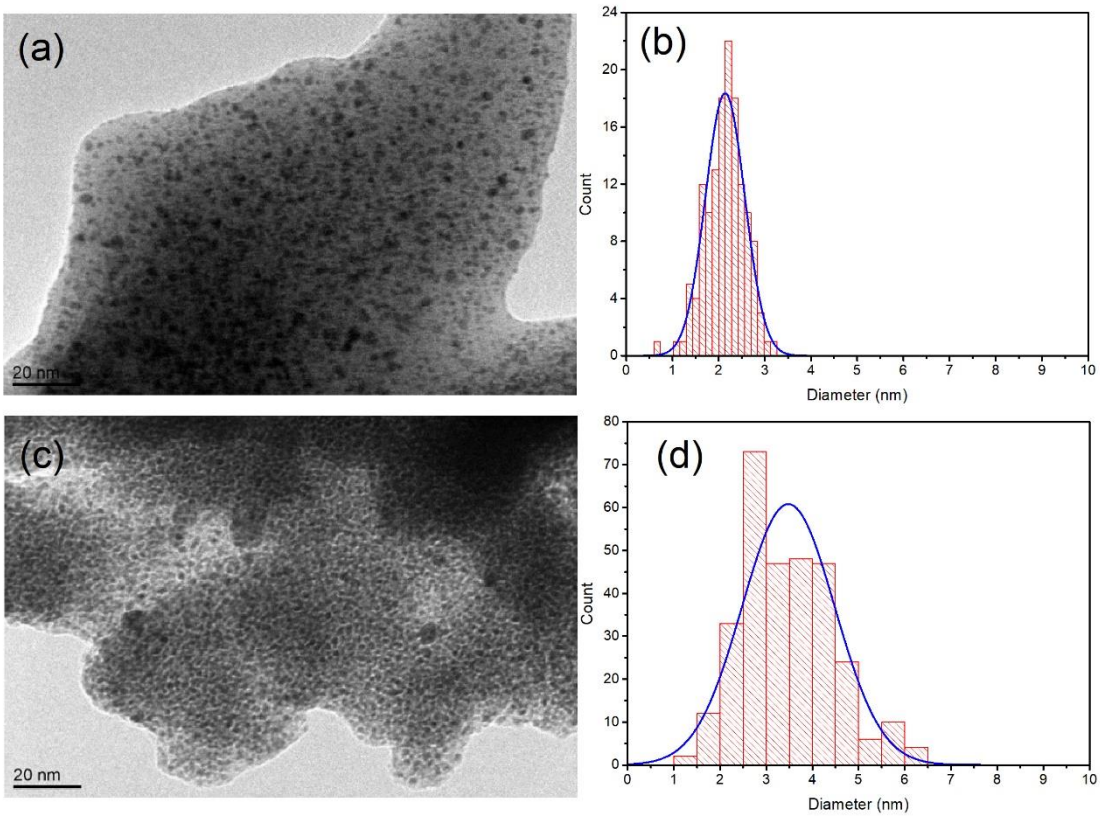

Figure S3.44. (a) TEM image of Au-Ru@dendrimer **2** before reaction; (b) size distribution of the Au-Ru@dendrimer **2** before reaction; (c) TEM image of Au-Ru@dendrimer **2** after reaction; (d) size distribution of the Au-Ru@dendrimer **2** after reaction.

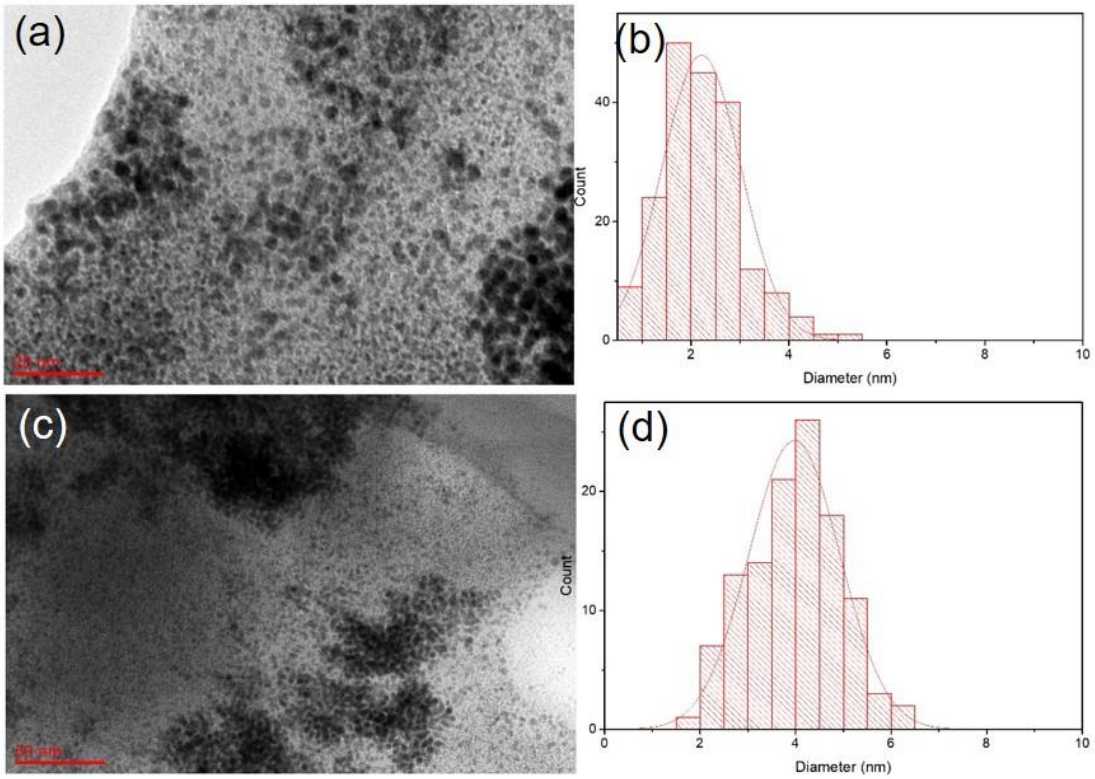

Figure S3.45. (a) TEM image of Au-Ru@ "click" polymer before reaction; (b) size distribution of the Au-Ru@ "click" polymer **3** before reaction; (c) TEM image of Au-Ru@ "click" polymer **3** after reaction; (d) size distribution of the Au-Ru@ "click" polymer **3** after reaction.

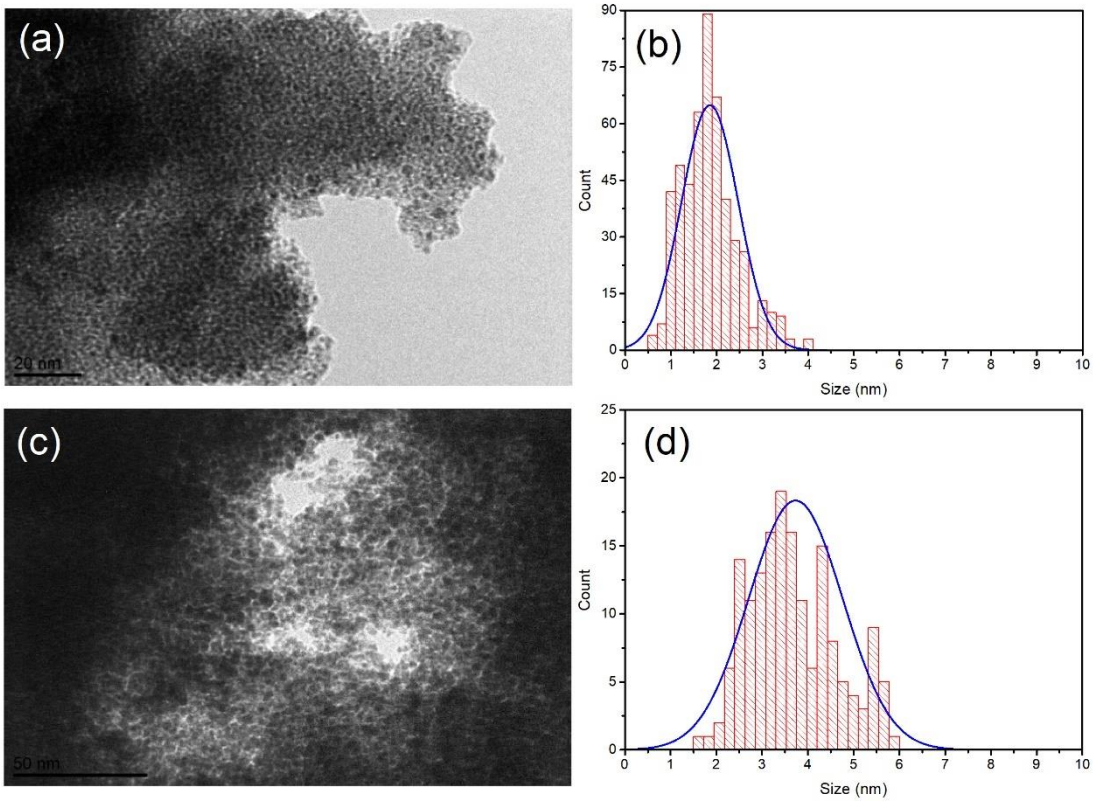

Figure S3.46. (a) TEM image of Au-Ru@PVP before reaction; (b) size distribution of the Au-Ru@PVP before reaction; (c) TEM image of Au-Ru@PVP after reaction; (d) size distribution of the Au-Ru@PVP after reaction.

Table S3.6. Size of Au-Ru particles supported on different stabilizers.

Supports	Size before reaction (nm)	Size after reaction (nm)
Dendrimer **1**	1.48	2.46
Dendrimer **2**	2.12	3.62
"Click" polymer **3**	2.27	3.92
PVP	1.69	4.13

Table S3.7. Finishing time of $NaBH_4$ hydrolysis in the process of recycling upon catalysis by Au-Ru catalysts supported on different stabilizers.

Supports	1st (min)	2 nd (min)	3 rd (min)	4 th (min)	5 th (min)
Dendrimer **1**	2.25	2.25	3	3.5	4
Dendrimer **2**	9	10	11	13	14.5
"Click" polymer **3**	14	15	16.5	18	19
PVP	5	13	/	/	/

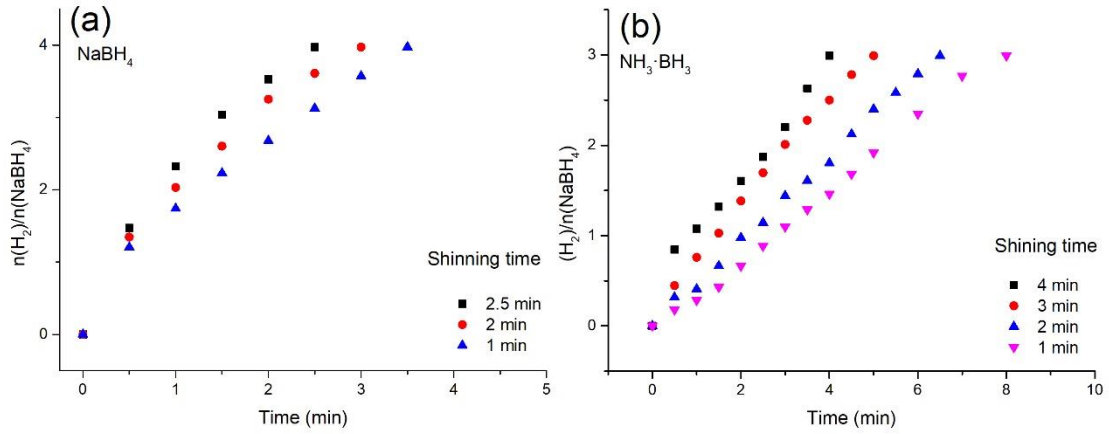

Figure S3.47. Efficiency of hydrogen generation derived by Au-Ru@dendrimer**1** with different illuminating time of visible light (a) rate for sodium borohydride and (b) rate for AB. Reaction conditions: amount of sodium borohydride (ammonia borane) used: 1 mmol, temperature: 25 ± 0.2 °C

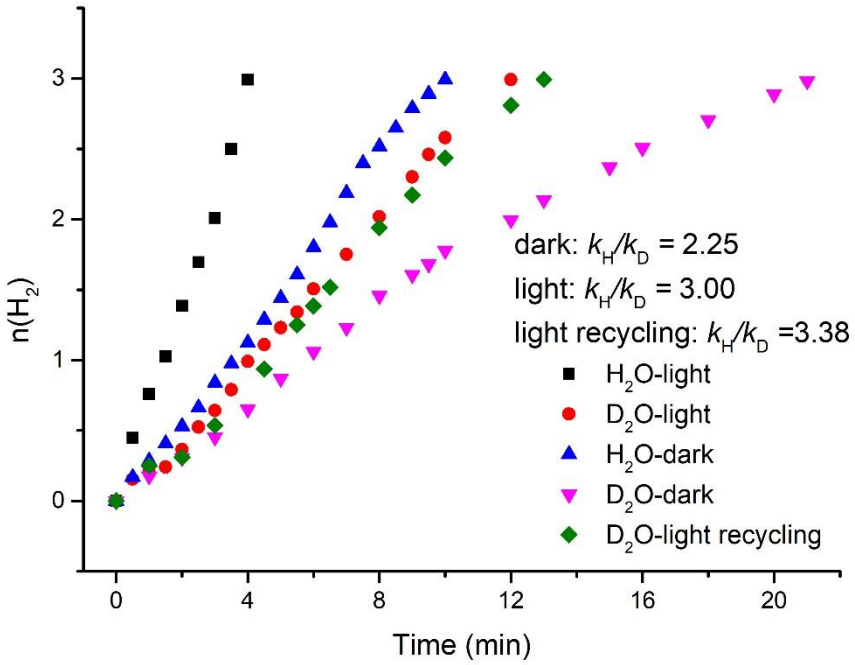

Figure S3.48. H_2 evolution from AB with H_2O and D_2O catalyzed by Au-Ru@dendrimer **1** under dark and visible light.

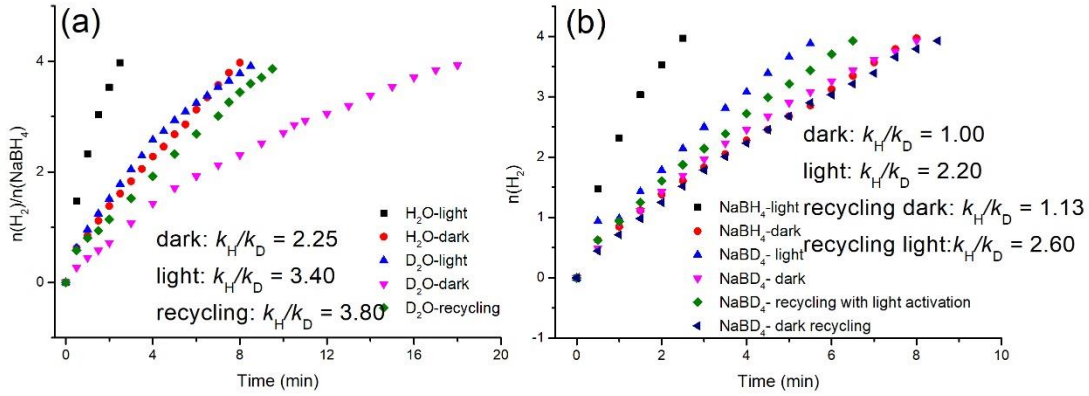

Figure S3.49 H_2 evolution from $NaBH_4$ with H_2O and D_2O catalyzed by Au-Ru@dendrimer **1** (b) H_2 evolution from H_2O with $NaBH_4$ and $NaBD_4$ catalyzed by Au-Ru@dendrimer **1**.

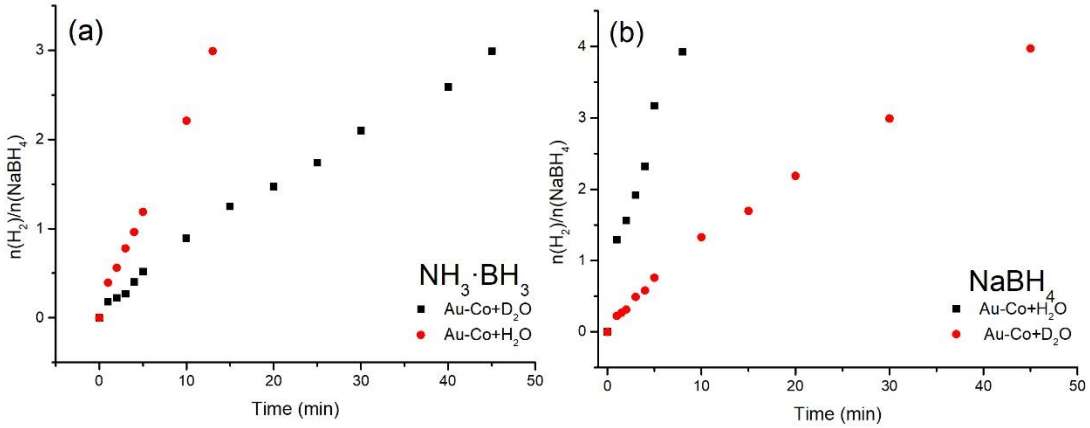

Figure S3.50. H_2 evolution with H_2O and D_2O catalyzed by Au-Co@dendrimer **1** under visible light from (a) AB (KIE = 3.1) and (b) $NaBH_4$ (KIE = 5.4).

Table S3.8. Catalytic activity of the reported plasmonic metal-based catalysts for AB hydrolysis with visible light. Semiconductor-based bimetallic nano catalysts show very slow reactions.

Catalysts	Catalyst/AB molar ratio	Temperature (°C)	Light Intensity (W)	Light enhancement	Recycling time	Average rate ($mol_{H2} \cdot h^{-1}$)	Reference
AuRh@polymer	0.2%	20	/	/	/	8.84	(S6)
Pt/Ag-SBA15	1.25%	25	350	1.5	/	1.24	(S7)
Au/Pd core-shell	<1%	25	500	3	3	10.8	(S8)
Au/Pd@MIL101	3%	30	500	1.6	/	1.09	(S9)
Au/TiO_2	2.5%	25	500	2	/	2.2×10^{-5}	(S10)
Au/Co@CN	2%	25	150	2	/	93.6	(S11)
Au/Ru@dendrimer **1**	1%	25	7	2.5	5	45.5	This work
Au/Rh@dendrimer **1**	1%	25	7	2.8	/	144	This work
Au/Co@dendrimer **1**	1%	25	7	1.6	5	16.4	This work

3.5 References

(1) Oshchepkov, A. G.; Braesch, G.; Bonnefont, A.; Savinova, E. R.; Chatenet, M. Recent advances in the understanding of nickel-based catalysts for the oxidation of hydrogen-containing fuels in alkaline media. *ACS Catal.* **2020**, *10*, 7043–7068.

(2) Luo, N.; Hou, T.; Liu, S.; Zeng, B.; Lu, J.; Zhang, J.; Li, H.; Wang, F. Photocatalytic coproduction of deoxybenzoin and H-2 through tandem redox reactions. *ACS Catal.* **2020**, *10* (1), 762–769.

(3) Fujishima, A.; Honda, K.; Electrochemical photolysis of water at a semiconductor electrode. *Nature* **1972,** *238,* 37–38.

(4) Deng, Y.; Tang, L.; Feng, C.; Zeng, G.; Chen, Z., Wang, J.; Feng, H.; Peng, B.; Liu, Y.; Zhou, Y. Insight into the dual-channel charge-charrier transfer path for nonmetal plasmonic tungsten oxide based composites with boosted photocatalytic activity under full-spectrum light. *Appl. Catal. B* **2018**, *235*, 225–237.

(5) Shiraishi, Y.; Takii, T.; Hagi, T.; Mori, S.; Kofuji, Y.; Kitagawa, Y.; Tanaka, S.; Ichikawa, S.; Hirai, T. Resorcinol-formaldehyde resins as metal-free semiconductor photocatalysts for solar-to-hydrogen peroxide energy conversion. *Nat. Mater*. **2019**, *18*, 985-993.

(6) Rej, S.; Mascaretti, L.; Santiago, E. Y.; Tomanec, O.; Kment, S.; Wang, Z.; Zboril, R.; Fornasiero, P.; Govorov, A. O.; Naldoni, A. Determining Plasmonic Hot Electrons and Photothermal Effects during H-2 Evolution with TiN-Pt Nanohybrids. *ACS Catal.* **2020**, *10* (9), 5261–5271.

(7) Balayeva, N. O.; Mamiyev, Z.; Dillert, R.; Zheng, N.; Bahnemann, D. W. Rh/TiO_2-Photocatalyzed Acceptorless Dehydrogenation of N-Heterocycles upon Visible-Light Illumination. *ACS Catal.* **2020**, *10* (10), 5542–5553.

(8) Wang, Y.; Shen, G.; Zhang, Y.; Pan, L.; Zhang, X.; Zou, J.J. Visible-light-induced unbalanced charge on NiCoP/TiO_2 sensitized system for rapid H_2 generation from hydrolysis of ammonia borane. *Appl. Catal. B* **2020**, *260*, 118183.

(9) Wang, C.; Astruc, D. Nanogold plasmonic photocatalysis for organic synthesis and clean energy conversion. *Chem. Soc. Rev*. **2014**, *43,* 7188-7216.

(10) Zheng, Z.; Tachikawa, T.; Majima, T.; Plasmon-enhanced formic acid dehydrogenation using anisotropic Pd-Au nanorods studied at the single-particle level. *J. Am. Chem. Soc.* 2015, *137*, 948–957.

(11) Linic, S.; Aslam, U.; Boerigter, C.; Morabito, M. Photochemical transformations on plasmonic metal nanoparticles. *Nat. Mater.* **2015**, *14,* 567–576. (c)

(12) Zada, A.; Muhammad, P.; Ahmad, W.; Hussain, Z.; Ali, S.; Khan, M.; Khan, Q.; Maqbool, M. Surface plasmonic-assisted photocatalysis and optoelectronic devices with noble metal nanocrystals: design, synthesis, and applications. *Adv. Funct. Mater*. **2019**, 1906744

(13) Wen, M.; Kuwahara, Y.; Mori, K.; Yamashita, H.; Enhancement of catalytic activity over AuPd nanoparticles loaded metal organic framework under visible light irradiation. *Top. Catal.* **2016**, *59,* 1765–1771.

(14) Rej, S.; Hsia, C.; Chen, T.; Lin, F.; Huang, J.; Huang, M. H.; Hydrogen evolution facet-dependent and light-assisted efficient hydrogen evolution from ammonia borane using gold–palladium core–shell nanocatalysts. *Angew. Chem., Int. Ed.* **2016**, *55*, 7222–7226.

(15) Verma, P.; Yuan, K.; Kuwahara, Y.; Mori, K.; Yamashita, H. Enhancement of plasmonic activity by Pt/Ag bimetallic nanocatalyst supported on mesoporous silica in the hydrogen production from hydrogen storage material. *Appl. Catal. B* **2018**, *223*, 10–15.

(16) Gelle, A.; Jin, T.; Garza, de la L.; Price, G. D.; Besteiro, L. V.; Moores, A.; Applications of plasmon-enhanced nanocatalysis to organic transformations. *Chem. Rev*. **2020**, *120,* 986–1041.

(17) Sun, D.; Hao, Y.; Wang, C.; Zhang, X.; Yu, X.; Yang, X.; Li, L.; Lu, Z.; Shang, W. TiO_2–CdS Supported CuNi Nanoparticles as a highly efficient catalyst for hydrolysis of ammonia borane under visible-light irradiation. *Int. J. Hydrog. Energy* **2020**, *45*, 4390–4402.

(18) Wu, Y.; Sun, Y.; Fu, W.; Meng, X.; Zhu, M.; Ramakrishna, S.; Dai, Y. Graphene-Based modulation on the growth of urchin-like $Na_2Ti_3O_7$ microspheres for photothermally enhanced H_2 generation from ammonia borane. *ACS Appl. Nano Mater.* **2020**, *3*, 2713–2722.

(19) Jo, S.; Verma, P.; Kuwahara, Y.; Mori, K.; Choi, W.; Yamashita, H.; Enhanced hydrogen production from ammonia borane using controlled plasmonic performance of Au nanoparticles deposited on TiO_2. *J. Mater. Chem. A* **2017**, *5*, 21883–21892.

(20) Kurnaravel, V.; Mathew, S.; Bartlett, J.; Pillai, S. C. Photocatalytic hydrogen production using metal doped TiO_2: A Review of recent advances. *Appl. Catal. B* **2019**, *244*, 1021–1064.

(21) Gao, M.; Yu, Y.; Yang, W.; Li, J.; Xu, S.; Feng, M.; Li, H. Ni Nanoparticles Supported on Graphitic Carbon Nitride as Visible Light Catalysts for Hydrolytic Dehydrogenation of Ammonia Borane. *Nanoscale* **2019**, *11*, 3506–3513.

(22) Zhang, H.; Gu, X.; Song, J. Co, Ni-Based nanoparticles supported on graphitic carbon nitride nanosheets as catalysts for hydrogen generation from the hydrolysis of ammonia borane under broad-spectrum light irradiation. *Int. J. Hydrog. Energy* **2020**, *45*, 21273–21286.

(23) Zhang, H.; Gu, X.; Liu, P.; Song, J.; Cheng, J.; Su, H. Highly Efficient Visible-Light-Driven Catalytic Hydrogen Evolution from Ammonia Borane Using Non-Precious Metal Nanoparticles Supported by Graphitic Carbon Nitride. *J. Mater. Chem. A* **2017**, *5*, 2288–2296.

(24) Zhu, Q.-L.; Xu, Q. Liquid organic and inorganic chemical hydrides for high-capacity hydrogen storage. *Energy Environ. Sci.* **2015**, *8*, 478−512.

(25) Akbayrak, S.; Ozkar, S. Ammonia borane as hydrogen storage materials. *Int. J. Hydrog. Energy* **2018**, *43*, 18592−18606.

(26) Wang, C.; Wang, Q.; Fu, F., Astruc, D. Hydrogen generation upon nanocatalyzed hydrolysis of rich boron derivatives: recent developments. *Acc. Chem. Res*. **2020**, *53*, 000, doi.org/10.1021/acs.accounts.0c00525

(27) (a) Kumar, R.; Karkamkar, A.; Bowden, M.; Autrey, T. Solid-state hydrogen rich boron-nitrogen compounds for energy storage, *Chem. Soc. Rev.* **2019**, *48,* 5350–5380.

(28) Asefa, T.; Koh, K.; Yoon, C. W. CO_2-mediated H_2 storage-release with nanostructured catalysts: recent progresses, challenges, and perspectives. *Adv. Energy Mater.* **2019**, *9,* 1901158.

(29) Alpaydin, C. Y.; Gülbay, S. K.; Colpan, G. O. A Review on the catalysts used for hydrogen production from ammonia borane. *Int. J. Hydrog. Energy* **2020**, *45,* 3414-3434.

(30) Wang, C.; Tuminetti, J.; Wang, Z.; Zhang, C.; Ciganda, R.; Moya, S.; Ruiz, J.; Astruc, D. Hydrolysis of ammonia-borane over Ni/ZIF-8 Nanocatalyst: High efficiency, mechanism, and controlled hydrogen release. *J. Am. Chem. Soc*. **2017**, *139,* 11610–11615.

(31) Rossin, A.; Tuci, G.; Luconi, L.; Giambastiani, G. Metal-Organic Frameworks as Heterogeneous Catalysts in Hydrogen Production from Lightweight Inorganic Hydrides. *ACS Catal.* **2017**, *7* (8), 5035–5045.

(32) Fu, F.; Wang, C.; Wang, Q.; Martinez-Villacorta, A. M.; Escobar, A.; Chong, H.; Wang, X.; Moya, S.; Salmon, L.; Fouquet, E.; Ruiz, J.; Astruc, D. Highly selective and sharp volcano-type synergistic Ni_2Pt@ZIF-8-catalyzed hydrogen evolution from ammonia borane hydrolysis. *J. Am. Chem. Soc.* **2018**, *140,* 10034–10042.

(33) Lu, N.; Zhang, Z.; Wang, Y.; Liu, B.; Guo, L.; Wang, L.; Xu, J.; Liu, K.; Dong, B. Direct evidence of IR-driven hot electron transfer in metal-free plasmonic $W_{18}O_{49}$/Carbon heterostructures for enhanced catalytic H_2 production. *Appl. Catal. B* **2018**, *233,* 19–25.

(34) Zhang, J.; Chen, W.; Ge, H.; Chen, C.; Yan, W.; Gao, Z.; Gan, J.; Zhang, B.; Duan, X.; Qin, Y.; Synergistic effects in atomic-layer-deposited $PtCo_x$/CNTs catalysts enhancing hydrolytic dehydrogenation of ammonia borane. *Appl. Catal. B* **2018**, *235*, 256–263.

(35) Yao, K.; Zhao, C.; Wang, N.; Li, T.; Lu, W.; Wang, J. An aqueous synthesis of porous PtPd nanoparticles with reversed bimetallic structures for highly efficient hydrogen generation from ammonia borane hydrolysis. *Nanoscale* **2020**, *12*, 638–647.

(36) Wang, Y.; Shen, G.; Zhang, Y.; Pan, L.; Zhang, X.; Zou, J.-J Visible-light-induced unbalanced charge on NiCoP/TiO_2 sensitized system for rapid H_2 generation from hydrolysis of ammonia borane. *Appl. Catal. B* **2020**, *260*, 118183.

(37) (a) de Vries, J. G.; Elsevier, C. J.; *In the Handbook of Homogeneous Hydrogenation*; Wiley-VCH: Weinheim, Germany 2007.

(38) Bronstein L. M.; Shiffrina, Z.; Dendrimers as Encapsulating, Stabilizing, and directing agents for inorganic nanoparticles, *Chem. Rev*. **2011**, *111*, 5301-5344.

(39) Myers, V. S.; Weir, M. G.; Carino, E. V.; Crooks, R. M. Dendrimer-encapsulated nanoparticles: New synthetic and characterization methods and catalytic applications, *Chem. Sci.* **2011**, *2,* 1632-1646.

(40) Imaoka, T.; Kitazawa, H.; Chun, T. W.-J.; Yamamoto, K.; Finding the most catalytically active platinum clusters with low atomicity, *Angew. Chem., Int. Ed.* **2015**, *54*, 9810−9815.

(41) Li, Z.; He, T.; Matsumura, D.; Miao, S.; Wu, A.; Liu, L.; Wu, G.; Chen, P. Atomically Dispersed Pt on the Surface of Ni Particles: Synthesis and Catalytic Function in Hydrogen Generation from Aqueous Ammonia-Borane. *ACS Catal.* **2017**, *7* (10), 6762–6769.

(42) Samantaray, M. K.; Pump, E.; Bendjeriou-Sedjerari, A.; D'Elia, V.; Pelletier, J. D. A.; Guidotti, M.; Psaro, R.; Basset, J. M. J. Surface organometallic chemistry in heterogeneous catalysis. *Chem. Soc. Rev.* **2018**, *47*, 8403- 8437.

(43) Liu, L.; Corma, A.; Metal catalysts for heterogeneous catalysis: From single atoms to nanoclusters and nanoparticl. *Chem. Rev*. **2018**, *118*, 4981-5079.

(44) Astruc, D. Introduction: Nanoparticles in Catalysis. *Chem. Rev*. **2020**, *120,* 461-463. (i) Sankar, M.; He, Q.; Engel, R. V.; Sai, M. A.; Logsdail, A. J.; Roldan, A.; Willock, D. J.; Agarwal, N.; Kiely, C.; Hutchings, G. Role of the support in gold-containing nanoparticles as heterogeneous catalysts. *J. Chem. Rev.* **2020**, *120,* 3890-3938.

(45) Xie, C.; Niu, Z.; Kim, D.; Li, M.; Yang, P. Surface and Interface Control in Nanoparticle Catalysis. *Chem. Rev*. **2020**, *120,* 1184-1249.

(46) Li, Y.; Cain, J. D.; Hanson, E. D.; Murthy, A. A.; Hao, S.; Shi F.; Li, Q.; Wolverton, C.; Chen, Q.; Dravid, V. P.; Au@MoS_2 core–shell heterostructures with strong light–matter interactions. *Nano Lett.* **2016**, *16*, 7696-7702.

(47) Mori, K.; Verma, P.; Hayashi, R.; Fuku, K.; Yamashita, H. Color-controlled Ag nanoparticles and nanorods within confined mesopores: Microwave-assisted rapid synthesis and application in plasmonic catalysis under visible-light irradiation. *Chem. Eur. J.* **2015**, *21,* 11885–11893.

(48) Wang, Q.; Fu, F.; Yang, S.; Moro, M. Martinez; Ramirez, M. de los A.; Moya, S.; Salmon, L.; Ruiz, J.; Astruc, D. Dramatic synergy in CoPt nanocatalysts stabilized by "click" dendrimers for evolution of hydrogen from hydrolysis of ammonia borane. *ACS Catal.* **2019**, *9,* 1110–1119.

(49) Daniel, M. C.; Astruc, D.; Gold nanoparticles: Assembly, supramolecular chemistry, quantum-size-related properties, and applications toward biology, catalysis, and nanotechnology. *Chem. Rev.* **2004**, *104,* 293–346.

(50) Jiang, N.; Zhuo, X.; Wang, J.; Active Plasmonics: principles, structures, and applications. *Chem. Rev.* **2018**, *118,* 3054–3099.

(51) Boisselier, E.; Diallo, K. A.; Salmon, L.; Ornelas, C.; Ruiz, J.; Astruc, D. Encapsulation and stabilization of gold nanoparticles with “click” polyethyleneglycol dendrimers. *J. Am. Chem. Soc.* **2010**, *132,* 2729–2742.

(52) Deraedt, C.; Rapakousiou, A.; Wang, Y.; Salmon, L.; Bousquet, M.; Astruc, D.; Multi-function redox polymers: Electrochrome, polyelectrolyte, sensor, electrode modifier, nanoparticle stabilizer and catalyst template. *Angew. Chem., Int. Ed.* **2014**, *53,* 8445-8449

(53) Goriachko, A.; Over, H. Subtle nanostructuring of the Au/Ru(0001) Surface. *Nanoscale Res. Lett.* **2018**, *13*, 203.

(54) Zhang, Q.; Kusada, K.; Wu, D.; Yamamoto, T.; Toriyama, T.; Matsumura, S.; Kawaguchi, S.; Kubota, Y.; Kitagawa, H.; Selective control of fcc and hcp crystal structures in Au-Ru solid-solution alloy nanoparticles. Nat. Commun. **2018**, 9,118612.

(55) Wang, D.; Astruc, D. Dendritic catalysis-basic concepts and recent trends. *Coord. Chem. Rev.* 257 **2013**, *257*, 2317–2334.

(56) Zhang, S.; Li, M.; Zhao, J.; Wang, H.; Zhu, X.; Han, J.; Liu, X. Plasmonic AuPd-Based Mott-Schottky Photocatalyst for Synergistically Enhanced Hydrogen Evolution from Formic Acid and Aldehyde. *Appl. Catal. B* **2019**, *252,* 24–32.

(57) Zhang, S.; Wang, H.; Tang, L.; Li, M.; Tian, J.; Cui, Y.; Han, J.; Zhu, X.; Liu, X. Sub 1 Nm Aggregation-Free AuPd Nanocatalysts Confined inside Amino-Functionalized Organosilica Nanotubes for Visible-Light-Driven Hydrogen Evolution from Formaldehyde. *Appl. Catal. B* **2018**, *220,* 303–313.

(58) Liu, X.; Ruiz, J.; Astruc, D. Compared Catalytic Efficiency of Click-Dendrimer-Stabilized Late Transition Metal Nanoparticles in 4-Nitrophenol Reduction. *J. Inorg. Organomet. Polym. Mater*. **2018**, *28,* 399–406.

(59) Tedsree, K.; Li, T.; Jones, S.; Chan, C. W. A.; Yu, K. M. K.; Bagot, P. A. J.; Marquis, E. A.; Smith, G. D. W.; Tsang, S. C. E. Hydrogen production from formic acid decomposition at room temperature using a Ag-Pd core-shell nanocatalyst. *Nat. Nanotechnol*. **2011**, *6,* 302–307.

(60) Liu, X.; Gregurec, D.; Irigoyen, J.; Martinez, A.; Moya, S.; Ciganda, R.; Hermange, P.; Ruiz, J.; Astruc, D.; Precise localization of metal nanoparticles in dendrimer nanosnakes or inner periphery and consequences in catalysis. *Nat. Commun.* **2016**, *7*, 1-8.

(61) Rablen, P. R. Large effect on borane bond dissociation energies resulting from coordination by lewis bases. *J. Am. Chem. Soc.* **1997**, *119*, 8350−8360.

(62) Westheimer, F. H. The magnitude of the primary kinetic isotope effect for compounds of hydrogen and deuterium. *Chem. Rev.* 1961, *61, 3,* 265–273.

(63) Zhan, W. W.; Zhu, Q. L.; Xu, Q. Dehydrogenation of ammonia borane by metal nanoparticle catalysts. A*CS Catal.* **2016**, *6*, 6892-6905.

(64) Li, Z.; He, T.; Liu, L.; Chen, W.; Zhang, M.; Wu, G.; Chen, P. Covalent triazine framework supported non-noble metal nanoparticles with superior activity for catalytic hydrolysis of ammonia borane: from mechanistic study to catalyst design. *Chem. Sci*. **2017**, *8*, 781-788.

(65) Astruc, D. *Organometallic Chemistry and Catalysis*. Springer, Berlin, **2007**, Chap. 3.

(66) Axet, M. R.; Philippot, K. Catalysis with Colloidal Ruthenium Nanoparticles. *Chem. Rev.* **2020**, *120*, 1085−1145.

(67) Peebles, L. R.; Marshall, P. High-accuracy coupled-cluster computations of bond dissociation energies in SH, H_2S, and H_2O. *J. Chem. Phys.* **2002**, *117*, 3132− 3138

(68) Sermiagin, A.; Meyerstein, D.; Bar-Ziv, R.; Zidki, T. The Chemical properties of hydrogen atoms adsorbed on M^0-nanoparticles suspended in aqueous solutions: The case of Ag^0-NPs and Au^0-NPs reduced by BD_4^-. *Angew. Chem.-Int. Ed*. **2018**, *57*, 16525–16528.

Chapter 4. Fast Au-Ni@ZIF-8-Catalyzed Ammonia Borane Hydrolysis Boosted by Dramatic Volcano-Type Synergy and Plasmonic Acceleration

4.1.Introduction

Hydrogen (H_2) has attracted wide attention as an extremely promising source of sustainable energy [1–3], but the challenge of storage and delivery of H_2 limits its development [4–6]. Hydrogen-storage materials, such as boranes that are stable, high-hydrogen capacity, non-toxic, and water soluble [7], might prove useful both as energy sources and H_2 reservoirs at the laboratory scale if a stimulus such as hydrolysis could rapidly and conveniently generate H_2 from the precursor [8,9]. Many studies have demonstrated that metal nanoparticles (NPs) are effective catalysts for H_2 evolution upon hydrolysis of ammonia borane (AB) according to Equation 4.1[10–15].

$$NH_3BH_3 + 2\,H_2O \xrightarrow{\text{catalyst}} NH_4BO_2 + 3H_2 \qquad (4.1)$$

Bimetallic catalysts are often particularly efficient because of the possible synergies between the two metals forming the NPs [16–22]. For instance, Wang et al. compared the catalytic activity between Ni NPs and CuNi alloy for hydrogen production from AB and found that the activity was significantly enhanced by alloying Ni with Cu atoms, which was attributed to the change of local charge density due to Cu-Ni interactions [23]. Photocatalysis, a useful means of accelerating reactions, has been applied using plasmonic and semiconductors to H_2 evolution from AB hydrolysis. Plasmon-induced visible light enhancement of AB hydrolysis rate, particularly with nanogold, also attracted the concern of scientists [24–27]. Indeed, the coinage metals Au, Ag and Cu have been widely studied because of their visible-light plasmonic response [28,29]. Rej's group reported visible-light accelerated AB hydrolysis catalyzed by core-shell AuPd NPs and theoretical calculations showing the presence of a special plasmonic resonance mode at the interphase of the catalyst [24]. Yamashita's group reported rate enhancement upon visible-light irradiation for H_2 generation from AB catalyzed by Santa Barbara Amorphous (SBA)-15-stabilized Pt-Ag NPs[25]. Concerning heterogeneous catalysts, if the support is a good conductor, light enhancement due to the Mott–Schottky effect with the help of separated photogenerated electrons from a semiconductor between metal NPs and the semiconductor needs to be considered. Wang's group reported that the catalyst CuNi/CNS accelerates AB hydrolysis upon visible light irradiation, one of the favorable factors being the Mott-Schottky junctions between CuNi and CNS [23]. It was found earlier that ZIF-8 was an excellent support of Ni [14] and Ni_2Pt [30] nanocatalysts for AB hydrolysis because of its

ease and greenness of synthesis in aqueous solutions and very high thermal and chemical stabilities. However, the effect of visible light irradiation on catalysis by metal NPs supported by ZIF-8 has never been considered. Therefore, we designed a new strategy involving both maximum synergy among the nanocomponents and plasmon-induced visible-light boosting catalytic AB hydrolysis performances. We fabricated such novel efficient alloyed nanomaterials consisting in ZIF-8-encapsulated Au-Ni catalysts for fast H_2 release from AB hydrolysis, and the results that are reported herein represent a great improvement with significant practical relevance[16,17]. Optimized cumulative effects of volcano-type positive synergy between nanogold and nickel, selective plasmonic visible-light excitation, and high selectivity and superiority of the ZIF-8 heterogeneous support are shown herein for nanocatalysis of AB hydrolysis by Ni-Au@ZIF-8. Any Mott–Schottky effect is shown to be discarded in this system. Kinetic isotope effects (KIEs) are used for the mechanistic study of this reaction, allowing the proposition of a viable hydrolysis mechanism. The efficiency of the best catalyst is also probed for a tandem hydrogenation reaction. Finally, Density functional theory (DFT) calculation on this process has been conducted to evaluate, together with the kinetic analysis, details of the reaction mechanism, and particular the rate-determining step (RDS) of this Ni-Au@ZIF-8-catalyzed AB hydrolysis in water under both dark and visible-light illumination conditions.

4.2. Results and discussion

4.2.1. Synthesis and characterization of the nanocatalysts

The synthesis of ZIF-8 was efficiently conducted according to previous reports upon mixing solutions of 2-methylimidazole and $Zn(NO_3)_2 \cdot 6H_2O$ [14], followed by rapid ZIF-8 precipitation (Fig. 4.1a); its framework structure was very stable in water and methanol [30]. The transmission electron microscopy (TEM) image in Fig. S4.2 shows that the ZIF-8 NPs are polyhedron nanocrystals and that their average size is 45.6 nm. The Au-based alloyed NPs supported on ZIF-8 were fabricated by the deposition-precipitation method producing a series of AuNi@ZIF-8 NPs with various Au and Ni percentages. The metal loading was determined by inductively coupled plasma-optical emission spectroscopy (ICP-AES, Table S4.1).

The TEM image in Fig. 4.1b shows that the AuNi NPs are packed in the ZIF-8 framework with an average size of 2.89 nm. The measured lattice distance of 0.22 nm corresponds to the (111) plane of AuNi NPs shown by the high-angle annular dark field scanning transmission electron microscopy (HAADF-STEM) image (insert in Fig. 4.1b). A distinct face center cubic (*fcc) (111)* phase for the AuNi NPs is confirmed by the fast Fourier transform pattern of AuNi@ZIF-8 (Fig. 4.1c). The corresponding STEM-EDX elemental mappings of AuNi@ZIF-8 display a distribution of Ni, Au elements throughout the AuNi NPs (Fig. 4.1d). Furthermore, the STEM-EDX mapping of a AuNi NP indicates that the Au and Ni elements are present in a single particle and that the distribution of Au and Ni along cross-section lines of the AuNi NPs have an alloy structure in the ZIF-8 framework (Fig. 4.1e-f).

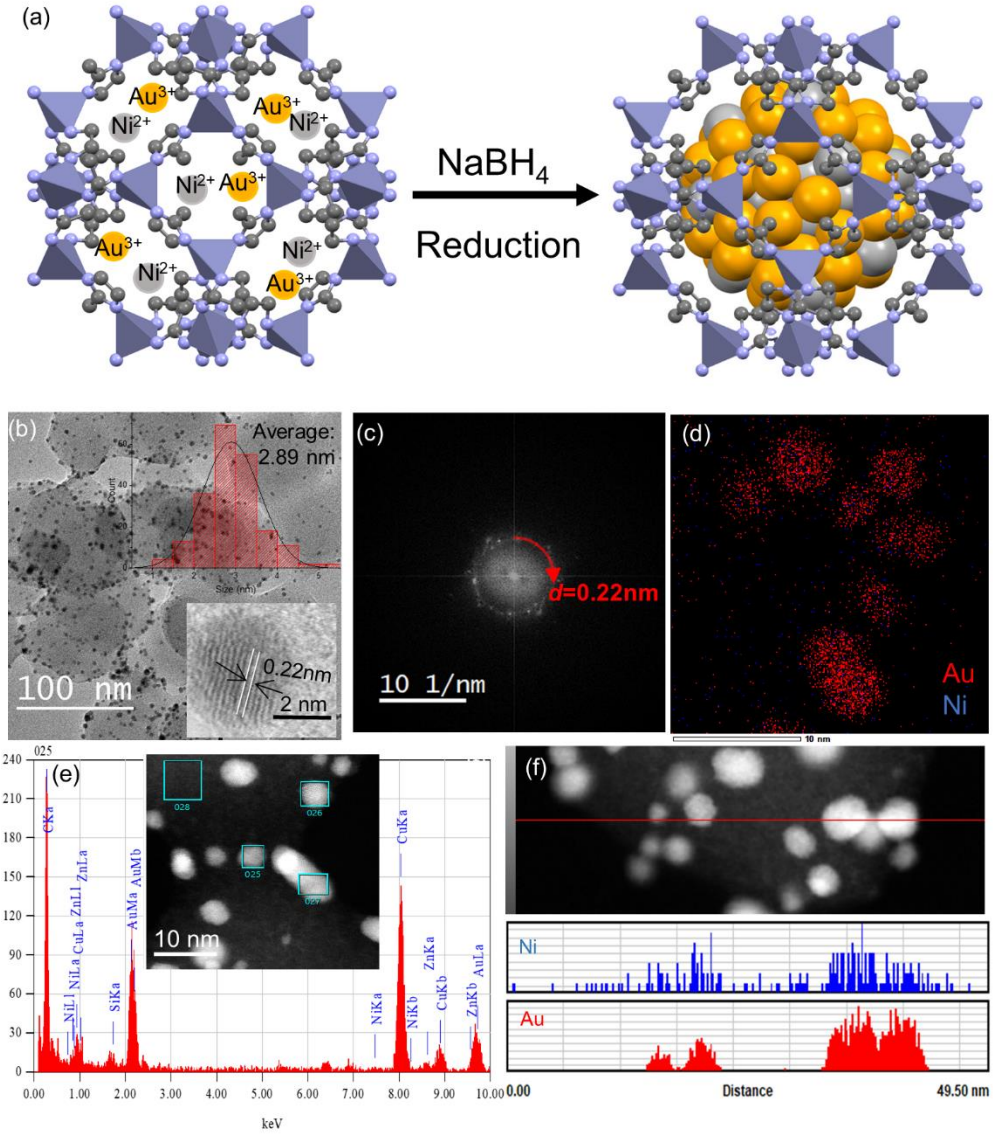

Fig. 4.1. (a) Synthesis of AuNi@ZIF-8; (b) TEM image of AuNi@ZIF-8 with size distribution and HAADF-STEM image inserted; (c) corresponding Fast Fourier Transform (FFT) pattern image of AuNi@ZIF-8; (d) Energy-Dispersive X-ray (EDX) mapping of different elements; (e) distributions of Au and Ni on 025 with the STEM image inserted. (f) HAADF-STEM image of AuNi@ZIF-8 and distributions of Au and Ni along cross-section lines.

The X-ray powder diffraction (XRD, Fig. 4.2a) shows the typical crystal pattern of ZIF-8,

and other ZIF-8-containing nanocatalysts have similar crystallinity as in Fig. 4.2a with ZIF-8 support. This suggests that the metal loading in the present case is low and that the NPs are inside ZIF-8. There are small changes in XRD spectra compared to pristine ZIF-8. The diffraction peak of Au@ZIF-8 at 38.1° corresponds to the Au (111) plane [34] with the addition of Ni to form the AuNi alloy; 2θ increased to 39.1° in accordance with AuNi (111), which is in agreement with the HAADF-STEM result [37].

The specific Brunauer-Emmet-Teller (BET) surface areas of the various samples were determined by N_2 adsorption/desorption isothermal measurements. The pristine ZIF-8 framework exhibited apparent type-I N_2 isotherms with the N_2 uptake predominantly occurring at a rather low relative pressure range (P/P_0 less than 0.03) (Fig. S4.3), indicating the presence of micropores within the structures. Fig. S4.3 presents the corresponding pore size distribution curves estimated by the non-local DFT model. The average size of the pore diameter is 1.6 nm, which is much smaller than the AuNi NP size (2.89 nm). The precursor metal cations are first introduced inside the ZIF cavity in which they interact with the N atoms of ZIF-8; then they are reduced by $NaBH_4$ [38] to NPs and, given their size, are trapped within the ZIF-8 cavity. Furthermore, after packing the AuNi NPs, the BET surface area decreases from 1787.3 $m^2 \cdot g^{-1}$ to 1011.3 $m^2 \cdot g^{-1}$ (Fig. 4.2b and Table S4.2), due to the presence of AuNi NPs inside ZIF-8, which is consistent with previous reports [14,30]. All the results including those of TEM, significant BET surface decrease and pore width therefore indicate that the AuNi NPs are located inside the ZIF-8 framework.

X-ray Photoelectron Spectroscopy (XPS) shows binding energies of 83.2 eV and 86.8 eV for Au (0) $4f_{7/2}$ and Au (0) $4f_{5/2}$, respectively, and the binding energy of 852.6 and 870.3 eV confirms the presence of metallic Ni (0) in the AuNi@ZIF-8 NPs (Fig. 4.2c and 2d). The binding energy peaks of Au 4f and Ni 2p also show the existence of the Au (I) and Ni (II) ions, attributed to some aerobic oxidation of the AuNi NPs, which has precedents [37,39,40]. The binding energies of Au 4f (83.2 eV and 86.8 eV) of the AuNi alloy are shifted to lower values compared to those (84.0 eV and 87.3 eV) of AuNPs (Fig. S4.4), indicating strong electronic interaction between the Au and Ni atoms. The lower binding energies of Au 4f for AuNi@ZIF-8 demonstrate that Au gains electron density upon alloying with Ni. The Ni 2p signals (852.6 eV and 870.3 eV) of the AuNi alloy are shifted to higher values compared to NiNPs (852.2 eV and 870.1 eV) [14] (Fig. S4.5), suggesting

strong electronic interaction between the Ni and Au atoms and increased positively charged Ni center, which is in accord with a literature report [37]. XPS data after catalysis is discussed comparatively in section 3.4.

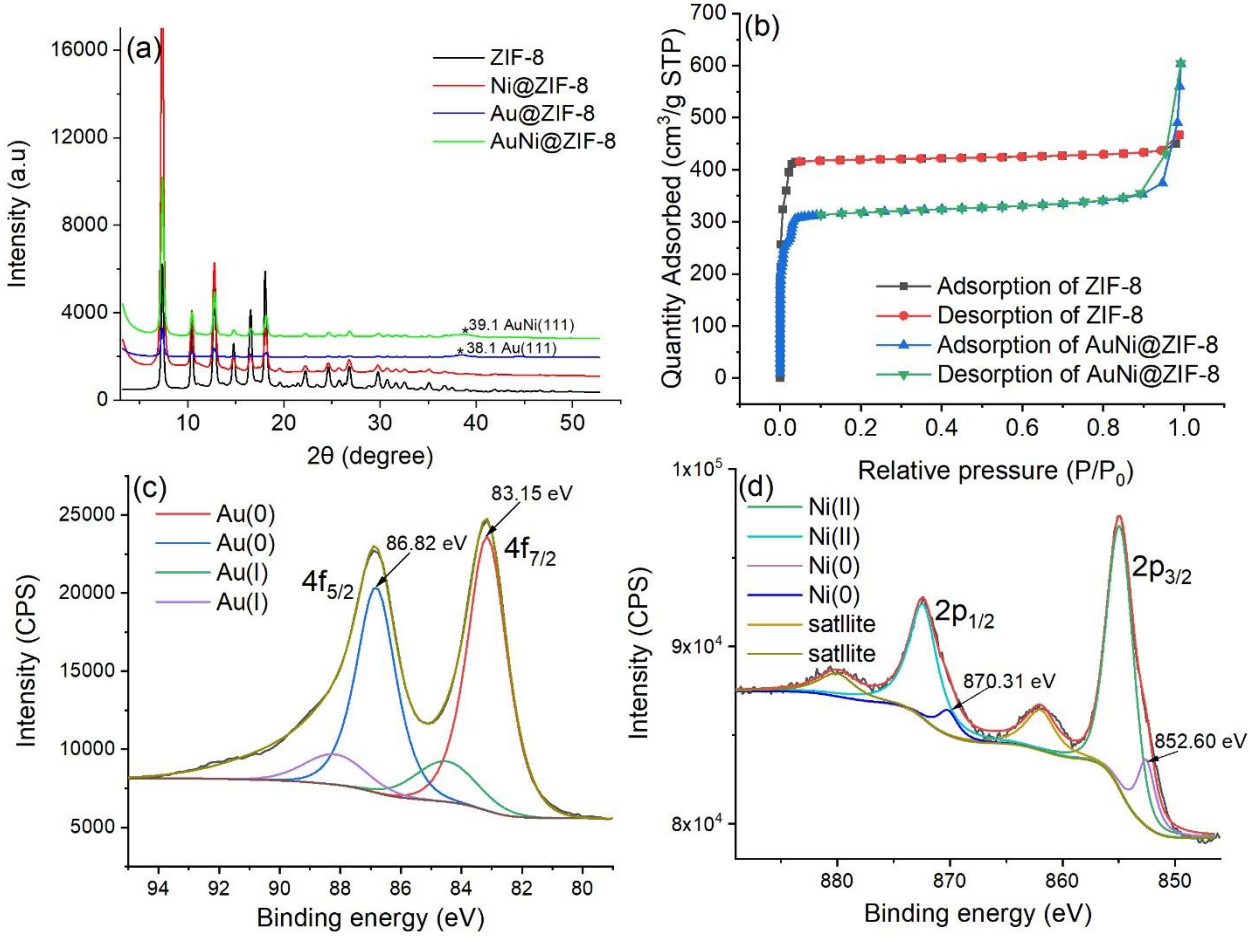

Fig. 4.2. (a) PXRD patterns of the prepared nanocatalysts. (b) Nitrogen adsorption-desorption isotherms of the nanocatalysts on ZIF-8 and AuNi@ZIF-8. (c) XPS spectra of AuNi@ZIF-8 in the Au 4f region, (d) XPS spectra of AuNi@ZIF-8 in the Ni 2p region.

4.2.2. Compared hydrolytic AB dehydrogenation catalyzed by a series of Au-based alloy NPs supported on ZIF-8

Searching for possible positive synergies in these alloyed nanocatalysts , we first chose to combine nanogold with non-noble late transition metals, these metals having priority as cheap, abundant and non-toxic elements. We compared Fe, Co, Ni and Cu which are

modest catalysts for AB hydrolysis. The nanocatalysts $Au_{0.5}Fe_{0.5}$@ZIF-8, $Au_{0.5}Co_{0.5}$@ZIF-8, $Au_{0.5}Ni_{0.5}$@ZIF-8 and $Au_{0.5}Cu_{0.5}$@ZIF-8 were probed immediately after their synthesis for AB hydrolysis. Only $Au_{0.5}Co_{0.5}$@ZIF-8 and $Au_{0.5}Ni_{0.5}$@ZIF-8 catalyzed quantitative H_2 formation with a turnover frequency (TOF) value of 40.0 $mol_{H2}·mol_{cat.}^{-1}·min^{-1}$ and 2.4 $mol_{H2}·mol_{cat.}^{-1}·min^{-1}$, respectively. $Au_{0.5}Fe_{0.5}$@ZIF-8 appears to be the least efficient among the four nanocatalysts. Indeed, after adding $\underline{Au_{0.5}Fe_{0.5}@ZIF\text{-}8}$ into the AB hydrolysis medium, the NPs of $\underline{Au_{0.5}Fe_{0.5}@ZIF\text{-}8}$ aggregated and rapidly precipitated due to their instability. Altogether, the order of catalytic activities found was: $Au_{0.5}Fe_{0.5}$@ZIF-8 < $Au_{0.5}Cu_{0.5}$@ZIF-8 < $Au_{0.5}Co_{0.5}$@ZIF-8 < $Au_{0.5}Ni_{0.5}$@ZIF-8 (Fig. 4.3). For the other catalysts including $Au_{0.5}Cu_{0.5}$@ZIF-8, $Au_{0.5}Co_{0.5}$@ZIF-8 and $\underline{Au_{0.5}Ni_{0.5}@ZIF\text{-}8}$, the catalytic activity depended on the d-band center of the transition metal (Co, Ni and Cu). Indeed, among these three transition metals, Ni (001) showed the smallest d-band center (-1.18 eV) compared to Co (001) and Cu (001) [41]. After alloying with Au, the d-band center of AuNi is also smaller than those of AuCu and AuCo. The upgrading of the d-band center energy level of AuNi indicates that the antibonding energy state rises, leading to stronger binding between alloy surface and the adsorbate species, which means that the adsorption energy between AuNi and AB is stronger than those with AuCo and AuCu [42,43]. Therefore, this is consistent with the catalytic activity following the order: $\underline{Au_{0.5}Ni_{0.5}@ZIF\text{-}8}$ > $\underline{Au_{0.5}Co_{0.5}@ZIF\text{-}8}$ > $\underline{Au_{0.5}Cu_{0.5}@ZIF\text{-}8}$.

Alloying Au with either Co, Fe or Cu did not provide positive synergy in these alloys $Au_{0.5}Co_{0.5}$@ZIF-8, $\underline{Au_{0.5}Fe_{0.5}@ZIF\text{-}8}$, $Au_{0.5}Cu_{0.5}$@ZIF-8, respectively, that were less efficient than the corresponding monometallic catalyst Co@ZIF-8, Fe@ZIF-8 or Cu@ZIF-8 (Fig. 4.3). On the contrary, Fig. 4.3b shows that catalysis of AB hydrolysis proceeds much more efficiently with $Au_{0.5}Ni_{0.5}$@ZIF-8 than with the monometallic catalysts Au@ZIF-8 and Ni@ZIF-8. The TOF value for $Au_{0.5}Ni_{0.5}$@ZIF-8 is 40.0 $mol_{H2}·mol_{cat.}^{-1}·min^{-1}$, which is twice more than that of Ni@ZIF-8 (20 $mol_{H2}·mol_{cat.}^{-1}·min^{-1}$), contrasting with the inefficiency of Au@ZIF-8 that showed almost no catalytic activity for this reaction (only 3.3% mol H_2 evolution in 1 h), and the nil catalytic activity of pristine ZIF-8 (Fig. 4.3a and 4.3b). Here, the size of the NPs Au@ZIF-8, Ni@ZIF-8 and $Au_{0.5}Ni_{0.5}$@ZIF-8 were compared. The results showed that the $Au_{0.5}Ni_{0.5}$@ZIF-8 NPs are smaller than the Ni@ZIF-8 NPs and of size similar to the Au@ZIF-8 NPs, consistent with the higher

catalytic activity of the AuNi@ZIF-8 NPs (Fig. S4.6 and S4.7). These results also show a strongly positive synergistic effect between Au and Ni alloyed in $Au_{0.5}Ni_{0.5}$@ZIF-8, which originates from the strong electronic interaction between these two metals in ZIF-8, these electronic interactions being beneficial to the catalyst performances[19]. As a consequence, a quantitative amount of H_2 evolved in 3 min with the catalyst $Au_{0.5}Ni_{0.5}$@ZIF-8 in the dark, whereas 6 min were needed with Ni@ZIF-8 under identical conditions.

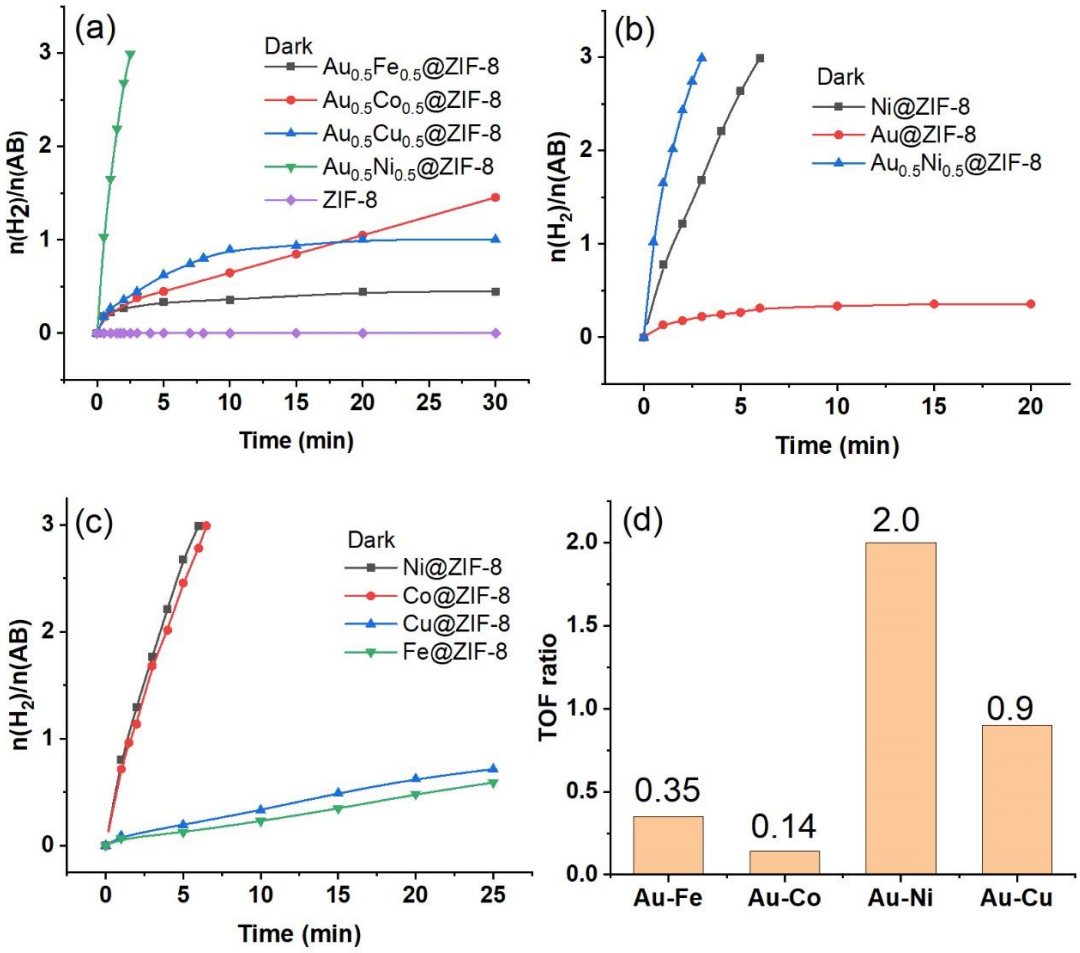

Fig. 4.3. (a) Plot of the molar amount of H_2 generated upon AB hydrolysis vs. time catalyzed by ZIF-8 supported Au-based alloy NPs. (b) Comparison of the catalytic efficiencies among Au@ZIF-8, Ni@ZIF-8 and $Au_{0.5}Ni_{0.5}$@ZIF-8 without visible light irradiation. (c) Plot of the molar amount of H_2 generated upon AB hydrolysis vs. time catalyzed by ZIF-8 supported monometallic NPs. (d) The synergistic effect is defined by

the ratio TOF (alloy NPs)/TOF (monometallic NPs) with the support ZIF-8; when the TOF ratio is >1, it means that there is a positive synergistic effect. Otherwise, there is no synergistic effect. In all the experiments, the reaction conditions are: 1 mmol of AB; 2.5% mmol MNP; temperature: 25 ± 0.5°C.

3.3. Nanomaterial optimization for the catalysis of AB hydrolysis

In order to optimize the performance of the catalyst under dark conditions, the percentages of the two metals in the nanoalloys were varied. As shown in Fig. 4.4a, the efficiencies obtained upon AB hydrolysis were different with various AuNi compositions. Plotting the TOF as a function of the Au content reveals a sharp volcano-type curve appearing between the different alloy compositions, with a maximum for a composition involving equal molar amounts of Au and Ni (TOF_t: 40.0 $mol_{H2}·mol_{cat.}^{-1}·min^{-1}$ and TOF_s: 102.6 $mol_{H2}·mol_{atom}^{-1}·min^{-1}$) (Fig. 4.4b and Table S4.3) [18].

The optimum of catalyst loading was investigated. Specifically, various loading amounts of $Au_{0.5}Ni_{0.5}$@ZIF-8 vs. ZIF-8 (3.7 wt%, 6.9 wt% and 13 wt%) were prepared, and the best performance was obtained with 6.9 wt.% (Fig. S4.8). Furthermore, this Au-Ni nanocatalyst was supported by various other nanomaterials for comparison and optimization. Herein, $Au_{0.5}Ni_{0.5}$@graphene oxide (GO), $Au_{0.5}Ni_{0.5}$@biochar and $Au_{0.5}Ni_{0.5}$@SBA-15 were synthesized using the same method as that used with ZIF-8, the loading being also 6.9%. Fig. 4.4c shows that, among the four stabilizers, the best one is by far ZIF-8 finishing complete hydrolysis of AB with well-dispersed NPs. In contrast, with GO, biochar and SBA-15, the hydrolysis reaction could not be completed due to aggregation during the reactions. These comparisons suggest that ZIF-8 stabilizes and protects the AuNi NPs well from aggregation [41], contrary to the other above supports. Synergistic effects between Au and Ni were observed with all the supports, but the largest one was by far obtained with ZIF-8 as the support, and the TOF ratio between $Au_{0.5}N_{0.5}$i@ZIF-8 and Ni@ZIF-8 reached 2 (Fig. 4.4d). This indicates that ZIF-8 exhibits high selectivity with AuNi NPs for AB hydrolysis among all the supports, and this support exerted a strong synergistic cooperativity involving optimized stereo-electronic interactions, protection and accessibility in its cavity. Thus, altogether the optimized synergy is disclosed among the

three nanocomponents Au, Ni and ZIF-8. This is rationalized as follows. ZIF-8 influences the interaction between Au and Ni by electronic (s) donation from the ZIF-8 imidazole N ligands inside the ZIF cavity that are coordinated to the NP surface. This enrichment of the electronic density at the NP surface enhances the electronic-density-dependent surface Ni sites towards water activation, which is the rate-determining step of AB hydrolysis. Sterically, the role of ZIF-8 as NP support is to protect, by encapsulation, these particles from over aggregation, which is not the case for the other supports.

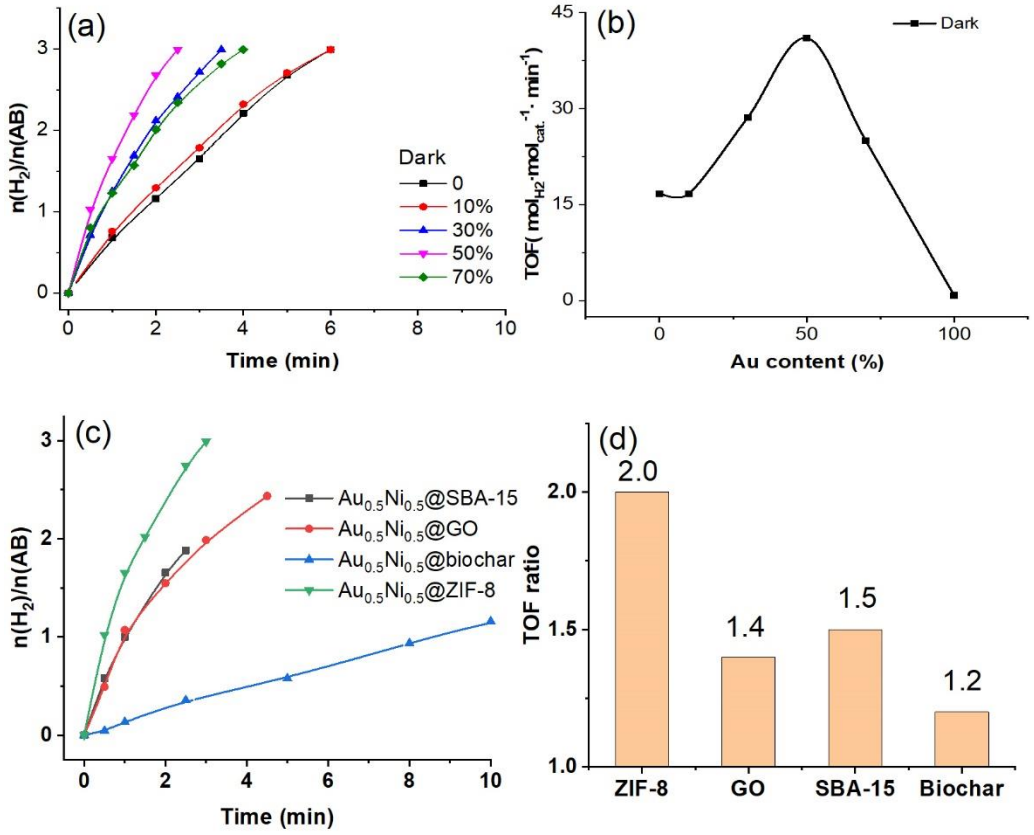

Fig. 4.4. (a) Plot of the molar amount of H_2 generated upon AB hydrolysis vs. time catalyzed by AuNi@ZIF-8 with various ratios of Au and Ni without visible-light irradiation. (b) TOF values with different ratios of Au/Ni without visible-light irradiation. (c) AB hydrolysis catalyzed by AuNi on the various supports without visible light; (d) synergy effect defined by the ratio {TOF(AuNi)/TOF (Ni)}; a ratio > 1 means a positive synergy effect in the dark. In all the experiments, the reaction conditions were: 1 mmol of AB; 2.5% mmol MNP; temperature: 25 ± 0.5°C.

4.2.3 Visible-light-induced acceleration of AuNi@ZIF-8-catalyzed AB hydrolysis

A low-power LED light was employed to irradiate the reaction medium in order to explore the plasmonic effect of the Au-based alloy catalytic NP system upon AB hydrolysis. Compared to the same reactions conducted without visible light irradiation, the efficiencies of all nanocatalyzed AB hydrolysis reactions were enhanced in the presence of visible light. The order of catalytic activity found was $Au_{0.5}Fe_{0.5}$@ZIF-8 < $Au_{0.5}Cu_{0.5}$@ZIF-8 < $Au_{0.5}Co_{0.5}$@ZIF-8 < $Au_{0.5}Ni_{0.5}$@ZIF-8 (Fig. 4.5a).

Impressively, the time for complete AB hydrolysis catalyzed by $Au_{0.5}Ni_{0.5}$@ZIF-8 was reduced from 3 min in the dark to 1 min 45 sec with visible light irradiation (Fig. 4.5b). Table S4.4 shows that the catalytic activity of AuNi@ZIF-8 compares advantageously with those of previously recorded plasmonic metal-based photocatalysts for AB hydrolysis.

It is remarkable that, in comparison, visible light did not exert any beneficial role on AB hydrolysis catalyzed by monometallic Au@ZIF-8 or Ni@ZIF-8. This is indicated by the fact that the reaction rates of AB hydrolysis remain similar in the presence or absence of visible light for both monometallic catalysts in ZIF-8 (Fig. S4.9). In order to understand the light enhancement of the AB hydrolysis reaction rate selectively observed in the presence of the nanocatalyst $Au_{0.5}Ni_{0.5}$@ZIF-8 and not in the presence of monometallic ZIF-8 supported AuNPs or NiNPs, UV-vis. spectra of these three nanocatalysts were recorded (Fig. 4.5c). As a result, both Au@ZIF-8 and $Au_{0.5}Ni_{0.5}$@ZIF-8 show obvious plasmon bands, but the absorption curve of Ni@ZIF-8 is flat. Although the catalytic activity of Au@ZIF-8 is only small in the dark, there is no enhancement upon visible light illumination in the presence of this nanocatalyst. This means that whatever hot electrons are generated on the surface of Au atoms that transfer to other Au surface atoms, Au@ZIF-8 remains a rather inert catalyst for AB hydrolysis even upon plasmonic excitation by visible light. To explore the best ratio between the two metals for the AuNi@ZIF-8 alloys under visible-light irradiation, different compositions of AuNi NPs were used for catalysis of AB hydrolysis. As shown in Fig. 4.5d, the ratio of 1 to 1 underwent the best catalytic activity with a TOF_t of 68.6 $mol_{H2} \cdot mol_{cat.}^{-1} \cdot min^{-1}$ and TOF_s of 175.9 $mol_{H2} \cdot mol_{atom}^{-1} \cdot min^{-1}$ (Fig. 4.5d and Table S4.3). Upon increasing the Au amount in the AuNi alloy, the whole catalytic activity of $Au_{0.5}Ni_{0.5}$@ZIF-8 decreased, because the AuNPs are a rather inert

catalyst upon AB hydrolysis, although the introduction of Au enhances the plasmon of such catalysts. Therefore, the balance of plasmon and catalytic activity is concerned [26].

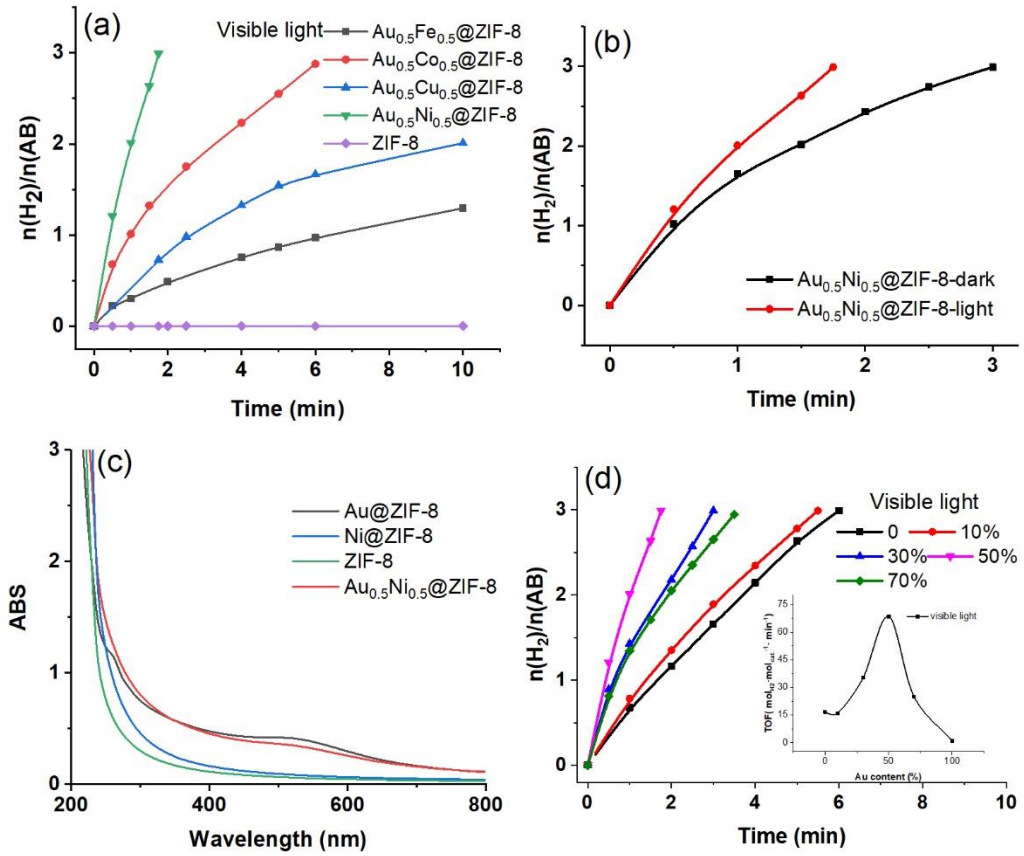

Fig. 4.5. (a) Plot of the molar amount of H_2 generated upon AB hydrolysis vs. time catalyzed by ZIF-8 supported Au-based alloy NPs with visible light irradiation. (b) Comparison of the catalytic efficiencies of $Au_{0.5}Ni_{0.5}$@ZIF-8 under visible light irradiation and dark conditions. (c) UV-vis. spectra of Au@ZIF-8, $Au_{0.5}Ni_{0.5}$@ZIF-8, and Ni@ZIF-8. (d) Plot of the molar amount of H_2 generated upon AB hydrolysis vs. time catalyzed by $Au_{0.5}Ni_{0.5}$@ZIF-8with various ratios of Au and Ni with visible-light irradiation and TOF values with different ratios of Au/Ni with visible-light irradiation. In all the experiments, the reaction conditions were: 1 mmol of AB; 2.5% mmol MNP; temperature: 25 ± 0.5°C.

Under visible-light irradiation, rate enhancement was observed with the Au-Ni alloy only upon employing ZIF-8 as support, whereas light did not accelerate the reaction when GO and biochar were used for that purpose (Fig. S4.10). This is in accord with the fact that the

AuNi alloy rapidly aggregates on other supports such as SBA-15, GO and biochar in the catalytic hydrolysis process. The UV-vis. spectra of all these supported nanocatalysts were recorded, and a plasmon band was observed for $Au_{0.5}Ni_{0.5}$@ZIF-8 ranging from 450 to 620 nm (Fig. S4.11). On the other hand, there were no plasmon band for $Au_{0.5}Ni_{0.5}$@GO or $Au_{0.5}Ni_{0.5}$@biochar. The UV-vis. spectra of the four supports were recorded in order to verify that the Localized Surface Plasmon Resonance (LSPR) comes from the AuNi alloy, i. e. not from the support alone. As shown in Fig. S4.12, all the support UV-vis. curves are flat, confirming that the LSPR is due to the AuNi alloy. However, both $Au_{0.5}Ni_{0.5}$@GO and $Au_{0.5}Ni_{0.5}$@biochar do not show plasmon bands in the UV-vis spectra. This is assigned to the very strong adsorption of GO and biochar (both black powders) in the UV-vis. region (Fig. S4.12), for which any plasmon band would be covered by GO and biochar. In contrast, the plasmon band was observed for $Au_{0.5}Ni_{0.5}$@ZIF-8, i. e. it was not obscured in the suspension (the ZIF-8 solid is white).

However, the support synergistically contributes to the overall LSPR as shown in Fig. 4.5c. One key feature of the plasmonic metal catalysts is that the performance depends on the wavelength of irradiation, since the light wavelength determines the energy of the incoming photons and thus the energy of the photogenerated charge carriers [42]. Thus, to verify the influence exerted by the plasmon-mediated catalyst, the catalytic efficiencies of AB hydrolysis were recorded under 450 nm, 520 nm and 620 nm light irradiation (Fig. S4.13). As a result, the 620 nm light is ineffective, which is shown by the fact that the reaction rate obtained using this light wavelength is the same as that of the reaction under dark conditions. By contrast, 450 nm and 520 nm light illuminations enhance the catalytic AB hydrolysis to some degree, which means that the visible light is only efficient within the range of the plasmon band of AuNi, further confirming the favorable role of the LSPR excitation in the photocatalytic system. The 520-nm light irradiation is more efficient than the 450-nm light in accelerating the hydrolytic dehydrogenation of AB catalyzed by $Au_{0.5}Ni_{0.5}$@ZIF-8. Therefore, photon fluxes at different wavelengths were calculated here following a standard ferrioxalate actinometry for the analysis of the influence of the quantity of photons on photocatalysis [44]. This analysis revealed that the 450-nm irradiation (2.92×10^{-9} einsteins.s^{-1}) possesses a higher photon flux than the 520-nm one (2.34×10^{-9} einsteins·s^{-1}). This shows that irradiation with more photons does not contribute

to increased efficiency, because it is only the light wavelength corresponding to the surface plasmon band of AuNi@ZIF-8 that provides enhanced catalytic efficiency. Indeed, the plasmon band of monometallic Au@ZIF-8 culminates at 530 nm, but upon alloying with Ni, it is broadened and culminates at 520 nm (Fig. 4.6c).

Usually, the plasmon-induced enhancement includes photo thermalization, photo local field and electron density transfer [45,46]. Thus, these three aspects need to be discussed here. The low-energy electrons couple to phonon modes after thermalization, increasing the temperature of the plasmonic metal, which is then dissipated to the environment. Therefore, in order to accurately demonstrate the influence of heating of the reactor itself upon continuous illumination, a temperature probe was placed inside the reaction flask to observe the temperature changes during AB hydrolysis over $Au_{0.5}Ni_{0.5}$@ZIF-8 (25 °C, 7 mW cm^{-1}), and a temperature increase of less than 1°C was observed over 5 min of irradiation (Fig. 4.6a). However, the efficient catalysts allowed delivery of hydrogen in reactions that were completed after only 1.75 to 3 min depending on the system. There was no significant increase in the hydrogen production rate at 26 °C compared to that recorded at 25 °C (Fig. 4.6b). Thus, it is concluded that the photothermal effect has no significant contribution to the visible light induced enhancement of the catalyzed AB dehydrogenation reaction.

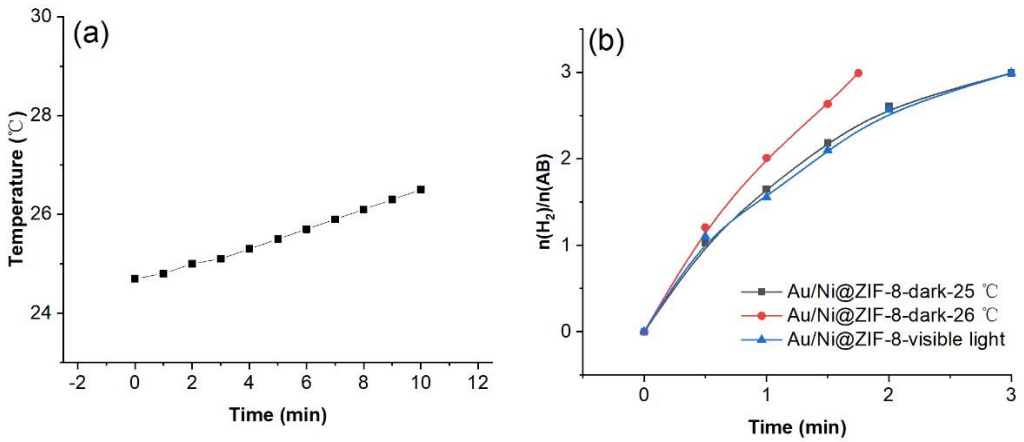

Fig. 4.6. (a) Temperature increase of the catalytic system under visible-light illumination. (b) Catalytic efficiency of AB hydrolysis by AuNi@ZIF-8 under different conditions. Reaction conditions: 1mmol of AB; 1:1 of Au and Ni ratio; 2.5% mmol MNP.

The electric field, induced by the plasmon, is dominated by the local electronic states at the NP interface, and these surface plasmonic fields are beneficial to provide sufficient energy for the activation of some chemical bonds [28]. Moreover, the local electric field decays almost exponentially with the distance away from the NP surface, accompanied by the generation of a gradient force. The stronger field-gradient force is important to capture reactant molecules and polarize the trapping target [47]. Finite Difference Time Domain (FDTD) simulation was employed to calculate the SPR-related local electric fields. The $|E/E_0|^2$ of AuNi is 8.7. The AuNiNP dimers exhibit a stronger near-field distribution compared with a single alloy particle, and $|E/E_0|^2$ reaches up to 37.4 (Fig. S4.14). Thus, the enhanced field confers superior hot electron generation and adsorption of molecular substrates to the alloyed AuNi NPs. Specifically, the stronger molecular adsorption allows the formation of metal-adsorbent complexes (metal-AB...water complexes) [22]. Meanwhile, favorable adsorption of reactants onto metal NPs is important to enhance the catalytic activity. Zheng et al. found that the field enhancement is beneficial to the adsorption between substrates and metal atoms [45]. Similarly, in this case, significant field enhancement of alloyed AuNi NPs enhances the adsorption of the AB...H_2O substrate, accelerating the energy transfer process and thus enhancing the catalytic activity.

The catalyst characterization by TEM and XPS were compared before and after light-accelerated reaction (Figs. 4.7 and S4.15). The TEM images show that the size of the AuNi NPs increased subsequent to light irradiation of the AB hydrolysis reaction medium from 2.89 nm before the reaction to 3.86 nm after reactions (Fig. S4.15). There was just a slight increase of NP size, as NPs tended to aggregate during the reaction, which has been reported in related publications, demonstrating the excellence of ZIF-8 as support [48,49]. Based on the result above, the durability of $\underline{Au_{0.5}Ni_{0.5}}$@ZIF-8 was evaluated. As illustrated in Fig. S4.16, the catalyst $\underline{Au_{0.5}Ni_{0.5}}$@ZIF-8 still showed high hydrogen production activity within 3 cycles. The XPS results show the presence of Au and Ni at the NP surface both before and after the reaction involving visible light irradiation. After the reaction, XPS shows binding energies of 87.2 and 83.5 eV for Au (0) $4f_{7/2}$ and Au (0) $4f_{5/2}$, respectively, and the binding energies of 869.9 and 852.4 eV confirm that the valence state of Ni remains Ni (0) (Fig. 4.7c and 4.7d). Even if the valence state of Au and Ni did not change in the process of AB hydrolysis catalyzed by AuNi@ZIF-8, shifts of binding energy were

observed as follows in the region of Au 4f and Ni 2p. The binding energy of Au 4f at 86.8 and 83.2 eV before reaction shifted after reaction to higher values (87.2 and 83.5 eV) (Fig. 4.7a and 4.7c), indicating that the Au atoms became more positively charged. Correlatively, the Ni 2p (870.3 and 852.6 eV) signals shifted to lower values (869.9 and 852.4 eV) after reaction (Fig. 4.7b and 4.7d), demonstrating that there was an electronic simulation after the photoreaction. These shifts imply that electron density was transferred from Au to Ni during the light irradiation reaction process, and consequently Ni has been electronically enriched at the expense of Au, as indicated by comparison to monometallic Au and Ni NPs [44]. This shows that even if the time scale of the plasmon-induced electron transfer is only of the order of the fs, this electron density shift has some irreversible character after the photoreaction involved in the restructuration.

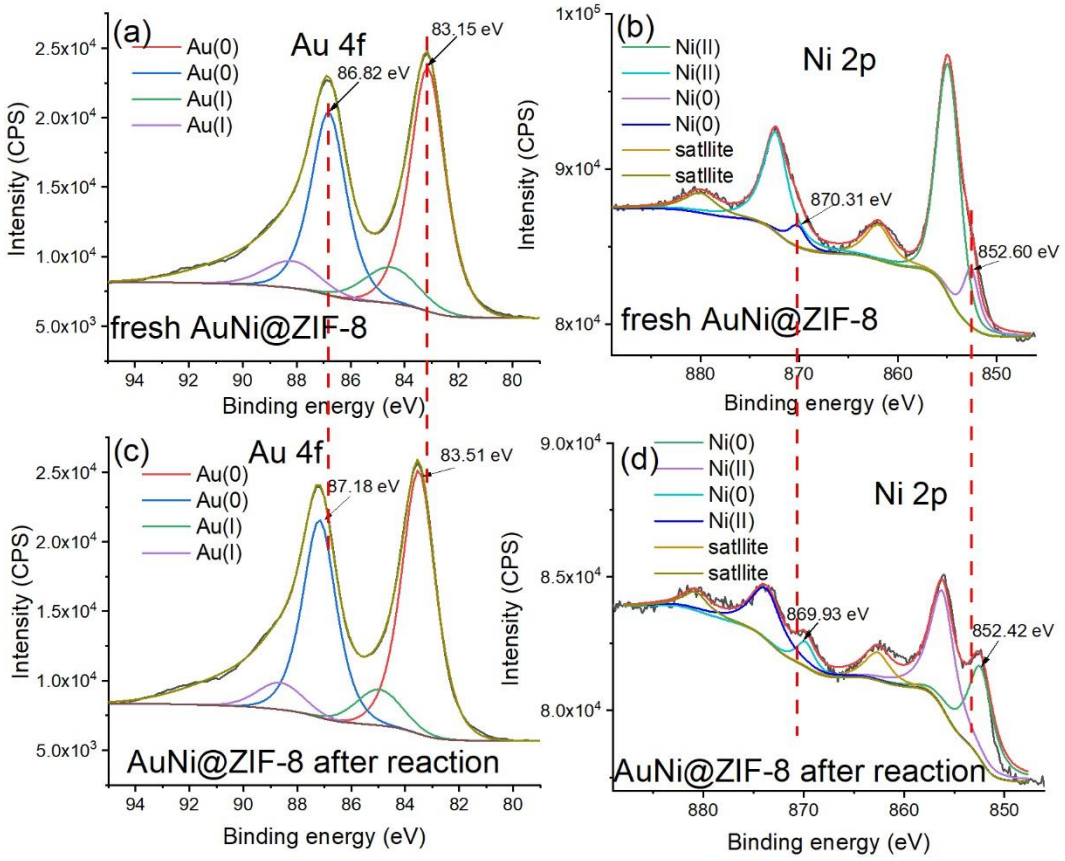

Fig. 4.7. XPS spectra of AuNi@ZIF-8, (a) Au 4f region of AuNi@ZIF-8 before reaction, (b) Ni 2p region of AuNi@ZIF-8 before reaction, (c) Au 4f region of AuNi@ZIF-8 after

reaction, (d) Ni 2p region of AuNi@ZIF-8 after reaction.

Concerning the heterogeneity of the catalyst in the reaction with visible-light irradiation, the electron transfer behavior that occurred between AuNiNPs and ZIF-8 was investigated. Comparison with the photocurrent density of pristine ZIF-8 and $Au_{0.5}Ni_{0.5}$@ZIF-8 during the several on-off cycles of visible light shows flat curves for both $Au_{0.5}Ni_{0.5}$@ZIF-8 and ZIF-8 (Fig. S4.17), and the photocurrent density is near to 0. This is taken into account by the fact that AuNi alloys are encapsulated by ZIF-8 that is an insulator. This indicates that ZIF-8 itself is not responsible for transferring and separating electrons induced by the LSPR of Au NPs, in accord with other reports [50,51]. ZIF-8 without any special treatment and addition is an insulator, i. e. it cannot be excited by visible light due to its high LUMO level, as reported [51]. Therefore, ZIF-8 cannot accept photo-generated electrons from Au NPs. The lack of observation of a photocurrent for $Au_{0.5}Ni_{0.5}$@ZIF-8 also confirmed this.

4.2.4. Kinetic study

The kinetic studies of the reactions were conducted with different dosages of catalyst, AB concentration and temperatures in the dark. The time plots of H_2 production are provided vs. various concentrations of AB with 2.5 mmol % $Au_{0.5}Ni_{0.5}$@ZIF-8 NPs. The reaction time is about 3 min for the different AB concentrations, and the logarithmic plot of H_2 generation rate vs. concentration of AB is shown in Fig. S4.19a. The slope of the curve is 0.07, indicating that hydrolysis of AB catalyzed by $Au_{0.5}Ni_{0.5}$@ZIF-8 nearly follows zero-order kinetics in AB. The slope of the logarithmic plot of H_2 generation vs. concentration of $Au_{0.5}Ni_{0.5}$@ZIF-8 NPs is 1.11 (Fig. S4.19b), leading to the result of a first-order reaction in catalyst concentration. The measurement of the time dependence of H_2 generation at different temperatures is shown in Fig. S4.19c. According to the Arrhenius equation, the activation energy (*E*a) of AB hydrolysis is lower (approximately 37.4± 1.1 kJ/mol) with the catalyst $Au_{0.5}Ni_{0.5}$@ZIF-8 than with the monometallic Ni@ZIF-8 (42.7 kJ/mol) [14], showing that the positive synergy between Au, Ni and ZIF-8 is beneficial in reducing the activation energy.

4.2.5. Mechanistic study

Concerning the reaction mechanism of AB hydrolytic hydrogen release in the dark, several reports have indicated that one of the hydrogen atoms of H_2 comes from AB and the other one from water[30,52]. The kinetic isotope effect (KIE: k_H/k_D) is an effective way to distinguish the rate-determining step (RDS) of a reaction[23,53]. Herein, D_2O was used instead of H_2O involved in the AB hydrolysis catalyzed by $Au_{0.5}Ni_{0.5}$@ZIF-8. With $Au_{0.5}Ni_{0.5}$@ZIF-8 as the catalyst for AB hydrolysis in the dark, the KIE found with D_2O was 4 (Fig. 4.8), which is consistent with earlier studies. This primary KIE with high value leads to the suggestion of water O-H bond cleavage in the RDS[30]. Under visible-light irradiation, this KIE value raised to 4.3 (Fig. 4.8), which further confirms water bond breaking in the RDS, because the electron density on Ni atoms is enriched by the hot electron transmitted from the Au plasmon under visible-light illumination. Visible light boosts the reaction, and the KIE with D_2O should thus be enhanced compared to the KIE of the dark reaction, which was indeed found [26].

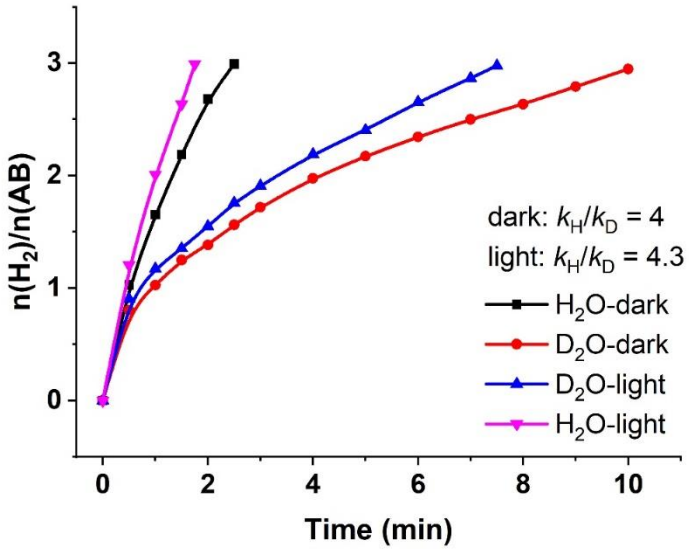

Fig. 4.8. Evolution of H_2 upon AB hydrolysis with H_2O and D_2O catalyzed by $Au_{0.5}Ni_{0.5}$@ZIF-8 under visible light and dark.

In order to track intermediate species, the Fourier-transformed infrared spectra (FT-IR) were recorded for the catalyst $Au_{0.5}Ni_{0.5}$@ZIF-8 to search for details of the hydrolysis

process and the source of hydrogen. First, FT-IR was conducted, and the results are shown in Fig. S4.20. The B-H bonds assigned at 1080 and 1177 cm^{-1} disappeared upon prolonging the reaction time from 0 to 2 min. At the same time, the B-OH and B-O bonds that show peaks located at 1270 and 1324 cm^{-1} gradually appeared, demonstrating that the B–H bonds were cleaved and the B–O bonds were formed during the reaction[23]. Moreover, in order to confirm that one hydrogen atom of H_2 is coming from water in the reaction of Equation 4.1 and the other from AB, hydrogen evolution from AB catalyzed by $Au_{0.5}Ni_{0.5}$@ZIF-8 was conducted in a sealed two-chamber reactor towards hydrogenation of styrene with the same catalyst whose optimization was indicated above (Fig. S4.21). In this hypothesis, HD gas would be generated upon AB hydrolysis catalyzed by $Au_{0.5}Ni_{0.5}$@ZIF-8 with D_2O as the solvent in the left tube and then would be transferred to the right tube in which hydrogenation of styrene proceeds in CD_3OD. The ^1H NMR spectroscopy and gas chromatography-mass spectrometry analyses were used to detect the hydrogenation product in the right tube. The hydrogenation of styrene with generated hydrogen gas was successfully accomplished and was complete (quantitative) after 12 h at 25 °C (Fig. S4.22-S4.23). Using the phenylethane methyl signals in the ^1H NMR spectrum, the total number of H atoms found for the ethyl fragment is 4 because, from the 5 H atoms of this fragment, the fifth H atom being replaced by a D atom. Moreover, the major molecular peak of 107 m/z in the mass spectrum further indicates that one D atom was transferred to styrene producing mono-deuterated phenylethane (Fig. S4.24). These results fully confirm that one of the hydrogen atoms of H_2 comes from AB and the other one from water. Furthermore, this present system shows that $Au_{0.5}Ni_{0.5}$@ZIF-8 is an efficient and versatile catalyst for this reaction.

The confirmation of the nature of the rate-determining step is a key challenge in the hydrogen generation process of AB. DFT calculation was conducted in order to confirm the corresponding mechanism (Fig. 4.9). The DFT calculation results show that the formation of *O-H requires the highest reaction energy barrier both in dark and visible-light conditions for the three nanocatalysts Au@ZIF-8, Ni@ZIF-8 and $Au_{0.5}Ni_{0.5}$@ZIF-8 (Fig. 4.10). This result provides further evidence for the catalytic mechanism. Summarily, oxidative addition of the water O-H bond is the only rate-limiting step in AB hydrolysis for the targeted catalyst (TS2 > TS1). The optimized catalyst also provides an appropriate

active site for the acceleration of the overall reaction via reducing the energy barrier of the RDS under light conditions. Upon visible light irradiation, a plasmonic hot electron is transferred from a gold atom to the excited state of the Ni-adsorbate ensemble, accelerating cleavage of the water **H---O** bond in the NiH---**H---O**H adsorbate by oxidative addition on Ni. Calculation of the Gibbs free energy under light condition, yields, compared to dark reaction, $TS1_{light} < TS1_{dark}$, $TS2_{light} < TS2_{dark}$.

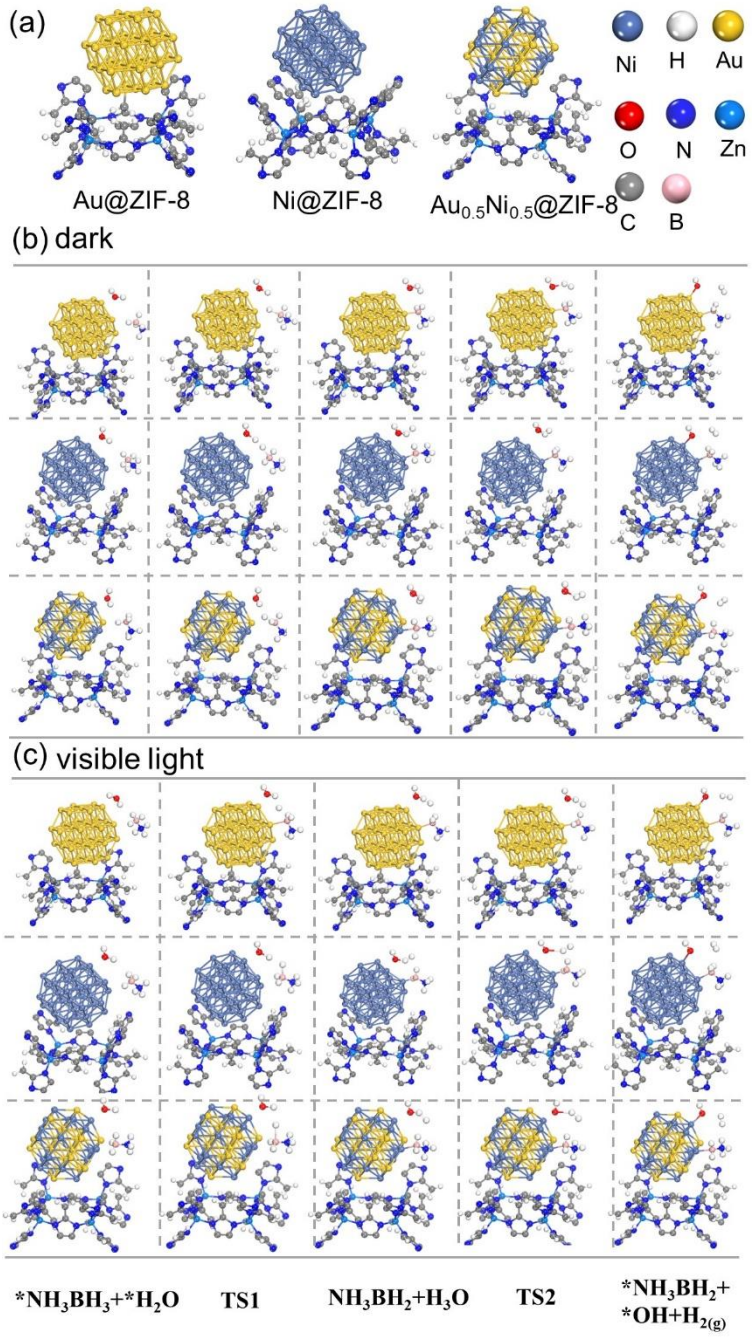

Fig. 4.9. (a) Calculated (DFT) adsorption structures of Au@ZIF-8 (left), Ni@ZIF-8 (middle), and $Au_{0.5}Ni_{0.5}$@ZIF-8 (right). (b) and (c) The 5 calculated intermediate structures for the reactions of NH_3BH_3 and H_2O with the catalysts Au@ZIF-8 (top line), Ni@ZIF-8 (middle line), and $Au_{0.5}Ni_{0.5}$@ZIF-8 (bottom line) (for their energy levels, see Fig 12) (b) under dark conditions; (c) with visible-light irradiation.

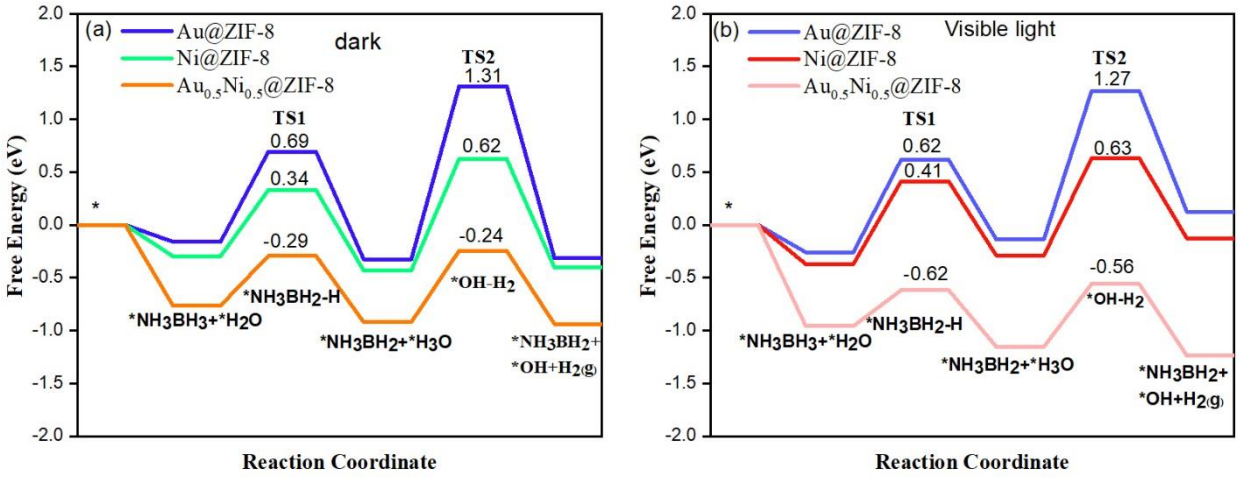

Fig. 4.10. DFT calculation for the free energy of NH_3BH_3 and H_2O along their reaction catalyzed by Au@ZIF-8, Ni@ZIF-8, and $Au_{0.5}Ni_{0.5}$@ZIF-8 alloy, (a) under dark (left) and (b) with visible light excitation (right).

Upon catalysis, AB is expected to transfer a hydride ligand to either a Ni or Au site of the nanoalloy. This hydridic surface ligand is electrostatically bonded to an acidic H atom of water, which brings this water molecule close to the alloy surface towards more facile water O-H bond cleavage than in free water. It has been reported that OH NP surface ligand resulting from water cleavage prefers interacting with Ni(111) to form an ionic bond [54]. On the other hand, the alloy-H atom formed upon water cleavage is a covalent Ni-H bond due to the low oxophilicity of Ni sites on the alloy surface [55].

In the present work, the experiments above have shown the very low catalytic activity of Au@ZIF-8 compared to Ni@ZIF-8, therefore the Au atoms alone are not competitive for this O-H activation step, but the AuNi@ZIF-8 alloy is, forming hydrido and hydroxy surface ligands. Finally, the first hydrido surface ligand formed upon hydride transfer from

AB and the second hydrido ligand formed upon water activation, eventually after "walking" near each other on the surface *via* successive bridging hydride bonds, reductively eliminate to form H_2[56]. (Scheme 4.1). From the XPS data, we know that the Au atoms are accepting charge transfer from Ni, which is only one parameter involved in water activation by the alloyed metals (*vide infra*). With visible-light irradiation, the generated hot electron resulting from the LSPR effect is transferred from Au to the Ni-adsorbate, enhancing electronic density on Ni, the water activation site. Furthermore, the electric field induced by the LSPR of AuNi@ZIF-8 generates energetic charge carriers, which is favorable for the adsorption of the reactants [28]. As a result, the cleavage of O–H bonds from H_2O (RDS) and B–H bonds from AB forming the intermediates M-H bonds and further reductive elimination are boosted by visible light irradiation to release H_2.

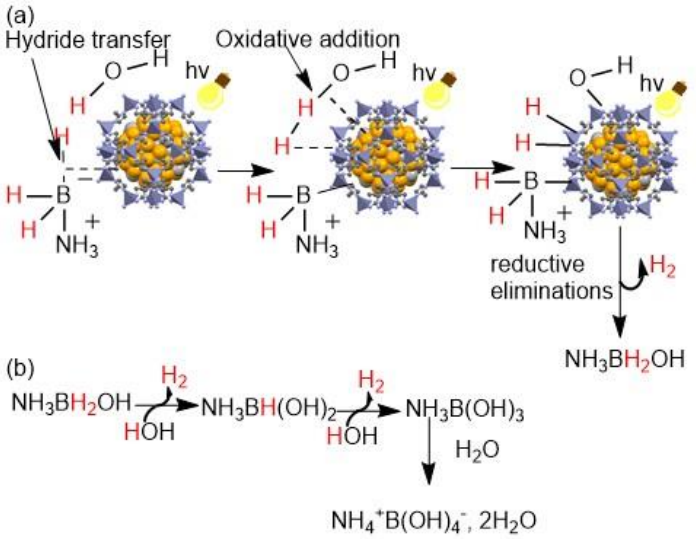

Scheme 4.1. Suggested mechanism for the visible-light-accelerated hydrolytic dehydrogenation of AB nanocatalyzed by $Au_{0.5}Ni_{0.5}$@ZIF-8.

Contrary to H_2 oxidative addition which is common and for instance working well here for styrene hydrogenation, H-OH oxidative addition (besides electroreduction) is a much more energetically demanding process, but it is known with a few mononuclear and binuclear noble-metal organo-bimetallic complexes (Scheme 4.2); case c) more or less mimics surface chemistry, although it is rarely encountered[57]. On the catalyst surface, the water, hydride and hydroxy ligands will likely be bonded in $_2$ or $_3$ fashion to surface atoms.

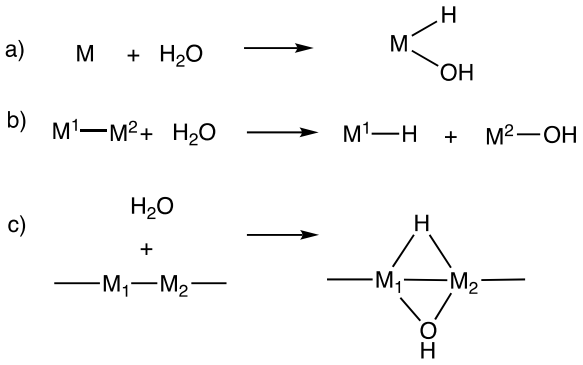

Scheme 4.2. Schematic examples of water activation by noble-metal organometallic complexes (the ancillary ligands are omitted for clarity).

The adsorption energies E_H and E_{OH} play an important role in the activation process. For instance, the adsorption energy E_H is about -1.2 eV on Ni and about 0.2 to 0.4 eV on Au (slightly different depending on the NP size) [58]. In this work, a strongly binding metal and a weakly binding metal are mixed in proportion (1/1) that were optimized for catalytic efficiency. Thus, a medium binding energy is obtained in the Au-Ni alloy (top of the volcano curve, -0.24 eV in the dark; -0.54 eV with visible light, from the present DFT study), and increased performances are indeed often obtained in nanocatalysis using such a strategy mixing a weakly binding and a strongly binding metal, for instance in AB hydrolysis catalyzed by Co-Pt [52] or Ni-Pt [30] alloys (i. e. mixing a late first-row transition metal and a noble metal)[59,60]. Likewise, reports on the simulations of electrochemical water dissociation showed that the activation energy correlated with the OH* adsorption strength [61].

The possible reasons provoking the remarkably positive synergy between two metals in heterobimetallic alloys classically are the electronic effects, the strain effects and the ensemble effect. The electronic effects involve the transfer of electron density between the two metals, resulting in modification of the electronic structure and catalytic activity of the two atoms[62]. The strain effect involves a metallic surface layer, and it also modifies the electronic structure of the atoms by its effect on the width and the center of the d-band[63]. The ensemble effect has an impact on the catalytic activity, because it reflects atomic configurations on the NP surface, and it is essential and also impacts the electronic effects[64]. Concerning the important strain effect, the catalysis optimization shows that

the *d*-band center position, which is related to the binding strength of the metal-adsorbate [65,66], here (AB---H--OH), is close to the Fermi level with the nanocatalyst $Au_{0.5}Ni_{0.5}$ alloy in ZIF-8. The H-bonding between water and the metal hydride resulting from AB hydride transfer to the surface very much facilitates both the water adsorption and the weakening of the H--OH bond, both factors being very favorable for water activation. The ZIF-8 shell also introduces a drastic stereo-electronic factor for the substrate in the confined space between the ZIF-8 and the alloy surface that impacts the strain effect. The experienced sensitivity of the synergy to the nature of the support confirms this hypothesis.

4.3.Conclusion

In conclusion, the novel efficient nanocatalysts, AuNi@ZIF-8 containing the plasmonic AuNi alloy and abundant metal Ni have been optimized and shown here to efficiently catalyze fast AB hydrolysis producing H_2 and other catalytic reactions. This nanocatalyzed H_2 generation upon AB hydrolysis is boosted by the dramatic synergy between nanogold, nanonickel and ZIF-8 already in the dark, and the reaction is still very much accelerated by selective visible-light illumination using the AuNi plasmon. Yet, the light effect is selective, as only the light wavelength corresponding to the plasmon band was shown to be active. Optimization of the support is shown with ZIF-8 which completely overtakes all the other supports in terms of beneficial synergy. Excitation of the Au plasmon upon visible-light illumination induces hot electron transfer from Au to the alloyed metal surface atoms, still activating the reaction, particularly the rate-determining step, water oxidative addition. The previous successful use of Ni@ZIF-8 allowing quantitative H_2 generation in 6 min at 25°C is boosted in this way to reach 1 min 45 sec, which makes this ecofriendly method a very valuable one for convenient transport and quick H_2 generation, and potentially also for many other organic reactions. Such a spectacular activation of a Ni catalyst is all the more valuable for the replacement of palladium with this cheap metal as the price of palladium very recently almost doubled that of gold.

4.4. **Experimental section**

Materials

Potassium gold chloride, nickel chloride, cobalt chloride, ferrous chloride, copper sulfate, sodium borohydride, AB, 2-methylimidazole, zinc nitrate hexahydrate and SBA-15 were

purchased from Sigma-Aldrich. All flasks were washed with aqua regia (HCl: HNO_3 = 3:1) prior to use. All solutions and reagents were prepared using ultrapure water from the Barnstead Nano water purification system (Thermo Fisher Scientific Inc., USA).

Catalyst preparation

The synthesis of ZIF-8 was carried out according to a previous report [14]. Specifically, 2-methylimidazole (0.28 mol, 22.95 g) was dissolved in 80 mL water and stirred at room temperature to form a homogeneous solution. Then, an aqueous solution of zinc nitrate hexahydrate (1.19 g, 4.0×10^{-3} mol) dissolved in 9 mL water was rapidly injected into the above aqueous solution. The mixture was stirred for 1 h, and the product was collected by centrifugation and washed 3 times with water. The obtained solid was then dried at 60 °C *in vacuo* overnight, and the white solids were collected for further use. Graphene oxide (GO) was prepared according to Hummers' method [31]. Biochar was obtained from the calcination of coffee husks as reported in the literature [32]. For the preparation of the nanocatalysts, generally, 100 mg ZIF-8 NPs dispersed in 5 mL water were injected into a 50 mL Schlenk flask under argon. The compositions of the Au-Ni alloyed NPs were adjusted by varying the molar ratios of the precursors. This mixture was stirred continuously at room temperature for 2 h, then degassed with nitrogen for 10 min. After degassing this solution, a 1-mL aqueous solution of freshly prepared $NaBH_4$ (10 equiv. per metal) was quickly added. The mixture was further stirred for another 30 min, and the resulting nanocatalyst was collected by centrifugation and washed with deoxygenated water. Then, it was dried at 60 ℃ *in vacuo* overnight. The metal content of the nanocatalysts was quantified by inductively coupled plasma atomic emission spectroscopy (ICP-AES). For the synthesis of AuMNPs@ZIF-8 and AuNiNPs stabilized by another supports (GO, SBA-15, biochar), the steps were similar to those used for the synthesis of AuNi@ZIF-8 (see SI). For characterization methods and parameters, see SI.

Catalysis of the hydrolytic dehydrogenation of AB by AuNi@ZIF-8 in the dark

Under dark reaction conditions, the hydrolysis of AB was conducted in a 50-mL Schlenk flask at 25 ± 0.2 °C. Specifically, 50 mg of the catalyst AuNi@ZIF-8 was added to a flask with 4 mL water, then 1 mL of the aqueous solution of AB was added to the solution. The reaction time and determination of the volume of H_2 produced began when the AB solution

was imported by a needle. In the standard treatment, the content of AuNi@ZIF-8 was 2.5% mmol, corresponding to a loading amount of AuNiNPs of 6.9%wt. The ratio between Au and the second metal (Fe, Co, Ni or Cu) was 1 to 1, and the amount of AB was 1 mmol.

Catalysis of hydrolytic dehydrogenation of AB by AuNi@ZIF-8 under visible-light irradiation

The photocatalytic reactions were performed by using 7-W visible LED strips (Sunshine Lighting Limited, France) at a light intensity of 1540 lx (each) with 520 nm light. The LED lamps were turned on for 15 min prior to irradiation to guarantee a stable light intensity. All the reactions under visible light were conducted with condensate circulation in order to keep the temperature at 25 ± 0.2 ℃. The thermometer was placed inside the reaction cell. The dosage of catalyst and AB concentration were the same as in dark reactions, and the other steps were also kept the same as for the reactions under dark.

Hydrogenation of styrene catalyzed by AuNi@ZIF-8 using AB hydrolysis as the H_2 source

A sealed two-chamber device with two stirring bars was prepared. AB (1.0 mmol, 30.87 mg) and $Au_{0.5}Ni_{0.5}$@ZIF-8 (50 mg, 2.5% mmol per AB) were added into the left tube; the nanocatalyst $Au_{0.5}Ni_{0.5}$@ZIF-8 (20 mg, 1 mmol % *per* mmol styrene) and styrene (0.5 mmol, 52 mg) in 2 mL CD_3OD were added into the right tube. After removing air *in vacuo*, the system was settled in an oil bath at 50 °C, and the mixture was stirred for 12 h. Then, the reaction solution in the right tube was collected by filtration for ^1H NMR and GC-MS analysis without any further treatment.

DFT calculations

The DFT methods are known to furnish an acceptable compromise between accuracy and applicability in large cell systems. Therefore, the ZIF-8 models have been simplified for ZIF-8 complex structures. Ni@ZIF-8, Au@ZIF-8 and AuNi@ZIF-8 have been established with the simplified ZIF-8 and 38 metal cluster atoms (Ni cluster, Au cluster and alloyed AuNi models). All spin-polarized calculations based on density functional theory (DFT) were performed utilizing DMol3 package [33]. The generalized gradient approximation (GGA) in the Perdew–Burke–Ernzerhof form and Semicore Pseudopotential method (DSPP) with the double numerical basis sets plus the polarization functional (DNP) were adopted [34]. The electronic properties, including density of states, electron density,

orbitals and population analysis, in dye free form, have been studied. The double numerical basis set DNP has been used to predict dye electronic properties. In order to simplify the calculation, it has been considered that under the condition of illumination, the electrons of the structure are excited. Therefore, the excited state for structure has been adopted to simulate the light effect. The photon energy of the wavelength of light used in the experiment is sufficient to reach the first excited states of Ni and Au. Thus, the Singlet option with 1st excited state has been chosen (operating options, Fig. S4.1). In addition, a DFT-D correction with Grimme scheme was used to account for the dispersion interaction [35]. The SCF convergence for each electronic energy was set as 1.0×10^{-5} Ha, and the geometry optimization convergence criteria were set up as follows: 1.0×10^{-5} Ha for energy, 0.001 Ha $Å^{-1}$ for force, and 0.01 Å for displacement, respectively. Energy barriers were examined by linear and quadratic synchronous transit methods in combination with the conjugated gradient (CG) refinement. The free energies were obtained by G=Etotal+EZPE-TS, where Etotal, EZPE and TS are the ground-state energy, zero-point energies, and entropy terms, respectively, with the latter two taking vibration frequencies from DFT. Finally, the reaction energies (G) of different intermediates are defined as ΔG=Gi-Greactant (Gi is the energy of intermediates and Greactant is the total energy of reactants).

-**Transmission Electron Microscopy (TEM)** and **high-resolution TEM (HRTEM)** were recorded using TEM JEOL JEM 1400 (120 kV)- 2100F.

-**Energy-dispersive X-ray Spectroscopy (EDS)** images were recorded using TEM-JEM-ARM200F Cold FEG equipped with an EDX spectrometer.

-**X-ray photoelectron spectra (XPS) System**: SPECS SAGE HR, X-Ray source: Mg Kα non-monochromatic, operated at 12.5 kV and 250 W. Take-off angle 90°, at ~10^{-8} Torr. Pass energy for survey spectra 30 eV, 15 eV for narrow scans. Analysis: spectra are calibrated to CC carbon 285 eV. Analysis consisted of Shirley background subtraction. Peaks are fitted with symmetrical Gaussian-Lorentzian (GL) line shapes. Samples were dispersed on a silica substrate, and its solvent was evaporated prior to measurement.

-**NMR spectra** were recorded at 25 °C with a Bruker AC 300, or 400 (300 or 400 MHz). All the chemical shifts are reported in parts per million (δ, ppm) with reference to Me_4Si for the 1H NMR spectra

-**Inductively coupled plasma atomic emission spectroscopy (ICP-AES)**: Thermo

Scientific iCAP 6300 DUO spectrometer with a 3-channel, 12-roller pump and a 27.12 MHz solid state RF plasma generator.

- **Brunauer-Emmet-Teller (BET)** areas were recorded with a 30% v/v N_2/He flow using pure N_2 (99.9%) as the internal standard. At least 2 cycles of N_2 adsorption-desorption in the flow mode were employed to determine total surface area using the standard single point method.

-**Gas Chromatography-Mass Spectrometer (GC-MS)** was performed by the CESAMO on a Thermo Trace GC ultra-gas chromatograph coupled to a Thermo ISQ mass detector.

-**Photoluminescence (PL)** characterization was conducted on a Jobin Yvon Fluorolog3-21 spectrophotometer at an excitation wavelength of 380 nm.

- **Photocurrent** was measured by AutoLab 302N Electrochemical System in 0.5 M Na_2SO_4 solution with Ag/AgCl (0.5 M Na_2SO_4) as the reference electrode and the Pt plate as the counter electrode.

- The **Fourier-transformed infrared spectra (FT-IR)** were obtained on a PerkinElmer 100 FT-IR spectrometer using the KBr tableting technique.

-**Finite-Difference-Time-Domain (FDTD**) calculations were performed by using Comsol Multiphysics 5.6 (COMSOL, Inc.) with perfectly matched layers (PML) boundary conditions. For these simulations, a total-field scattered-field (TFSF) light source with wavelength ranges from 300 nm to 700 nm was used. The optical constant (n) of the AuNi@ZIF was according to the literature [S1]. The size of the alloy and nanoparticle spacing were measured via TEM maps.

H_2 detection. The reaction flask was connected by the gas outlet to a water-filled gas burette. When the gas was generated, the volume of gas evolved was determined periodically by measuring the displacement of water in the burette. In our two cases, 1 mmol AB produced to 67 mL H_2 corresponding to 3 mmol H_2 at atmospheric pressure. Prior to the reactions, the volumes were measured at atmospheric pressure and corrected for water vapor pressure at room temperature. Every reaction has been conducted three times, and the results are averaged.

NH_3 gas detection. The gas generated from the hydrolysis was passed through a 25 mL standard HCl solution (0.01 M) at room temperature, by which the ammonia gas was captured. After gas generation ceased, the resulting solution was titrated with standard NaOH solution (0.01 M) using the acid-base indicator phenolphthalein. The quantity of the liberated ammonia gas was calculated from the difference between two HCl solutions before and after the reaction.

TOF Calculation; TOF = $mol_{H2\ released}$/(total $mol_{cat.}$ × reaction time (min))

TOF_s: the TOF value is related to the NP surface atoms number (Ns)

$V_{NP} = NV_{atom}$ (eq. 1)

$4/3\pi(R_{NP})^3 = N\ 4/3\pi(R_{atom})^3$ (eq. 2)

Where V is the atom volume of the NP, R is the atomic radius of the NP, and N is the total number of atoms within the NP. Rearranging, we obtain:

$N = (R_NP/R_{atom})^3$ (eq. 3)

Knowing the NP radius, we can also calculate the surface area (S) of a NP with the following equation:

$S_{NP} = 4\pi(R_{NP})^2$ (eq. 4)

So, we may also calculate the number of surface atoms (Ns) directly by dividing the surface area of the NP by the cross section of an individual NP atom and then simplifying using the relationship in (eq. 3):

$N_s = (4\pi(R_{NP})2) / (\pi\ (R_{atom})2) = 4\ N\ (R_{atom}/R_{NP})$ (eq. 5)

The ratio of the $N_s/N = 4\ (R_{atom}/R_{NP})$

So $TOF_s = TOF/(N_s/N)$

Schematic illustration of visible light excitation inducing plasmonic hot electron transfer

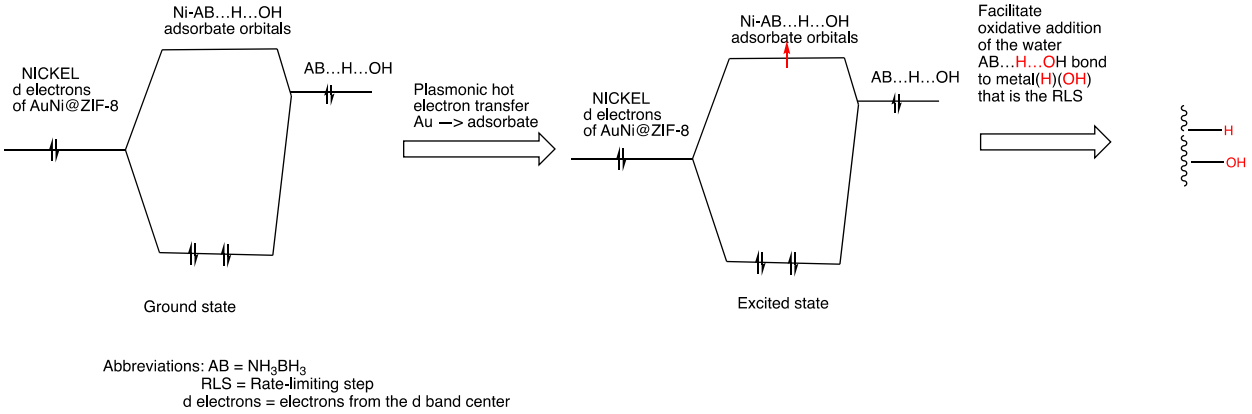

Fig. S4.1. The process of visible light excitation.

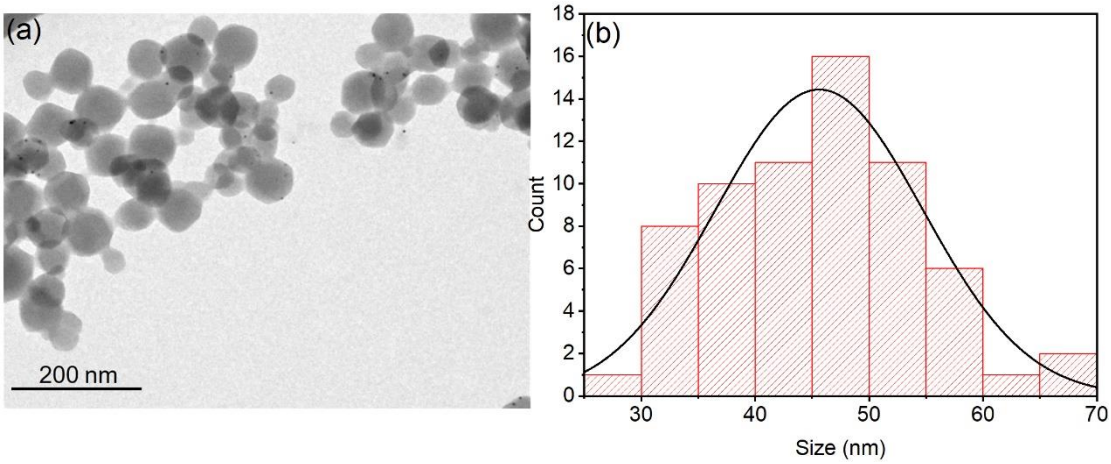

Fig. S4.2. (a) TEM image and (b) size distribution of the ZIF-8.

Table S4.1. Metal loading and atomic ratios of a series of catalysts measured by ICP-AES

Catalysts	Metal loading (wt%)	Atomic ratios
Au@ZIF-8	9.7	-
$Au_{0.7}Ni_{0.3}$@ZIF-8	7.3	1.8:1
$Au_{0.5}Ni_{0.5}$@ZIF-8	6.9	1.1:1
$Au_{0.3}Ni_{0.7}$@ZIF-8	4.1	1:2.2
$Au_{0.1}Ni_{0.9}$@ZIF-8	4.7	1:10
Ni@ZIF-8	2.8	-
Fe@ZIF-8	2.4	-
Co@ZIF-8	2.6	-
Cu@ZIF-8	2.7	-
$Au_{0.5}Fe_{0.5}$@ZIF-8	6.3	1.2:1
$Au_{0.5}Co_{0.5}$@ZIF-8	6.0	1.1:1
$Au_{0.5}Cu_{0.5}$@ZIF-8	5.2	0.9:1

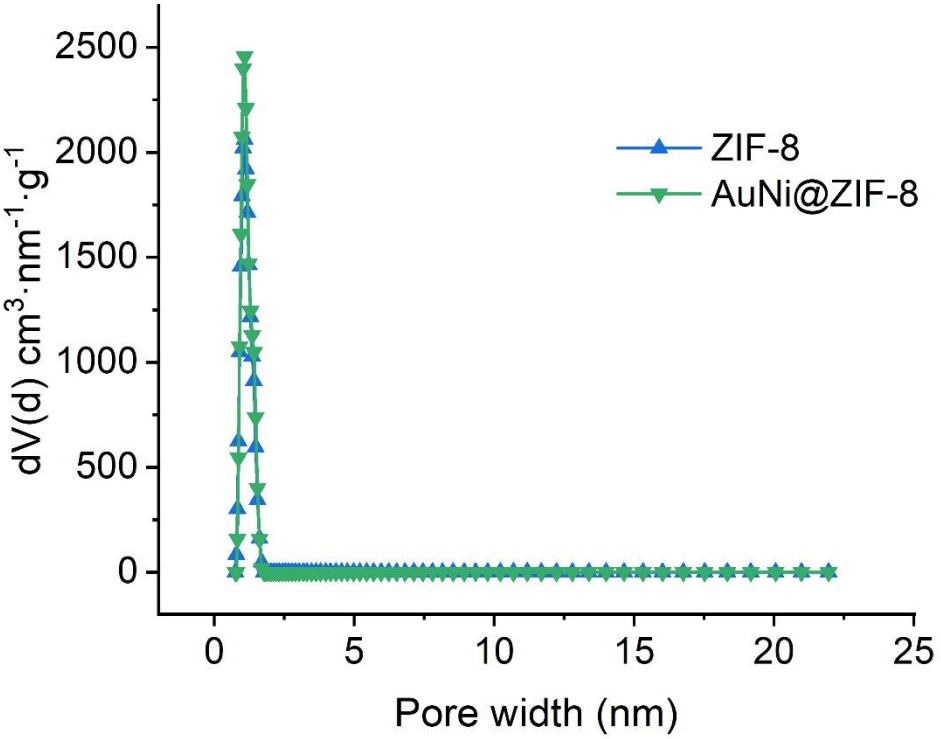

Fig. S4.3. Pore size distribution curves of ZIF-8 and AuNi@ZIF-8.

Table S4.2. Physical Properties of the Nanocatalysts on ZIF-8.

Sample	BET surface area ($m^2 \cdot g^{-1}$)	Pore width (nm)	Pore volume ($cm^3 \cdot g^{-1}$)
ZIF-8	1787.3	1.6	0.6614
AuNi@ZIF-8	1,011.3	1.7	0.6710

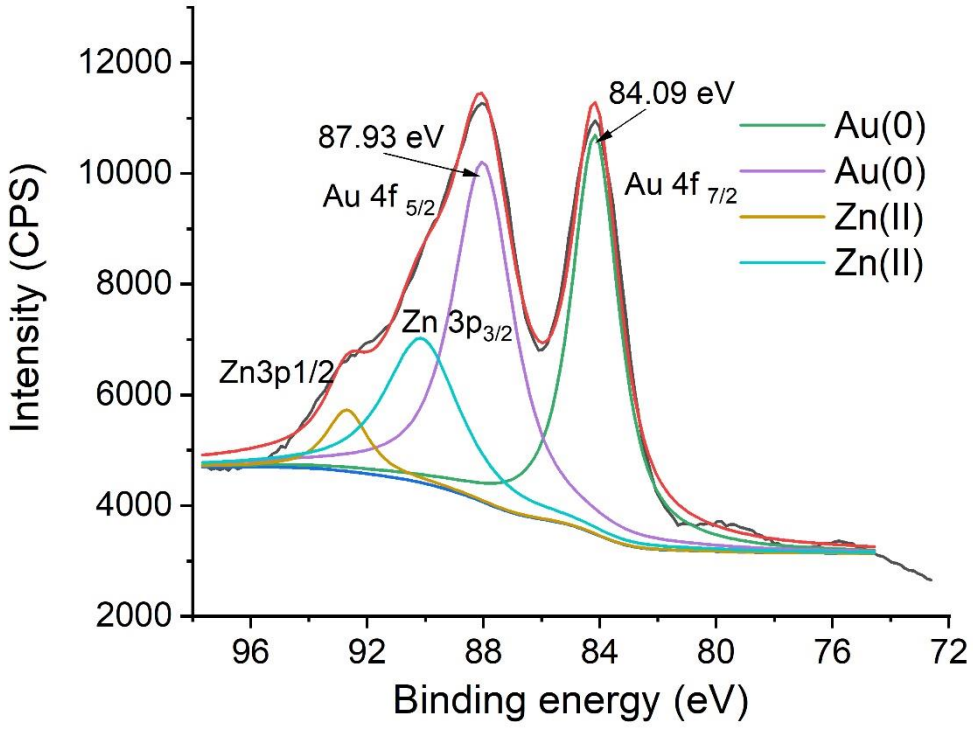

Fig. S4.4. XPS spectra of Au 4f in Ni@ZIF-8

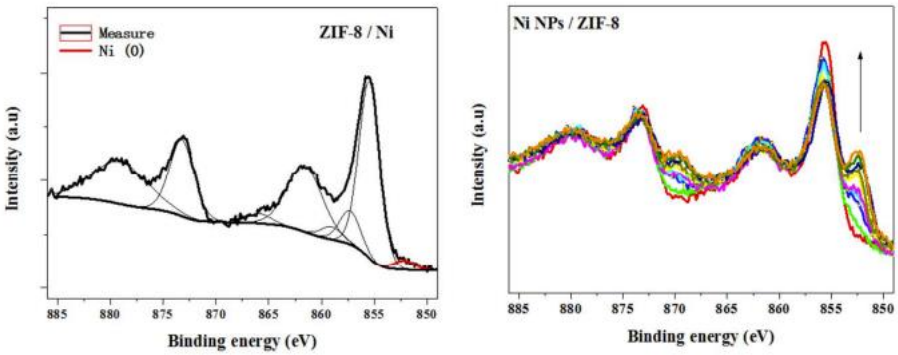

Fig. S4.5. XPS spectra of Ni 2p in Ni@ZIF-8 nanocatalyst.[2]

The analysis of the composition in the peak of Ni shows the presence of Ni in the zero-oxidation state without any Ar sputtering, although a small quantity is enough to insure the presence of Ni0 (left). On the other hand, upon Ar sputtering in the different depths,

the binding energy at 852.2 and 870.1 eV are detected for the $2p_{3/2}$ and $2p_{1/2}$ levels (right), respectively, of metallic Ni.[S2]

Table S4.3. Physical properties and TOF values

AuNi@ZIF-8	R_{atom} (nm)	R_{NP} (nm)	Ns/N[a] (nm)	TOF[b]	TOF_s[c]
Dark	0.14	1.44	0.39	40	102.6
Light	0.14	1.44	0.39	68.6	175.9

[a] Ns/N = Number of surface atoms / Number of total atoms; [b] TOF= mol*H2* released / (total mol*catalyst* × reaction time*(min)*); [c] TOF_s = TOF / (N_s/N)

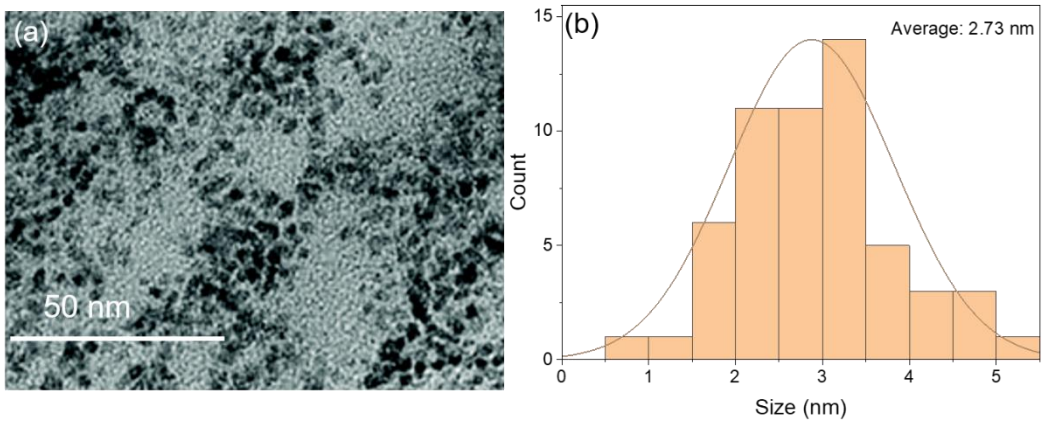

Fig. S4.6 (a) TEM image and (b) size distributions of the Au NPs after digestion of nanocatalysts with EDTA, and nanoparticles capping with PVP.

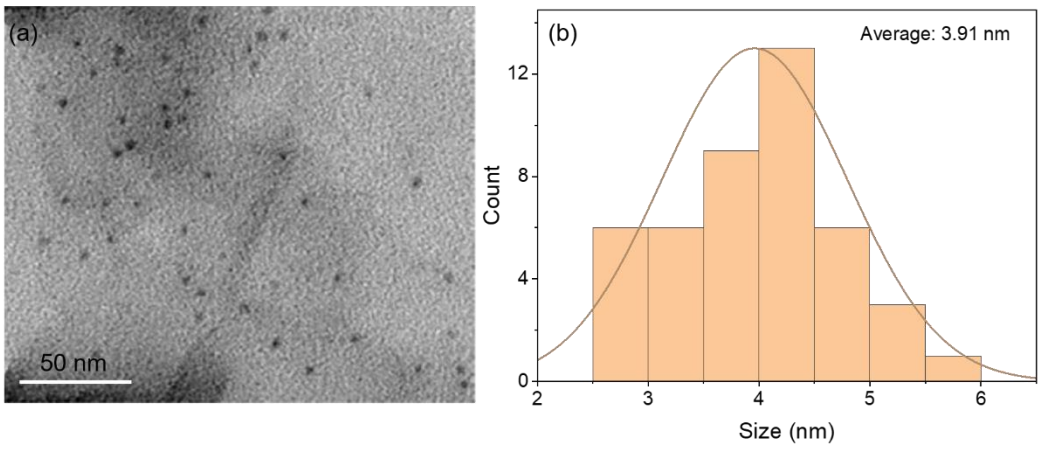

Fig. S4.7 (a) TEM image and (b) size distributions of the Ni NPs after digestion of nanocatalysts with EDTA, and nanoparticles capping with PVP.

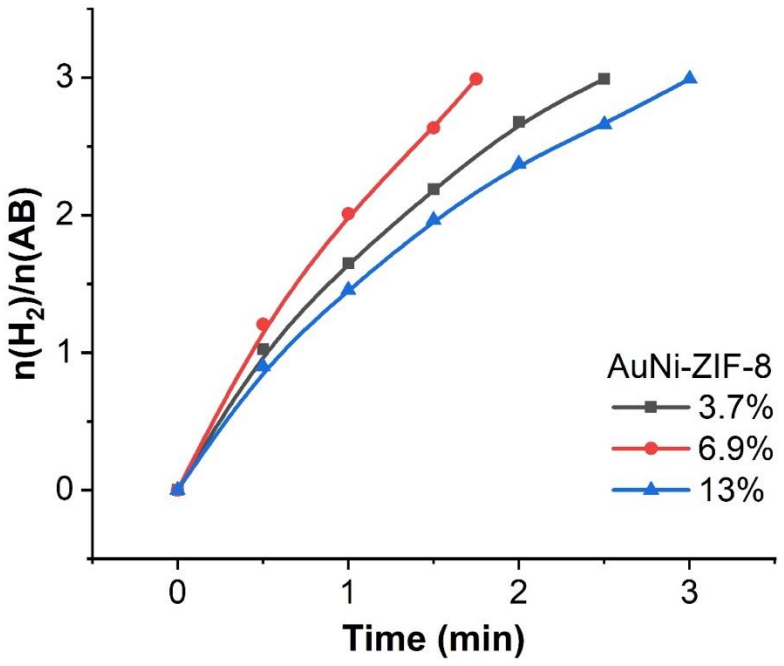

Fig. S4.8. Plot for molar amount of H_2 generated from AB hydrolysis vs. time taken by different ZIF-8-stabilized Au-base bimetallic catalysts with different AuNi loading under visible light.

Table S4.4. Catalytic activity of the reported plasmonic metal-based catalysts for AB hydrolysis with visible light. Semiconductor-based bimetallic nano catalysts show very slow reactions.

Catalysts	Catalyst/AB molar ratio	Temperature (°C)	Light Intensity (W)	Light enhancement	Recycling time	Average rate ($mmol_{H2} \cdot h^{-1}$)	Reference
AuRh@polymer	0.2%	20	/	/	/	8.84	[3]
Pt/Ag-SBA15	1.25%	25	350	1.5	/	1.24	[4]
Au/Pd core-shell	<1%	25	500	3	3	10.8	[5]
Au/Pd@MIL101	3%	30	500	1.6	/	1.09	[6]
Au/TiO_2	2.5%	25	500	2	/	2.2×10^{-5}	[7]
Au/Co@CN	2%	25	150	2	/	93.6	[8]
$Cu_{0.4}Ag_{0.5}$	/<1%	25	300	3.9	/	0.1	[9]
NiCu/CN	/	25	300	3.5	5	30.9	[10]
$Au_{0.5}Ni_{0.5}$@ZIF-8	2.5%	25	7	1.7	3	102.8	This work

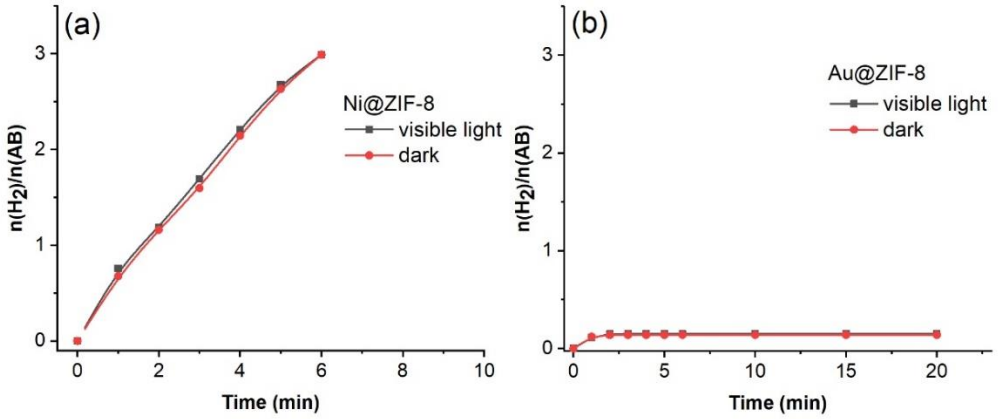

Fig. S4.9. (a) Plot for molar amount of H_2 generated from AB hydrolysis vs. time taken by ZIF-8-stabilized NiNPs with visible light and without visible light irradiation. (b) Plot for molar amount of H_2 generated from AB hydrolysis vs. time taken by ZIF-8-stabilized AuNPs with visible light and without visible light irradiation. Reaction conditions: 1mmol of AB; 2.5% mmol MNP; temperature: 25 ± 0.5°C

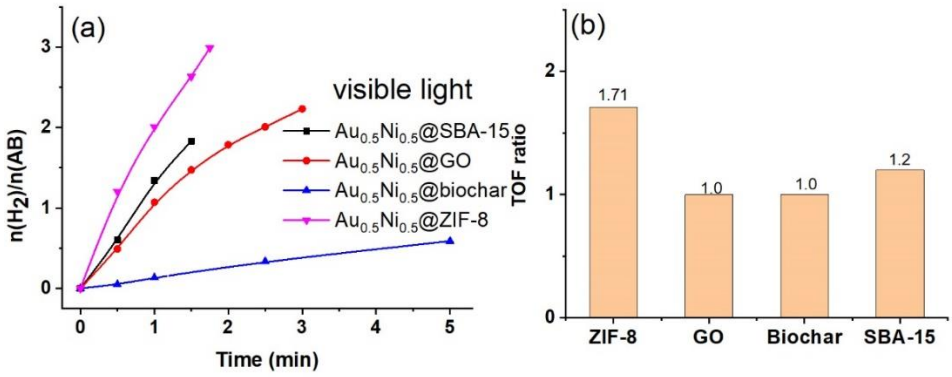

Fig. S4.10. (a) TOF values with different ratios of Au/Ni in the presence of visible-light irradiation. (b) plasmonic effect defined by the ratio TOF (visible light)/TOF (dark); when the ratio is > 1, it means that there is a plasmonic effect. In all the experiments, the reaction conditions were: 1 mmol of AB; 2.5% mmol MNP; temperature: 25 ± 0.5°C. With GO and biochar, the light effect is nil.

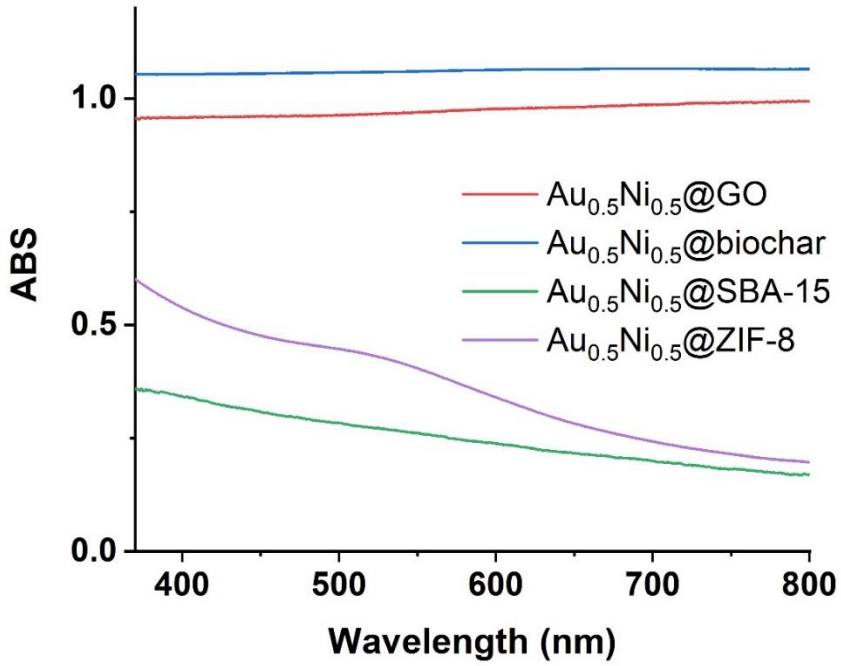

Fig. S4.11. UV-vis. spectra of AuNi NPs supported on ZIF-8, GO and biochar, respectively.

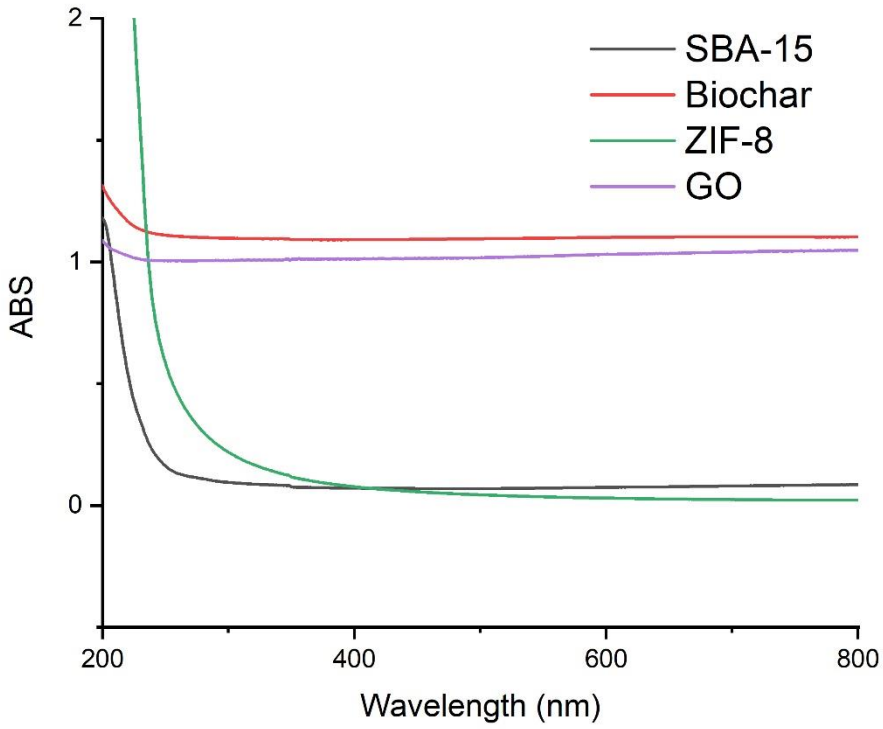

Fig. S4.12. UV-vis spectra of SBA-15, biochar, ZIF-8 and GO

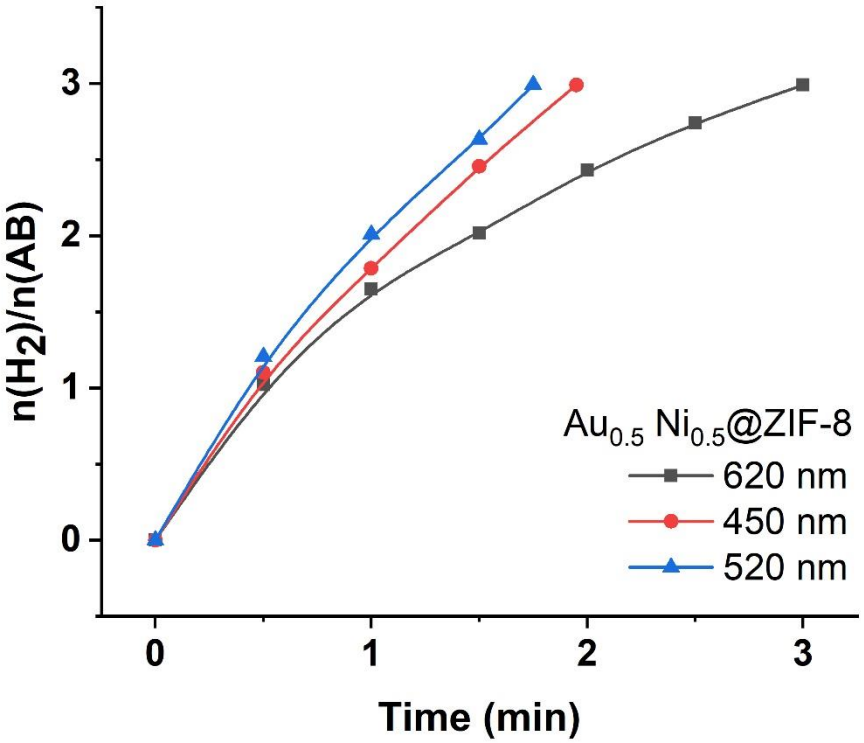

Fig. S4.13. AB hydrolysis catalyzed by $Au_{0.5}Ni_{0.5}$@ZIF-8 under visible-light irradiation with different wavelengths.

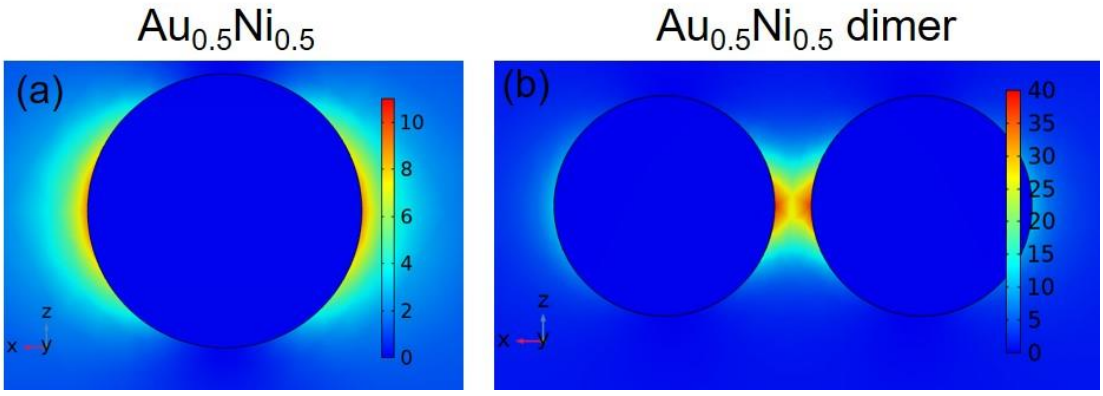

Fig. S4.14. Spatial distribution of the SPR-induced enhancement of electric field intensity from FDTD simulation calculated at the plasmon peak for $Au_{0.5}Ni_{0.5}$ and $Au_{0.5}Ni_{0.5}$ dimer.

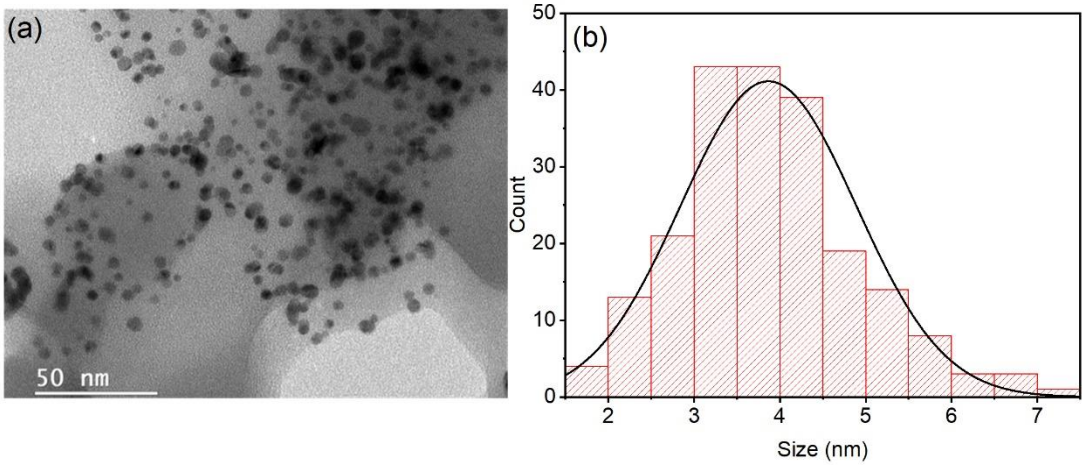

Fig. S4.15. (a) TEM image and (b) size distribution of the AuNi@ZIF-8 after reaction.

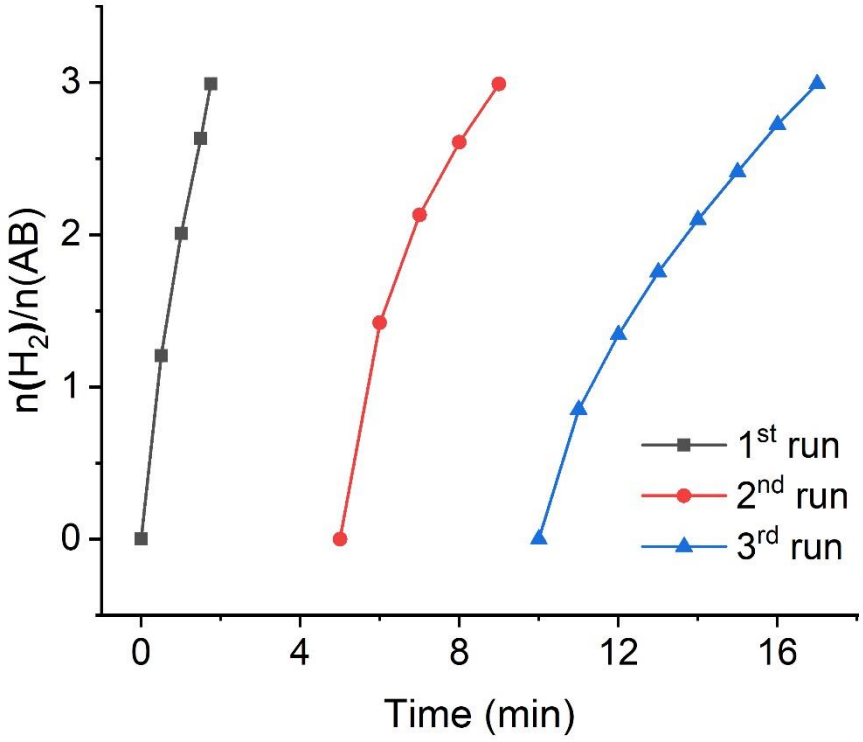

Fig. S4.16. Time plots of H_2 evolution for AB hydrolysis catalyzed by $Au_{0.5}Ni_{0.5}$@ZIF-8 in the first, second, and third recycling tests with visible light irradiation.

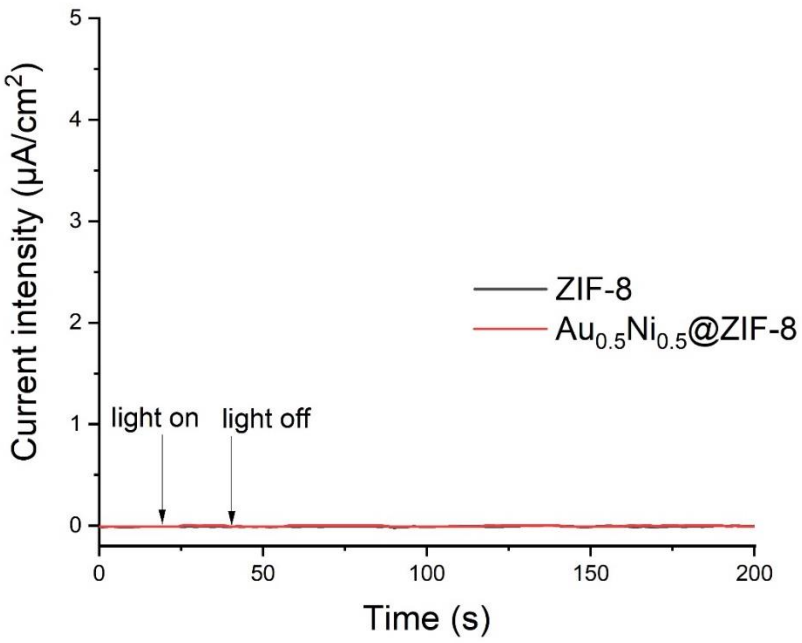

Fig. S4.17. Transient photocurrent responses under open-circuit potential and periodic visible light (20s) irradiation for ZIF-8 and $Au_{0.5}Ni_{0.5}$@ZIF-8.

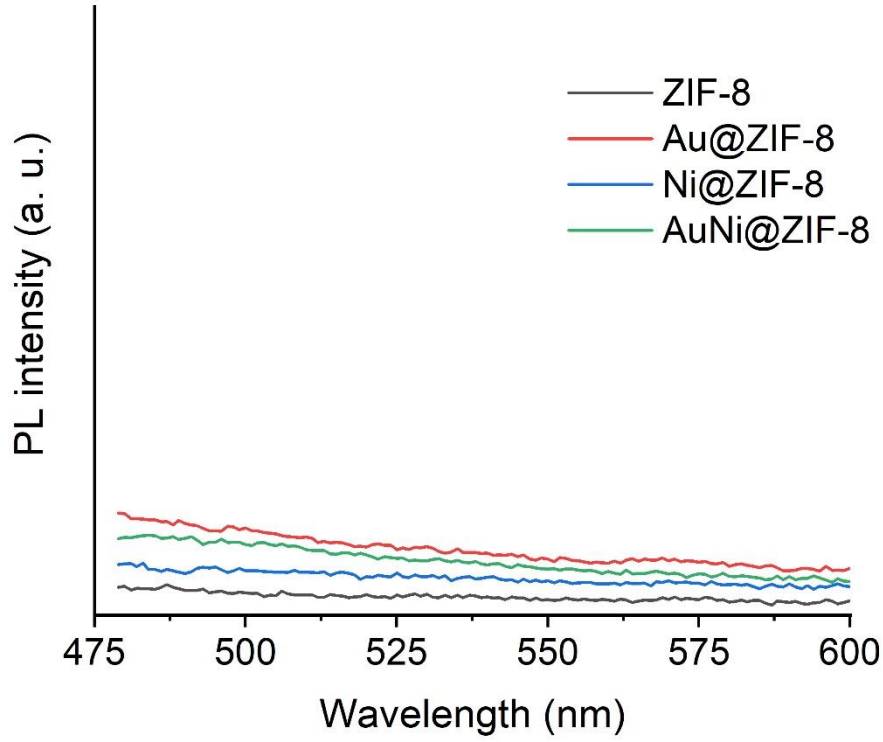

Fig. S4.18. Photoluminescence (PL) spectra of different catalysts.

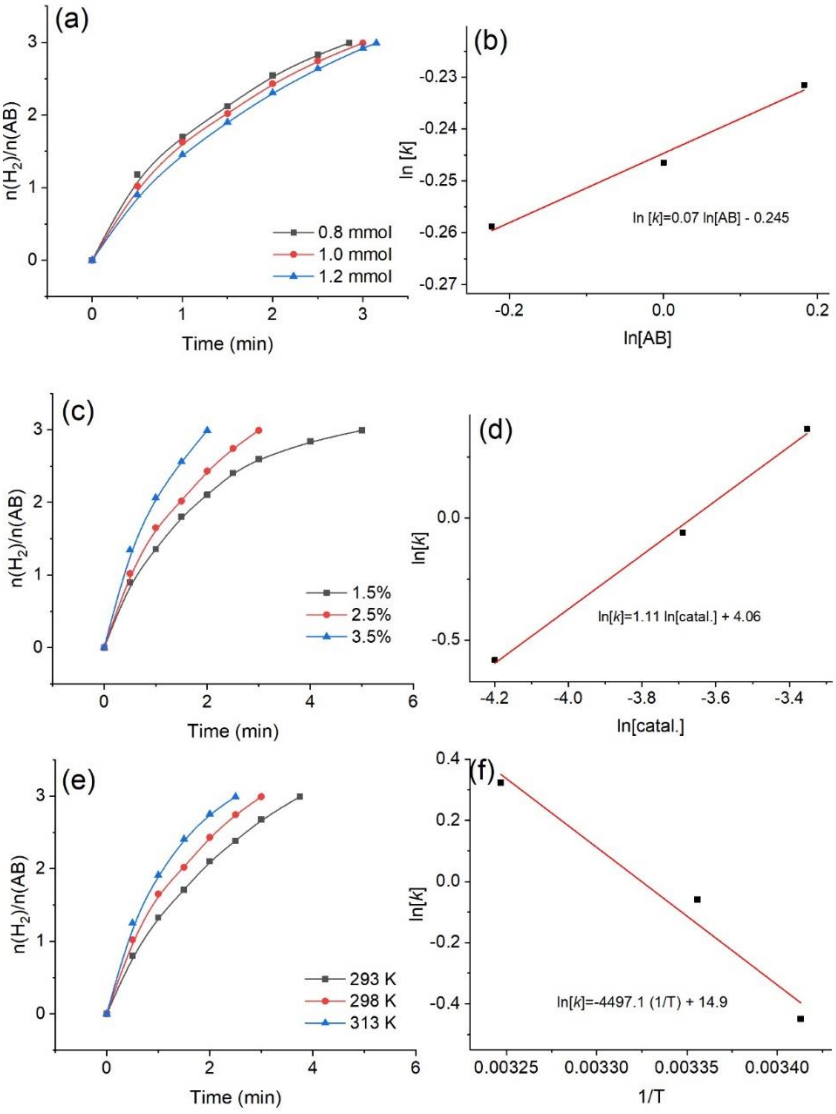

Fig. S4.19. (a) time plots of the catalytic dehydrogenation of AB by 2.5 mol % $Au_{0.5}Ni_{0.5}$@ZIF-8 with various AB concentrations under dark; (b) plot of H_2 generation rate vs the concentration of AB both in natural logarithmic scale (R^2=0.99); (c) time plots of the catalytic dehydrogenation of AB with various catalytic amounts under dark; (d) plot of H_2 generation rate vs the concentration of catalyst both in natural logarithmic scale (R^2=0.99); (e) time plots of the catalytic dehydrogenation of AB at various temperatures under dark; (f) Arrhenius plots obtained from the kinetic data (R^2=0.97).

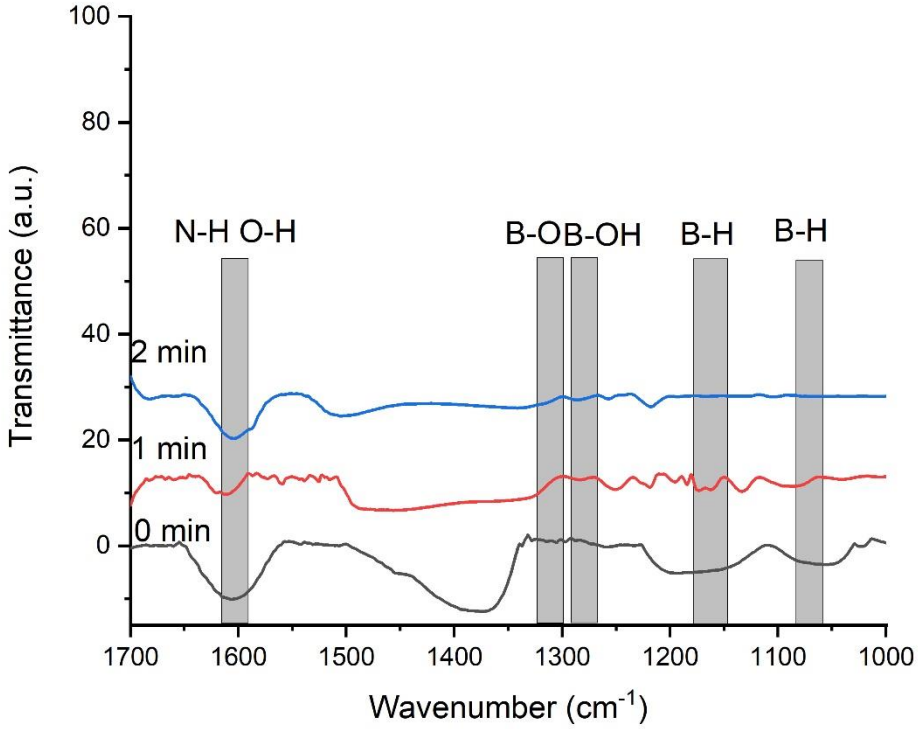

Fig. S4.20. FT-IR spectra of ammonia borane hydrolysis over AuNi@ZIF-8 recorded after various irradiation times.

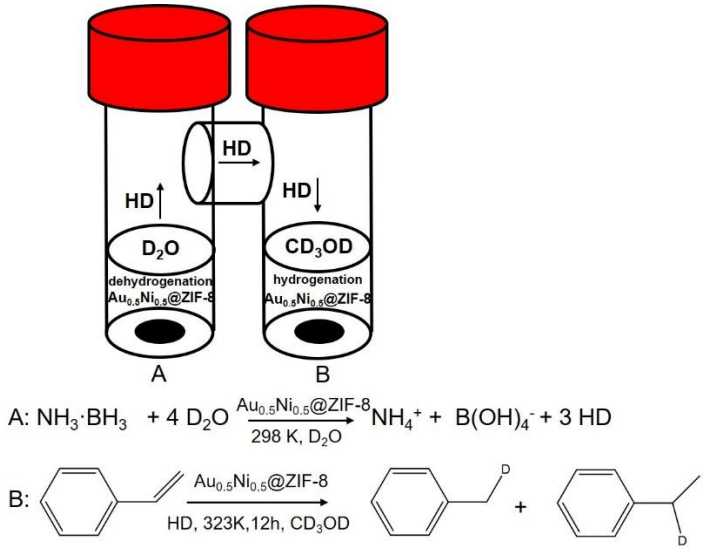

Fig. S4.21. Tandem reaction for the hydrogenation with "HD" generated from AB hydrolysis catalyzed by AuNi@ZIF-8

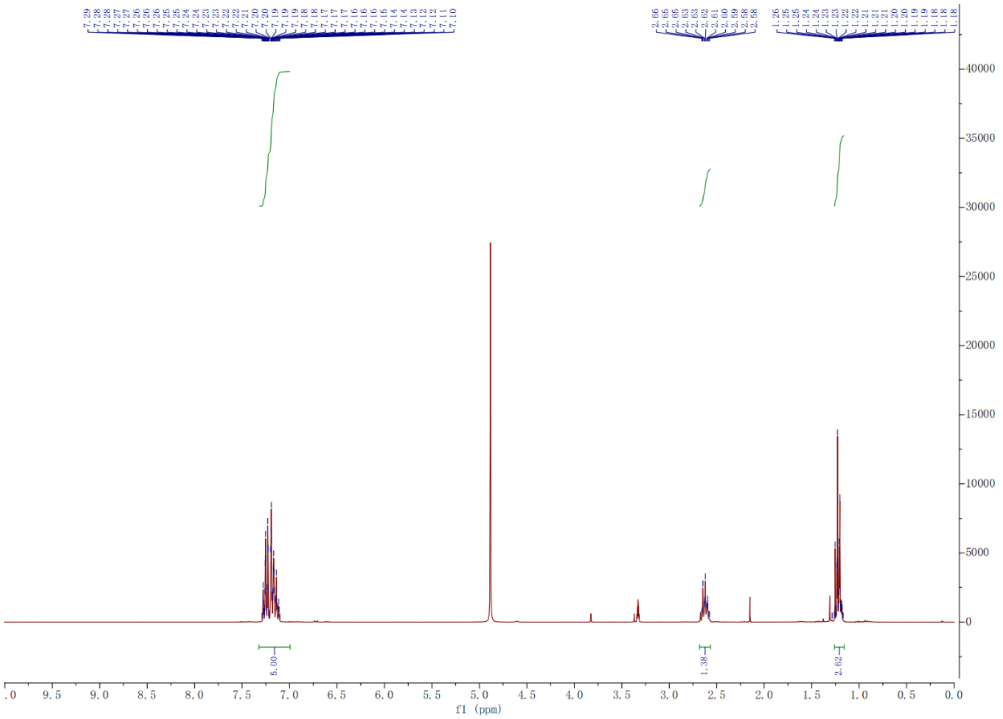

Fig. S4.22. ^{1}H NMR spectrum of ethylbenzene generated from the hydrogenation of styrene in tandem reaction ^{1}H NMR (300MHz, CD_3OD), δ 7.29-7.10 (aromatic H, 5H), 2.66-2.58 (-CH_2, 1.38H), 1.26-1.18 (-CH_3, 2.62H)

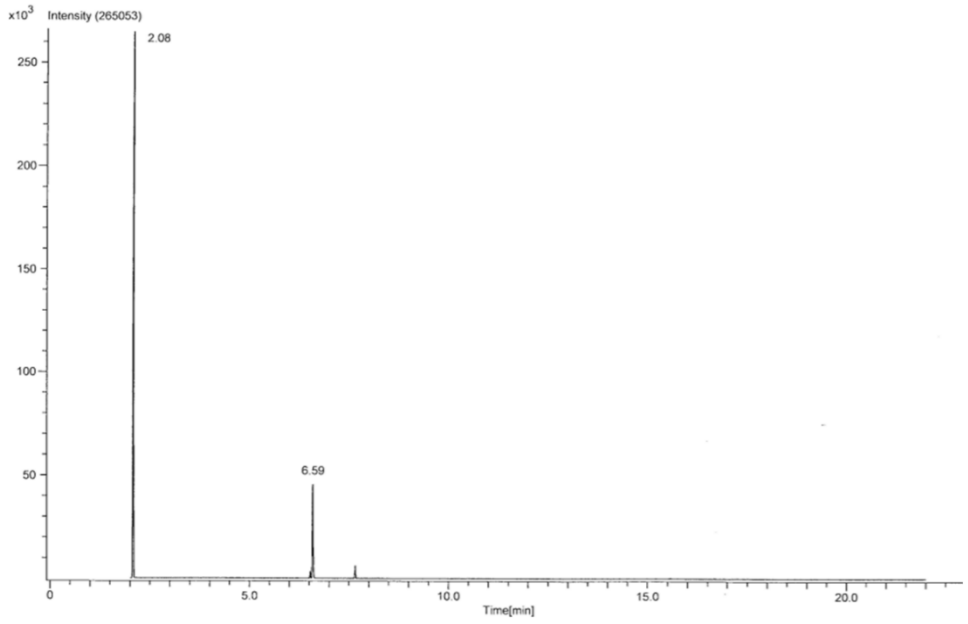

Fig. S4.23. GC-MS spectrum of the hydrogenation product of styrene.

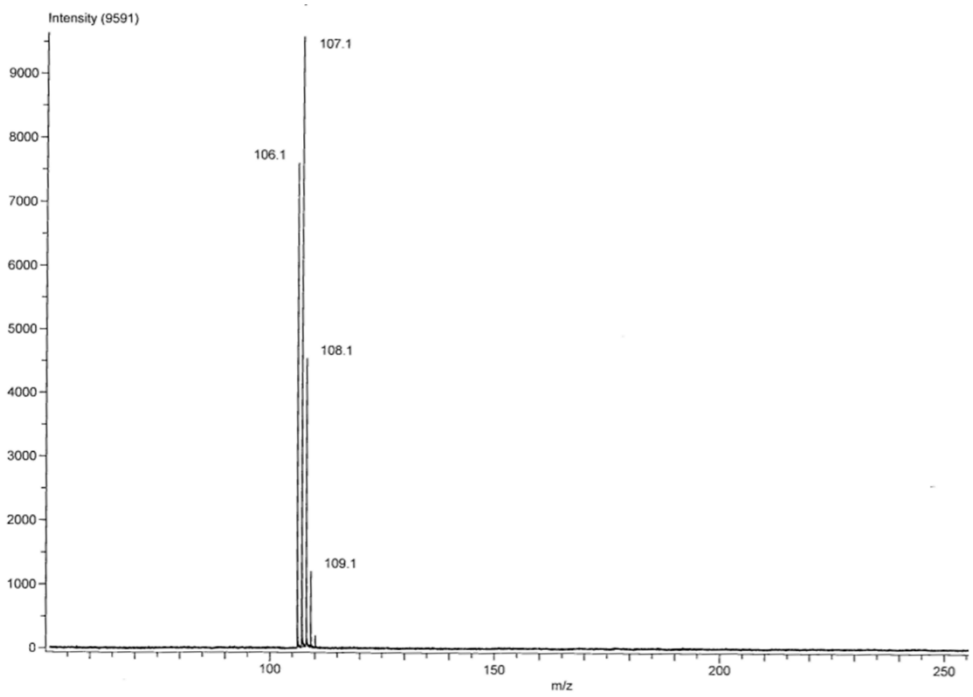

Fig. S4.24. MS spectrum at 2.08 min in Fig.S13. m/z 107.1 ($C_6H_5CHDCH_3$, $C_6H_5CHCH_2D$)

References

[1] T. He, P. Pachfule, H. Wu, Q. Xu, P. Chen, Hydrogen carriers, Nat. Rev. Mater. 1 (2016) 1-17.

[2] Q.-L. Zhu, Q. Xu, Liquid organic and inorganic chemical hydrides for high-capacity hydrogen storage, Energy & Environ. Sci. 8 (2015) 478–512.

[3] Q. Wang, D. Astruc, State of the Art and Prospects in Metal-Organic Framework (MOF)-Based and MOF-Derived Nanocatalysis, Chem. Rev. 120 (2020) 1438–1511.

[4] W. Xu, W. Li, H. Wen, J. Ding, Y. Liu, W. Li, B. Li, Metal/metal-organic framework interfacial ensemble-induced dual site catalysis towards hydrogen generation, Appl. Catal. B-Environ. 286 (2021) 119946.

[5] W.-W. Zhan, Q.-L. Zhu, Q. Xu, Dehydrogenation of Ammonia Borane by Metal Nanoparticle Catalysts, ACS Catal. 6 (2016) 6892–6905.

[6] Q. Yao, Z.-H. Lu, W. Huang, X. Chen, J. Zhu, High Pt-like activity of the Ni-Mo/graphene catalyst for hydrogen evolution from hydrolysis of ammonia borane, J. Mater. Chem. A. 4 (2016) 8579–8583.

[7] Z. Huang, S. Wang, R.D. Dewhurst, N. V Ignat'ev, M. Finze, H. Braunschweig, Boron: Its Role in Energy-Related Processes and Applications, Angew. Chem. Int. Ed. 59 (2020) 8800–8816.

[8] A. Staubitz, A.P.M. Robertson, I. Manners, Ammonia-Borane and Related Compounds as Dihydrogen Sources, Chem. Rev. 110 (2010) 4079–4124.

[9] C. Wang, D. Astruc, Recent developments of nanocatalyzed liquid-phase hydrogen generation, Chem. Soc. Rev. 50 (2021) 3437–3484.

[10] C.W. Hamilton, R.T. Baker, A. Staubitz, I. Manners, B-N compounds for chemical hydrogen storage, Chem. Soc. Rev. 38 (2009) 279–293.

[11] F. Yao, S. Guan, L. Bian, Y. Fan, X. Liu, H. Zhang, B. Li, B. Liu, Ensemble-Exciting Effect in Pd/alk-Ti3C2 on the Activity for Efficient Hydrogen Production, ACS Sustain. Chem. & Eng. 9 (2021) 12332–12340.

[12] Q. Sun, N. Wang, Q. Xu, J. Yu, Nanopore-Supported Metal Nanocatalysts for Efficient Hydrogen Generation from Liquid-Phase Chemical Hydrogen Storage Materials, Adv. Mater. 32 (2020) 2001818.

[13] C.Y. Alpaydin, S.K. Gulbay, C.O. Colpan, A review on the catalysts used for hydrogen production from ammonia borane, Int. J. Hydrogen Energy. 45 (2020) 3414–3434.

[14] C. Wang, J. Tuninetti, Z. Wang, C. Zhang, R. Ciganda, L. Salmon, S. Moya, J. Ruiz, D. Astruc, Hydrolysis of Ammonia-Borane over Ni/ZIF-8 Nanocatalyst: High Efficiency, Mechanism, and Controlled Hydrogen Release, J. Am. Chem. Soc. 139 (2017) 11610–11615.

[15] M. Li, S.B. Zhang, J.K. Zhao, H. Wang, Maximizing Metal-Support Interactions in Pt/Co3O4 Nanocages to Simultaneously Boost Hydrogen Production Activity and Durability, ACS Appl.

Mater. Interfaces. 13 (2021) 57362–57371.

[16] C. Wang, Y. Ren, J. Zhao, S. Sun, X. Du, M. Wang, G. Ma, H. Yu, L. Li, X. Yu, Oxygen Vacancy-attired Dual-active-sites Cu/$Cu_{0.\ 7}6Co_{2.\ 24}O_4$ drives Electron Transfer for Efficient Ammonia Borane Dehydrogenation, Appl. Catal. B Environ. (2022) 121494.

[17] S. Zhang, M. Li, J. Zhao, H. Wang, X. Zhu, J. Han, X. Liu, Plasmonic AuPd-based Mott-Schottky photocatalyst for synergistically enhanced hydrogen evolution from formic acid and aldehyde, Appl. Catal. B Environ. 252 (2019) 24–32.

[18] Y. Kang, B. Jiang, J. Yang, Z. Wan, J. Na, Q. Li, H. Li, J. Henzie, Y. Sakka, Y. Yamauchi, T. Asahi, Amorphous Alloy Architectures in Pore Walls: Mesoporous Amorphous NiCoB Alloy Spheres with Controlled Compositions via a Chemical Reduction, ACS Nano. 14 (2020) 17224–17232.

[19] X. Huang, Y. Liu, H. Wen, R. Shen, S. Mehdi, X. Wu, E. Liang, X. Guo, B. Li, Ensemble-boosting effect of Ru-Cu alloy on catalytic activity towards hydrogen evolution in ammonia borane hydrolysis, Appl. Catal. B-Environ. 287 (2021) 119960.

[20] Y. Yuan, L. Sun, G. Wu, Y. Yuan, W. Zhan, X. Wang, X. Han, Engineering Nickel/Palladium Heterojunctions for Dehydrogenation of Ammonia Borane: Improving the Catalytic Performance with 3D Mesoporous Structures and External Nitrogen-Doped Carbon Layers, Inorg. Chem. 59 (2020) 2104–2110.

[21] C. Cui, Y. Liu, S. Mehdi, H. Wen, B. Zhou, J. Li, B. Li, Enhancing effect of Fe-doping on the activity of nano Ni catalyst towards hydrogen evolution from NH_3BH_3, Appl. Catal. B-Environ. 265 (2020) 118612.

[22] K. Guo, Y. Ding, J. Luo, M. Gu, Z. Yu, NiCu Bimetallic Nanoparticles on Silica Support for Catalytic Hydrolysis of Ammonia Borane: Composition-Dependent Activity and Support Size Effect, ACS Appl. Energy Mater. 2 (2019) 5851–5861.

[23] S. Zhang, M. Li, L. Li, F. Dushimimana, J. Zhao, S. Wang, J. Han, X. Zhu, X. Liu, Q. Ge, H. Wang, Visible-Light-Driven Multichannel Regulation of Local Electron Density to Accelerate Activation of O-H and B-H Bonds for Ammonia Borane Hydrolysis, ACS Catal. 10 (2020) 14903–14915.

[24] S. Rej, C. Hsia, T. Chen, F. Lin, J. Huang, M.H. Huang, Hydrogen Evolution Facet-Dependent and Light-Assisted Efficient Hydrogen Evolution from Ammonia Borane Using Gold – Palladium Core – Shell Nanocatalysts, 30013 (2016) 7222–7226.

[25] P. Verma, K. Yuan, Y. Kuwahara, K. Mori, H. Yamashita, Enhancement of plasmonic activity by Pt/Ag bimetallic nanocatalyst supported on mesoporous silica in the hydrogen production from hydrogen storage material, Appl. Catal. B-Environ. 223 (2018) 10–15.

[26] N. Kang, Q. Wang, R. Djeda, W. Wang, F. Fu, M.M. Moro, M. de los A. Ramirez, S. Moya, E. Coy, L. Salmon, J.-L. Pozzo, D. Astruc, Visible-Light Acceleration of H-2 Evolution from

Aqueous Solutions of Inorganic Hydrides Catalyzed by Gold-Transition-Metal Nanoalloys, ACS Appl. Mater. Interfaces. 12 (2020) 53816–53826.

[27] C. Wang, D. Astruc, Nanogold plasmonic photocatalysis for organic synthesis and clean energy conversion, Chem. Soc. Rev. 43 (2014) 7188–7216.

[28] L. Mascaretti, A. Dutta, S. Kment, V.M. Shalaev, A. Boltasseva, R. Zboril, A. Naldoni, Plasmon-Enhanced Photoelectrochemical Water Splitting for Efficient Renewable Energy Storage, Adv. Mater. 31 (2019) 1805513.

[29] M.C. Daniel, D. Astruc, Gold nanoparticles: Assembly, supramolecular chemistry, quantum-size-related properties, and applications toward biology, catalysis, and nanotechnology, Chem. Rev. 104 (2004) 293–346.

[30] F. Fu, C. Wang, Q. Wang, A.M. Martinez-Villacorta, A. Escobar, H. Chong, X. Wang, S. Moya, L. Salmon, E. Fouquet, J. Ruiz, D. Astruc, Highly Selective and Sharp Volcano-type Synergistic Ni2Pt@ZIF-8-Catalyzed Hydrogen Evolution from Ammonia Borane Hydrolysis, J. Am. Chem. Soc. 140 (2018) 10034–10042.

[31] C. Wang, R. Ciganda, L. Yate, J. Tuninetti, V. Shalabaeva, L. Salmon, S. Moya, J. Ruiz, D. Astruc, Redox synthesis and high catalytic efficiency of transition-metal nanoparticle-graphene oxide nanocomposites, J. Mater. Chem. A. 5 (2017) 21947–21954.

[32] R.P. Lopes, T. Guimarães, D. Astruc, Magnetized biochar as a gold nanocatalyst support for p-nitrophenol reduction, J. Braz. Chem. Soc. 32 (2021) 1680–1686.

[33] B. Delley, From molecules to solids with the DMol 3 approach, J. Chem. Phys. 113 (2000) 7756–7764.

[34] J.P. Perdew, K. Burke, M. Ernzerhof, Generalized gradient approximation made simple, Phys. Rev. Lett. 77 (1996) 3865–3868.

[35] S. Grimme, Semiempirical GGA-type density functional constructed with a long-range dispersion correction, J. Comput. Chem. 27 (2006) 1787–1799.

[36] Q. Zhang, Y. Zhang, K. Xiao, Z. Meng, W. Tong, H. Huang, Q. An, Plasmonic gold particle generation in layer-by-layer 2D titania films as an effective immobilization strategy of composite photocatalytsts for hydrogen generation, Chem. Eng. J. 358 (2019) 389–397.

[37] J. Hao, H. Zhu, Y. Li, P. Liu, S. Lu, F. Duan, W. Dong, Y. Lu, T. Liu, M. Du, Tuning the electronic structure of AuNi homogeneous solid-solution alloy with positively charged Ni center for highly selective electrochemical CO2 reduction, Chem. Eng. J. 404 (2021) 126523.

[38] P. Michaud, D. Astruc, J.H. Ammeter, Electron-Transfer Pathways in the Reduction of d^6 and d^7 Organoiron Cations by $LiAlH_4$ and $NaBH_4$, J. Am. Chem. Soc. 104 (1982) 3755–3757.

[39] J.L. Wang, F.Y. Chen, Y.C. Jin, R.L. Johnston, Highly active and stable AuNi dendrites as an electrocatalyst for the oxygen reduction reaction in alkaline media, J. Mater. Chem. A. 4 (2016) 17828–17837.

[40] G. Darabdhara, M.R. Das, M.A. Amin, G.A.M. Mersal, N.Y. Mostafa, S.S. Abd El-Rehim, S. Szunerits, R. Boukherroub, Au-Ni alloy nanoparticles supported on reduced graphene oxide as highly efficient electrocatalysts for hydrogen evolution and oxygen reduction reactions, Int. J. Hydrogen Energy. 43 (2018) 1424–1438.

[41] C. Wang, X. Liu, Y. Wu, D. Astruc, PtNi@ZIF-8 nanocatalyzed high efficiency and complete hydrogen generation from hydrazine borane: origin and mechanistic insight, J. Mater. Chem. A. (2022) Adv. article. https://doi.org/10.1039/D2TA04411K

[42] X. Zhang, Y. Zhao, X. Jia, Y. Zhao, L. Shang, Q. Wang, G. I. N. Waterhouse, L. Wu, C. Tung, T. Zhang, Silica-protected ultrathin Ni3FeN nanocatalyst for the efficient hydrolytic dehydrogenation of NH_3BH_3, Adv. Energy Mater. 8 (2018) 1702780.

[43] Z. Chen, Y. Song, J. Cai, X. Zheng, D. Han, Y. Wu, Y. Zang, S. Niu, Y. Liu, J. Zhu, Tailoring the d-band centers enables Co_4N nanosheets to be highly active for hydrogen evolution catalysis, Angew. Chemie. 130 (2018) 5170–5174.

[44] K.S. Park, Z. Ni, A.P. Côté, J.Y. Choi, R. Huang, F.J. Uribe-Romo, H.K. Chae, M. O'Keeffe, O.M. Yaghi, Exceptional chemical and thermal stability of zeolitic imidazolate frameworks, Proc. Natl. Acad. Sci. 103 (2006) 10186–10191.

[45] F.I. Pambudi, Electronic properties of heterometallic zeolitic imidazolate framework and its encapsulation with Ni , Pd and Pt, Inorg. Chem. Commun. 143 (2022) 109798.

[46] T. Cornilleau, P. Hermange, E. Fouquet, Gold-catalysed cross-coupling between aryldiazonium salts and arylboronic acids: Probing the usefulness of photoredox conditions, Chem. Commun. 52 (2016) 10040–10043.

[47] F. Tong, X. Liang, Z. Wang, Y. Liu, P. Wang, H. Cheng, Y. Dai, Z. Zheng, B. Huang, Probing the Mechanism of Plasmon-Enhanced Ammonia Borane Methanolysis on a CuAg Alloy at a Single-Particle Level, ACS Catal. 11 (2021) 10814–10823.

[48] P. Xu, W. Lu, J. Zhang, L. Zhang, Efficient Hydrolysis of Ammonia Borane for Hydrogen Evolution Catalyzed by Plasmonic Ag@Pd Core-Shell Nanocubes, ACS Sustain. Chem. & Eng. 8 (2020) 12366–12377.

[49] F.X. Tong, X.Z. Liang, M. Liu, Z.Y. Wang, Y.Y. Liu, P. Wang, H.F. Cheng, Y. Dai, Z.K. Zheng, B.B. Huang, Plasmon-Enhanced Water Activation for Hydrogen Evolution from Ammonia-Borane Studied at a Single-Particle Level, ACS Catal. 12 (2022) 3558–3565.

[50] L. Zhou, N. Li, G. Owens, Z. Chen, Simultaneous removal of mixed contaminants, copper and norfloxacin, from aqueous solution by ZIF-8, Chem. Eng. J. 362 (2019) 628–637.

[51] H. Dai, X. Yuan, L. Jiang, H. Wang, J. Zhang, J. Zhang, T. Xiong, Recent advances on ZIF-8 composites for adsorption and photocatalytic wastewater pollutant removal: Fabrication, applications and perspective, Coord. Chem. Rev. 441 (2021) 213985.

[52] Y. Zhang, Q. Li, C. Liu, X. Shan, X. Chen, W. Dai, X. Fu, The promoted effect of a metal-

organic frameworks (ZIF-8) on Au/TiO2 for CO oxidation at room temperature both in dark and under visible light irradiation, Appl. Catal. B Environ. 224 (2018) 283–294.

[53] M. Wen, S. Song, Q. Liu, H. Yin, K. Mori, Y. Kuwahara, G. Li, T. An, H. Yamashit, Manipulation of plasmon-induced hot electron transport in Pd/MoO_{3-x}@ZIF-8: Boosting the activity of Pd-catalyzed nitroaromatic hydrogenation under visible-light irradiation, Appl. Catal. B-Environ. 282 (2021) 119511.

[54] Q. Wang, F. Fu, S. Yang, M. Martinez Moro, M. de los A. Ramirez, S. Moya, L. Salmon, J. Ruiz, D. Astruc, Dramatic Synergy in CoPt Nanocatalysts Stabilized by "Click" Dendrimers for Evolution of Hydrogen from Hydrolysis of Ammonia Borane, ACS Catal. 9 (2019) 1110–1119.

[55] F.H. Westheimer, The Magnitude of the Primary Kinetic Isotope Effect for Compounds of Hydrogen and Deuterium, Chem. Rev. 61 (1961) 265–273.

[56] M.T.M. Koper, R.A. van Santen, Interaction of H, O and OH with metal surfaces, J. Electroanal. Chem. 472 (1999) 126–136.

[57] A.P. Grosvenor, M.C. Biesinger, R.S.C. Smart, N.S. McIntyre, New interpretations of XPS spectra of nickel metal and oxides, Surf. Sci. 600 (2006) 1771–1779.

[58] D. Astruc, Organometallic chemistry and catalysis, Springer, 2007, Chapter 3.

[59] O. V Ozerov, Oxidative addition of water to transition metal complexes, Chem. Soc. Rev. 38 (2009) 83–88.

[60] L. Luo, Z. Duan, H. Li, J. Kim, G. Henkelman, R.M. Crooks, Tunability of the adsorbate binding on bimetallic alloy nanoparticles for the optimization of catalytic hydrogenation, J. Am. Chem. Soc. 139 (2017) 5538–5546.

[61] S. García, L. Zhang, G.W. Piburn, G. Henkelman, S.M. Humphrey, Microwave synthesis of classically immiscible rhodium–silver and rhodium–gold alloy nanoparticles: Highly active hydrogenation catalysts, ACS Nano. 8 (2014) 11512–11521.

[62] P. Kunal, H. Li, B.L. Dewing, L. Zhang, K. Jarvis, G. Henkelman, S.M. Humphrey, Microwave-Assisted Synthesis of Pd_xAu_{100-x} Alloy Nanoparticles: A Combined Experimental and Theoretical Assessment of Synthetic and Compositional Effects upon Catalytic Reactivity, ACS Catal. 6 (2016) 4882–4893.

[63] I.T. McCrum, M. Koper, The role of adsorbed hydroxide in hydrogen evolution reaction kinetics on modified platinum, Nat. Energy. 5 (2020) 891–899.

[64] D.A. Dowden, 56. Heterogeneous catalysis. Part I. Theoretical basis, J. Chem. Soc. (1950) 242–265.

[65] M. Mavrikakis, B. Hammer, J.K. Nørskov, Effect of strain on the reactivity of metal surfaces, Phys. Rev. Lett. 81 (1998) 2819.

[66] V. Ponec, Alloy catalysts: the concepts, Appl. Catal. A Gen. 222 (2001) 31–45.

[67] J.K. Nørskov, T. Bligaard, J. Rossmeisl, C.H. Christensen, Towards the computational design of

solid catalysts, Nat. Chem. 1 (2009) 37–46.

[68] C. Wei, Y. Sun, G.G. Scherer, A.C. Fisher, M. Sherburne, J.W. Ager, Z.J. Xu, Surface composition dependent ligand effect in tuning the activity of nickel–copper bimetallic electrocatalysts toward hydrogen evolution in alkaline, J. Am. Chem. Soc. 142 (2020) 7765–7775.

Chapter 5. Efficient light-boosted tandem hydrogen production and selective alkyne semi-hydrogenation upon ammonia-borane methanolysis catalyzed by AuPd@ZIF-8

5.1. Introduction

Hydrogen production from solid or liquid sources is a promising alternative energy source and avoids hydrogen storage in laboratories[1–3]. Ammonia borane (AB) is an excellent hydrogen storage material and the most studied one because of its high hydrogen gravimetric capacity (19.6 wt %), good solubility in water or alcohols, stability, nontoxicity and accessible release of H_2 on the surface of catalysts [4–8].

Nanoparticles (NPs) are excellent candidates as catalysts (nanocatalysts) because of their high surface-area-to-volume ratio and ability to catalyze many different types of reactions on a well-controlled surface [9–11]. Pt or Pd alloying with other metals can tune NP surface electronic and geometric effects to optimize the catalysis of multiple reactions[12–15]. For example, NiPt and PtCo alloy NPs have been reported to enhance AB dehydrogenation, as well as to exhibit activity in tandem hydrogenation reactions [16,17].

AB methanolysis (equation 1) is a promising, although much less used than AB hydrolysis as means of facile H_2 generation.

$$NH_3BH_3 + 4\,CH_3OH \xrightarrow{\text{catalyst}} NH_4B(OCH_3)_4 + 3H_2 \qquad (1)$$

However, since the seminal reports by Ramachandran and Gagare of ammonia borane preparation in high yield and purity, methanolysis, and regeneration [18] and by Jagirdar's group of Co, Ni and Cu-based nanocatalyst [19,20] of AB methanolysis a number of publications have appeared on this way of hydrogen generation and the area has been reviewed in 2016 by Xu's group [21] and in 2022 by Li's group [22]. This H_2 generation method possesses several important advantages towards current applications [21,22]. Indeed, AB is highly soluble in methanol (23% wt at 23 °C) [23], and it is highly stable in methanol in the absence of the catalyst, H_2 produced by AB methanolysis is pure from ammonia impurities that are poisoning fuel cells, and it can generate H_2 below 0°C upon catalysis, which might be useful for portable devices under cold temperature conditions, and the AB methanolysis product formed [24], $NH_4B(OCH_3)_4$ can regenerate AB upon reaction with $LiAlH_4$ and NH_4Cl under ambient conditions [24]. Although first-row late transition-metal-based nanocatalysts are priviledged [18, 24-26], there are also reports using more efficient noble-metal catalysts [23,27].

Recently, plasmonic enhancing of catalytic reactivity has received attention for AB dehydrogenation under visible light irradiation [25,26]. Plasmonic nanostructures collect the energy of visible light through the excitation of localized surface plasmon resonance (LSPR) and concentrate it near the NP surface in the form of elevated electric fields, which activates photosensitive reactions [26–30]. Energy is dissipated either through radiative photon scattering or formation of energetic charge carriers, which induces photochemical transformation [31]. It has been proposed that collective local heating contributes to a significant enhancement of AB dehydrogenation [30]. To boost dehydrogenation of AB, it has also been reported that surface charge heterogeneity on the nanocrystal surface in the presence of light favored enhanced binding of AB [32]. Recently, it has been further suggested that plasmonic hot electrons can be injected into a chemically attached molecule (AB and methanol), which effectively reduces the activation barrier, hence enhancing the hydrogen production rate [31–33].

Here we report the dramatic visible-light acceleration in catalytic AB methanolysis with alloyed AuPd NPs supported by ZIF-8, the high selectivity and superiority of this support and a proposed mechanism using isotopic labelling upon tandem styrene hydrogenation reaction, the finding of high primary KIE, and DFT calculations. The impressive visible light-induced acceleration involves nanogold plasmon excitation with contributions of hot electron transfer, photoinduced thermal effects and the photoinduced local-field plasmon-enhanced methanolysis of AB, and these components are revealed and discussed.

5.2.Results and discussions

5.2.1. Catalyst characterizations

The AuPd NPs stabilized by ZIF-8 were fabricated by the deposition-precipitation method with $NaBH_4$ as the reductant [38,39]. Specially, these nanocatalysts were synthesized through co-reduction of $KAuCl_4$ and $NaPdCl_4$ in water and methanol (volume ratio: 1:1) by $NaBH_4$ under ambient conditions (Fig. 1a), then collected by centrifugation and dried. The metal loading was determined by inductively coupled plasma-optical emission spectroscopy (ICP-AES, Table S1). Fig. 1b-1c show the representative transmission electron microscopy (TEM) images of the AuPd NPs, packed in the ZIF-8

framework with an average size of 2.43 nm. The measured lattice distance of 0.22 nm corresponds to the (111) plane of AuPd NPs[40]. The X-ray powder diffraction (XRD, Fig. 1d) shows the typical crystal pattern of ZIF-8, but without noticeable peaks of metallic Au or Pd from the similar crystallinity of AuPd@ZIF-8 with ZIF-8 support [41]. This suggests that the metal loading in the present case is low and that some NPs are inside ZIF-8. Fig. 1e shows AuPd@ZIF-8 framework exhibiting apparent type-IN_2 isotherms with the N_2 uptake predominantly occurring at a rather low relative pressure range (P/P_0 less than 0.03), indicating the presence of micropores within the structures. Moreover, Fig. 1e also presents the corresponding pore size distribution curves estimated by the non-local DFT model. The average size of the pore diameter is 1.5 nm, which is much smaller than the AuPd NP size (2.43 nm). The precursor metal cations are first introduced inside the ZIF cavity in which they interact with the N atoms of ZIF-8, then they are reduced by $NaBH_4$ [42] to NPs and, given their size, are trapped within the ZIF-8 cavity. Furthermore, after packing the AuPd NPs, the BET surface area decreases from 1787.3 $m^2 \cdot g^{-1}$ to 1269.0 $m^2 \cdot g^{-1}$ (Fig. S1 and Table S2), due to the presence of AuPd NPs inside ZIF-8, which is consistent with previous reports [16,26]. The HAADF-STEM images were used to identify the alloy nanostructure and the chemical composition of the individual NP. As shown in Fig. 1f and Fig. S2, they indicate that the Au and Pd elements are located in a single NP, and the distribution of Au and Pd along cross-section lines of the AuPd NPs confirms the alloy nanostructure of AuPd.

X-ray Photoelectron Spectroscopy (XPS) is employed to investigate the chemical composition and electronic interaction of prepared nanocatalysts. The XPS results show binding energies of 83.4 eV and 87.1 eV for Au (0) $4f_{7/2}$ and Au (0) $4f_{5/2}$, respectively, and the binding energy of 334.3 and 339.6 eV, corresponding to Pd $3d_{3/2}$ and $3d_{1/2}$ respectively, confirming the presence of metallic Pd(0) in the AuPd@ZIF-8 NPs [43] (Fig. S3 and Table S3). The binding energy peaks of Au 4f and Pd3d also show the existence of the Au (I) and Pd (II) ions, attributed to unavoidable aerobic oxidation of the AuPdNPs, which has precedents [26]. Through the comparison between bimetallic alloy and monometallic NPs, the electronic interaction between two metals is analyzed. Here, the binding energies of Au 4f (83.4 eV and 87.1 eV) of the AuPd alloy are shifted to lower values compared to those (84.0 eV and 87.9 eV) of AuNPs (Table S3). In addition, the binding energies of Pd 3d (334.3 eV and 339.6 eV) of the AuPd alloy are also shifted to lower values compared to

those (334.9 eV and 340.2 eV) of PdNPs (Table S3). The direction of charge transfer is the same, indicating that the electronic interaction between Au and Pd is not strong [44].

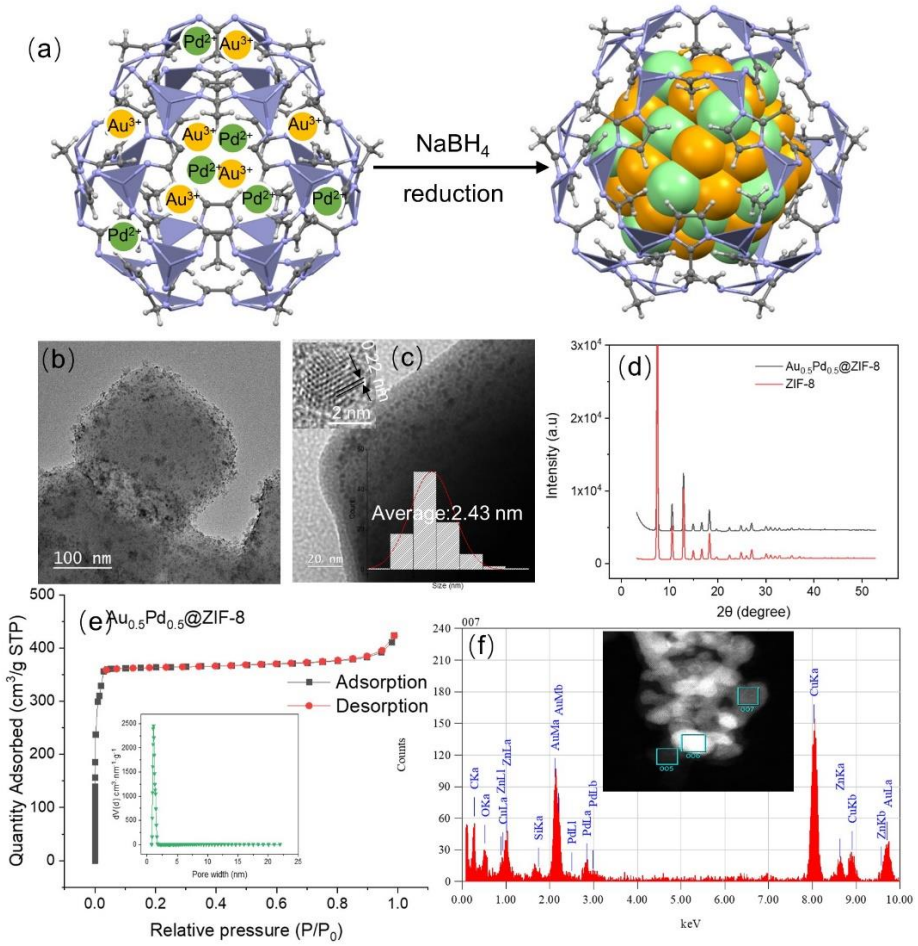

Fig.1. (a) Synthesis of AuPd@ZIF-8; (b) TEM image of AuPd@ZIF-8; (c) TEM image of AuPd@ZIF-8 with size distribution and HRTEM image inserted; (d) PXRD patterns of ZIF-8 and AuPd@ZIF-8; (e) Nitrogen adsorption-desorption isotherms of the nanocatalysts on AuPd@ZIF-8;(f) distributions of Au and Pd on 007 with the STEM image inserted.

5.2.2. Visible-light-induced acceleration of catalyzed AB methanolysis

The volumes of gas collected represent nearly 3 equiv of H_2 per AB. As shown in Fig. 2a, under dark, the efficiency of AB methanolysis catalyzed by Pd@ZIF-8 is higher than AB methanolysis catalyzed by Au@ZIF-8. The catalytic activity of $Au_{0.5}Pd_{0.5}$@ZIF-8 upon AB

methanolysis is intermediate at the beginning of the reactions between those of the two monometallic catalysts, but the hydrogen production catalyzed by these three catalysts is not quantitative. Here, a strongly positive synergistic effect in the AuPd alloy was not observed, although the AB methanolysis derived by AuPd alloy is slightly faster than by Pd NPs after 15 min. There is no strong positive synergy upon alloying Au and Pd in the dark, in accord with the fact that strong electronic interaction between Au and Pd in the AuPd alloy is not found from the XPS results.

Remarkably, when the AB methanolysis reactions were moved from dark to visible-light irradiation, the efficiency of AB methanolysis catalyzed by $Au_{0.5}Pd_{0.5}$@ZIF-8 was considerably enhanced, and the hydrogen generation was complete (Fig. 2). Under visible light, the TOF value increased more than 3.7 folds compared to the reaction conducted in the dark, which implies that visible light played a major role on AB methanolysis in this $Au_{0.5}Pd_{0.5}$@ZIF-8 catalytic reaction system. Moreover, given the crucial influence of visible light exerted on $Au_{0.5}Pd_{0.5}$@ZIF-8 catalysis, the light effect was also evaluated for comparison with the monometallic catalysts Au@ZIF-8 and Pd@ZIF-8(Fig. S4 and S5). In the presence of visible light irradiation, the rate of AB methanolysis catalyzed by Au@ZIF-8 was enhanced compared to that in the dark, but these reactions catalyzed by either Au@ZIF-8 or Pd@ZIF-8 are not complete. Although AuNPs have a strong plasmon, hot electron transfer generated on Au NPs surface is not efficient because AuNPs are not an effective catalyst for AB methanolysis. As a result, only a very modest enhancement of AB methanolysis efficiency for Au@ZIF-8is observed with light. For Pd@ZIF-8, no improvement of catalytic H_2 evolution activity was noted upon visible-light illumination compared to the reaction in the dark, which is due to the fact that the plasmon resonance of Pd cannot be excited under visible light of 550 nm.

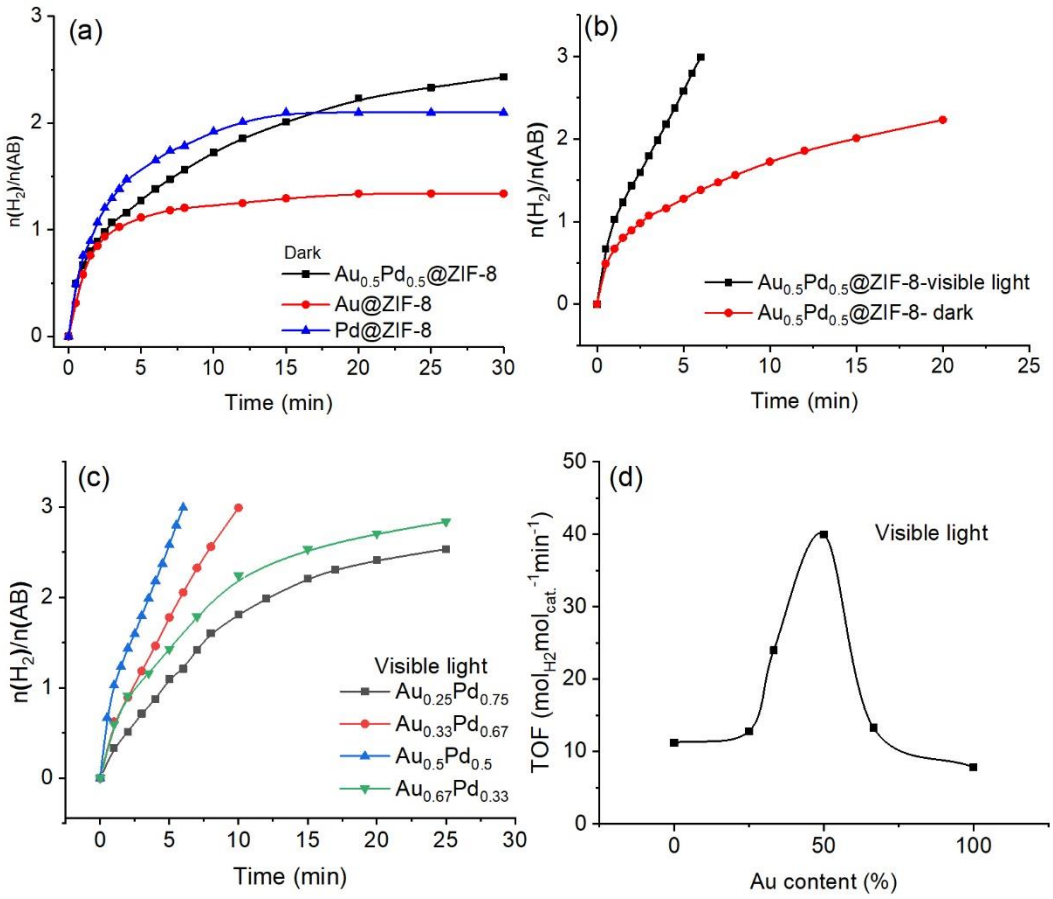

Fig. 2. (a) Plot of the molar amount of H_2 generated upon AB methanolysis vs. time catalyzed by ZIF-8 supported AuNPs, PdNPs and $Au_{0.5}Pd_{0.5}$NPs. (b) Comparison of catalytic efficiencies among $Au_{0.5}Pd_{0.5}$@ZIF-8 without visible light irradiation. (c) Plot of the molar amount of H_2 generated upon AB methanolysis vs. time catalyzed by $Au_{0.5}Pd_{0.5}$@ZIF-8 with various ratios of Au and Pd with visible-light irradiation. (d) TOF values with different ratios of Au/Pd with visible-light irradiation. In all the experiments, the reaction conditions are: 1 mmol of AB; 1.25% mmol MNP; temperature: 25 ± 0.5°C.

Since the AuPd alloyed nanocatalysts showed excellent performances for AB methanolysis under visible light irradiation, it was necessary to optimize the proportion of Au and Pd in the alloy (Fig. 2c). Under visible-light irradiation, the best ratio of Au to Pd is 1 to 1, with the high TOF value of 40$mol_{H2}\cdot mol_{cat.}^{-1}\cdot min^{-1}$ (86.7 $mol_{H2}\cdot mol_{atom}^{-1}\cdot min^{-1}$). As the Au content increases from Pd NP to AuPd alloy, the reaction rate of AB methanolysis increases until the proportion of 50% Au is reached in the AuPd alloy. Then, the catalytic performance continually decreases upon raising the Au proportion above 50%.

5.2.3.Methanolytic AB dehydrogenation catalyzed by AuPd on various heterogeneous supports

The loading of the nanocatalyst AuPd in @ZIF-8 was varied, and the variation effect was investigated in order to improve the catalyst. Thus, AuPd NPs with a series of amounts of ZIF-8 (2.6 wt%, 4.2 wt%, 5.7 wt% and 7.1%) were prepared, and the catalytic efficiencies upon AB methanolysis were evaluated. The best catalytic performance was obtained when the MNP load was 5.7 wt% (Fig. S6). The catalysts stabilized by other supports (ZIF-67, UIO-66, GO) were synthesized and evaluated in the AB methanolysis reaction using the same method with 5.7% loading of MNPs for $Au_{0.5}Pd_{0.5}$@ZIF-8, and the catalytic performances were compared. The catalytic activities measured by the TOF values for AuPd NPs supported by ZIF-8, ZIF-67, UIO-66, and GO are compared, showing that ZIF-8 is by far the best support obtained with AuPd whatever dark or visible light irradiation conditions are used (Fig. 3). The AuPd NPs tend to aggregate quickly when they are supported by GO, which results in uncomplete methanolysis, contrasting with catalysis using the other supports. Therefore, the characterization of $Au_{0.5}Pd_{0.5}$@GO was not considered. The specific order of support performances without light irradiation follows the order: $Au_{0.5}Pd_{0.5}$@GO > $Au_{0.5}Pd_{0.5}$@ZIF-8 > $Au_{0.5}Pd_{0.5}$@ZIF-67 > $Au_{0.5}Pd_{0.5}$@UIO-66. The differences in performances find their origin in the various particle sizes and BET surfaces. The sizes of the nanoalloys between the four catalysts follows the order: $Au_{0.5}Pd_{0.5}$@ZIF-8 < $Au_{0.5}Pd_{0.5}$@ZIF-67 = $Au_{0.5}Pd_{0.5}$@UIO-66 (Fig. S8-9). Moreover, the BET surfaces of the three other catalysts follow the order: $Au_{0.5}Pd_{0.5}$@ZIF-67 > $Au_{0.5}Pd_{0.5}$@ZIF-8 > $Au_{0.5}Pd_{0.5}$@UIO-66 (Fig. S10 and Table S4). Under dark conditions, the MOF-embedded AuPd NP nanocatalysts do not perform better than GO-supported AuPd nanocatalyst in the initial reaction. This is due to the fact that when a MOF packs the nanostructure, some NPs become encapsulated inside of MOF, as confirmed by BET, and their surface is protected. In the presence of visible light irradiation, the performances are significantly enhanced for the three MOF-supported nanocatalysts $Au_{0.5}Pd_{0.5}$@ZIF-8, $Au_{0.5}Pd_{0.5}$@ZIF-67 and $Au_{0.5}Pd_{0.5}$@UIO-66 (Fig.3b), and this reactivity order remains the same as for the reactions in the dark. The rate multiplication factor is 3.7, 2.9 and 2.1, respectively. Among the four supported reactions, only the reaction catalyzed by $Au_{0.5}Pd_{0.5}$@GO keeps a similar rate under of dark and visible irradiation. Moreover, the

reaction with this nanocatalyst, $Au_{0.5}Pd_{0.5}$@GO, generates insufficient hydrogen, which is due to the fact that GO does not protect the NPs well, as these NPs quickly aggregate at the beginning of the reaction. Concerning MOF-supported AuPd NPs ($Au_{0.5}Pd_{0.5}$@ZIF-8, $Au_{0.5}Pd_{0.5}$@ZIF-67, and $Au_{0.5}Pd_{0.5}$@UIO-66), plasmonic bands were observed (Fig. S11), correspondingly showing significant light enhancement upon catalysis. This indicates that ZIF-8 exhibits high selectivity for AuPd NPs. In sum, there is an impressive light effect on the $Au_{0.5}Pd_{0.5}$@ZIF-8 nanocatalyst for AB methanolysis, ZIF-8 being the optimized support for the catalytic activation of the substrates AB and ethanol.

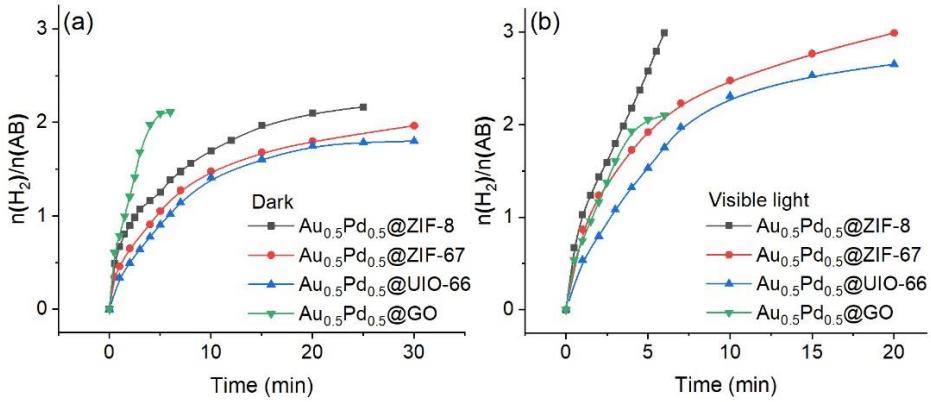

Fig. 3. (a) AB methanolysis catalyzed by $Au_{0.5}Pd_{0.5}$ on the various supports without visible light; (b) AB methanolysis catalyzed by $Au_{0.5}Pd_{0.5}$ on the various supports with visible light. In all the experiments, the reaction conditions are: 1 mmol of AB; 1.25% mmol MNP; temperature: 25 ± 0.5°C.

Concerning the plasmonic metal-based catalysts, the important feature is that their performance depends on the wavelength of illumination, because the wavelength of light determines the energy of the incoming photons and thus the energy of the photogenerated charge carriers. Therefore, in order to verify the effects produced by plasmon metal-mediated catalysts, the catalytic efficiency of AB methanolysis was evaluated under light irradiation at the wavelengths 450 nm, 520 nm and 620 nm (Fig. S12). As a result, irradiation at 550 nm was the most effective among the three visible light wavelengths. It is known that, compared to the light at 550 nm, the 450 nm-light possessed more photons, but the performance of AB methanolysis at 550 nm is better than that at 450nm. This

suggests that irradiation with more photons does not contribute to increased efficiency, as only light wavelengths corresponding to the surface plasmon band of $Au_{0.5}Pd_{0.5}$@ZIF-8 provides enhancement of catalytic efficiency. In Fig. S7, the plasmon band of $Au_{0.5}Pd_{0.5}$@ZIF-8 culminates at 560 nm.

5.2.4. Photoinduced enhancement upon AB methanolysis catalyzed by $Au_{0.5}Pd_{0.5}$@ZIF-8

It has been reported that enhancement introduced by photons includes photo-thermalization, photo local field and hot-electron transfer[45]. The photoinduced enhancement of AB methanolysis efficiency has been analyzed from these three aspects. First, low-energy electrons coupled to phonon modes after thermalization increase the temperature of the NP, and this effect then dissipates into the environment[46]. Therefore, in order to accurately demonstrate the effect of heating the reactor itself after continuous illumination, a temperature probe was placed inside the mixing flask to observe the temperature change during AB methanol decomposition on$Au_{0.5}Pd_{0.5}$@ZIF-8 (25 °C, 7 mW cm^{-1}). Due to the fact that the reaction time is about 6 min, the contribution from heating by visible light should be considered. The flask was covered by tin paper to avoid direct visible light irradiation. From the result, the temperature change between before and after the reaction was approximately 1.2 °C, and the reaction rates under dark or heating by the visible light only showed a tiny difference (Fig. S13). Thus, the contribution from photo-thermalization is not mainly responsible for light enhancement. This result was related to previous reports[47,48].

The plasmon-induced electric field is dominated by localized electronic states at the NP interface, and these surface plasmon fields facilitate the provision of sufficient energy for the activation of some chemical bonds[49]. Furthermore, the local electric fields decay almost exponentially with distance from the NP surface and are accompanied by the generation of gradient forces[50]. Stronger electric field-gradient forces are essential for trapping reactant molecules and polarizing capture targets[50]. Difference Time Domain (FDTD) simulations were used to calculate the local electric field associated with SPR (Fig. S14). Alloying Au with Pd improves the spatial distribution of electric field strength in NPs. The addition of Au to Pd NPs increases $|E/E_0|^2$ from 6.4 to 13.1. Notably, the NP dimer exhibits a stronger near-field distribution compared to individual alloy particles, with

$|E/E_0|^2$ reaching 49.7. Thus, the enhanced field confers superior hot electron generation and molecular substrate adsorption to $Au_{0.5}Pd_{0.5}$ alloy NPs function. Specifically, the stronger molecular adsorption enables the formation of metal-adsorbent complexes [51]. At the same time, favorable adsorption of reactants onto the metal NPs is important to enhance the catalytic activity. Lu et al. observed that the local electric field generated by Ag NPs enhanced the adsorption and subsequent photodehydrogenation of ammonia borane molecules [52]. Similarly, here, the increased electric field of AuPd alloy NPs enhanced the adsorption of MeOH and AB to form metal-AB-MeOH complexes, resulting in more efficient hot electron transfer, further enhancing the catalytic activity.

The structural modification of catalyst between before and after light-accelerated reaction was characterized by TEM and XPS. From Fig. S15, there was a slight increase of AuPd NP size from 2.43 nm before reaction to 2.77 nm after reaction, indicating the excellence of ZIF-8 as support. Given this result, the durability of $Au_{0.5}Pd_{0.5}$@ZIF-8 was tested. As illustrated in Fig. S16, the catalyst $Au_{0.5}Pd_{0.5}$@ZIF-8 remained highly catalytically active upon AB methanolysis within 3 cycles. The XPS results show the oxidation state and shifts of binding energies. After AB methanolysis, XPS shows binding energies of 83.5 and 87.2 eV, corresponding to Au (0) 4f, and the binding energies of 334.5 and 339.7 eV demonstrate that Pd remains in the 0-valence state. (Fig. 4). Comparing the Au 4f and Pd 3d region before and after reaction, shifts of binding energy were observed. The binding energy of Au 4f at 83.4 and 87.1 eV before reaction shifted to higher values (83.5 and 87.2 eV) (Fig. 4a and 4c), indicating that the Au surface became more positively charged after the photoreaction. Moreover, the binding energy of Pd 3d (339.6 and 334.3 eV) shifted to lower values (339.5 and 334.1 eV) after reaction (Fig. 4b and 4d), demonstrating that there was an electronic stimulation on Pd atoms. During the photo-acceleration reaction, the electron density transfers from Au to Pd, and Pd atoms were consequently electronically enriched. This suggests that even if the time scale of proton-induced electron transfer is only on the order of fs, this electron density transfer has some irreversible properties after the photo reaction involved in restructuration[25]. Usually, the electron transfer between NPs and support should be considered due to the heterogeneity of the catalyst in the reaction with visible-light irradiation. However, ZIF-8 without any special treatment and addition is an insulator, and it has been proved that it is not

responsible for transferring and separating electrons induced by the LSPR of Au NPs, and it cannot be excited by visible light due to its high LUMO level, as reported[26,53,54].

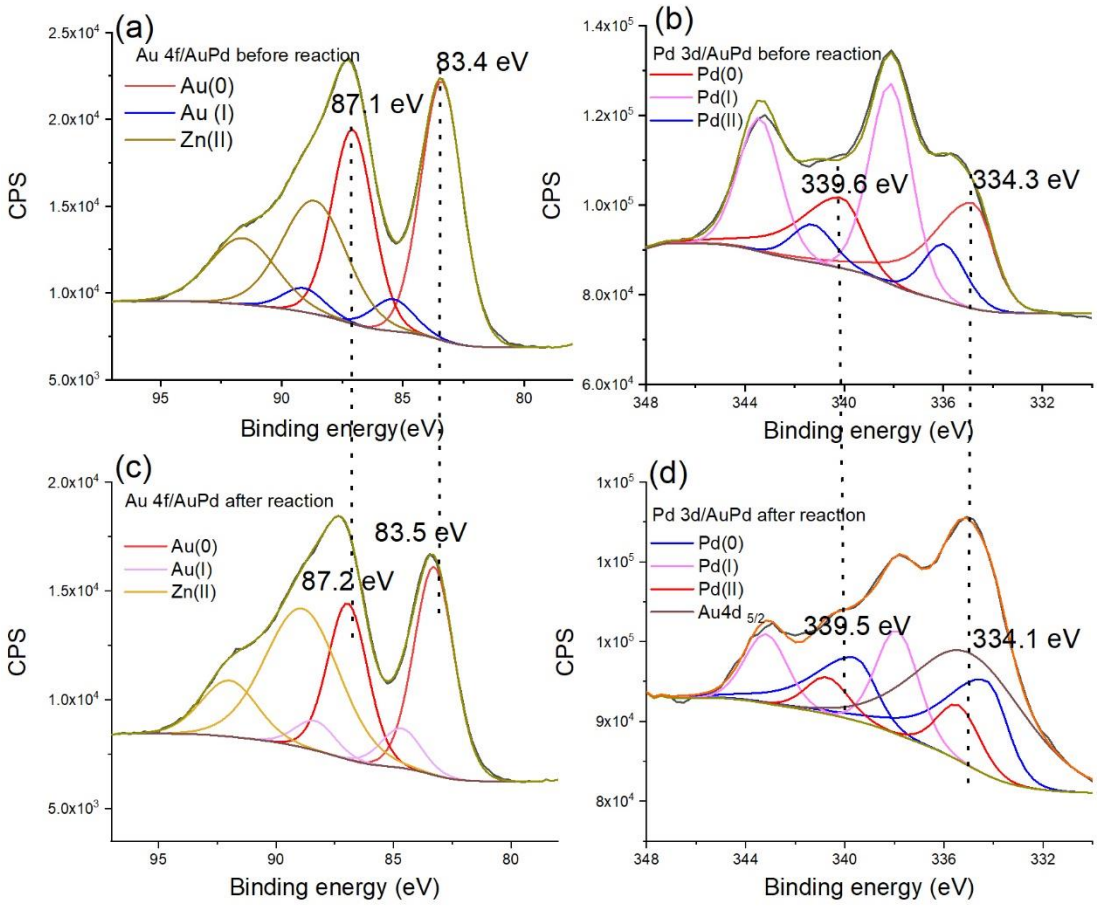

Fig. 4. XPS spectra of AuPd@ZIF-8, (a) Au 4f region of AuPd@ZIF-8 before reaction, (b) Pd 3d region of AuPd@ZIF-8 before reaction, (c) Au 4f region of AuPd@ZIF-8 after reaction, (d) Pd 3d region of AuPd@ZIF-8 after reaction.

5.2.5. Mechanism of H_2 formation upon nanocatalyzed AB methanolysis

Concerning the reaction mechanism of AB methanolytic hydrogen release, it has been reported that one of the hydrogen atoms of generated H_2 was provided by AB and the other one by methanol [48,55,56]. The kinetic isotope effect (KIE: k_H/k_D) conducted with d^4

methanol is an effective way to identify the rate-determining step (RDS) of the reaction. In the present reaction, the KIE value is 2.2 in the dark and 3.4 under visible light illumination (Fig. S17). These values clearly show that methanol O-H bond cleavage is the rate-limiting step of the reaction in both cases. The higher KIE value under light compared to that in the dark may be due to the additional necessary adsorption rearrangement of methanol in the course of plasmonic electron transfer. [57]

The tandem reaction was conducted in order to demonstrate that one hydrogen atom of H_2 is coming from methanol in the reaction of AB methanolysis and the other from AB. Typically, AB methanolysis catalyzed by $Au_{0.5}Pd_{0.5}$@ZIF-8 was conducted in a sealed two-chamber reactor towards hydrogenation of styrene with the same catalyst (Fig. S18). The hydrogen gas produced from AB methanolysis catalyzed by $Au_{0.5}Pd_{0.5}$@ZIF-8 with CD_3OD as the solvent in the left tube was transferred to the right tube in which hydrogenation of styrene proceeds in CD_3OD, and deuteration of this hydrogen gas was investigated. ^{1}H NMR spectroscopy and gas chromatography-mass spectrometry analyses were used to detect the hydrogenation product without any treatment in the right tube. The nanocatalyzed hydrogenation of styrene with generated quantitative hydrogen after 12 h at 25 °C produced ethylbenzene that was analyzed using its ethyl signals in the ^{1}H NMR spectrum. The total number of H atoms found for this ethyl fragment is 4 , out of the 5 H atoms of this fragment. We conclude that the missing fifth H atom has been replaced by a D atom (Fig. S19). Furthermore, the molecular peak of 106, 107 (major), and 108 m/z in the mass spectrum, corresponding to CH_8H_{10}, C_8H_9D, $C_8H_8D_2$, respectively, indicates that statistically one D atom was transferred to styrene producing mono-deuterated phenylethane (Fig. S20-21). These results fully confirm that one of the hydrogen atoms of H_2 comes from AB and the other one from water. In addition, the present system demonstrated that $Au_{0.5}Pd_{0.5}$@ZIF-8 is an efficient and versatile catalyst for AB methanolysis.

In order to explain the difference of catalytic activity among Au@ZIF-8, Pd@ZIF-8 and AuPd@ZIF-8, the projected d-orbital density of states (DOS) of different NPs were studied to evaluate the d-band center position. The d-band center of Au (111) and Pd (111) shows -3.2 and -2.4 eV, respectively (Fig. 5a). After alloying Au and Pd, the d-band center of AuPd (111) shows -1.5 eV, which is higher than that of both Au (111) and Pd (111). The

upgrading of the d-band center energy level of AuPd indicates that the electron in d-orbital of the metal is closer to the energy level of the antibonding orbital of the adsorbate species. The closing tendency between d-orbital and antibonding orbital induces an easier adsorption of reactant molecules on catalyst surface., which means that the adsorption energy between AuPd and AB is stronger than those with Pd and Au [58,59].

DFT calculation was conducted to confirm the corresponding mechanism H_2 formation upon nanocatalyzed AB methanolysis. It is delicate to optimize real models based on catalysts, but it was most representative to establish the calculation model based on AB methanolysis occuring at the contact between Au_1Pd_1 and ZIF-8. As shown in the DFT results, the formation of NP-coordinated O-CH_3 ligand requires the highest reaction energy barrier both in dark and visible-light conditions for the three nanocatalysts Au@ZIF-8, Pd@ZIF-8 and $Au_{0.5}Pd_{0.5}$@ZIF-8. This result provides further evidence for the catalytic mechanism. The energy barriers for AB methanolysis under dark condition on the surfaces of Au@ZIF-8, Pd@ZIF-8 and $Au_{0.5}Pd_{0.5}$@ZIF-8 show the following respective tendency 1.07 eV > 0.81 eV > 0.46 eV (Fig. 5c). The above results confirm that the cleavage of the H-OCH_3 bond is the only rate-limiting step in AB methanolysis for the targeted catalyst (TS1 > TS2). The optimized catalyst also provides an appropriate active site for the acceleration of the overall reaction via reducing the energy barrier of the RDS under light conditions. With light illumination, the charge excitation/transfer at the interface of plasmonic NPs and chemically attached substrates proceeded, turning CH_3OH into vibrationally or electronically excited states and then increasing the reactivity of the reactant molecule. A plasmonic hot electron is transferred from a gold atom to the excited state of the Pd-adsorbate ensemble, enhancing the overall electron density of states of Pd-adsorbate sites, accelerating cleavage of the methanol **H---O** bond in the PdH---**H---OC**H_3 adsorbate by oxidative addition on Pd. The energy barriers for AB methanolysis under light conditions on the surfaces of Au@ZIF-8, Pd@ZIF-8 and $Au_{0.5}Pd_{0.5}$@ZIF-8 convey a tendency with respectively 0.88 eV > 0.51 eV > 0.45 eV (Fig. 5c). Calculation of the Gibbs free energy under light condition yields compared to dark reaction, $TS1_{light} < TS1_{dark}$.

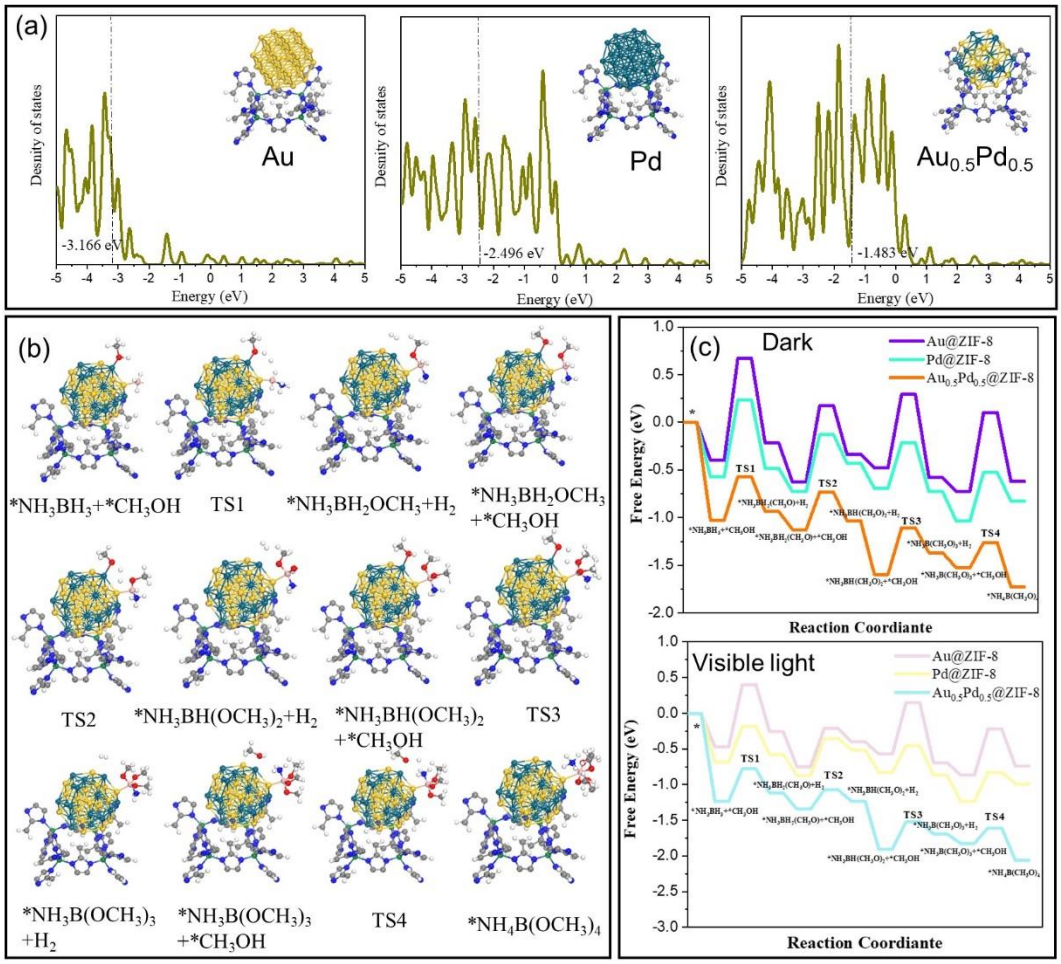

Fig. 5 DFT calculation for the free energy of NH_3BH_3 and MeOD along their reaction catalyzed by Au@ZIF-8, Pd@ZIF-8, and $Au_{0.5}Pd_{0.5}$@ZIF-8 alloy, (a) under dark (left) and (b) with visible light excitation (right).

In sum, a proposed mechanism for the plasmon-enhanced AB methanolysis catalyzed by $Au_{0.5}Pd_{0.5}$@ZIF-8 is shown in Scheme 1.

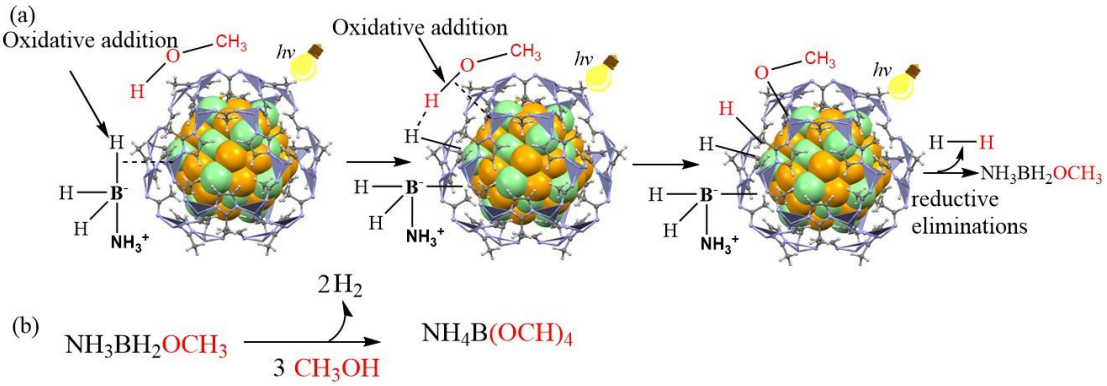

Scheme 1. Suggested mechanism for the visible-light-accelerated methanolytic dehydrogenation of AB nanocatalyzed by $Au_{0.5}Pd_{0.5}$@ZIF-8.

Hot-electron transfer and photoinduced local-field enhancement both contribute to the enhanced catalytic activity under light irradiation. The AB and CH_3OH molecules are absorbed on the surface of the NPs to form a NP/substrates complex. The plasmon-induced hot electron transfers onto the unoccupied state of the metal–CH_3OH-AB complex, and a hydrogen bond $[H_3NBH_2H]\cdots H–OCH_3$ is formed between the hydridic B–H bond of AB and the acidic H atom of methanol. This activation results in the formation of metal-BH_2NH_3, metal-OCH_3, and two metal-hydride intermediates. Reductive elimination of these metal-ligand species subsequently releases H_2 and $H_3NBH_2(OCH_3)$. The latter compound continues undergoing two similar processes to finally produce in total three equivalents of H_2 and $NH_3B(OCH_3)_3$, the methanolysis of which yields $NH_4B(OCH_3)_4$, fulfilling the stoichiometry of eq. 1.

In-situ terminal alkyne chemo-selective semi-hydrogenation reaction catalyzed by AuPd@ZIF-8

The above results showed that AB is a suitable hydrogen source, and also AuPd@ZIF-8 can be a hydrogenation catalyst. This led us to explore the potential selective catalysis including at high conversions toward the semi-hydrogenation of alkynes that is an important industrial challenge.[44–47] Therefore, the methanolysis of AB over AuPd@ZIF-8 steadily proceeding to the efficient production of pure H_2, particularly under light irradiation, the semi-hydrogenation of phenylacetylene was examined by utilizing NH_3BH_3 as hydrogen source. Significantly, compared to the 34% conversion of phenyl acetylene to styrene within 1.5 h, light irradiation further leads to its high conversion (96%)

with 93% selectivity to styrene within 20 min, based on the Au_1Pd_2@ZIF-8 catalyst. In contrast, Pd@ZIF-8 and Au@ZIF-8 give only 34% and 5% conversion in 1.5 h, respectively.

To verify the effect of Au and Pd in terms of promoting the conversion and selectivity, a series of AuPdNPs@ZIF-8 nanocatalysts with various ratios of Au and Pd was conducted in semi-hydrogenation reaction of phenylacetylene with light and under dark. As shown in Figure 5, when the hydrogenation of phenylacetylene was conducted in the dark, increasing the proportion of Au in AuPd@ZIF-8, the conversion significantly enhanced until the highest yield (96%) where the ratio of Au and Pd is 1 to 2. Accompanied by the rising conversion, the selectivity decreased to 93%, implying that the proportion of Au and Pd exert significant influence on conversion and selectivity of hydrogenation of phenylacetylene. To explore the role of ZIF-8 in the catalytic hydrogenation of phenylacetylene, ZIF-8 and AuPd@GO were employed for this reaction, but no ethylbenzene or styrene were produced with ZIF-8. The conversion and selectivity were 99% and 0 upon AuPd@GO, indicating that ZIF-8 play an important role in protecting phenylacetylene from over reduction. The high efficiency implies that the introduction of NH_3BH_3 might boost the conversion by sufficient contact between the substrate and the hydrogen donor, which *in situ* generates hydrogen active species.

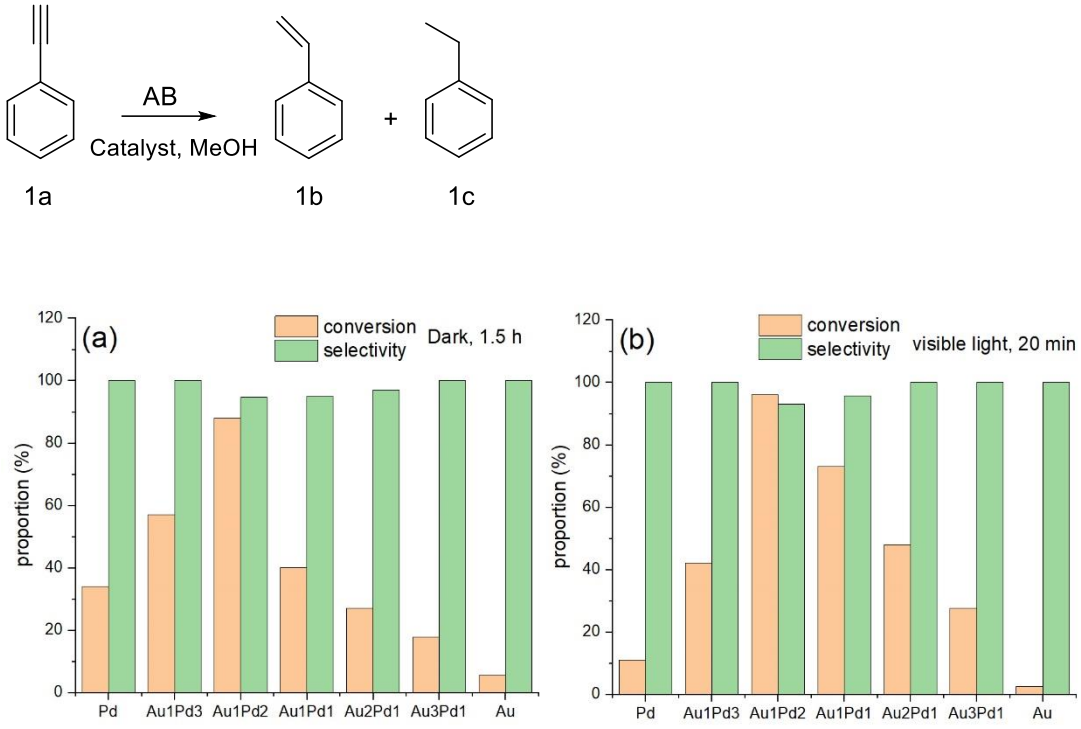

Figure 5.4. (a) Semi-hydrogenation of phenylacetylene in CH_3OH over AuPd@ZIF-8 with different ratio in the dark. (b) Semi-hydrogenation of phenylacetylene in CH_3OH over AuPd@ZIF-8 with different ratio in the presence of visible light.

In-situ internal alkyne Regio-selective semi-hydrogenation reaction catalyzed by AuPd@ZIF-8

Encouraged by the outstanding catalytic performance of Au_1Pd_2@ZIF-8 toward the semihydrogenation of phenylacetylene in terms of conversion and selectivity. The hydrogenation of the internal alkyne is attempted to obtain the cis- or tans- alkene which is an important reaction in the chemical industry. Incredibly, the product is obtained with more than 99% conversion, 93.6% chemo-selectivity and 99% regio-selectivity upon semi hydrogenation of diphenylacetylene upon AuPd@ZIF-8 (entry1). Meanwhile, for the semi hydrogenation of (phenylethynyl)ferrocenium, the conversion, chemoselevity and regioselectivity is 99%, 92% and 99%, respectively. Therefore, the ZIF-8 shell not only contributes to the stabilization of AuPd NPs but also offers the high regioselectivity via the space steric hindrance.

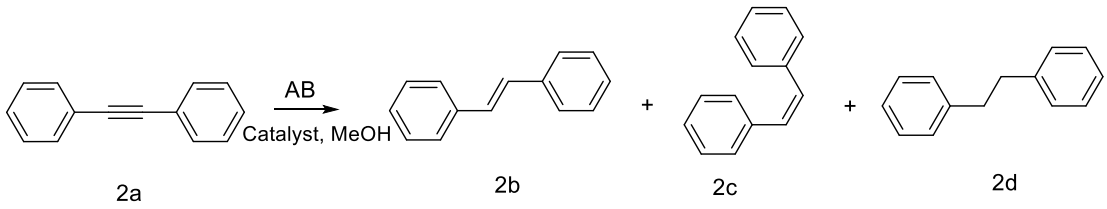

Entry	Cat.	Con. (%)	2b	2c	2d
1	Au_1Pd_2@ZIF-8	99.9	93.6	0	5.3
2	Au_1Pd_2@GO	99.9	0	0	99.9

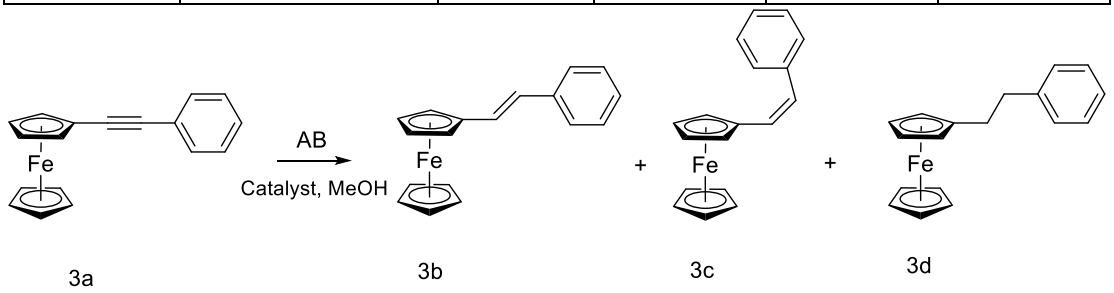

Entry	Cat.	Con. (%)	2b	2c	2d
1	Au_1Pd_2@ZIF-8	99.9	92.4	0	7.9
2	Au_1Pd_2@GO	99.9	0	0	99.9

5.3.Conclusion

Whereas Au@ZIF-8 does not catalyze AB methanolytic dehydrogenation, alloying Au with various metals allows partial H_2 evolution using this reaction in the dark, best conducted with AuPt and AuPd alloys. Upon light irradiation, neither Au@ZIF-8 nor Pd@ZIF-8-catalyzed reaction is improved compared to reactions in the dark, but the system is considerably boosted upon visible-light illumination, the best alloyed nanocatalyst being, after optimization, $Au_{0.5}Pd_{0.5}$@ZIF-8. Comparison between various supports including ZIF-8, ZIF-67, UIO-66, and GO shows rate superiority but instability of GO (incomplete H_2 evolution due to aggregation), whereas ZIF-8 largely overtakes the other supports under visible light with complete evolution of 3 mol H_2. By varying the proportions of Au and Pd, Au_1Pd_1 alloy was found to exhibit maximum rate enhancement (more than 3.7 folds) and superior catalytic activity with a reaction rate of 500 μmol min^{-}

[1] at room temperature. The contribution of hot electron transfer, photoinduced thermal effects, and the photoinduced local-field enhancement to plasmon-enhanced methanolysis of AB have been discussed. Excitation of the Au plasmon upon visible-light illumination inducing hot electron transfer from Au to the Pd-AB-methanol adsorbate along with the hydrogen bond $[H_3NBH_2H]\cdots H–OCH_3$ provokes oxidative addition of the O-H bond in methanol, the rate-determining step leading the H_2 production. This mechanism is ascertained by isotope labelling in a tandem hydrogenation reaction, kinetic isotope effect and DFT calculations. The dramatic rate enhancement provoked by irradiation precisely corresponding to the visible-light wavelengths of plasmon gold alloy activity illustrates the difficulty of methanol O-H bond activation requiring more driving force compared water O-H bond activation upon AB hydorlysis. Nevertheless, the cleanness of the hydrogen produced in this system and the recyclability of the product $NH_4B(OCH_3)_4$ offer here with a good choice for the potential design of low temperature devices.

5.4. Experimental section

Materials

Potassium tetrachloroaurate, sodium tetrachloropalladate, zirconium tetrachloride sodium borohydride, acetic acid, zinc nitrate hexahydrate, *p*-phthalic acid, cobalt nitrate hexahydrate, 2-methylimidazole, methanol (> 99.9% HPLC), and methanol-D4 (>99.95%, NMR) were purchased from Sigma-Aldrich. Graphene oxide (GO) was prepared according to Hummers' method[34]. All flasks were washed by aqua regia (HCl: HNO_3 = 3:1) and acetone. All solutions and reagents were prepared using ultrapure water from Barnstead Nanowater purification system (Thermo Fisher Scientific Inc., USA).

Preparation of the nanocatalysts

Generally, 100 mg ZIF-8 NPs dispersed in 5 mL water and 5 mL methanol mixture were injected into a 50-mL Schlenk flask under argon. The compositions of the AuPd alloy NPs were adjusted by varying the molar ratios of the precursors. This mixture was stirred continuously at room temperature for 2 h. After degassing this solution for 10 min, 1 mL aqueous solution of freshly prepared $NaBH_4$ (10 equiv. per equiv. metal) was quickly added. The mixture was allowed to further stir for another 30 min, and the resulting nanocatalyst

was collected by centrifugation and washed with deoxygenated methanol, and then dried at 60°C *in vacuo* overnight. The metal content was quantified by inductively coupled plasma atomic emission spectroscopy (ICP-AES). For the synthesis of AuPd NPs stabilized by other supports, the steps were similar to those used for AuPd@ZIF-8.

Catalysis of the AB methanolysis by AuPd @ZIF-8 in the dark reaction

Under dark reaction conditions, the methanolysis of AB was conducted in a 50-mL Schlenk flask at 25 ± 0.2 °C. Specifically, 50 mg AuPd@ZIF-8 catalyst was added into a flask with 4 mL water, then 1mL of the aqueous solution of AB was added into the solution. In the standard treatment, the content of MNPs was 1.25% mmol per mmol AB, the ratio between Au and Pd was 1 to 1, and the concentration of AB was 1 mmol. The reaction time and determination of the volume of H_2 produced began when importing the AB solution using a needle.

Catalysis of AB methanolysis by AuPd @ZIF-8 under visible-light irradiation

The photocatalytic reactions were performed by using the 7 W visible LED strips (Sunshine Lighting Limited, France) at a light intensity of 1540 lx (each) with a wavelength of 550 nm. The LED lamps were turned on for 15 min prior to irradiation to guarantee a stable light intensity. All the reactions under visible light were conducted in a condensate circulation system in order to keep the temperature at 25 ± 0.2°C. The thermometer was placed inside the reaction cell. The dosage of catalyst and AB concentrations were the same as in dark reactions, and the other steps were also kept the same.

Hydrogenation of styrene catalyzed by AuPd@ZIF-8 in tandem reaction

A sealed two-chamber system with two stirring bars was prepared. AB (1.0 mmol, 30.87 mg), AuPd@ZIF-8 (17mg, 1.25 mmol% per AB) and 2 mL CD_3OD were added into the left tube. AuPd@ZIF-8 catalyst (15 mg, 2 mmol % per styrene) and styrene (0.5 mmol, 52 mg) in 2 ml CD_3OD were added into the right tube. After removing the air *in vacuo*, the reaction mixture was stirred for 12h tat room temperature. Then, the solution in the right tube was collected by centrifugation for analysis by ^{1}H NMR and GC-MS analysis without any further treatment.

DFT calculations

The DFT methods are known to furnish an acceptable compromise between accuracy and applicability in large cell systems. Therefore, the ZIF-8 models have been simplified for ZIF-8 complex structures. Au@ZIF-8, Pd@ZIF-8 and AuPd@ZIF-8 have been established with the simplified ZIF-8 and 38 metal cluster atoms (Au cluster, Au cluster and alloyed AuPd models). All spin-polarized calculations based on density functional theory (DFT) were performed utilizing DMol3 package [35]. The generalized gradient approximation (GGA) in the Perdew–Burke–Ernzerhof form and Semicore Pseudopotential method (DSPP) with the double numerical basis sets plus the polarization functional (DNP) were adopted [36]. The electronic properties, including density of states, electron density, orbitals and population analysis, in dye free form, have been studied. The double numerical basis set DNP has been used to predict dye electronic properties. In order to simplify the calculation, it has been considered that under the condition of illumination, the electrons of the structure are excited. Therefore, the excited state for structure has been adopted to simulate the light effect. The photon energy of the wavelength of light used in the experiment is sufficient to reach the first excited states of Pd and Au. Thus, the Singlet option with 1st excited state has been chosen. In addition, a DFT-D correction with Grimme scheme was used to account for the dispersion interaction [37]. The SCF convergence for each electronic energy was set as 1.0×10^{-5} Ha, and the geometry optimization convergence criteria were set up as follows: 1.0×10^{-5} Ha for energy, 0.001 Ha $Å^{-1}$ for force, and 0.01 Å for displacement, respectively. Energy barriers were examined by linear and quadratic synchronous transit methods in combination with the conjugated gradient (CG) refinement. The free energies were obtained by $G=E_{total}+E_{ZPE}-TS$, where E_{total}, E_{ZPE} and TS are the ground-state energy, zero-point energies, and entropy terms, respectively, with the latter two taking vibration frequencies from DFT. Finally, the reaction energies (G) of different intermediates are defined as $\Delta G=G_i-G_{reactant}$ (G_i is the energy of intermediates and $G_{reactant}$ is the total energy of reactants).

Materials and methods

-**Transmission Electron Microscopy (TEM)** and **high-resolution TEM (HRTEM)** were recorded using TEM JEOL JEM 1400 (120 kV)- 2100F.

-**Energy-dispersive X-ray Spectroscopy (EDS)** images were recorded using TEM-JEM-ARM200F Cold FEG equipped with a EDX spectrometer.

-**X-ray photoelectron spectra (XPS) System**: SPECS SAGE HR, X-Ray source: Mg Kα non-monochromatic, operated at 12.5 kV and 250 W. Take-off angle 90°, at ~10^{-8} Torr. Pass energy for survey spectra 30 eV, 15 eV for narrow scans. Analysis: spectra are calibrated to CC carbon 285 eV. Analysis consisted of Shirley background subtraction. Peaks are fitted with symmetrical Gaussian-Lorentzian (GL) line shapes. Samples were dispersed on a silica substrate, and its solvent was evaporated before measurement.

-**NMR spectra** were recorded at 25 °C with a Bruker AC 300, or 400 (300 or 400 MHz). All the chemical shifts are reported in parts per million (δ, ppm) concerning Me_4Si for the 1H NMR spectra

-**Inductively coupled plasma atomic emission spectroscopy (ICP-AES)**: Thermo Scientific iCAP 6300 DUO spectrometer with a 3-channel, 12-roller pump and a 27.12 MHz solid state RF plasma generator.

-**BET** areas were recorded with a 30% v/v N_2/He flow using pure N_2 (99.9%) as internal standard. At least 2 cycles of N_2 adsorption-desorption in the flow mode were employed to determine the total surface area using the standard single point method.

-**Finite-Difference-Time-Domain (FDTD**) calculations were performed by using Comsol Multiphysics 5.6 (COMSOL, Inc.) with perfectly matched layers (PML) boundary conditions. For these simulations, a total-field scattered-field (TFSF) light source with wavelength ranges from 300 nm to 700 nm was used. The optical constant (n) of the AuPd@ZIF was according to the literature [1]. The size of the alloy and nanoparticle spacing were measured via TEM maps.

Synthesis of the ZIF-8 and ZIF-67

The method used for the preparation of ZIF-8 followed that reported previously [2]. Specifically, 2-methylimidazole (0.25 mol, 22.95 g) was dissolved in 250 mL methanol and stirred at room temperature to form a homogeneous solution. Then, an aqueous solution of $Zn(NO_3)_2 \cdot 6H_2O$ (13.7 g, 0.25 mol) dissolved in 250 mL methanol was rapidly injected into the above aqueous solution. The mixture was stirred for 8 h, and the product was collected by centrifugation and washed 3 times with water. The obtained solid was then

dried at 60 °C *in vacuo* overnight, and the white solids were collected for further use. The synthesis methods of ZIF-76 is as same as the ZIF-8 with replace $Zn(NO_3)_2 \cdot 6H_2O$ with $Co(NO_3)_2 \cdot 6H_2O$.

Synthesis of the UIO-66.

In a 250 mL Erlenmeyer flask, $ZrCl_4$ (334 mg) and CH_3COOH (7 mL) were completely dissolved in DMF (50 mL) under ultrasonic conditions. Then, *p*-phthalic acid (250 mg) dissolved in DMF (50 mL) was added to the aforementioned solution. The resulting mixture was sonicated for 10 min and kept at 120 °C for 24 h. After cooling to room temperature, the UIO-66 crystals were finally obtained by centrifugation and repeatedly washed with DMF [3].

H_2 detection. The reaction flask was connected by the gas outlet to a water-filled gas burette. When the gas was generated, the volume of gas evolved was determined periodically by measuring the displacement of water in the burette. In our two cases, 1 mmol AB produced 3 mmol H_2, corresponding to 67 H_2 at atmospheric pressure. Prior to the reactions, the volumes were measured at atmospheric pressure and corrected for water vapor pressure at room temperature. Every reaction has been conducted three times, and the results are averaged.

NH_3 gas detection.

The gas generated from the methanolysis was passed through a 25 mL standard HCl solution (0.01 M) at room temperature, by which the ammonia gas was captured. After gas generation ceased, the resulting solution was titrated with standard NaOH solution (0.01 M) using the acid-base indicator phenolphthalein. The quantity of the liberated ammonia gas was calculated from the difference between two HCl solutions before and after the reaction.

TOF Calculation.

$TOF = mol_{H2\ released}/(\text{total } mol_{cat.} \times \text{reaction time (min)})$

TOF_s: the TOF value is related to the NP surface atoms number (Ns)

$V_{NP} = NV_{atom}$ (eq. 1)

$4/3\pi(R_{NP})^3 = N\ 4/3\pi(R_{atom})^3$ (eq. 2)

Where V is the atom volume of the NP, R is the atomic radius of the NP, and N is the total number of atoms within the NP. Rearranging, we obtain:

$N = (R_NP/R_{atom})^3$ (eq. 3)

Knowing the NP radius, we can also calculate the surface area (S) of a NP with the following equation:

$S_{NP} = 4\pi(R_{NP})^2$ (eq. 4)

So, we may also calculate the number of surface atoms (Ns) directly by dividing the surface area of the NP by the cross section of an individual NP atom and then simplifying using the relationship in (eq. 3):

$N_s = (4\pi(R_{NP})2) / (\pi\ (R_{atom})2) = 4\ N\ (R_{atom}/R_{NP})$ (eq. 5)

The ratio of the $N_s/N = 4\ (R_{atom}/R_{NP})$

So $TOF_s = TOF/(N_s/N)$

Characterization of nanocatalysts

Table S5.1. Metal loading and atomic ratios of a series of catalysts measured by ICP-AES

Catalyst	Metal loading (wt%)	Atomic ratios
Au@ZIF-8	6.5	-
Pd@ZIF-8	4.2	-
$Au_{0.33}Pd_{0.67}$@ZIF-8	4.8	1:1.7
$Au_{0.25}Pd_{0.75}$@ZIF-8	4.5	1:2.6
$Au_{0.67}Pd_{0.33}$@ZIF-8	6.1	2.3:1
$Au_{0.5}Pd_{0.5}$@ZIF-8	5.7	1.1:1

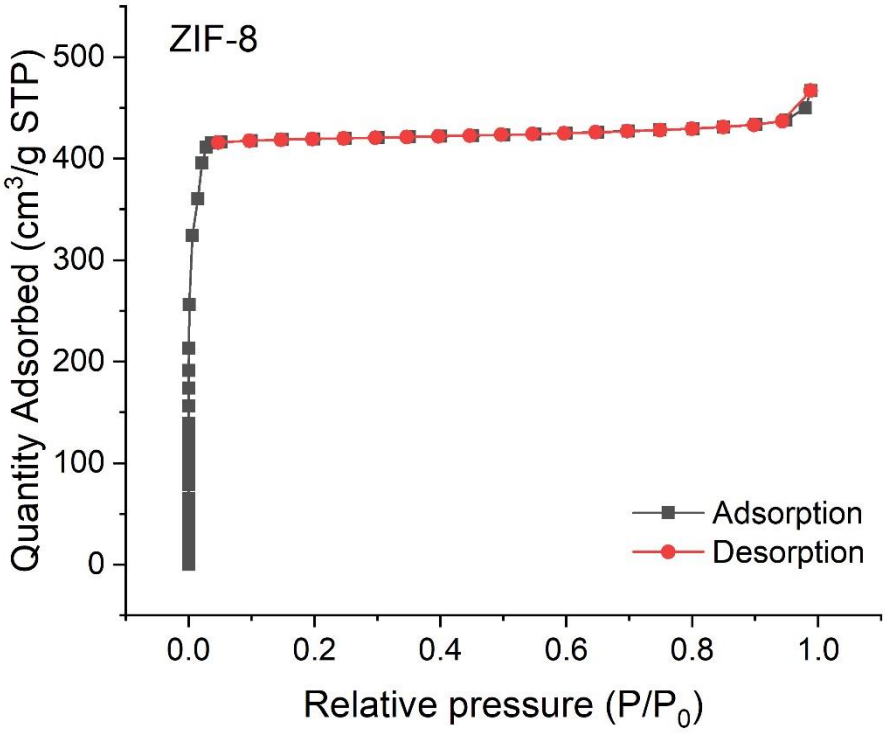

Fig. S5.1. Nitrogen adsorption-desorption isotherms of ZIF-8

Table S5.2. Physical properties of ZIF-8 and $Au_{0.5}Pd_{0.5}$@ZIF-8.

Sample	BET surface area ($m^2 \cdot g^{-1}$)	Pore width (nm)	Pore volume ($cm^3 \cdot g^{-1}$)
ZIF-8	1787.3	1.6	0.661
$Au_{0.5}Pd_{0.5}$@ZIF-8	1269.0	1.6	0.594

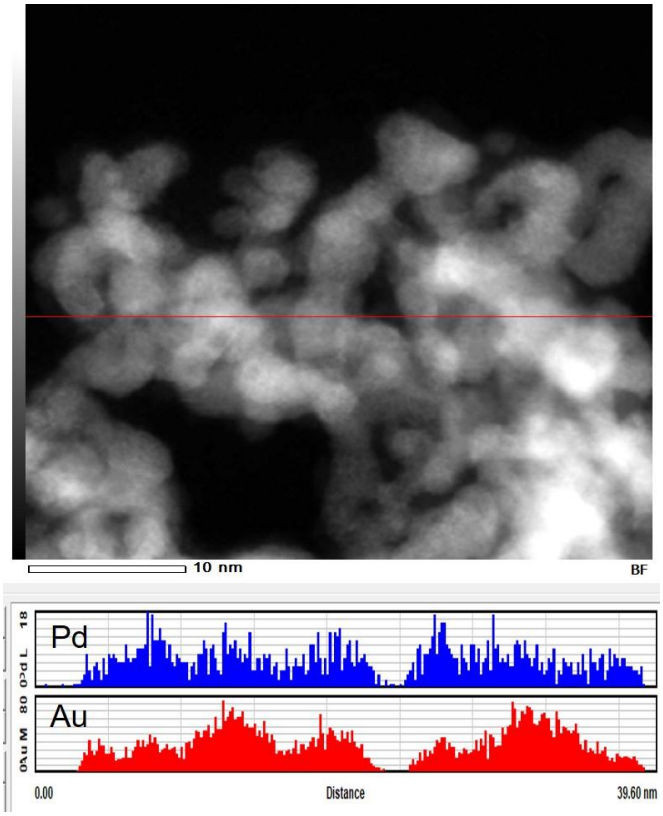

Fig. S5.2. HAADF-STEM image of AuPd@ZIF-8 and distributions of Au and Pd along cross-section lines.

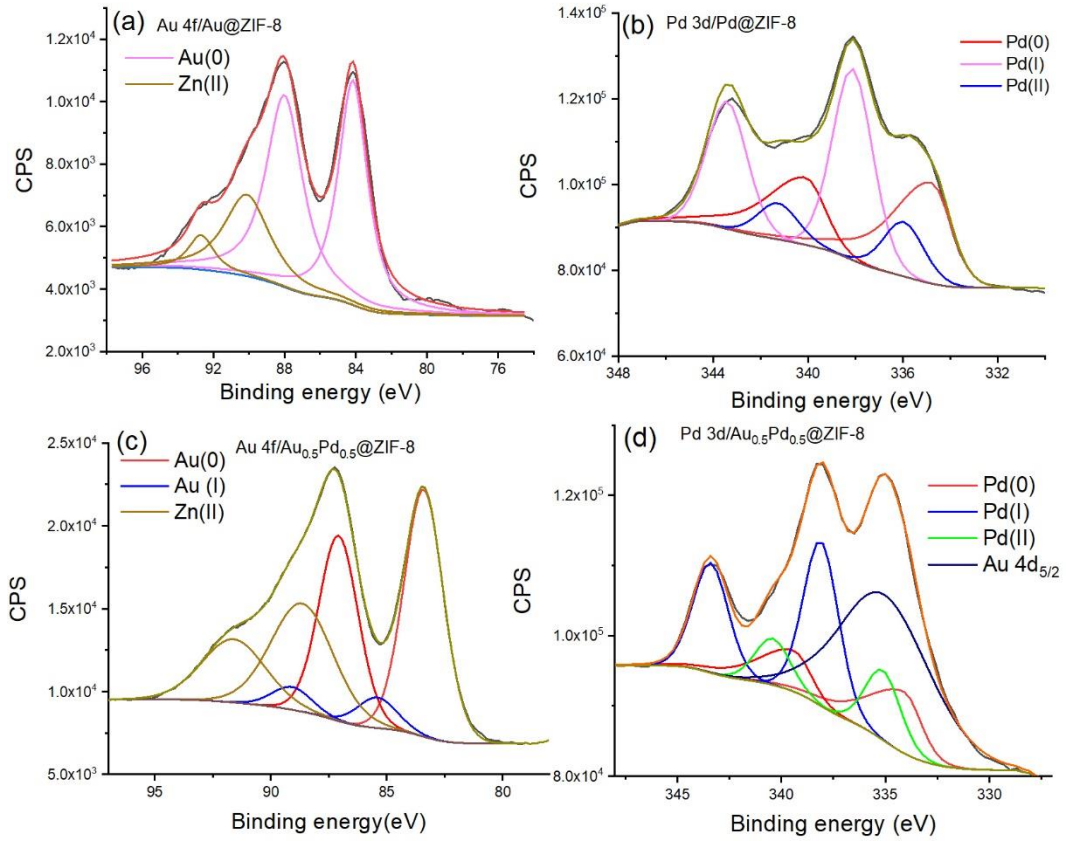

Fig. S5.3. (a) XPS spectra of Au@ZIF-8 in the Au 4f region, (b) XPS spectra of Pd@ZIF-8 in the Pd 3d region, (c) XPS spectra of $Au_{0.5}Pd_{0.5}$@ZIF-8 in the Au 4f region, (d) XPS spectra of $Au_{0.5}Pd_{0.5}$@ZIF-8 in the Pd 3d region.

Table S5.3. Binding energies of Au(0) and Pd(0) in Au 4f anf Pd 3d regions.

Samples	Au $4f_{7/2}$	Au $4f_{5/2}$	Pd $3d_{5/2}$	Pd $3d_{1/2}$
Au@ZIF-8	84.0	87.9	/	/
Pd@ZIF-8	/	/	334.9	340.2
$Au_{0.5}Pd_{0.5}$@ZIF-8	83.4	87.1	334.3	339.6

Methanolysis of Ammonia borane

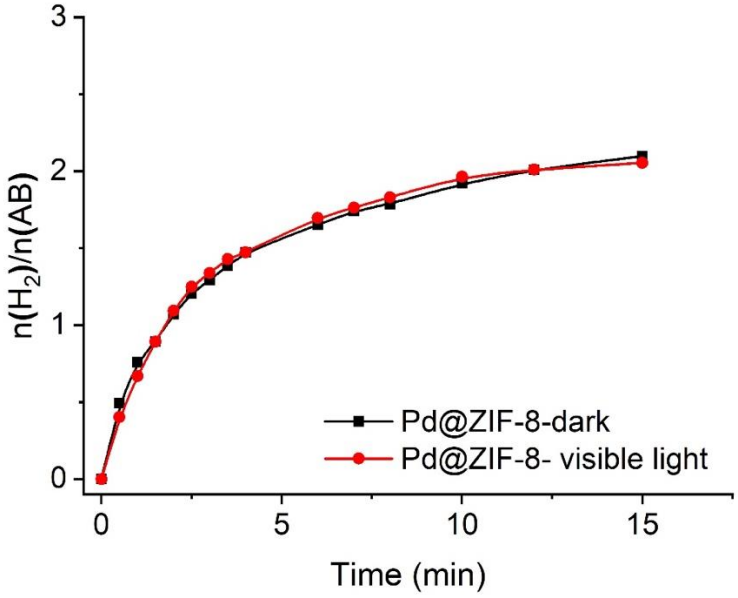

Fig. S5.4. Plot of the molar amount of H_2 generated upon AB methanolysis vs. time catalyzed by Pd@ZIF-8 with visible light and dark.

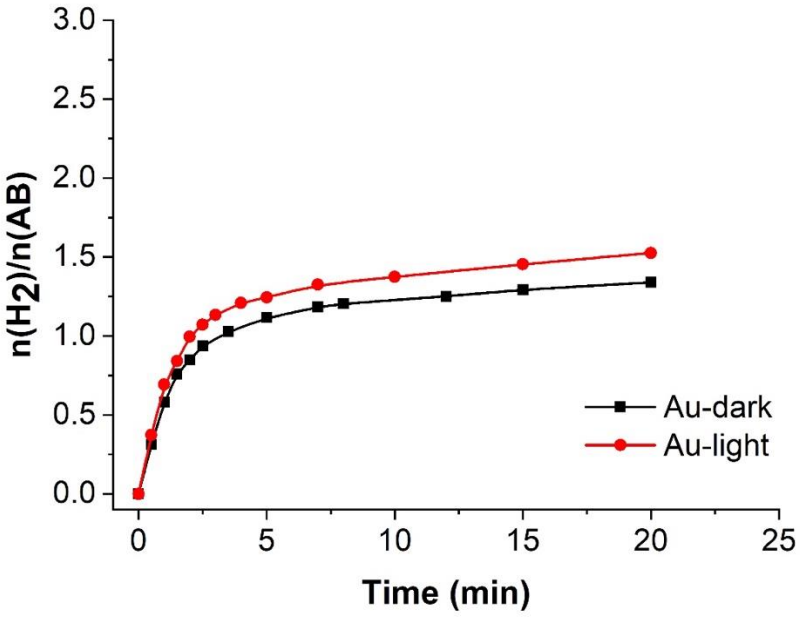

Fig. S5.5. Plot of the molar amount of H_2 generated upon AB methanolysis vs. time catalyzed by Au@ZIF-8 with visible light and dark.

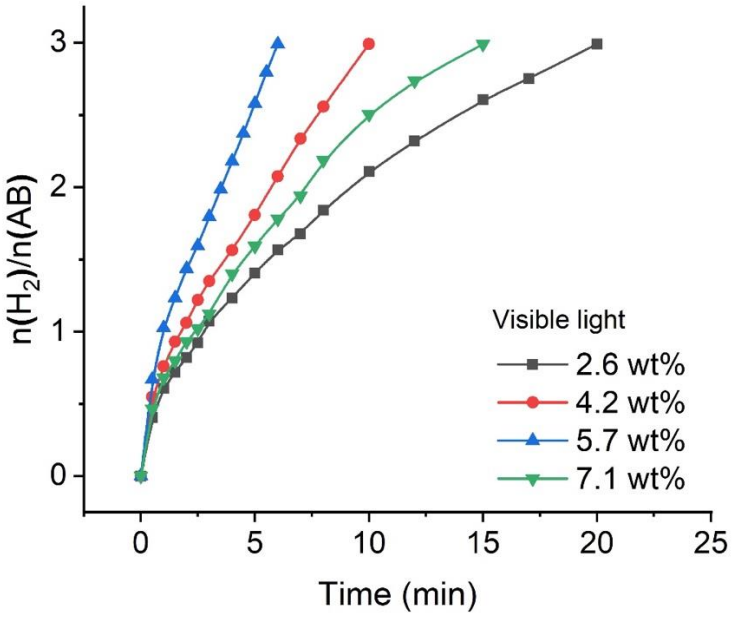

Fig. S5.6. Plot of molar amount of H_2 generated from AB methanolysis vs. time taken by different ZIF-8-stabilized Au-base bimetallic catalysts with different AuPd loading under visible light.

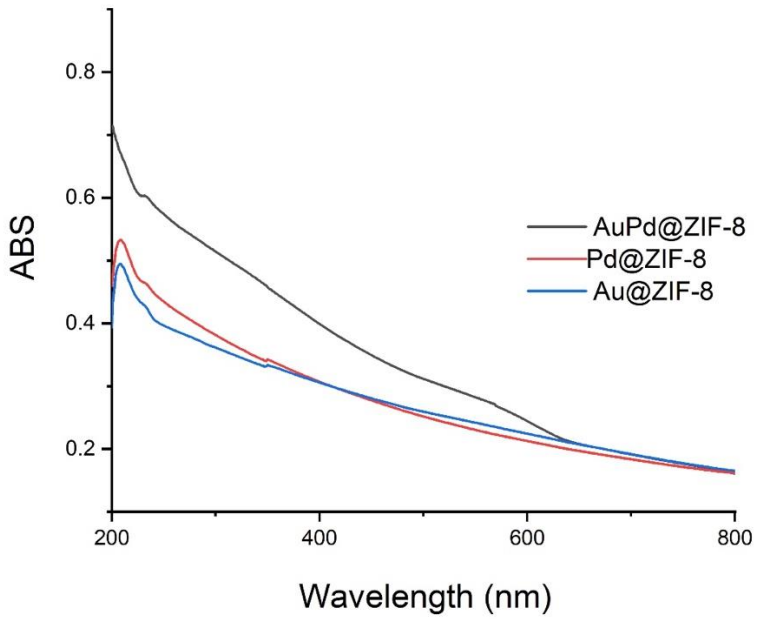

Fig. S5.7. UV-vis. spectra of Au@ZIF-8, $Au_{0.5}Pd_{0.5}$@ZIF-8, and Pd@ZIF-8.

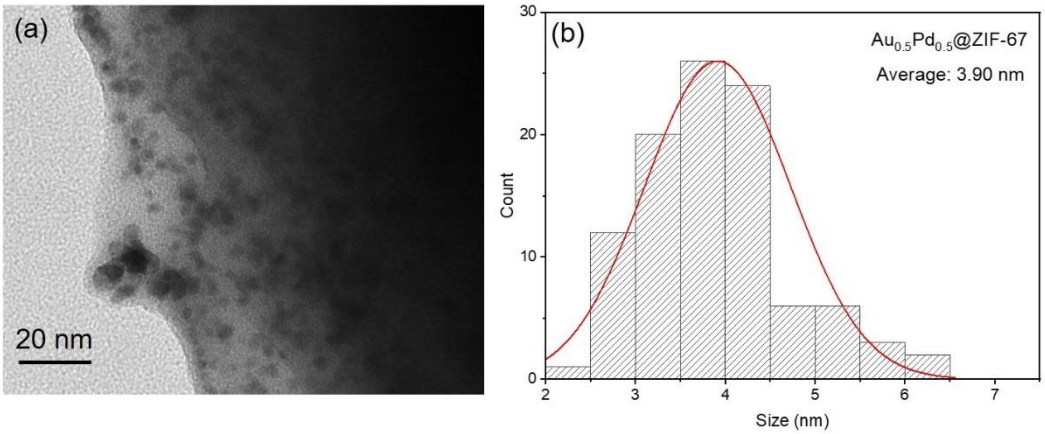

Fig. S5.8. (a) TEM image and (b) histogram of size distribution of the AuPd@ZIF-67.

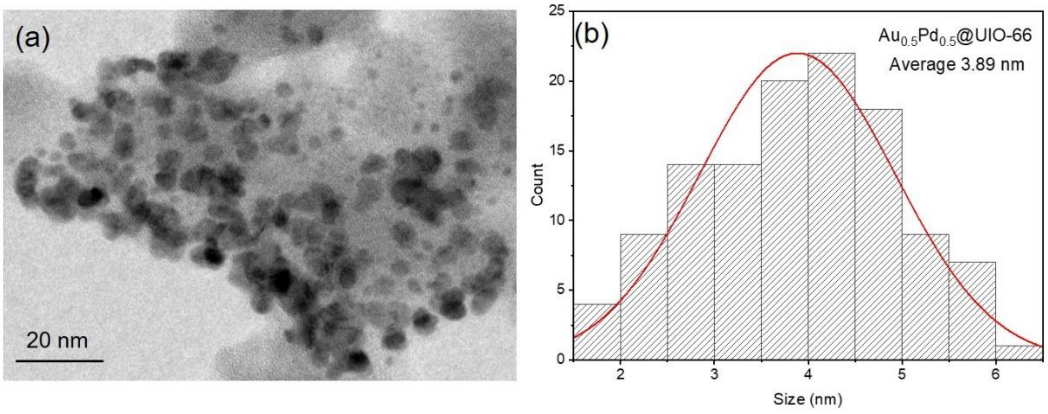

Fig. S5.9. (a) TEM image and (b) histogram of size distribution of the AuPd@UIO-66.

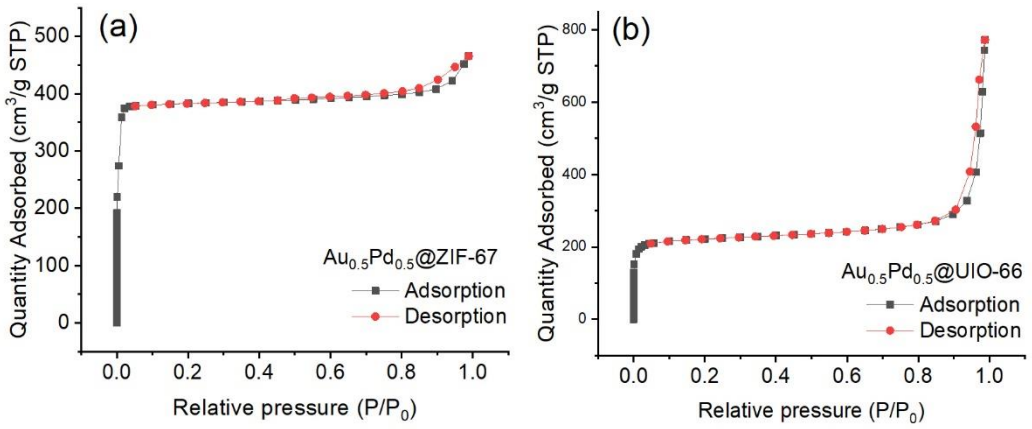

Fig. S5.10. Nitrogen adsorption-desorption isotherms of the AuPdNPs on different support (a) ZIF-67 and (b) UIO-66.

Table S4. Physical Properties of the AuPdNPs on ZIF-8, ZIF-67 and UIO-66.

Sample	BET surface area ($m^2 \cdot g^{-1}$)	Pore width (nm)	Pore volume ($cm^3 \cdot g^{-1}$)
$Au_{0.5}Pd_{0.5}$@ZIF-8	1269.0	1.6	0.594
$Au_{0.5}Pd_{0.5}$@ZIF-67	1511.3	1.7	0.671
$Au_{0.5}Pd_{0.5}$@UIO-66	877.0	5.4	0.780

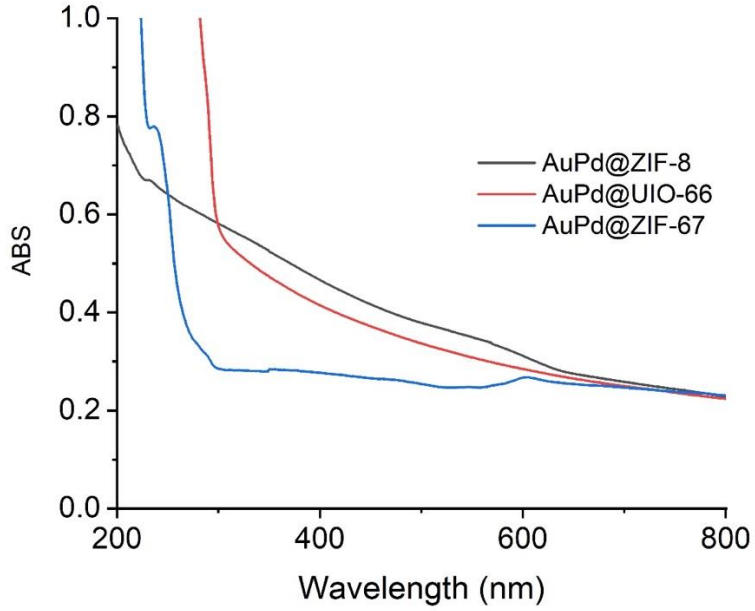

Fig. S5.11. UV-vis. spectra of $Au_{0.5}Pd_{0.5}$@ZIF-8, $Au_{0.5}Pd_{0.5}$@UIO-66 and $Au_{0.5}Pd_{0.5}$@ZIF-67.

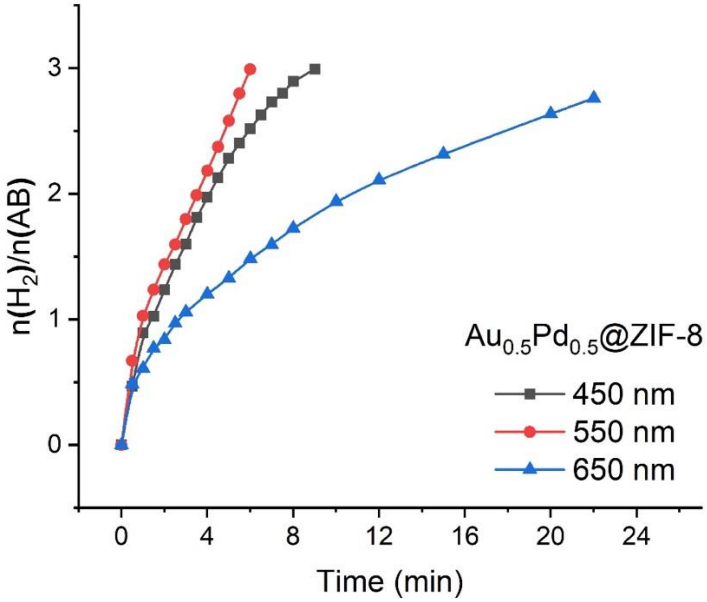

Fig. S5.12. AB methanolysis catalyzed by $Au_{0.5}Pd_{0.5}$@ZIF-8 under visible light irradiation with different wavelength.

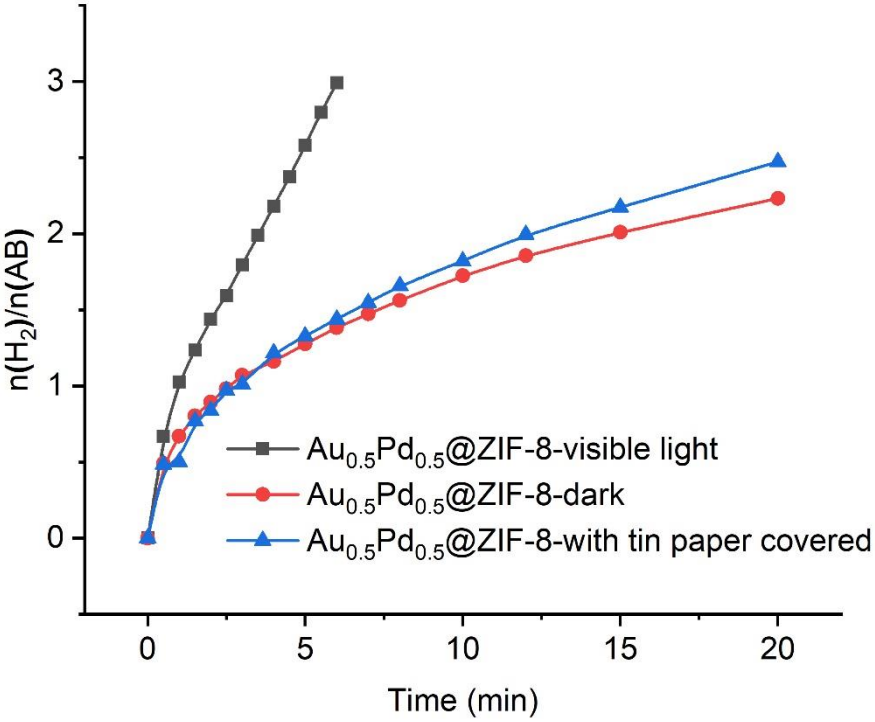

Fig. S5.13. Plot for molar amount of H_2 generated from AB methanolysis vs. time taken by AuPd@ZIF-8 under visible light irradiation, dark and tin paper covered.

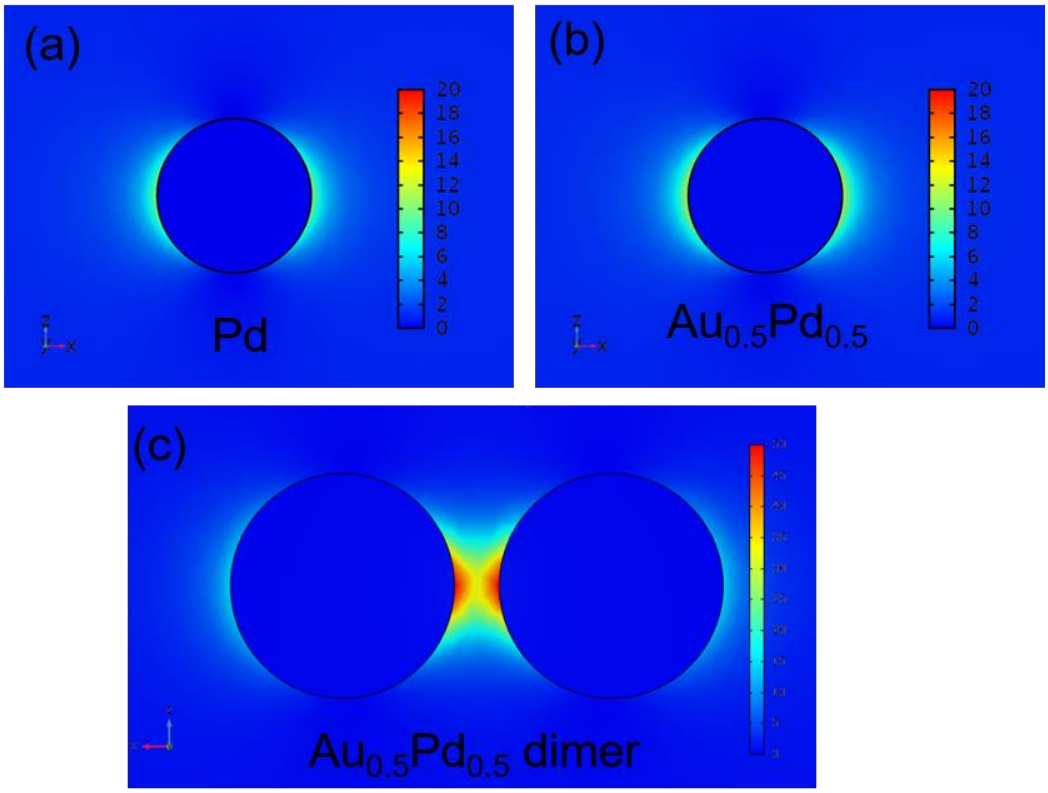

Fig. S5.14. Spatial distribution of the SPR-induced enhancement of electric field intensity from FDTD simulation calculated at the plasmon peak for (a) Pd (b) $Au_{0.5}Pd_{0.5}$ and $Au_{0.5}Pd_{0.5}$ dimer.

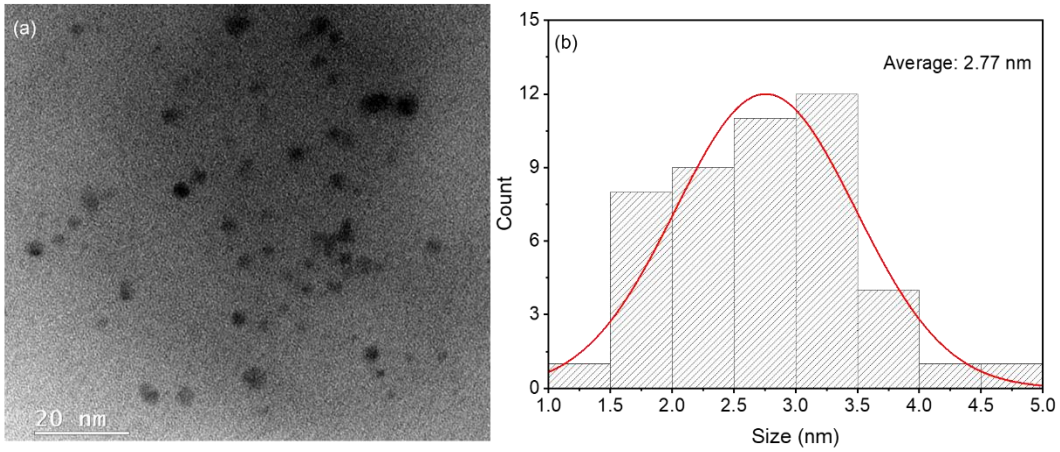

Fig. S5.15. (a) TEM image and (b) size distribution of the $Au_{0.5}Pd_{0.5}$@ZIF-8 after reaction.

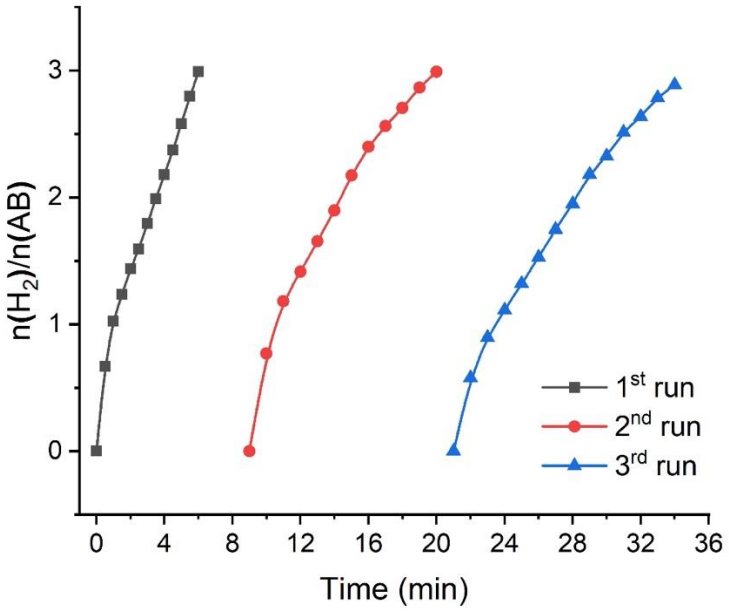

Fig. S5.16. Time plots of H_2 evolution for AB methanolysis catalyzed by $Au_{0.5}Pd_{0.5}$@ZIF-8 in the first, second, and third recycling tests with visible light irradiation.

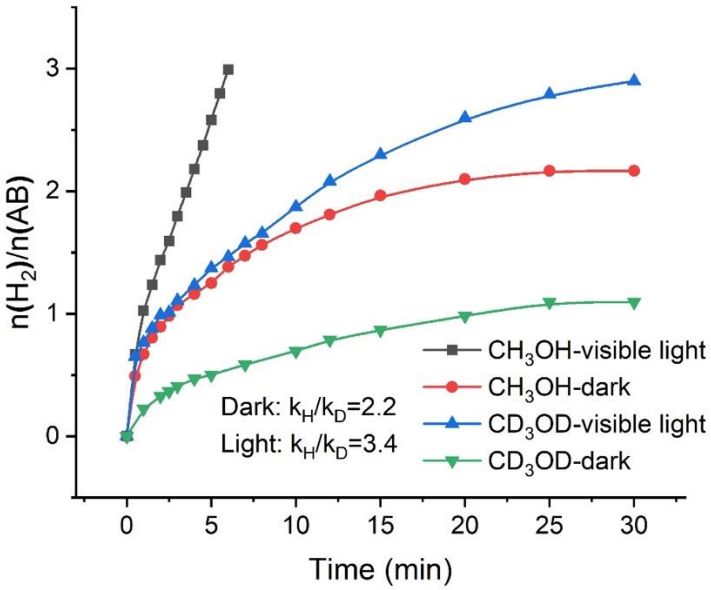

Fig. S5.17. Evolution of H_2 upon AB methanolysis with CH_3OH and CD_3OD catalyzed by $Au_{0.5}Pd_{0.5}$@ZIF-8 under visible light and dark.

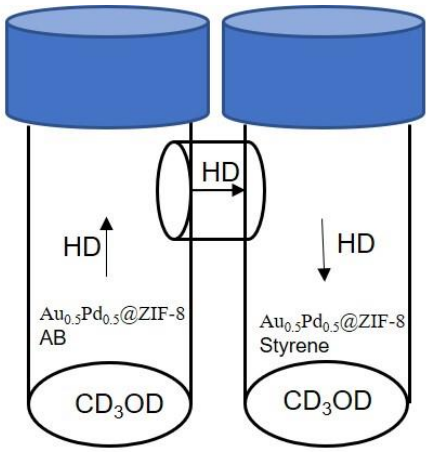

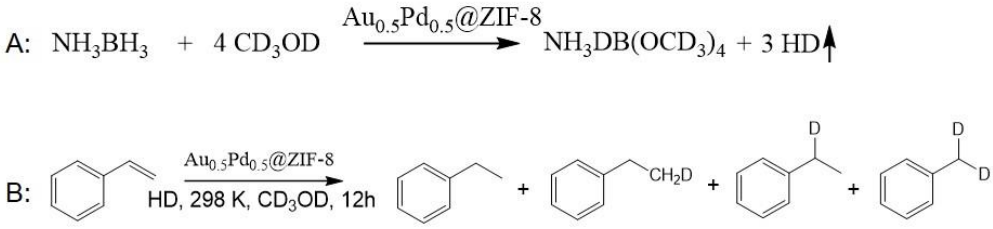

Fig. S5.18. Tandem reaction for the hydrogenation with “HD” generated from AB methanolysis catalyzed by $Au_{0.5}Pd_{0.5}$@ZIF-8.

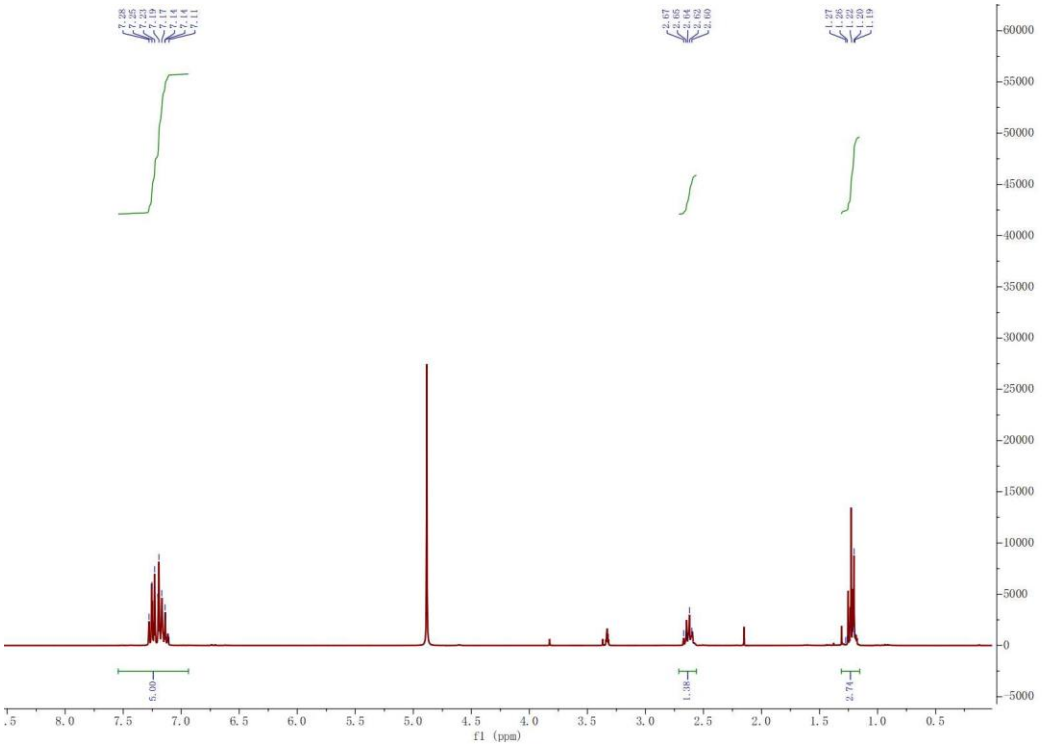

Fig. S5.19. ^{1}H NMR spectrum of ethylbenzene generated from the hydrogenation of styrene in tandem reaction ^{1}H NMR (300 MHz, CD_3OD), δ 7.31-7.12 (aromatic H, 5H), 2.67-2.60 (-CH_2, 1.38H), 1.27-1.19 (-CH_3, 2.74H).

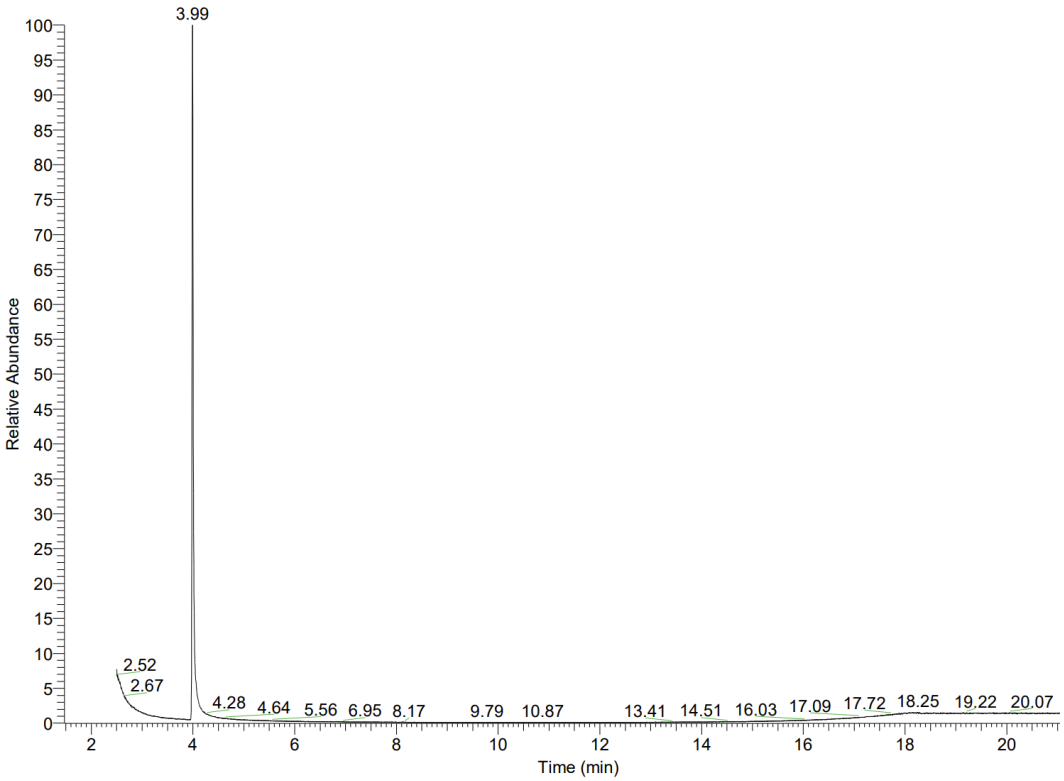

Fig. S5.20. GC-MS spectrum of the hydrogenation product of styrene.

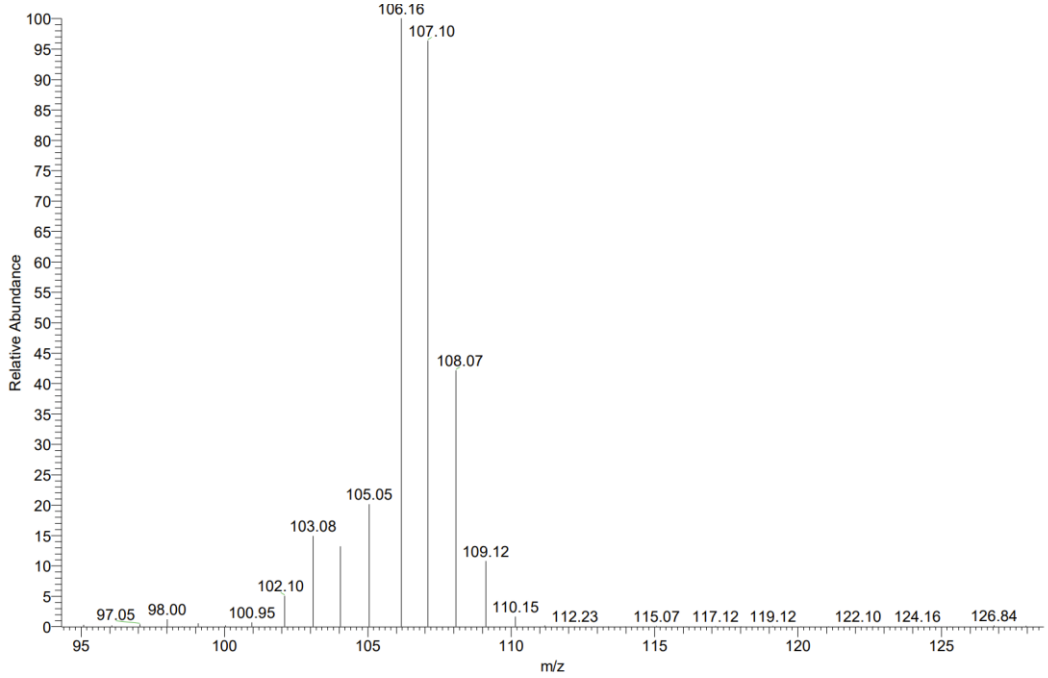

Fig. S5.21. MS spectrum at 3.99 min in Fig.S20 m/z 107.1 ($C_6H_5CHDCH_3$, $C_6H_5CHCH_2D$)

5.5 References

[1] T. He, P. Pachfule, H. Wu, Q. Xu, P. Chen, Hydrogen carriers, Nat. Rev. Mater. 1 (2016) 16059.

[2] M. Yue, H. Lambert, E. Pahon, R. Roche, S. Jemei, D. Hissel, Hydrogen energy systems: A critical review of technologies, applications, trends and challenges, Renew. Sustain. Energy Rev. 146 (2021) 111180.

[3] M. Yadav, Q. Xu, Liquid-phase chemical hydrogen storage materials, Energy & Environ. Sci. 5 (2012) 9698–9725.

[4] Z. Huang, T. Autrey, Boron-nitrogen-hydrogen (BNH) compounds: recent developments in hydrogen storage, applications in hydrogenation and catalysis, and new syntheses, Energy Environ. Sci. 5 (2012) 9257–9268.

[5] C. Wang, D. Astruc, Recent developments of nanocatalyzed liquid-phase hydrogen generation, Chem. Soc. Rev. 50 (2021) 3437–3484.

[6] R. Lan, J.T.S. Irvine, S. Tao, Ammonia and related chemicals as potential indirect hydrogen storage materials, Int. J. Hydrogen Energy. 37 (2012) 1482–1494.

[7] C. Wang, Q. Wang, F. Fu, D. Astruc, Hydrogen generation upon nanocatalyzed hydrolysis of hydrogen-rich boron derivatives: recent developments, Acc. Chem. Res. 53 (2020) 2483–2493.

[8] A. Staubitz, A.P.M. Robertson, I. Manners, Ammonia-Borane and Related Compounds as Dihydrogen Sources, Chem. Rev. 110 (2010) 4079–4124.

[9] D. Astruc, Introduction: Nanoparticles in Catalysis, Chem. Rev. 120 (2020) 461–463.

[10] L. Liu, A. Corma, Metal catalysts for heterogeneous catalysis: from single atoms to nanoclusters and nanoparticles, Chem. Rev. 118 (2018) 4981–5079.

[11] Q. Sun, N. Wang, Q. Xu, J. Yu, Nanopore-Supported Metal Nanocatalysts for Efficient Hydrogen Generation from Liquid-Phase Chemical Hydrogen Storage Materials, Adv. Mater. 32 (2020) 2001818.

[12] M. Rakap, The highest catalytic activity in the hydrolysis of ammonia borane by poly(N-vinyl-2-pyrrolidone)-protected palladium-rhodium nanoparticles for hydrogen generation, Appl. Catal. B-Environ. 163 (2015) 129–134.

[13] Y.-H. Zhou, X. Cao, J. Ning, C. Ji, Y. Cheng, J. Gu, Pd-doped Cu nanoparticles

confined by ZIF-67@ZIF-8 for efficient dehydrogenation of ammonia borane, Int. J. Hydrogen Energy. 45 (2020) 31440–31451.

[14] X. Zhao, H. Hu, G. Li, J. Cai, Y. Wang, G. Fan, Low-temperature control over deposition of ultrafine Pd nanoparticles on porous carbon nanosheets for highly efficient dehydrogenation of ammonia borane, J. Alloys Compd. 912 (2022). https://doi.org/10.1016/j.jallcom.2022.165076.

[15] C. Wang, X. Liu, C.Wu, D. Astruc, PtNi@ ZIF-8 nanocatalyzed high efficiency and complete hydrogen generation from hydrazine borane: origin and mechanistic insight, J. Mater. Chem. A. (2022)17614-17623.

[16] F. Fu, C. Wang, Q. Wang, A.M. Martinez-Villacorta, A. Escobar, H. Chong, X. Wang, S. Moya, L. Salmon, E. Fouquet, J. Ruiz, D. Astruc, Highly Selective and Sharp Volcano-type Synergistic Ni2Pt@ZIF-8-Catalyzed Hydrogen Evolution from Ammonia Borane Hydrolysis, J. Am. Chem. Soc. 140 (2018) 10034–10042.

[17] Q. Wang, F. Fu, S. Yang, M. Martinez Moro, M. de los A. Ramirez, S. Moya, L. Salmon, J. Ruiz, D. Astruc, Dramatic Synergy in CoPt Nanocatalysts Stabilized by "Click" Dendrimers for Evolution of Hydrogen from Hydrolysis of Ammonia Borane, ACS Catal. 9 (2019) 1110–1119.

[18] P.V. Ramachandran, P.D. Gagare, Preparation of ammonia borane in high yield and purity, methanolysis, and regeneration, Inorg. Chem. 46 (2007) 7810–7817.

[19] S. B. Kalidindi, U. Sanyal, B. R. Jagirdar, Nanostructured Cu and Cu@Cu_2O core shell catalysts for hydrogen generation from ammonia–borane, Phys. Chem. Chem. Phys. 2008, 10, 5870-5874.

[20] S.B. Kalidindi, A.A. Vernekar, B.R. Jagirdar, Co–Co 2 B, Ni–Ni_3B and Co–Ni–B nanocomposites catalyzed ammonia–borane methanolysis for hydrogen generation, Phys. Chem. Chem. Phys. 11 (2009) 770–775.

[21] W.-W. Zhan, Q.-L. Zhu, Q. Xu, Dehydrogenation of Ammonia Borane by Metal Nanoparticle Catalysts, ACS Catal. 6 (2016) 6892–6905. https://doi.org/10.1021/acscatal.6b02209.

[22] H. Li, Z. Yao, X. Wang, Y. Zhu, Y. Chen, Review on Hydrogen Production from Catalytic Ammonia Borane Methanolysis: Advances and Perspectives, Energy & Fuels, 2022. DOI 10.1021/acs.energyfuels.2c02314.

[23] N. Tunc, M. Rakap, Preparation and characterization of Ni-M (M: Ru, Rh, Pd) nanoclusters as efficient catalysts for hydrogen evolution from ammonia borane methanolysis, Renew. Energy. 155 (2020) 1222–1230.

[24] M. Yurderi, A. Bulut, İ.E. Ertas, M. Zahmakiran, M. Kaya, Supported copper–copper oxide nanoparticles as active, stable and low-cost catalyst in the methanolysis of ammonia–borane for chemical hydrogen storage, Appl. Catal. B Environ. 165 (2015) 169–175.

[25] N. Kang, Q. Wang, R. Djeda, W. Wang, F. Fu, M.M. Moro, M. de los A. Ramirez, S. Moya, E. Coy, L. Salmon, J.-L. Pozzo, D. Astruc, Visible-Light Acceleration of H-2 Evolution from Aqueous Solutions of Inorganic Hydrides Catalyzed by Gold-Transition-Metal Nanoalloys, ACS Appl. Mater. Interfaces. 12 (2020) 53816–53826.

[26] N. Kang, X. Wei, R. Shen, B. Li, E.G. Cal, S. Moya, L. Salmon, C. Wang, E. Coy, M. Berlande, Fast Au-Ni@ ZIF-8-Catalyzed Ammonia Borane Hydrolysis Boosted by Dramatic Volcano-Type Synergy and Plasmonic Acceleration, Appl. Catal. B Environ. (2022) 121957.

[27] S. Zhang, M. Li, L. Li, F. Dushimimana, J. Zhao, S. Wang, J. Han, X. Zhu, X. Liu, Q. Ge, H. Wang, Visible-Light-Driven Multichannel Regulation of Local Electron Density to Accelerate Activation of O-H and B-H Bonds for Ammonia Borane Hydrolysis, ACS Catal. 10 (2020) 14903–14915.

[28] Z. Hu, D. Meng, F. Lin, X. Zhu, Z. Fang, X. Wu, Plasmonic Circular Dichroism of Gold Nanoparticle Based Nanostructures, Adv. Opt. Mater. 7 (2019) 1801590.

[29] Q. Zhang, Y. Zhang, K. Xiao, Z. Meng, W. Tong, H. Huang, Q. An, Plasmonic gold particle generation in layer-by-layer 2D titania films as an effective immobilization strategy of composite photocatalytsts for hydrogen generation, Chem. Eng. J. 358 (2019) 389–397.

[30] J.R. McLaughlan, D.M.J. Cowell, S. Freear, Gold nanoparticle nucleated cavitation for enhanced high intensity focused ultrasound therapy, Phys. Med. Biol. 63 (2018) 015004.

[31] Y. Liu, Z. Zhang, Y. Fang, B. Liu, J. Huang, F. Miao, Y. Bao, B. Dong, IR-Driven strong plasmonic-coupling on Ag nanorices/W18O49 nanowires heterostructures for photo/thermal synergistic enhancement of H-2 evolution from ammonia borane,

Appl. Catal. B-Environ. 252 (2019) 164–173.

[32] S. Jo, P. Verma, Y. Kuwahara, K. Mori, W. Choi, H. Yamashita, Enhanced hydrogen production from ammonia borane using controlled plasmonic performance of Au nanoparticles deposited on TiO2, J. Mater. Chem. A. 5 (2017) 21883–21892.

[33] P. Verma, Y. Kuwahara, K. Mori, H. Yamashita, Design of Silver-Based Controlled Nanostructures for Plasmonic Catalysis under Visible Light Irradiation, Bull. Chem. Soc. Jpn. 92 (2019) 19–29.

[34] W.S. Hummers, R.E. Offeman, Preparation of graphitic oxide, J. Am. Chem. Soc. 80 (1958) 1339.

[35] B. Delley, From molecules to solids with the DMol 3 approach, J. Chem. Phys. 113 (2000) 7756–7764.

[36] J.P. Perdew, K. Burke, M. Ernzerhof, Generalized gradient approximation made simple, Phys. Rev. Lett. 77 (1996) 3865–3868.

[37] S. Grimme, Semiempirical GGA-type density functional constructed with a long-range dispersion correction, J. Comput. Chem. 27 (2006) 1787–1799.

[38] Q. Wang, D. Astruc, State of the Art and Prospects in Metal-Organic Framework (MOF)-Based and MOF-Derived Nanocatalysis, Chem. Rev. 120 (2020) 1438–1511.

[39] P. Michaud, D. Astruc, J.H. Ammeter, Electron-transfer pathways in the reduction of d6 and d7 organoiron cations by lithium tetrahydroaluminate and sodium tetrahydroborate, J. Am. Chem. Soc. 104 (1982) 3755–3757.

[40] L. Wang, Y. Zhou, J. Timoshenko, S. Liu, Q. Qiao, K. Kisslinger, M. Cuiffo, Y.-C. Chuang, X. Zuo, Y. Xue, Y. Guo, C. Pan, H. Li, C.-Y. Nam, S. Bliznakov, P. Liu, A.I. Frenkel, Y. Zhu, M.H. Rafailovich, Designing Nanoplatelet Alloy/Nafion Catalytic Interface for Optimization of PEMFCs: Performance, Durability, and CO Resistance, ACS Catal. 9 (2019) 1446–1456.

[41] G. Xu, A. Yu, Y. Xu, C. Sun, Selective oxidation of methane to methanol using AuPd@ZIF-8, Catal. Commun. 158 (2021) 106338.

[42] P. Michaud, D. Astruc, J.H. Ammeter, Electron-transfer pathways in the reduction of d^6 and d^7 organoiron cations by $LlAlH_4$ and $NaBH_4$, J. Am. Chem. Soc. 104 (1982) 3755–3757.

[43] L. Zhang, Z. Xie, J. Gong, Shape-controlled synthesis of Au–Pd bimetallic

nanocrystals for catalytic applications, Chem. Soc. Rev. 45 (2016) 3916–3934.

[44] S.K. Das, B. Mohanty, S.C. Sahu, T.J. Sruthi, B. Chakraborty, S. Basu, B.K. Jena, The experimental and theoretical insights on the interaction of AuPd bimetallic nanoentities on graphene: A study on electrocatalytic activity towards oxygen reduction reaction, Electrochim. Acta. 356 (2020) 136820.

[45] H. Kang, J.T. Buchman, R.S. Rodriguez, H.L. Ring, J. He, K.C. Bantz, C.L. Haynes, Stabilization of Silver and Gold Nanoparticles: Preservation and Improvement of Plasmonic Functionalities, Chem. Rev. 119 (2019) 664–699.

[46] Y. Dubi, I.W. Un, Y. Sivan, Thermal effects - an alternative mechanism for plasmon-assisted photocatalysis, Chem. Sci. 11 (2020) 5017–5027.

[47] A. Rossin, M. Peruzzini, Ammonia-Borane and Amine-Borane Dehydrogenation Mediated by Complex Metal Hydrides, Chem. Rev. 116 (2016) 8848–8872.

[48] F. Tong, X. Liang, Z. Wang, Y. Liu, P. Wang, H. Cheng, Y. Dai, Z. Zheng, B. Huang, Probing the Mechanism of Plasmon-Enhanced Ammonia Borane Methanolysis on a CuAg Alloy at a Single-Particle Level, ACS Catal. 11 (2021) 10814–10823.

[49] H.S. Kojori, J.-H. Yun, Y. Paik, J. Kim, W.A. Anderson, S.J. Kim, Plasmon Field Effect Transistor for Plasmon to Electric Conversion and Amplification, NANO Lett. 16 (2016) 250–254.

[50] S. Wu, Z. Xu, S. Tian, T. Luo, G. Xiong, Enhanced water evaporation under spatially gradient electric Fields: A molecular dynamics study, J. Mol. Liq. 360 (2022) 119410.

[51] Milon, M.K. Hossain, D. Roy, F. Ahmed, Boron nanocluster as a heavy metal adsorbent in aqueous environment: A DFT Study, J. Mol. Struct. 1237 (2021) 130302.Fi

[52] P. Xu, W. Lu, J. Zhang, L. Zhang, Efficient Hydrolysis of Ammonia Borane for Hydrogen Evolution Catalyzed by Plasmonic Ag@Pd Core-Shell Nanocubes, ACS Sustain. Chem. & Eng. 8 (2020) 12366–12377.

[53] Y. Zhang, Q. Li, C. Liu, X. Shan, X. Chen, W. Dai, X. Fu, The promoted effect of a metal-organic frameworks (ZIF-8) on Au/TiO_2 for CO oxidation at room temperature both in dark and under visible light irradiation, Appl. Catal. B Environ. 224 (2018) 283–294.

[54] M. Wen, S. Song, Q. Liu, H. Yin, K. Mori, Y. Kuwahara, G. Li, T. An, H. Yamashit, Manipulation of plasmon-induced hot electron transport in Pd/MoO_{3-x}@ZIF-8: Boosting the activity of Pd-catalyzed nitroaromatic hydrogenation under visible-light irradiation, Appl. Catal. B-Environ. 282 (2021) 119511.

[55] X. Su, S. Li, PVP-stabilized Co-Ni nanoparticles as magnetically recyclable catalysts for hydrogen production from methanolysis of ammonia borane, Int. J. Hydrogen Energy. 46 (2021) 14384–14394.

[56] Y. Feng, X. Zhang, Y. Shao, X. Chen, H. Wang, J. Li, M. Wu, H. Dong, Q. Liu, H. Li, Modulating the Acidic Properties of Mesoporous Mox-Ni0.8Cu0.2O Nanowires for Enhanced Catalytic Performance toward the Methanolysis of Ammonia Borane for Hydrogen Production, ACS Appl. Mater. Interfaces. 14 (2022) 27979–27993.

[57] D. Astruc, Organometallic chemistry and catalysis, Springer, 2007.

[58] X. Zhang, Y. Zhao, X. Jia, Y. Zhao, L. Shang, Q. Wang, G.I.N. Waterhouse, L. Wu, C. Tung, T. Zhang, Silica-protected ultrathin Ni3FeN nanocatalyst for the efficient hydrolytic dehydrogenation of NH_3BH_3, Adv. Energy Mater. 8 (2018) 1702780.

[59] Z. Chen, Y. Song, J. Cai, X. Zheng, D. Han, Y. Wu, Y. Zang, S. Niu, Y. Liu, J. Zhu, Tailoring the d-band centers enables Co4N nanosheets to be highly active for hydrogen evolution catalysis, Angew. Chemie. 130 (2018) 5170–5174.

Chapter 6. A sustainable system for H_2 generation and olefin hydrogenation derived by hydride reservoir complexes

6.1. Introduction

Hydrogenation of olefins is one of the most important and fundamental transformations in organic synthesis, and has a long history since the Sabatier's seminal work on catalytic hydrogenation.[1] Using gaseous hydrogen as hydrogen donor is the most comment technique for hydrogenation, but the utilization of hydrogen gas presents some problems such as transport, storage, risk of explosion and lower efficiency, which strongly demands other hydrogenation methods to be introduced. Transfer hydrogenation is an abundantly practiced technique that has been reviewed.[2] first example of transfer hydrogenation reported by van Tamelen, who used azodicarboxylic acid as a hydrogen source. Chirik *et al.* reported the bis(arylimidazol-2-ylidene) pyridine cobalt methyl complex, (^{iPr}CNC)$CoCH_3$, for the hydrogenation of inactivated, sterically hindered olefins. Spectroscopic observation reveals that it is the cobalt hydride complex, (^{iPr}CNC)CoH, obtained by hydrogenation of (^{iPr}CNC)$CoCH_3$, that facilitates the reaction.[3] Murakami *et al*. reported a solar-driven system to transfer hydrogen from ethanol to alkenes in the presence of aryl ketone under light irradiation.[4]

Late transition metal sandwich complexes such as those of the series $[FeCp(arene)]^{+/0}$ have been introduced as reservoirs of electrons,[5] protons,[6] hydrogen atoms,[7] and hydrides.[8] Hydride-rich organometallic complexes obtained by the reduction of 18-electron organometallic cations have received increasing attention due to their roles as n-type dopants, intercalated complexes, reducing agents, and hydride donors for organic semiconductors in recent scientific advances.[9-13] By transferring a hydride ion to a suitable hydride absorber substrate, such as Ph_3C^+, a hydride-rich neutral complex is converted to the corresponding cation by an initial two-electron, proton-coupled reaction. Hydricity, which refers to the free energy required to cleavage a metal-H bond, is the most commonly used parameter to describe the hydride donor ability.[14] Appel *et al*. reviewed the three primary methods for the determination of thermodynamic hydricity of metal hydrides, offering a valuable predictive tool for the prediction of chemical reactivity in a catalytic reaction[15] Glusac *et al*. reported the role of metal-free hydrides in catalysis and summarized the experimental and calculated hydricity values for more than 200 metal-free hydride donors, including carbon-, boron-, nitrogen- and silicon-based hydrides.[14] In transition-

metal organometallic chemistry, the pentahapto cyclopentadienyl (Cp) ligand has exerted a crucial influence in stabilizing organometallic complexes by occupying three of the metal's coordination sites and by providing the metal center with five valence electrons (in the neutral electron count). The introduction of five methyl substituents on the Cp ligand provides in the ligand C_5Me_5 (Cp*) that is a strongly electron-releasing ligand resulting in more stable complexes owing to the stereo-electronic stabilization benefitting from both an increased electronic density of the metal center and a large steric protection.

Herein we report a sustainable system to transfer hydrogen from ethanol and hydride reservoirs to alkenes. A series of hydride-reservoir complexes (Scheme 6.1) with different Cp methylation, was prepared using the hydride-rich (hydridic) reductant $NaBH_4$. (Scheme 6.1) The complexes are investigated for H_2 generation and as hydride donors for the hydrogenation of olefins in ethanol. The results show that **2RH** with one Cp* ligand exhibits high thermodynamic stability as well as good hydride donor capacity in the model hydrogenation of 1,1-diphenylethylene catalyzed by Pd/C. Given the stable 18-electron sandwich structure, the cationic form of **2RH**, (**2R**$^+$) is easily recycled upon precipitation of **2R** using HPF_6. The isotope experiment and tandem reaction show that the two H atoms in the produced 1,1- diphenylethane are provided from **2RH** and the methanol solvent.

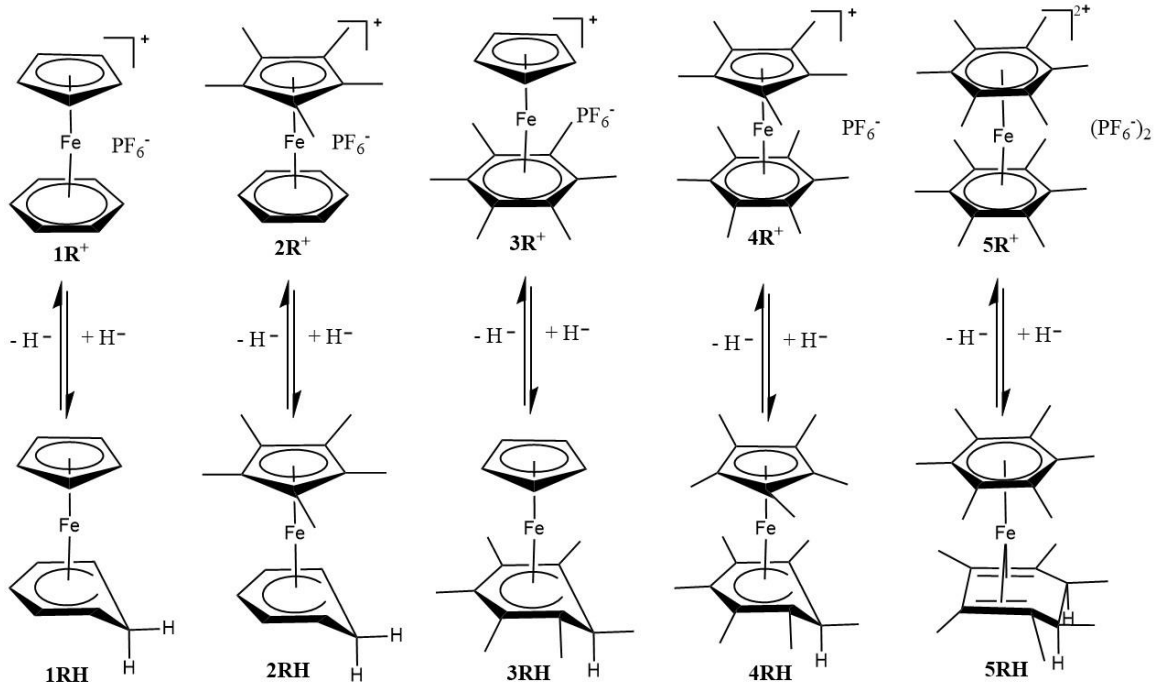

Scheme 6.1. Different iron sandwich hexafluorophosphates (empty hydride reservoirs, $\mathbf{R}^+$) and corresponding filled hydride reservoirs (**RH**).

6.2. Results and discussion

In the first step, the hydride reservoir complex was synthesized according to the literature procedure. For instance $[(\eta^5\text{-}C_5Me_5)Fe(C_6H_6)][PF_6]$ ($\mathbf{2R}^+$) (50 mg) and $NaBH_4$ (5 equiv.) were dissolved in a Schlenk flask under N_2, and the mixture was stirred overnight under room temperature. The solution changed color progressively from yellow to orange, indicating the formation of **2RH**. The pure targeted product was obtained by cannula filtration (Figure S6.1). Another four hydride reservoirs were synthesized according to the above steps (details in SI), but the temperature was increased, and the reaction time was prolonged according to the need, due to stability of the various hexafluorophosphate salts.

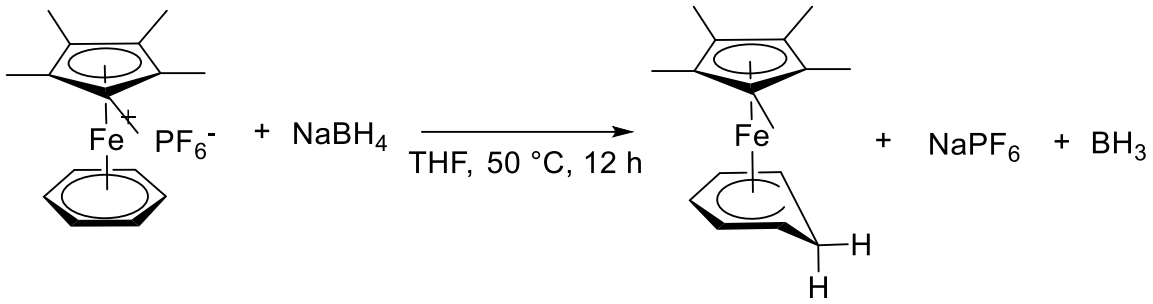

Scheme 6.2 Hydrogenation of **2R**$^+$**.**

Next, we examined hydrogenation derived by a series of hydride reservoir complexes (Scheme 6.3). Here, taken **2RH** as the example, diphenylethylene **1** (0.25 mmol, 1.0 equiv.) and 2**RH** (0.625 mmol, 2.5 equiv.) in the presence of Pd/C (2.5 mol % Pd) were stirred in 3 mL absolute ethanol (99.99%) at 25 °C under an argon atmosphere. After 18 h, Pd/C was removed by filtration and then evaporated. An aqueous 6 M HPF_6 (5 mL) solution and ether were added for extraction, and an organic phase containing the hydrogenated product was separated from an acidic aqueous phase containing the regenerated reservoir hexafluorophosphate. The volatiles were removed from the organic phase under reduced pressure to furnish the hydrogenated product in NMR-pure form in almost quantitative yield (Fig. S6.2). The acidic aqueous phase was basified and extracted with ether to recover the empty hydride reservoir complex **2R**$^+$ in 99% yield (0.62 mmol) based on the amount of **2RH** initially put in the flask. No reaction occurred when the hydrogenation reaction was performed in the absence of **2RH** or the Pd/C catalyst under the otherwise identical conditions. The recovered hydride reservoir complex **2R**$^+$ was reused and reduced to **2RH** for hydrogenation of diphenylethylene as indicated above, the NMR showing a 97% yield.

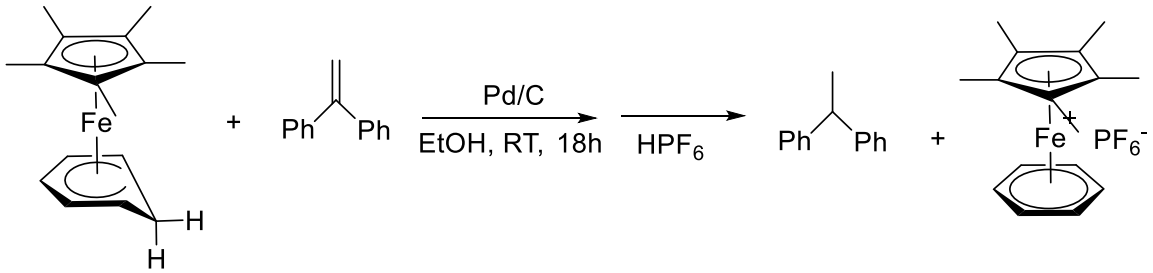

Scheme 6.3 Use of **2RH** as filled hydride reservoir complex for alkene hydrogenation

Comparing the five hydride reservoir complexes in the hydrogenation of diphenylethylene. all reactions are conducted in the same conditions as with **2RH**; after 18 h, the yield was measured. From table 2, the yield and recovery rate for hydrogenation of diphenylethylene showed differences among the various hydride reservoir complexes. More than 99% yield is obtained with **2RH** in 18 h; for other hydride reservoir complexes, the yields are lower. The reactivity is in following order, **2RH** > **5RH** > **3RH** > **4RH** > **1RH**. Furthermore, **1RH**, **3RH** and **5RH** were not fully stable under the reaction conditions, and they decomposed in the process of hydrogenation, as shown from the recovery rate (Table S6.1). In addition, the amount of hydrogen generated from the hydride reservoir complexes were measured to confirm their stabilities. The dehydrogenation of the hydride reservoir complexes was conducted in a 50-mL Schlenk flask at 25 ± 0.2 °C. Specifically, after preparation of the hydride reservoir complex (0.0625 mmol) and introduction of Pd/C (2.5% mmol) under nitrogen, the reaction flask was quickly connected via the gas outlet to a water-filled gas burette. When the gas was generated, the volume of gas evolved was determined periodically by measuring the displacement of water in the burette. 3 mL of absolute ethanol degassed for 10 min was added into the Schlenk flask. The reaction time and determination of the volume of H_2 produced began when importing the absolute ethanol by a needle. Only **2RH** and **4RH** generated hydrogen quantitatively. For **1RH, 4RH** and **5RH** as the hydrogen source, only part of the expected hydrogen was produced.

Given to above result, **2RH** showed the best stability and reactivity. Other alkenes were examined in the Pd/C catalyzed hydrogenation reaction using **2RH** as a hydrogen storage material (Fig. S6.3-S6.7). The terminal alkenes **2** and **3** were successfully hydrogenated. In the case of the aliphatic alkenes **4**, Pt/C proved to be more effective as catalyst than Pd/C. The carbonyl-containing alkenes **5** were successfully hydrogenated on both the carbon-carbon double bond and carbonyl group. The electron-deficient alkenes **6** were successfully hydrogenated.

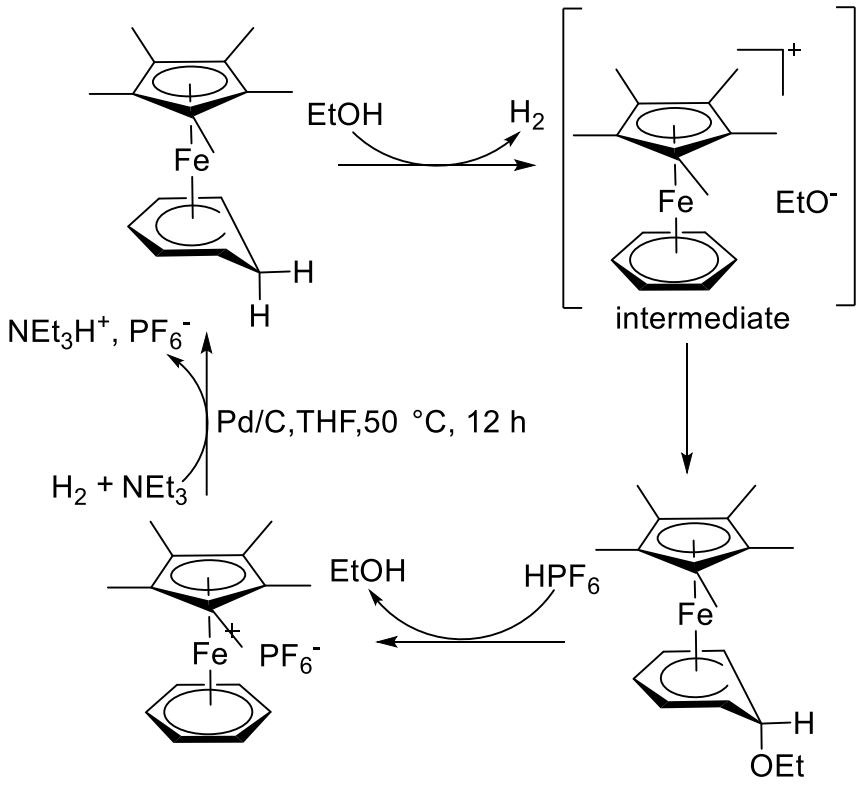

Scheme 6.4. Proposed mechanism for the cycling H_2 generation from **2RH**. The proposed intermediate and ethoxycyclohexadienyl complexes have not (yet) been characterized.

To demonstrate that the reaction (scheme 6.4) is "cyclic", $\mathbf{2R}^+$ was hydrogenated by H_2 and Pd/C as catalyst. The reaction was conducted in a 10-mL Schlenk tube, $\mathbf{2R}^+$ (0.2 mmol) with Pd/C (1.5% mmol) in 3 mL dry THF and 0.5 mL NEt_3 under 1 atm H_2 at 50°C. After 12 h, Pd/C was filtered under nitrogen and the hydride reservoir complexes with 72% yield were obtained for measurement. The NMR and MS results confirm that $\mathbf{2R}^+$ was hydrogenated by H_2 in the presence of Pd/C as catalyst. In the absence of NEt_3, the yield of **2RH** obtained is approximately stoichiometric vs. the mol Pd amount, i. e. weak.

2RH was very active and easily donated a hydride. In the reaction (Scheme 6.4), there is hydrogen generated even though we did not add any catalyst. The reaction was very fast to yield the full expected hydrogen gas within 49 s.

Mechanism

Finally, we applied the complex **2RD** to a device having two connected reaction chambers

A and B; in the chamber A containing the Pd/C catalyst, H_2 generated gaseous hydrogen that transferred to the chamber B containing the Pd/C catalyst and styrene, where hydrogenation proceeded at room temperature (Scheme 6.5). In this experiment, HD gas was generated upon reaction by Pd/C with EtOH as solvent transferred to the right tube in which hydrogenation of styrene proceeds in CD_3OD. ^1H NMR spectroscopy and gas chromatography-mass spectrometry analyses were used to detect the hydrogenation product in the right tube. The hydrogenation of styrene with generated hydrogen gas was successfully accomplished and was complete (quantitative) after 12 h at 25 °C (Fig. S6.8). Using the phenylethane methyl signals in the ^1H NMR spectrum, the total number of H atoms found for the ethyl fragment is 4 because, from the 5 H atoms of this fragment, the fifth H atom is replaced by a D atom. Moreover, the major molecular peak of 107 m/z in the mass spectrum further indicates that one D atom was transferred to styrene producing mono-deuterated phenylethane (Fig. S6.9-S6.10). These results fully confirm that one of the hydrogen atoms of H_2 comes from the hydride reservoir complex and the other from ethanol-D.

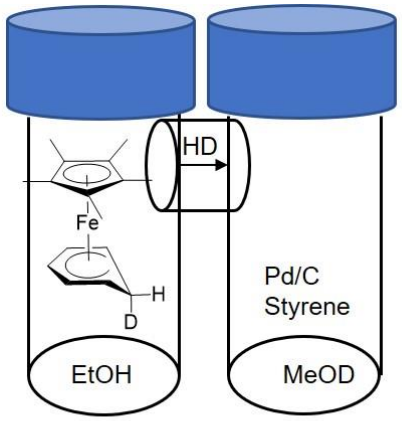

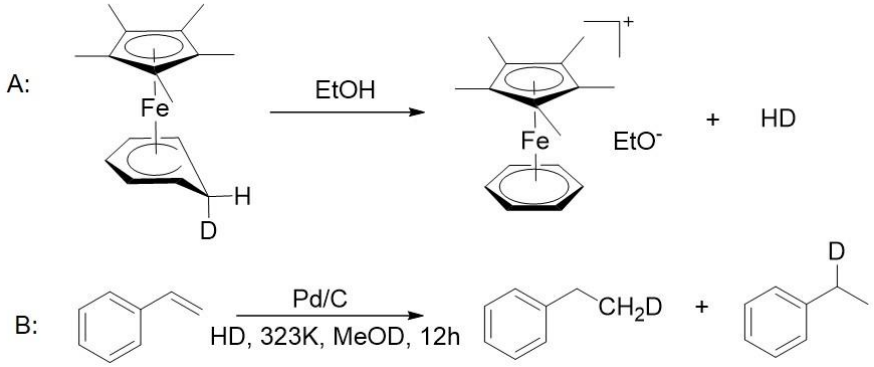

Scheme 6.5 Hydrogenation of styrene in a tandem reaction system.

6.3. Conclusion

The hydride-rich forms of various complexes [FeCp(arene]$^{+}PF_6^{-}$, abbrevated $\mathbf{R}^{+}$, i. e. the complexes [FeCp(h^5-cyclohexadienyl)], abbreviated **RH**, in which 0, 1 (either), or 2 ligands are permethylated have been probed as hydride reserviours, because both the 18-electron complexes $\mathbf{R}^{+}$ and **RH** are quite stable. This is in contrast with other hydridic 18-electron metal hydride complexes for which hydride removal by $[Ph_3C][BF_4]$ yields 16-electron metal cationic complexes that are often unstable or at least very sensitive to nucleophilic attack. The complexes **RH** are easily synthesized by reduction of by $\mathbf{R}^{+}$ with $NaBH_4$. They are also formed by PdC-catalyzed reaction of 1 atm H_2, which remarkably makes the hydride reservoir complexes also H_2 reservoir systems in adequate solvents, optimized with **2R+/2RH**. All the various **RH** complexes quickly produce H_2 in ethanol, and comparison of these various complexes of the **RH** series showed that **2RH** with permethylated Cp* but no cyclohexadienyl permethylation provides the best results (full stability and fast quantitative H_2 formation). In the presence of olefins and standard Pd/C catalyst, two reactions are compared: a single tube reaction that provides fast olefin hydrogenation, and a two-tube reaction where H_2 produced upon **2RH** ethanolysis in the first tube is transferred to the second tube containing the olefin and the Pd/C catalyst. This second reaction is considerably slower than the single-tube reaction, showing that in a single tube direct Pd-catalyzed olefin hydrogenation proceeds without H_2 intermediacy (Pd(H) formed from **2RH** directly inserts the olefin into the Pd-H bond, etc.).

6.4. Experimental section

Hydride-reservoir sandwich complexes; the example of 2RH: $[Fe(C_5Me_5)(C_6H_6)]^{+}PF_6^{-}$ (50 mg, 0.13 mmol), $NaBH_4$ (5 equiv.) and THF (20 mL) were added in a 50-mL Schlenk flask. Then, the mixture was stirred for 12 h under N_2 at room temperature. The solution changed color progressively from yellow to orange, indicating the formation of **2RH**. The solvent was removed in vacuo, providing the crude product, which was redissolved in pentane to eliminate the insoluble $NaPF_6$ salt by cannula filtration. Finally, dry pentane was removed in vacuo with a harvest of pure product (**2RH**, 47.7 mg, yield: 91%)

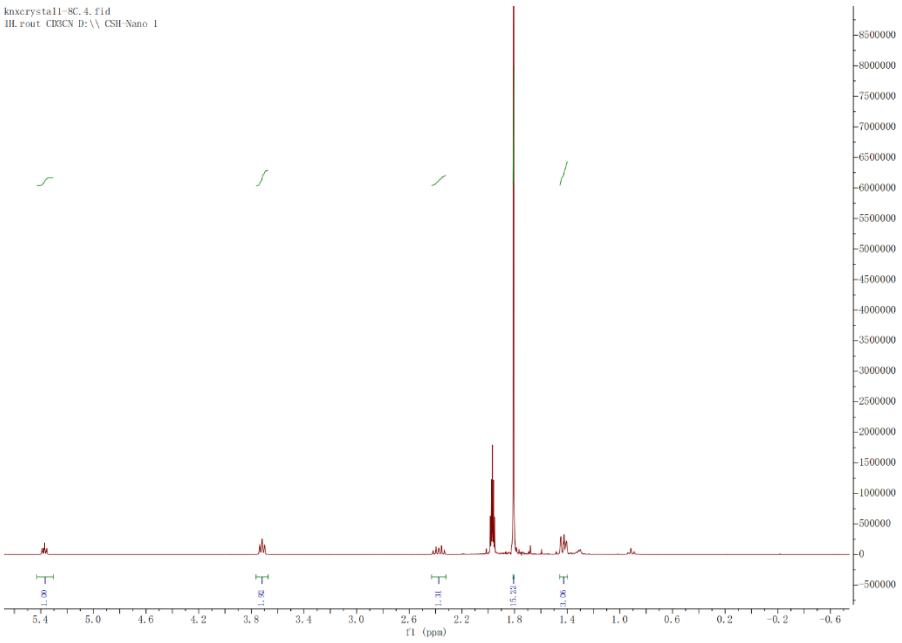

Figure S6.1. ^{1}H NMR spectrum of **2RH** (300 MHz, CD_3CN)

Hydrogenation of alkenes

2RH (95.1 mg, 0.25mmol), Pd/C (23.2 mg, 0.5% mmol Pd), diphenylethylene (35.6 mg, 0.10 mmol) and ethanol (3.0 mL) were added to an oven-dried 10 mL Schlenk tube. The vial was capped with a screw cap. The reaction mixture was stirred at 50 °C for 18 hours. Then, the resulting mixture was filtrated through a short pad of celite, and washed with AcOEt. The filtrate was concentrated under reduced pressure. The residue was dissolved in Et_2O (50 mL), and the organic layer was extracted with 6 M HCl aq. (15 mL, 3 times). The remaining organic layer was washed with H_2O (10 mL, 3 times) and sat. NaCl aq. (10 mL), and dried over Na_2SO_4. The solvent was removed under reduced pressure to give **4** (35.8 mg, 0.20 mmol, 99%) as a colorless oil. Adding HPF_6 in the acidic aqueous solutions, filtering the precipitation and washing it with water (50 mL) and Et_2O (50 mL) finally generated **2R**$^{+}$ (89.7 mg, 0.46 mmol, 97%).

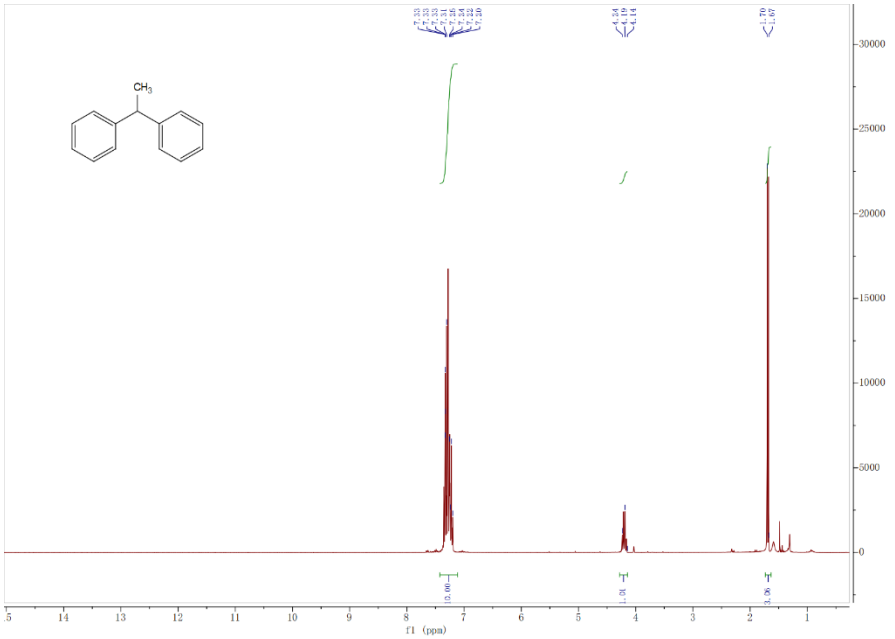

Figure S6.2 ^{1}H NMR spectrum (300 MHz, $CDCl_3$)) of the hydrogenation of 1,1-diphenylethylene **1** using **2RH** and EtOD.

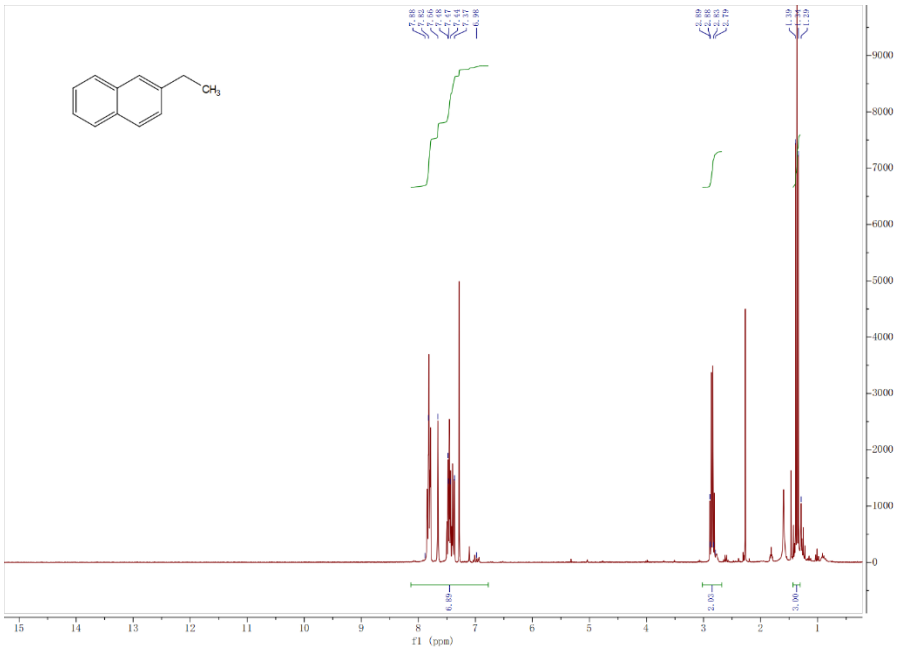

Figure S6.3 ^{1}H NMR spectrum (300 MHz, $CDCl_3$)) of the hydrogenation product **2** using **2RH** and EtOD.

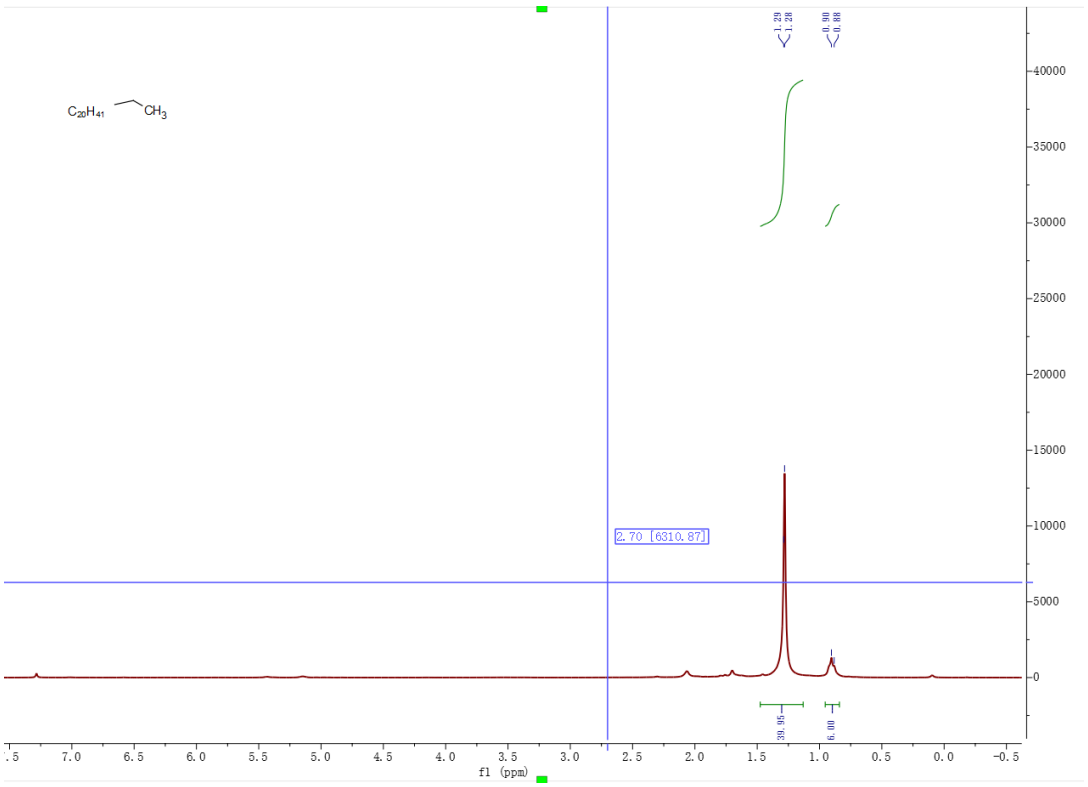

Figure S6.4 ^{1}H NMR spectrum (300 MHz, $CDCl_3$)) of the hydrogenation product **3** using **2RH** and EtOD.

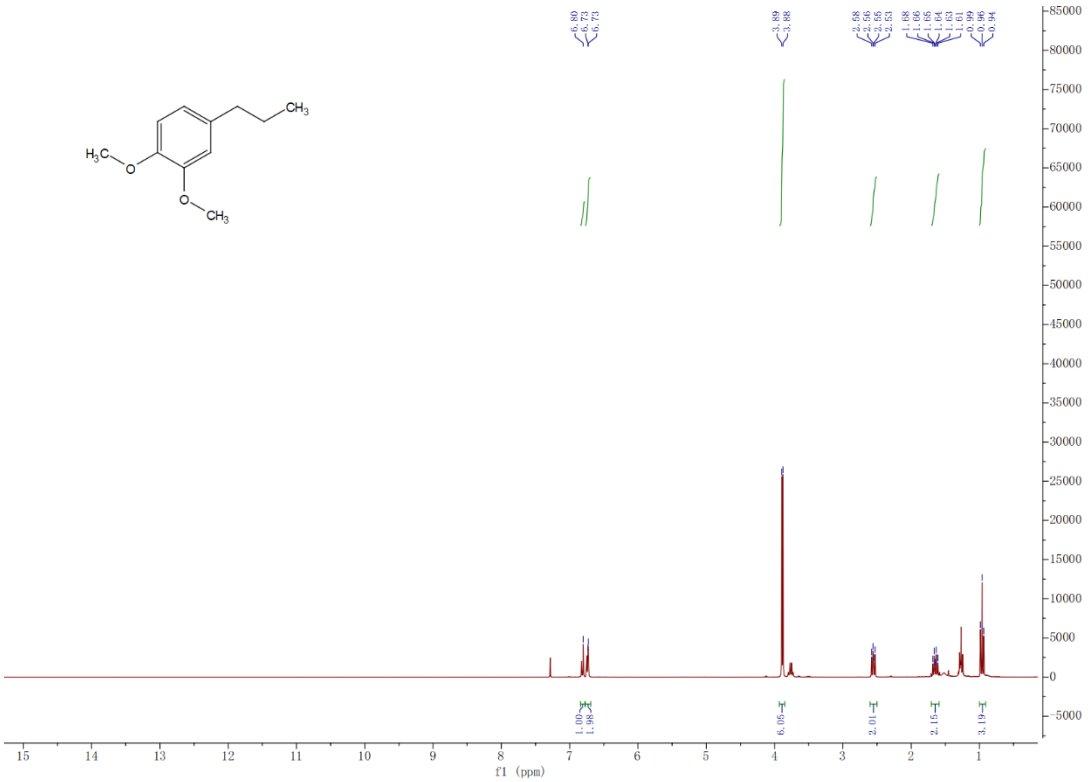

Figure S6.5 ^{1}H NMR spectrum (300 MHz, $CDCl_3$)) of the hydrogenation product **4** using **2RH** and EtOD.

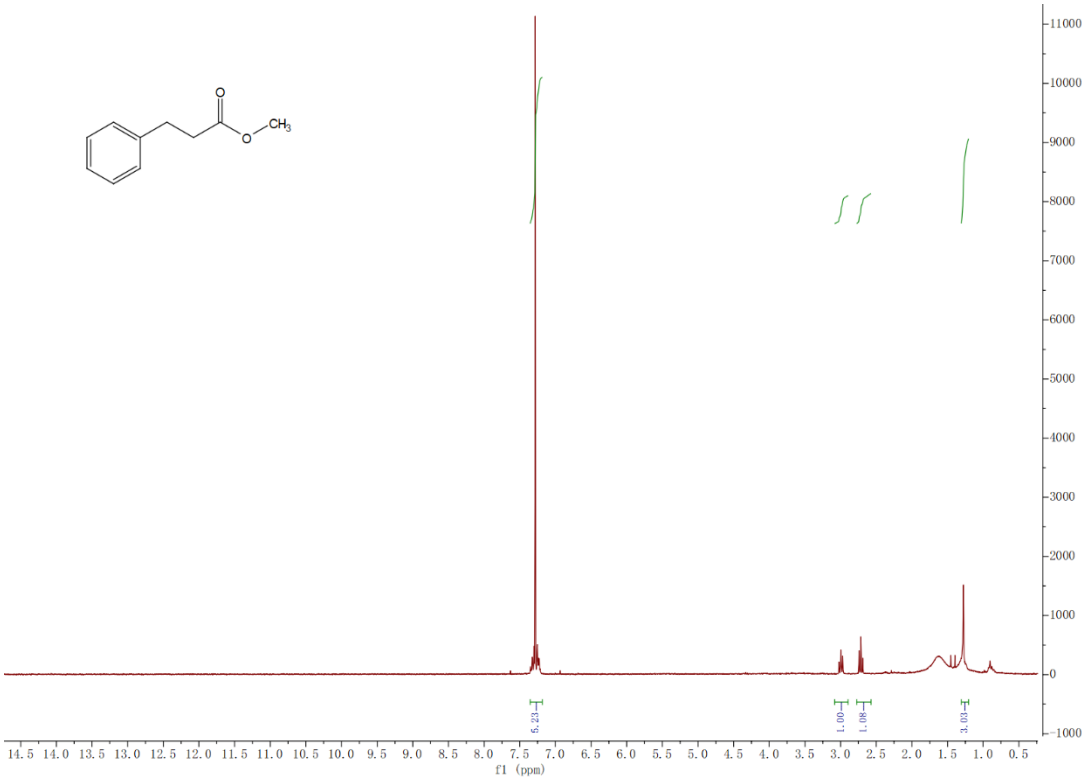

Figure S6.6 ^{1}H NMR spectrum (300 MHz, $CDCl_3$)) of the hydrogenation product **5** using **2RH** and EtOD.

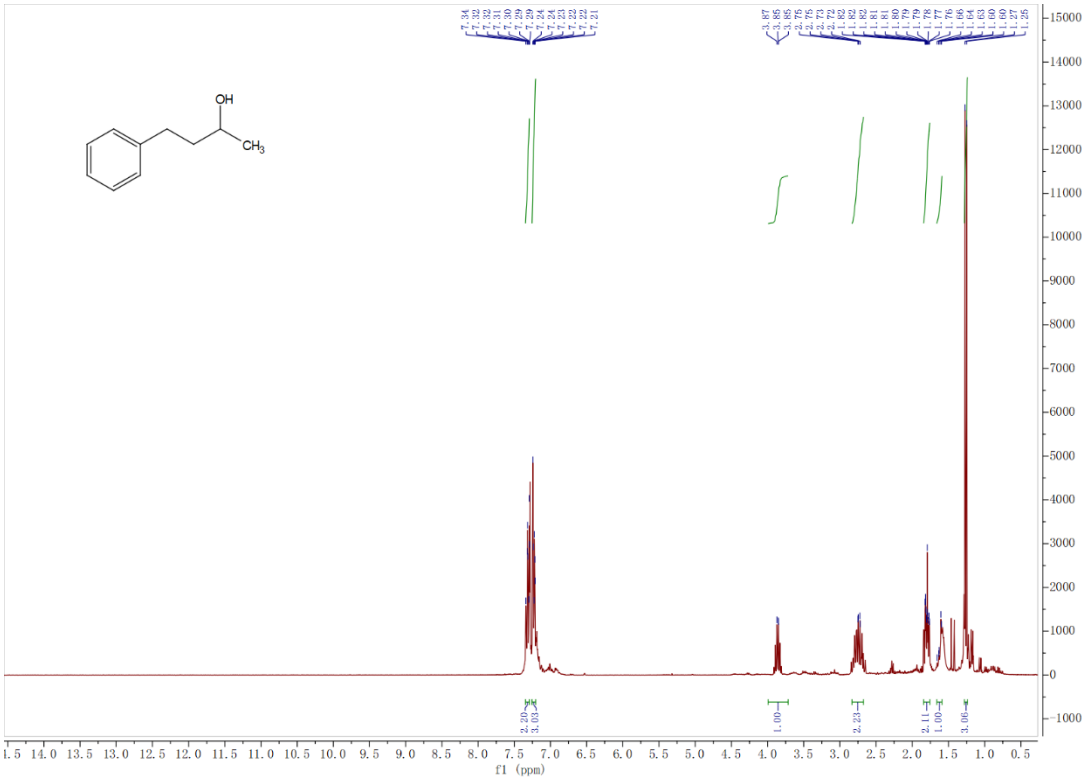

Figure S6.7 ^{1}H NMR spectrum (300 MHz, $CDCl_3$)) of the hydrogenation product **6** using **2RH** and EtOD.

"Cycling" of the H_2 generation reaction

An oven-dried 10 mL Schlenk tube containing a stirring bar was charged with **2R**$^+$ (45 mg). The Schlenk tube was then evacuated and back-filled under a hydrogen flow (this sequence was repeated three times) and finally an atmospheric pressure of H_2 was established. The dry THF were subsequently added by syringe, and the solution was warmed up to 50 ℃. After 12 h, the product was obtained and the work up gave the same hydride reservoir complex as that obtained by reduction with $NaBH_4$. Upon addition of triethylamine (3 equiv.), the operation was the same as above.

Hydrogen generation reaction.

Hydrogen generation from **2RH** was conducted in a 50-mL Schlenk flask at 25 ± 0.2 ℃. Specifically, after **2RH** preparation and removal of the solvent, 5 mL ethanol (or other

solvent) was added into the flask with a needle. The reaction time and determination of the volume of H_2 produced began when the AB solution was imported by a needle.

Table S6.1. Time and recyclability of complete hydrogen generation from **2RH** in different solvents

solvent	MeOH+H_2O	H_2O	MeOH	EtOH
Pd/C	32 s	/	59 s	98 s
No catalyst	47 s	/	63 s	104 s
recyclability	Yes	/	Yes	Yes

Hydrogenation of styrene using H_2 produced from 2RH in tandem reactions

The tandem reaction was conducted in a sealed two-chamber system. The left tube was used for hydrogen generation, and the right one was used for hydrogenation. The generated hydrogen transports to the hydrogenation reaction through the connected glass tube.

Hydrogenation of styrene: 8 mg (0.5 mmol% per AB) AuPd@ZIF-8 was added into the left tube. Meanwhile, 10 mg (1.5 mmol % per styrene) AuPd@ZIF-8 catalyst was added to the right tube. Air was removed in vacuo, and 2 mL methanol included 52 mg (0.5 mmol) styrene was injected into the right tube. Then 37.5 mg (1.215 mmol) AB dissolved in 2 mL water was injected into the left tube. After 5 min, rection was conducted at 50 °C for 12h. Then, the reaction solution was collected by centrifugation for GC-MS analysis without any work-up.

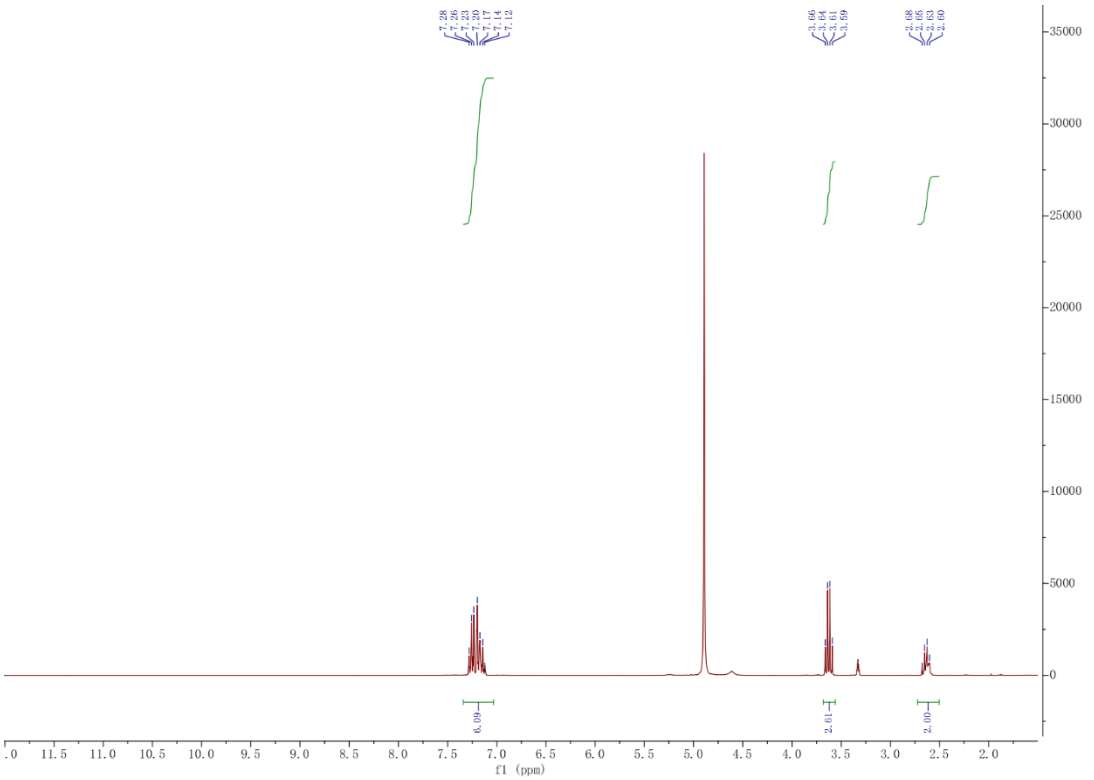

Figure S 6.8. ^{1}H NMR spectrum of the styrene hydrogenation product obtained using **2RH** and EtOD. (300 MHz, $CDCl_3$)

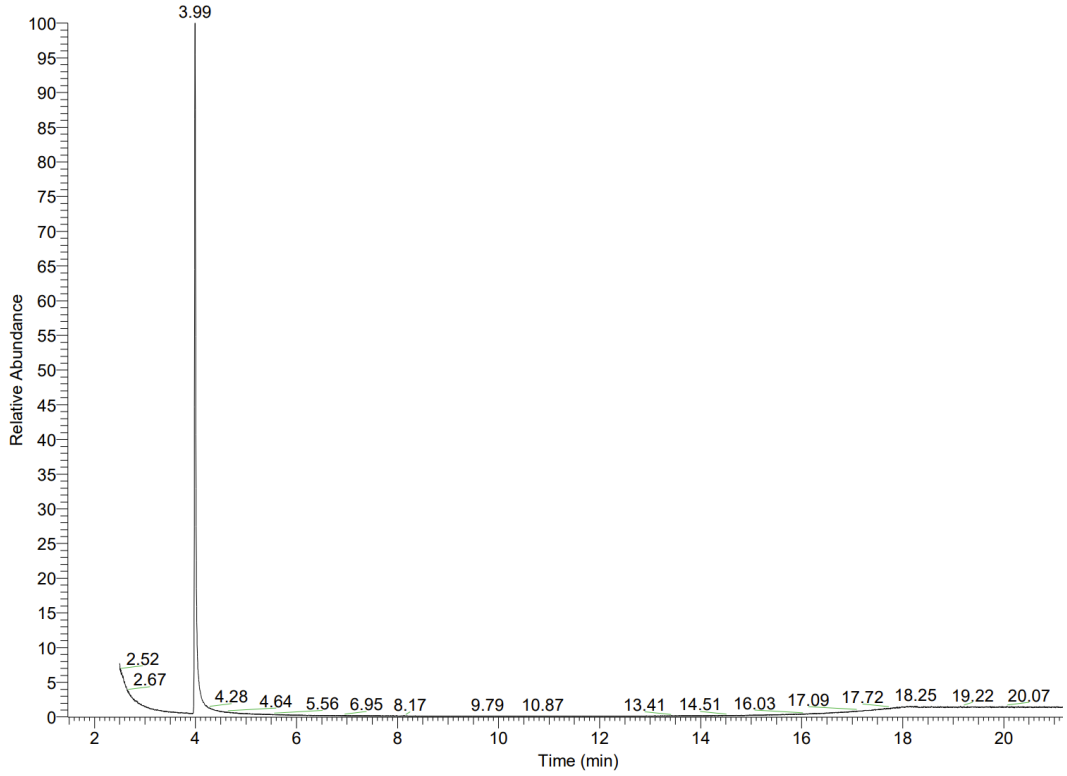

Fig. S6.9. GC-MS spectrum of the hydrogenation product of styrene.

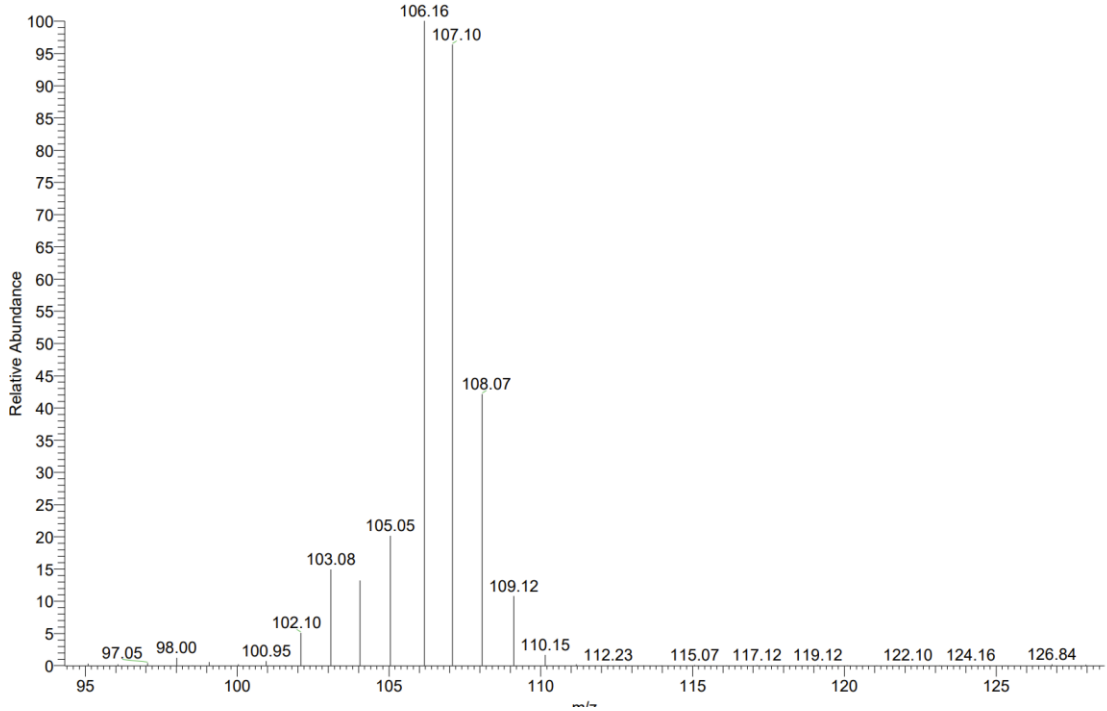

Fig. S6.10. MS spectrum at 3.99 min in Fig.S8. m/z 107.1 ($C_6H_5CHDCH_3$, $C_6H_5CHCH_2D$)

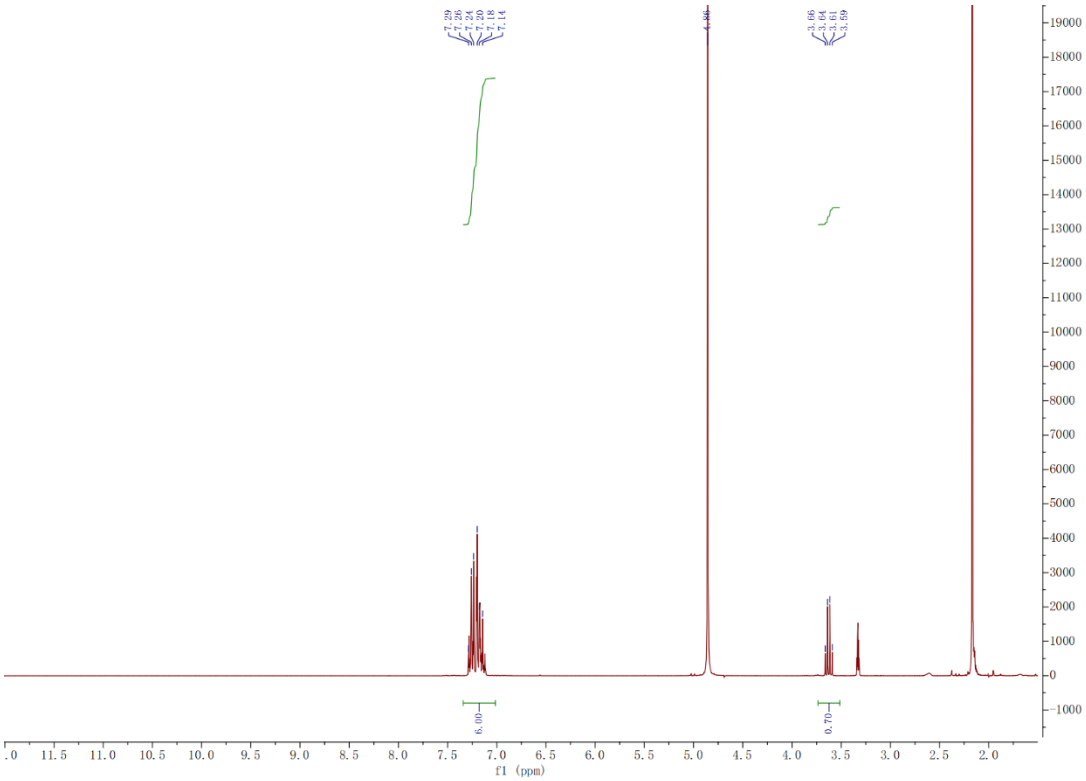

Figure S 6.11. ^{1}H NMR spectrum of the product resulting from hydrogenation of styrene using **2RH$_D$** and EtOD. (300 MHz, $CDCl_3$)

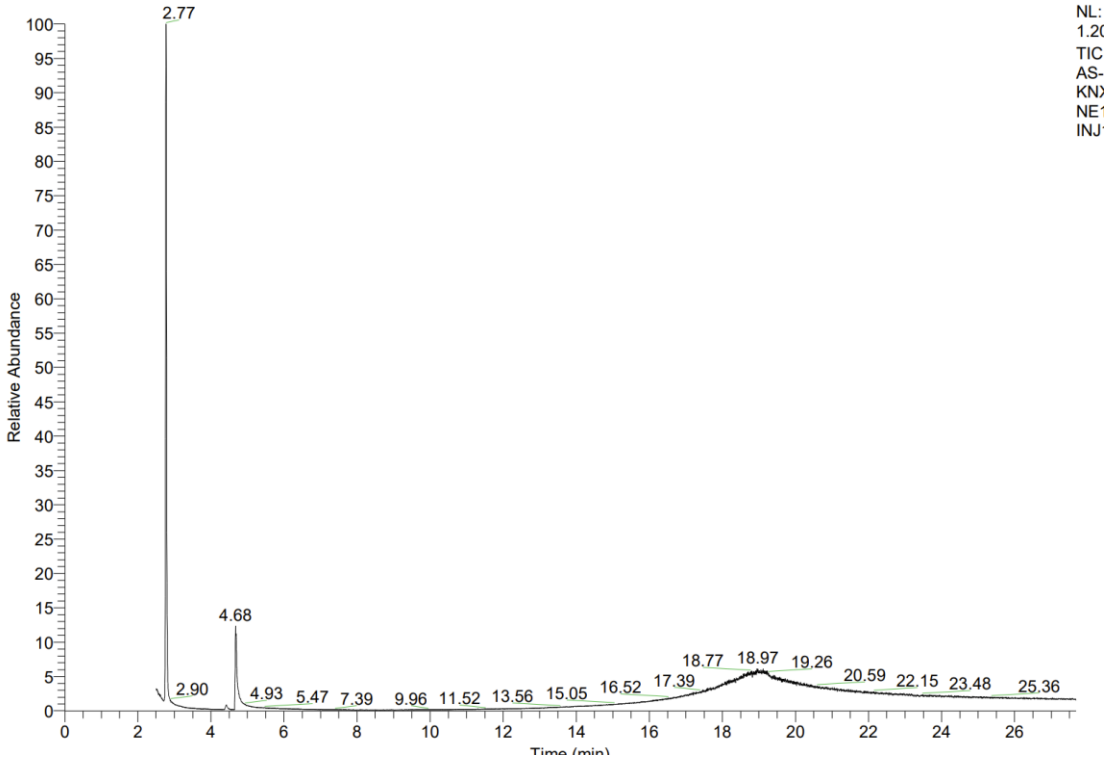

Fig. S6.12. GC-MS spectrum of the product resulting from hydrogenation of styrene.

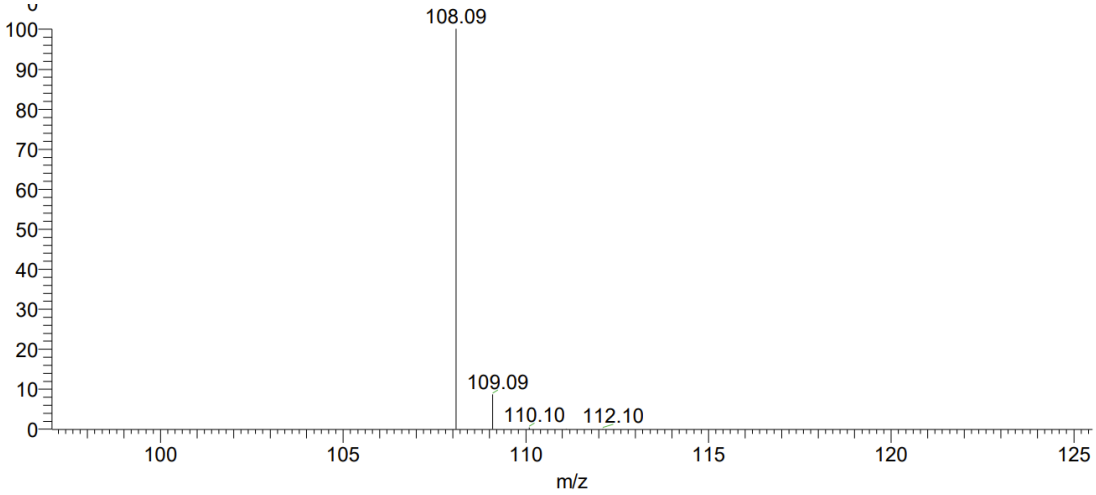

Fig. S6.13. MS spectrum at 2.77 min in Fig.S11. m/z 108.1 ($C_6H_5CHD_2CH_3$,)

6.5. References

1. Wang, D.; Astruc, D. The Golden Age of Transfer Hydrogenation. *Chem. Rev.* **2015,** *115*, 6621-6686.

2. Zhang, G.; Scott, B. L.; Hanson, S. K. Mild and Homogeneous Cobalt-Catalyzed Hydrogenation of C=C, C=O, and C=N Bonds. *Angew. Chem. Int. Ed.* **2012,** *51*, 12102-12106.

3. Yu, R. P.; Darmon, J. M.; Milsmann, C.; Margulieux, G. W.; Stieber, S. C. E.; DeBeer, S.; Chirik, P. J. Catalytic Hydrogenation Activity and Electronic Structure Determination of Bis(arylimidazol-2-ylidene)pyridine Cobalt Alkyl and Hydride Complexes. *J. Am. Chem. Soc.* **2013,** *135*, 13168-13184.

4. Ishida, N.; Kamae, Y.; Ishizu, K.; Kamino, Y.; Naruse, H.; Murakami, M. Sustainable System for Hydrogenation Exploiting Energy Derived from Solar Light. *J. Am. Chem. Soc.* **2021,** *143*, 2217-2220.

5. Astruc, D. ; Hamon, J.-R. ; Althoff, G. ; Román, E. ; Batail, P. ; Michaud, P. ; Mariot, J.-P. ; Varret, F. ; Cozak, D. *J. Am. Chem. Soc.*, 1979, *101*, 5445-5447.

6. Hamon, J.-R. ; Saillard, J.-Y. ; Le Beuze, A. ; McGlinchey, M. ; Astruc, D. *J. Am. Chem. Soc.*, 1982, *104*, 7549-7555.

7. Michaud, P. ; Astruc, D. *Angew. Chem. Int. Ed. Engl.*, 1982, *21*, 918.

8. Astruc, D. in "*Mechanisms and Processes in Molecular Chemistry. In Honor of Bianca Tchoubar*" Astruc, D. Ed., Gauthier- Villars, Paris, *New J. Chem.*, 1992, *16*, 305-328.

9. Fu, F.; Wang, Q.; Ciganda, R.; Martinez-Villacorta, A. M.; Escobar, A.; Moya, S.; Fouquet, E.; Ruiz, J.; Astruc, D. Electron- and Hydride-Reservoir Organometallics as Precursors of Catalytically Efficient Transition Metal Nanoparticles in Water. *Chem. Eur. J* **2018,** *24*, 6645-6653.

10. Szajek, L. P.; Shapley, J. R. Unexpected synthesis of CpIr(.eta.4-C5H6) and a proton and carbon-13 NMR comparison with its cobalt and rhodium congeners. *Organometallics* **1991,** *10*, 2512-2515.

11. Pfeffer, M.; Grellier, M., 7.01 - Cobalt Organometallics. In *Comprehensive Organometallic Chemistry III*, Mingos, D. M. P.; Crabtree, R. H., Eds. Elsevier: Oxford, 2007; pp 1-119.

12. Koelle, U.; Fuss, B.; Rajasekharan, M. V.; Ramakrishna, B. L.; Ammeter, J. H.; Boehm, M. C. Pentamethylcyclopentadienyl transition-metal complexes. 7. Electrochemistry of transition-metal .pi.-complexes. 7. Cyclopentadienyl (arene)cobalt

cations: preparation, electrochemical reduction, and spectroscopic investigation of the paramagnetic d7 monocations. *J. Am. Chem. Soc.* **1984,** *106*, 4152-4160.
13. Zhang, S.; Moudgil, K.; Jucov, E.; Risko, C.; Timofeeva, T. V.; Marder, S. R.; Barlow, S. Organometallic hydride-transfer agents as reductants for organic semiconductor molecules. *Inorg. Chim. Acta* **2019,** *489*, 67-77.
14. Ilic, S.; Alherz, A.; Musgrave, C. B.; Glusac, K. D. Thermodynamic and kinetic hydricities of metal-free hydrides. *Chem. Soc. Rev.* **2018,** *47*, 2809-2836.

Conclusion and Perspectives

In this thesis, our investigation focused on the design and catalytic application of late transition metal nanomaterials and hydride-reservoir complexes with four areas.

1） The synthesis, optimization and catalytic properties of LTMNPs stabilized by “click” TEG-dendrimers for hydrogen evolution reaction from sodium borohydride.

2） The light effect for Au-based alloys stabilized by “click” TEG-dendrimers for hydrogen evolution reaction from sodium borohydride and ammonia borane .

3） The synthesis, optimization and catalytic properties AuNi alloy supported by ZIF-8 for hydrogen evolution reaction from ammonia borane and discussion about visible light enhancement.

4） Efficient light-boosted tandem hydrogen production and selective alkyne semi-hydrogenation upon ammonia-borane methanolysis catalyzed by AuPd@ZIF-8

5） The design, synthesis of organometallic hydride-reservoir complexes for H_2 generation and the hydrogenation of olefins.

Hydrogen is efficiently generated upon “click” dendrimer-supported catalysis of $NaBH_4$ hydrolysis by a series mono- and bimetallic nanoparticles (NPs) of the late transition metals. Among the monometallic NPs, PtNPs show the best performances, Co being the best first-raw transition metal. A remarkable synergy between Pt and Co in Pt/CoNP@dendrimer is also disclosed, compared with various other bimetallic NP catalysts, achieving a TOF of 303 $mol_{H2}\cdot mol_{catal.}^{-1}\cdot min^{-1}$ when the ratio of Pt to Co is 1:1. In the presence of NaOH, the catalytic activity is boosted for all monometallic NPs except PtNPs, but NaOH exerted a negative influence on the bimetallic NP catalysts. The kinetic studies with the catalyst Pt_1Co_1NP@dendrimer involve in particular a primary kinetic isotope effect k_D/k_H = 3.41 obtained for the hydrolysis reaction with D_2O, suggesting that O-H bond cleavage of water is involved in the rate-determining step, and an overall reaction mechanism is proposed.

Then visible-light irradiation of aqueous solutions of ammonia-borane (AB) or $NaBH_4$ containing “click”-dendrimer-stabilized alloyed nanocatalysts composed of nanogold and

another late transition-metal nanoparticle (LTMNP) highly enhances catalytic activity for H_2 generation while also inducing alloy to Au core@M shell nanocatalyst restructuration. In terms of visible-light-induced acceleration of H_2 production from both AB and $NaBH_4$, the Au_1Ru_1 alloy catalysts show the most significant light boosting effect. Au-Rh and Au-PtNPs are also remarkable with total H_2 release time from AB and $NaBH_4$ down to 1.3 min at 25°C (AuRh), three times less than in the dark, and Co is the best earth-abundant metal alloyed with nanogold. This boosting effect is explained by the transfer of plasmon-induced hot electron from the Au atoms to the LTMNP atoms facilitating water O-H oxidative addition on the LTMNP surface, as shown by the large primary kinetic isotope effect k_H/k_D upon using D_2O obtained for both AB and $NaBH_4$. The second simultaneous and progressive effect of visible-light irradiation during these reactions, alloy to Au core@M shell restructuration, enhances the catalytic activity in the recycling, because, in the resulting Au core@M shell, the surface metal (such as Ru) is much more active that the original Au-containing alloy surface in dark reactions. There is no light effect on the rate of hydrogen production for the recycled nanocatalyst due to the absence of Au on the NP surface, but it is still very efficient in hydrogen release during 4 cycles, due to the initial light-induced restructuration, although it is slightly less efficient than the original nanoalloy in the presence of light. The dendritic triazole coordination on each LTMNP surface appears to play a key role in these remarkable light-induced processes.

Moreover, AuNi@ZIF-8 alloys are very efficient nanocatalysts for H_2 evolution upon ammonia borane hydrolysis under visible-light illumination with turnover frequency 3.4 times higher than with the monometallic Ni catalyst in the dark. This improvement is attributed to dramatic volcano-type positive synergy optimized in $Au_{0.5}Ni_{0.5}$@ZIF-8, for which ZIF-8 is by far the superior support, as well as to the localized surface plasmon resonance induced between 450 and 620 nm. Infrared spectra analysis and tandem reaction confirm the origin of the hydrogen atoms, reveal the reaction mechanism, and suggest how the cleavage of the B–H and O–H bonds proceeds in this reaction. Deuteration experiments with D_2O including primary kinetic isotope effects and density functional theory calculation under both dark and visible light conditions show that activation of H_2O always is the rate-determining step.

Finally, a series of hydride-reservoir complexes with different Cp methylation were prepared using the hydride-rich (hydridic) reducing agent $NaBH_4$. When the complexes were mixed with ethanol, **2RH** in 1 min showing rapid H_2 evolution within 1 min. After H_2 evolution, the complex $\mathbf{2R^+}$ is recovered by precipitation using HPF_6. As for 1H, rapid H_2 evolution (within 1 min) was also observed when **1RH** was mixed with methanol, but it could not be recovered, indicating that **1RH** had decomposed. In contrast, **3RH** was inert to hydrogen evolution but could be recycled when mixed with methanol. The hydrogenation of 1,1-diphenylethylene by these complexes was also investigated as a model reaction in the presence of a Pd/C catalyst. The results show that **2RH** completes the reaction at room temperature (25°C), while **3RH** requires a higher temperature (50°C) and **1RH**, in contrast, requires a lower temperature (0°C) to complete the reaction. Isotope experiments and tandem reactions using **2RH** showed that the two H atoms in the resulting 1,1-diphenylethane were supplied by **2RH** and methanol solvent. These results can be attributed to variations in the thermodynamic stability and hydride donor capacity of the three complexes. It is known that permethylation of at least one Cp ligand stabilizes metallocenes and other organometallics because of the stereoelectronic influence of the five methyl substituents and the substantial steric protection of Cp*. Thus, for **2RH** with one Cp* ligand, it has not only considerable thermodynamic stability but also desirable chemical activity due to the methylation of its Cp* ligand, which leads to the best performance of 2RH in H_2 evolution and hydrogenation reactions at room temperature. **1RH** with a non-methylated ligand is chemically active but loses stability; **3RH** with a fully methylated ligand is thermodynamically stable but requires high energy to drive its hydride release.

In summary, our thesis has led to progress in the development of current knowledge on late transition metal nanomaterials and hydrogen-rich complexes for catalytic applications. Through the study of dendrimer and ZIF-8 stabilized transition metal NPs, we have gained a good understanding of the relationship between nanoparticle stability, catalytic performance. The studies in hydride rich metal complex stabilized transition metal NPs provide a new strategy for efficient H_2 generation and olefin hydrogenation. The hydrogen evolution and hydrogenation reactions occurring in the presence of hydride rich organometallic complexes provide an ideal approach to the development of recyclable H_2

generation systems and their utilizations.

The PhD study has provided us with a good understanding of the parameters that guide the design, efficiency, stability, recyclability of nanoparticles and their catalytic uses, and has enhanced our unprecedented understanding of simple and robust sandwich systems that regulate simple H_2 generation as well as substrate hydrogenation avoiding H_2 intermediacy under ambient conditions.

Publications related to this work

Kang, N., Djeda, R., Wang, Q., Fu, F., Ruiz, J., Pozzo, J. L., Astruc, D. (2019). Efficient "Click"-Dendrimer-Supported Synergistic Bimetallic Nanocatalysis for Hydrogen Evolution by Sodium Borohydride Hydrolysis. *ChemCatChem*, *11*(9), 2341-2349.

Kang, N., Wang, Q., Djeda, R., Wang, W., Fu, F., Moro, M. M., Moya, S., Coy, E., Salmon, L., Astruc, D. (2020). Visible-Light Acceleration of H2 Evolution from Aqueous Solutions of Inorganic Hydrides Catalyzed by Gold-Transition-Metal Nanoalloys. *ACS Applied Mater. Interfaces*, *12*(48), 53816-53826.

Kang, N., Wei, X., Shen R., Li B., Cal, E., Moya, S., Salmon, L., Wang, C., Coy, E., Berlande, M., Pozzo, J-L., Astruc, D., Fast Au-Ni@ZIF-8-Catalyzed Ammonia Borane Hydrolysis Boosted by Dramatic Volcano-Type Synergy and Plasmonic Acceleration. *Applied Catal. B Environ.* (accepted)

Zhao, Q.; **Kang, N.**; Martínez Moro, M.; Guisasola, E.; Moya, S.; Coy, E.; Salmon, L.; Liu, X.; Astruc, D. Sharp Volcano-Type Synergy and Visible Light Acceleration in H_2 Release upon $B_2(OH)_4$ Hydrolysis Catalyzed by Au-Rh@Click-Dendrimer Nanozymes. *ACS A.E.M.* **2022,** *5*, 3834–3844.

Zhao, Q.; Espuche, B.; **Kang, N.**; Moya, S.; and Astruc, D. Cobalt sandwich-stabilized rhodium nanocatalysts for ammonia borane and tetrahydroxydiboron hydrolysis. *Inorg. Chem. Front.*, 2022. 9, 4651-4660